Membrane Protein Nanoclustering as a Functional Unit of Immune Cells

-from nanoscopy to single molecule dynamics-

Juan Andrés Torreño Piña

ICFO-Institut de Ciències Fotòniques
Universitat Politècnica de Catalunya
Barcelona, 2 October 2015

Membrane Protein Nanoclustering as a Functional Unit of Immune Cells

-from nanoscopy to single molecule dynamics-

Juan Andrés Torreño Piña

under the supervision of

Professor María F. García Parajó

submitted this thesis in partial fulfillment
of the requirements for the degree of

DOCTOR

by the

Universitat Politècnica de Catalunya
Barcelona, 2 October 2015

Thesis Supervisor: Prof. Maria Garcia-Parajo (ICREA, ICFO-The Institute of Photonic Sciences, Spain)

Thesis Co-Supervisor: Dr. Carlo Manzo (ICFO-The Institute of Photonic Sciences, Spain)

Thesis Committee Members:

1. Prof. Vincenzo Cerundolo (University of Oxford, UK)
2. Prof. Gerhard Schütz (Technische Universität Wien, Austria)
3. Prof. Pau Gorostiza (ICREA, IBEC-Institute of Bioengineering of Catalonia, Spain)
4. Prof. Melike Lakadamyali (ICFO-The Institute of Photonic Sciences, Spain)
5. Dr. Alessandra Cambi (Radboud University, The Netherlands)

a Lidia, por haberlo hecho posible.

Table of Contents

Abstract

State-of-the-art biophysical techniques featuring high temporal and spatial resolution have allowed for the first time the direct visualization of individual transmembrane proteins on the cell membrane. These techniques have revealed that a large amount of molecular components of the cell membrane do not organize in a random manner but they rather grouped together forming so-called clusters at the nanoscale. Moreover, the lateral behavior of these clusters shows a great dependence on the compartmentalization of the cell membrane by, e.g., the actin cytoskeleton at multiple temporal and spatial scales. Since these lateral and temporal organizations have been shown to be crucial for the regulation of the biological activity by these transmembrane proteins, the understanding of the spatiotemporal behavior of membrane receptors, and of proteins in general, is a necessary step towards understanding the biology of the cell. Protein nanoclustering and membrane compartmentalization have been shown to play a crucial role on leukocytes, particularly on the surface of antigen presenting cells. Hence, the direct visualization of membrane proteins on the cell membrane of antigen presenting proteins represents a crucial step in understanding how an immune response can be controlled by leukocytes at the molecular level.

In Chapter 1, the immune system, the membrane receptor DC-SIGN and the antigen presenting protein CD1d are briefly introduced. Moreover, recent advances in superresolution microscopy and single particle tracking techniques which allow the study of membrane proteins at the nanoscale are discussed. Finally, an updated review of protein nanoclustering on the cell membrane shows examples of the importance of protein nanoclustering in regulating biological function in the immune system. Chapter 2 presents the quantitative methodology for analyzing STED nanoscopy images and multi-color single particle tracking data used throughout this thesis. In particular, we have developed a new algorithm, which reconstructs STED nanoscopy images based on the Bayesian Inference Criterion. The algorithm faithfully reconstructs raw STED nanoscopy images generating new super-resolution synthetic images with higher lateral resolution than the original STED images. Chapter 2 also describes the single-molecule fluorescence sensitive microscopes implemented in this thesis for multi-color single particle tracking experiments and the corresponding data analysis. At the end of Chapter 2, cartography maps combining high temporal with micron-scale spatial information on the basis of single-molecule detection are presented.

The following chapters in this thesis describe the major results obtained on two important receptors of the immune system. In Chapter 3, we address the role of the neck region of DC-SIGN in fine-tuning the nanoclustering degree of DC-SIGN on the cell membrane. Moreover, Chapter 3 also links the nanoclustering capability of DC-SIGN with its virus binding capability. The meso-scale organization of DC-SIGN and its dependence on a glycan-based connectivity is addressed on Chapter 4. This glycosylation network enhances the interaction between DC-SIGN and clathrin beyond stochastic random encountering. In Chapter 5, we showed that DC-SIGN shows subdiffusive behavior and weak ergodicity breaking (wEB). Moreover, we show that weak ergodicity breaking on the diffusion of DC-SIGN is incompatible with its immobilization on the plasma membrane, as previously shown for other proteins and well-described using the continuous time random walk (CTRW) model. Instead, our data are more consistent with a model in which the plasma membrane is composed of "patches" that change in space in time, so that the receptor experiences changes in diffusivity as it diffuses through these patches. Importantly, we show that weak ergodicity breaking of DC-SIGN correlates with its nanoclustering degree and biological function, establishing for the first time a relationship between ergodicity breaking and function.

In Chapter 6, we demonstrate that the antigen presenting protein CD1d organizes in nanoclusters on the cell membrane of antigen presenting cells whose size and density are tightly controlled by the actin cytoskeleton. Moreover, we also showed that this cytoskeletal control of the CD1d nanoclustering predominantly occurs on the pool of CD1d that has undergone lysosomal recycling, including under inflammatory conditions. We also showed a clear correlation between an enhanced CD1d nanoclustering and enhanced invariant Natural Killer T (iNKT) cell activation defining a new mechanism by which antigen presenting cells can control iNKT cell activation or even autoreactivity. Finally, in Chapter 7 we summarize the main results of this thesis and highlight future experiments that will expand the knowledge obtained so far regarding the role of plasma membrane organization and biological regulation.

Resumen

Gracias a su alta resolución temporal y espacial, las técnicas biofísicas de última generación han permitido la observación directa de proteínas de transmembrana de forma individual en la membrana celular. Estas técnicas han mostrado que la organización de una gran parte de las proteínas de transmembrana no es aleatoria sino que éstas están agrupadas en la membrana celular formando nano-agregados, o "clusters". A su vez, se ha observado que la formación de dichos "clusters" depende de compartimentos de la membrana celular que puede estar regulados por distintos componentes moleculares, como por ejemplo el citoesqueleto de actina en diversas escalas de espacio y tiempo. Estas técnicas también han demostrado que la organización lateral de proteínas en la membrana celular juega un papel determinante en la regulación de la actividad biológica de dichas proteínas. Por tanto, entender esta organización lateral es un paso crucial para un entendimiento más global de la función celular a la escala molecular. En el caso concreto del sistema inmune, se ha demostrado que el agrupamiento de proteínas y los compartimentos de la membrana celular juegan un papel determinante en las células presentadoras de antígenos a la hora de controlar la iniciación de una respuesta inmune. Por tanto, la visualización directa de proteínas de membrana en células presentadoras de antígenos a la escala nanométrica representa un paso crucial en el entendimiento del sistema inmune y en un futuro desarrollo de terapias basadas en el sistema inmune humano.

En el primer capítulo de esta tesis, se presentará al lector una breve introducción del sistema inmune y una descripción general de las dos proteínas que se han estudiado extensivamente en esta tesis: el receptor reconocedor de patógenos DC-SIGN y la proteína presentadora de antígenos glicolipídicos CD1d. Se discutirán además los últimos avances en técnicas de microscopía de fluorescencia con alta resolución temporal y espacial que permiten el estudio de proteínas a la escala nanométrica. Finalmente, el primer capítulo concluye con una revisión de los últimos avances en la caracterización de la organización lateral de proteínas de membrana mostrando cómo dicha organización determina la función biológica de estas proteínas.

En el capítulo 2, se presentan los distintos tipos de metodología utilizados en esta tesis para cuantificar imágenes de microscopía de super-resolución STED así como para analizar datos provenientes del seguimiento de partículas individuales usando varios colores. En concreto, hemos desarrollado un algoritmo que reconstruye imágenes de STED basado en el método de inferencia bayesiano. El algoritmo es capaz de reconstruir, paso a paso, imágenes originales STED para producir imágenes sintéticas

con una resolución lateral mayor que la original. En el capítulo 2 también se presenta una descripción de los microscopios de detección de moléculas individuales por fluorescencia implementados y utilizados a lo largo de esta tesis, y que permiten el estudio de la dinámica de partículas individuales en células vivas. Además, se describen como se han analizado dichos experimentos tanto en el caso de uno o varios colores. Al final del capítulo 2 se presenta una nueva metodología desarrollada en esta tesis que permite el estudio lateral de proteínas de membrana con una alta resolución temporal y una escala espacial de orden de micras y a la que hemos denominado mapas cartográficos.

Los siguientes capítulos de esta tesis se enfocan en el estudio de dos importantes proteínas involucradas en el sistema inmune. En el capítulo 3 se describe como la parte central de la estructura del receptor captador de patógenos DC-SIGN determina su grado de nano-agrupamiento sobre la membrana celular. A su vez, este agrupamiento tiene una incidencia clave en la capacidad de DC-SIGN en unirse a partículas virales. La organización de DC-SIGN a la escala mesoscópica y la dependencia de dicha organización de una conectividad en la membrana celular basada en la glicosilación de proteínas es descrita en el capítulo 4. Además, dicha conectividad promueve la interacción entre DC-SIGN y clatrina pudiendo ser determinante para la endocitosis de patógenos mediante DC-SIGN y clatrina. En el capítulo 5 descubrimos que DC-SIGN tiene un comportamiento que no solo es sub-difusivo en la membrana celular sino que también conlleva a la ruptura de ergodicidad por parte de este receptor. Además, demostramos que la ruptura de la ergodicidad por parte de DC-SIGN no es compatible con procesos de inmovilización temporales característicos del modelo “continous time random walk” (CTRW). Por el contrario, nuestros datos son consistentes con un modelo donde la difusión de la partícula cambia constantemente en el espacio y en el tiempo. De manera importante, demostramos que la ruptura de ergodicidad de DC-SIGN correlaciona directamente con su capacidad de agregación así como con su función biológica.

En el capítulo 6 de esta tesis describimos como la molécula CD1d forma nano-agrupamientos en la membrana celular cuyo tamaño y densidad son controlados por el citoesqueleto de actina. Además, observamos que dicho control mayoritariamente sucede cuando CD1d ha sido reciclado a través de compartimentos lisosomales, incluyendo procesos inflamatorios. También mostramos como la activación de las células iNKT correlaciona con un mayor nanoagrupamiento de CD1d en la membrana celular. Esto define un nuevo mecanismo por el cual las células presentadoras de antígenos controlan la activación de las células iNKT no solo ante antígenos presentados por CD1d sino también ante glicolípidos propios del cuerpo humano.

Finalmente, en el capítulo 7 se discuten las conclusiones generales de esta tesis y se sugieren experimentos a futuro de manera de incrementar, en base a los resultados obtenidos en esta tesis, nuestro conocimiento de la membrana celular y el papel que la organización espacial y temporal juega en el control del sistema inmune.

Chapter 1

Protein nanoclustering in the immune system and related biological function

The role of the spatiotemporal behavior of transmembrane proteins as a regulator of their function is an emerging concept in human immunology. In this introductory Chapter, a short overview of the immune system is presented with a particular emphasis on two main receptors involved in immunity: the pathogen recognition receptor DC-SIGN and the antigen presenting protein CD1d. Then, state-of-the-art advanced fluorescence techniques such as single particle tracking and super-resolution microscopy will be presented and their capability in characterizing the compartmentalization of the cell membrane at the nanoscale will be discussed. In the last part of this Chapter a general overview on receptor nanoclustering is given, highlighting recent findings in the field that allow us to conclude that nanoclustering is a prevalent feature that characterizes the organization of the cell membrane and that controls biological function.

This work has been partially published as M.F. Garcia-Parajo, A. Cambi, J.A. Torreno-Pina, N. Thompson, K. Jacobson, “Nanoclustering as a dominant feature of plasma membrane organization”, *Journal of Cell Science* **127**, 4995 (2014).

The immune system

The immune system represents the main defense system of the human body against invading pathogens (1). The hallmark of the immune system is its ability to distinguish self from non-self (2). Any alteration of this sensitive balance can have dramatic consequences for the host body such as infection or autoimmunity. The human immune response can be divided into two different types of defense: innate and adaptive immunity. The first one relies on conserved molecular patterns among the very different pathogens which are recognized by toll-like receptors (TLRS) expressed on the cell membrane of, e.g., macrophages or dendritic cells (3). In contrast, adaptive immunity is characterized by a specific response against a particular structure of the pathogen, principally mediated by activated T cells which can lead to the production of antibodies by effector B cells (4). The key event responsible for initiating adaptive immune responses is the interplay between T cells and dendritic cells (5).

Dendritic cells (DCs) were discovered by Ralph Steinman in the lab of Zanvil A. Cohn at The Rockefeller University in the 1970s (6-9), a discovery that led him winning the Nobel Prize in Physiology and Medicine in 2011 (nobelprize.org). DCs capture and digest pathogens in order to present them to T cells. There are two main routes for pathogen processing and presentation by DCs which depend on whether the antigen is located in the cytoplasm of the DC or in its endocytic pathway (10). The first pathway leads to presentation to CD8-T cells by antigen loaded major-histocompatibility complex I (MHC-I). On the other hand, if the pathogen has entered the endocytic pathway of the DCs, it will be degraded and loaded into MHC-II complexes for a later presentation to CD4-T cells (11). Nevertheless, DCs can also present captured antigens via their MHC-I complex in a process called “cross-presentation” (12). Hence, the combination and the interplay between pathogen receptors and antigen presenting molecules located on the cell membrane of DCs are the principal components of the initiation of DC-mediated adaptive immunity.

DCs reside in the human body in two very different states: mature and immature (Fig. 1.1) (13-15). Immature DCs have the role of surveilling the human body in order to capture invading pathogens in peripheral tissues or in secondary lymphoid organs (15). Immature DCs display a remarkable endocytic capacity but express low levels of MHC complexes on their surface. Hence, the role of immature DCs is antigen accumulation rather than antigen presentation. The process of DC maturation is initiated after DC stimulation via inflammatory signals such as TLR agonists (14). In the process of maturation, the different phenotypic changes in immature DCs are dramatic and comprise not only changes at the molecular level but also on the overall morphology of

DCs. For instance, matured DCs express the chemokine CCL21 receptor CCR7 that produces rapid integrin-independent migration of DCs to the lymph node where mature DCs will present the antigens to T cells (16, 17). Moreover, mature DCs enhance the surface expression of antigen-bound MHC-I and MHC-II complexes and T cell co-stimulatory molecules such as CD80, CD86 and CD40 (18). On the other hand, not fully mature DCs in peripheral lymphoid tissues have been associated with being tolerogenic (18). The transition from immature to mature DCs with pro-inflammatory stimuli represents the hallmark of DC-mediated T cell immunity. The importance of the maturation process is such that nowadays it is well accepted that traditional adjuvants used in vaccination strategies promote the DC maturation process (13, 14). Hence, DC maturation is the key event that allows DCs to link innate and adaptive immunity (19).

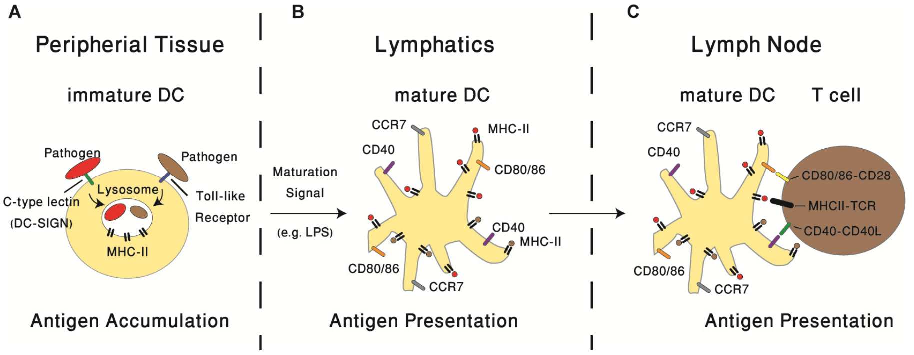

Figure 1.1 Different maturation states of DCs and associated DC function. (**A**) Immature DCs continuously patrol the human body seeking potential invading pathogens in peripheral tissues. The pathogens are internalized by the binding to pathogen receptors such as lectins or TLRs on the surface of DCs. After pathogen internalization and (partial and inefficient) lysosomal degradation (20, 15), MHC-II complexes located in lysosomal compartments might bind to antigen peptides. (**B**) After the DC maturation signal, pathogens are degraded very efficiently in the lysosomal compartment. Antigen peptide loading of MHC-II complexes also occur very fast, and surface expression of peptide-bound MHC-II increases dramatically (20). Moreover, the mature DC expresses costimulatory molecules such as CD40, CD80/86 and the chemokine receptor CCR7. The mature DC enters the lymphatic system in order to migrate to the T-cell-rich lymph node. (**C**) In the lymph node, T cells recognize the antigen-bound MHC-II through the T cell receptor and become activated.

C-type lectins are a canonical example of protein receptors responsible for, among other functions, pathogen uptake on the cell membrane of DCs (21). **D**endritic **C**ell-**S**pecific **I**ntercellular adhesion molecule-3-**G**rabbing **N**onintegrin (DC-SIGN) is a C-type lectin that can bind to carbohydrate structures present not only on pathogens but also on the intercellular adhesion receptor ICAM-3 (22). The structure of DC-SIGN consists on a carbohydrate-recognition domain (CRD), a tandem-neck-repeat domain and a cytoplasmic tail (23). The CRD is responsible for binding to adhesion molecules or pathogens by DC-SIGN. The neck domain has been shown to promote the tetramerization of DC-SIGN (24) and the cytoplasmic tail contains signaling and internalization motifs (23). DC-SIGN binds to mannose- and fucose-containing glycoproteins on the surface of a large group of pathogens such as bacteria or viruses, including HIV (22). Moreover, depending on the type of glycan bound to DC-SIGN, the DC-SIGN signalosome can tailor the profile of cytokines released after TLR stimulation of DCs (25). DC-SIGN ligands are mainly internalized via clathrin-coated pits (26, 27) and they are degraded in lysosomal compartments. Using transmission electron microscopy, it has been shown that DC-SIGN forms microclusters on immature but not mature DCs (28). Moreover, microcluster formation was shown to favor the virus-binding capability by the receptor (28). Hence, the lateral organization of DC-SIGN has a significant impact on its biological function.

MHC-I and MHC-II are the classical examples of antigen presenting proteins expressed on the cell membrane of DCs. Their ability of presenting foreign peptides on the surface for the recognition of CD8-T cells and CD4-T cells represents the key component of T cell mediated immunity. There is another class of antigen presenting proteins that instead of peptides, they present glycolipids coming from exogenous antigens: the CD1 family (29). The CD1 members (CD1a, CD1b, CD1c, CD1d and CD1e) are transmembrane glycoproteins which share a similar structural architecture as the MHC-I complex. The CD1 family can be divided according to their structure into two groups with CD1a, CD1b, CD1c, CD1e forming subgroup I and CD1d as subgroup II. While most of the members of the CD1 family can be found exclusively on antigen presenting cells (APCs), CD1d is expressed among a greater subset of cells, including epithelial cells (30, 31). Moreover, the type of T cells that recognize CD1 proteins of the subgroup I strongly deviates from the T cells that recognize CD1d, the invariant Natural Killer T cells (iNKT). iNKT cells share properties of innate lymphocytes and their main characteristics are the expression of, contrary to classical T cells, a conserved T cell receptor with a Vα24-Jα18 TCRα chain coupled to a Vβ11 TCRβ in humans. Importantly, iNKT cells can be stimulated in a CD1d dependent manner via TLR stimulation of DCs (32). Hence, the CD1d-iNKT cell system can link innate and adaptive immunity (33). This makes CD1d a very powerful target in therapies aiming for the stimulation and activation of immune responses such asin cancer immunotherapy (34, 35). Thus, the study of CD1d represents a key point in defining future anti-cancer therapies using human immunology.

Both CD1d and DC-SIGN are transmembrane glycoproteins expressed on the surface of DCs (Fig. 1.2). The study of their behavior on their natural environment, the cell membrane, represents a crucial step in understanding their biological function in the human immune system. In the recent years, advanced biophysical techniques have allowed the study of the spatiotemporal behavior of transmembrane proteins on the cell membrane of leukocytes. These studies have revealed that most of these proteins are not individually organized in a random manner on the cell membrane but are rather grouped together forming so called protein nanoclusters (36, 37). Moreover, the formation and integrity of these protein nanoclusters appear to play an essential role in regulating their biological function. Therefore, studying and understanding how DC-SIGN and CD1d are laterally organized on the cell membrane of DCs represents a crucial step in further deepening our knowledge in how immune reactions are fine-tuned at the molecular level by DCs. This type of studies will improve the rational development of promising treatments in oncology such like cancer immunotherapy in the near future.

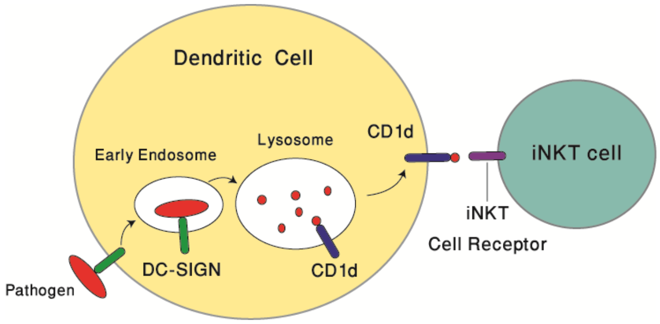

Figure 1.2 Proposed schematic of the working principle of the interplay between DC-SIGN and CD1d on DCs (29). (**A**) A glycosylated protein on the cell membrane of the pathogen might be recognized by DC-SIGN on the surface of DCs. After internalization through DC-SIGN-mediated endocytosis, the pathogen is exposed to degradation on lysosomal compartments where at the same time, CD1d molecules can undergo trafficking from the cell membrane. These recycling CD1d molecules might encounter and possibly bind glycolipids coming from the pathogen previously internalized by DC-SIGN and degraded in the lysosome. Eventually, CD1d traffics back to the cell membrane presenting the exogenous glycolipid to iNKT cells which might initiate an immune response by fast cytokine release.

Optical nano-tools for studying receptor organization in the cell membrane

The study of the lateral organization of transmembrane proteins such as CD1d and DC-SIGN imposes a need for using techniques capable of performing measurements at the relevant temporal and spatial scales of transmembrane proteins. Moreover, these techniques must perform in a minimally invasive manner in order to characterize these peptides in their natural context, the living cell. Light is probably one of the best resources available in nature to match these requirements. Indeed, its manipulation through the use of lenses has consistently resulted in major breakthroughs in the history of scientific discoveries. The classical example is the invention of the optical microscope which is able of magnifying living micron-sized objects such as bacteria due to its high spatial lateral resolution (≈250 nm). The possibility of observing directly microorganisms or human cells has had a tremendous impact in the way we understand biology nowadays (38).

However, when it comes to the visualization of individual molecules, such as transmembrane proteins in living cells with a typical size of 1-10 nm and expression levels of 500-2000 protein/μm^2 (39), optical microscopy stops being a suitable imaging technique. This is mainly due to the so-called Abbe diffraction limit, which defines the maximum focusing power (d) of a microscope depending on the numerical aperture (NA) of the objective and the wavelength λ of the excitation light as $d \approx \lambda/2NA$ (38). This limit makes a light emitting point source to appear in the detector as a diffraction-pattern with a shape of concentric rings having decaying intensities as the distance from the center increases (40). The central ring, known as the Airy disk, has a full width at half maximum (FWHM) in the visible of ≈250 nm and it is also referred as to the point-spread function (PSF) of the microscope (41). Hence, the diffraction limit of light implies that two objects cannot be resolved individually if their mutual distance is smaller than 250 nm. Since the density of proteins on the cell membrane can be extremely high, standard optical microscopy cannot faithfully image individual components at physiologically relevant concentration levels.

In the last 10 years, a group of super-resolution optical techniques were invented based on the ability of precisely controlling the photophysics of individual fluorophores by carefully switching them between "on" and "off" states (38). Since the Abbe´s diffraction limit cannot be overcome using traditional lenses, the labeling probe is now the key component to make nanoscopy imaging possible. One way of exploiting the "on/off" switching behavior of individual fluorescent molecules to achieve super-resolution is to allow the emission of fluorescence from only a reduced group of labeled proteins having nearest-neighbor distances (*nnd*) larger than the diffraction limit (42, 43). In these sparse emission conditions, the lateral position of each individual molecule can be determined with nanometer precision by fitting the emission intensity profile using a 2D Gaussian function. By repeating the localization step for many different images having at each time a different subset of molecules emitting light, a super-resolution image can be reconstructed. This is finally done by adding all the localizations detected in every frame into one final reconstructed super-resolution image (Fig. 1.3A). Nanometer localization of dyes is possible because it ultimately depends on the number of photons N emitted by fluorescent dyes as $\sigma \sim \mathrm{FWHM}/\sqrt{N}$ (44), where the FWHM corresponds to the size of the PSF of the microscope. Localization-based super-resolution imaging is the working principle of techniques such as photo-activated localization microscopy (PALM) (42) and stochastic optical reconstruction microscopy (STORM) (43) (Fig. 1.3A).

Stimulated emission depletion (STED) microscopy is another super-resolution technique that works conceptually different but it also based on the control of the photophysics of a fluorophore (Fig. 1.3B) (45-47). In STED, a predetermined number of dyes are first excited with an excitation laser using diffraction limited optics, and then de-excited to the ground state by stimulated emission using a red-shifted STED laser (using also conventional lenses) (38). The diffraction limit is overcome in STED by doughnut-shaping the STED depletion laser beam and overlapping it with the excitation beam. Thus, only fluorophores located in the area of the hole of the doughnut are allowed to emit fluorescence leading to an effective reduced illumination area below the diffraction limit. As anticipated, the resolution of STED nanoscopy ultimately depends on the intensity of the STED laser beam and not on the optics used.

An alternative nanoscopy imaging approach to PALM, STORM or STED is near-field scanning optical microscopy (NSOM) (Fig. 1.3C), which is not based on the control of the photophysics of fluorescent molecules but rather, on the detection of the near-field component of the emitted fluorescence before it undergoes diffraction (48-50). In NSOM, the fluorophore is excited in the near-field using a subwavelength source and the emitted fluorescence is collected in the far-field through an objective. Thus, the resolution in NSOM does not depend on the fluorophore or on the used optics but ultimately, on the final diameter of the sub-wavelength source (51-53). In summary, both far-field and near-field nanoscopy approaches are nowadays capable of breaking the diffraction limit of light. These techniques are being currently used to directly visualize proteins on the cell membrane at endogenous expression levels and in a minimally invasive manner (54, 49, 55) having a major impact in the way we try to understand biology.

The main current limitation of super-resolution techniques is their temporal resolution and as a consequence the sample needs to be fixed before imaging. For instance, to create a localization-based super-resolution (PALM or STORM) image, the nanometer localizations of fluorophores coming from typically, more than 50.000 frames, need to be collected. On the other hand, STED and NSOM also suffer from poor temporal resolution due to their sample scanning operating principle. As a consequence, although super-resolution techniques offer detailed imaging with nanometer resolution, temporal information of the sample of interest is hard to access.

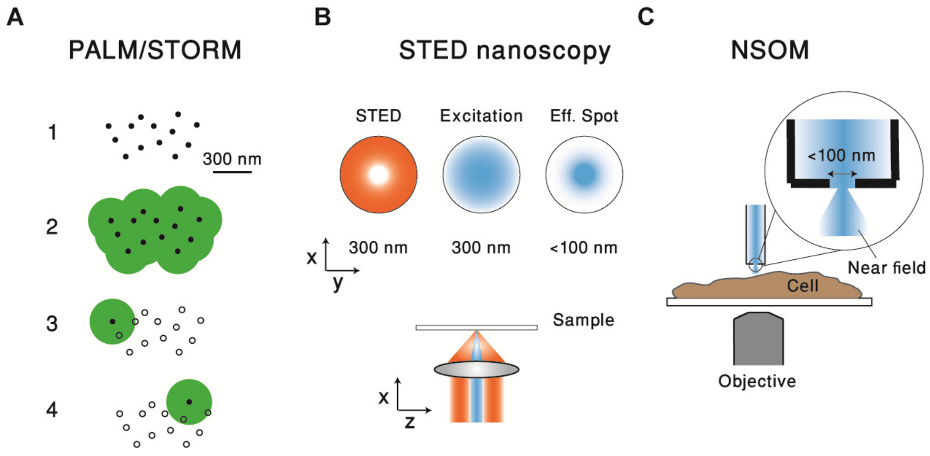

Figure 1.3 Far field and near field super-resolution techniques. (**A**) If all the molecules within a dense sample are allowed to emit fluorescence (1), individual molecules cannot be resolved due to the diffraction limit (2). However, if one molecule is allowed to emit fluorescence at a time and its localization determined with nm accuracy, a final super-resolution image can be constructed after repeating the activation/localization cycle many times (3 and 4). This is the working principle of PALM/STORM. (**B**) In STED nanoscopy, the diffraction limit is broken by de-exciting fluorophores under a doughnut shaped STED beam (orange). Only the fluorophores located in the zero intensity region of the STED beam are allowed to emit fluorescence. (**C**) NSOM is based on the excitation of fluorophores by the near-field emitted by a tip with a sub-wavelength aperture.

To gain access to the temporal information of diffusing proteins on the cell membrane, fluorescence recovery after photobleaching (FRAP) has been the main imaging technique used in most biology Labs in the last decades (Fig. 1.4A) (56-58). FRAP is based on the photobleaching of a given area on the cell membrane using a very intense laser illumination. Diffusing fluorescently labeled molecules located in the periphery of the photobleached area will gradually fill the photobleached space in time. By monitoring the recovery of the fluorescence within the photobleached area in time, one can determine the overall mobility of the fluorescently labeled molecules (Fig. 1.4A). However, FRAP is an ensemble averaging imaging technique. Hence, any sensitive dynamic information within potentially different subpopulations of the molecule of interest cannot be accessed beyond that provided by data averaging. Fluorescence correlation spectroscopy (FCS) is another imaging technique which, similar to FRAP, also allows characterizing the diffusion of fluorescently labeled diffusing molecules (Fig. 1.4B) (59, 60). In FCS, the fluorescence emission of molecules diffusing through a fixed illumination volume (usually confocal volume) is recorded over a given period of time (Fig. 1.4B). By analyzing the fluctuation of the fluorescence intensity over time, the number of molecules and the diffusion coefficient, among other parameters, can be extracted. One of the main drawbacks of standard FCS is that it is still diffraction limited. Hence, the influence of local variations in the structure of the cell membrane on the diffusion of the molecule of interest cannot be extracted. To obtain illumination areas at the nanoscale, close to the size of those local variations, two different methods have been developed: STED-FCS and NSOM-FCS (61, 62). Since both techniques offer sub-diffraction illumination areas, the effect of, e.g., confinement zones <100 nm on the diffusion of molecules can be addressed (61, 62).

An alternative imaging approach to FRAP and FCS which features high temporal resolution and single molecule fluorescence sensitivity is single particle tracking (SPT) (63-65). The technique is based on the ability of detecting diffusing single molecules over a given number of frames with millisecond time resolution. By reconnecting the coordinate positions of each fluorescent spot with nanometer accuracy and as a function of time, fluorescent trajectories can be generated and the diffusion of individually labeled proteins can be characterized (Fig. 1.4C) (66). Unfortunately, the reduced fluorescence emission and photobleaching of traditional organic dyes impose limitations in the length of the trajectory as well as in the localization accuracy that can be achieved, typically 40 nm (67). Quantum dots (QDs) are nanocrystals that have been

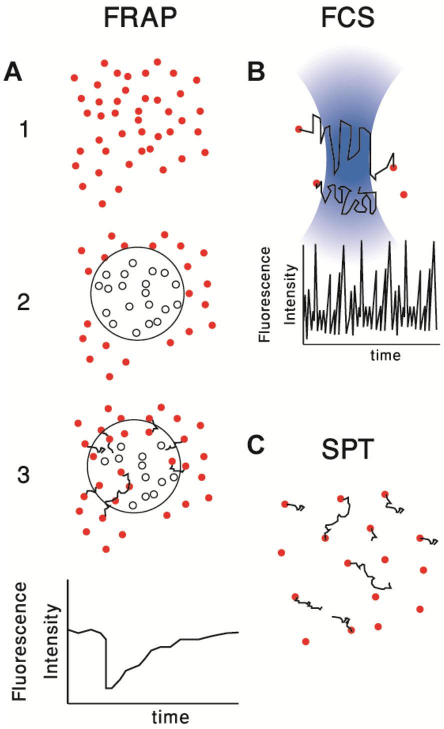

Figure 1.4 Different biophysical techniques to extract temporal information of diffusing molecules. (**A**) FRAP is based on the recovery of the fluorescence of a previously photobleached area by diffusing molecules located in the surrounding area. (1) A given area within the cell membrane is photobleached by an intense laser illumination (2). By recording the recovery of the fluorescence intensity in time (3 and lower plot) due to the diffusion of molecules inside the photobleached area, the averaged mobility of the protein of interest is extracted. (**B**) FCS extracts the number of molecules and diffusion coefficient of fluorescent molecules diffusing through the excitation volume after autocorrelating their fluorescence fluctuations in time. (**C**) SPT is a single molecule based imaging technique. By connecting the detected localizations of individual diffusing molecules in every frame of a movie, trajectories can be built up.

consistently replacing traditional organic dyes as imaging probes for SPT (68, 69). Due to their high brightness and enhanced photostability, longer trajectories with localization accuracies of 15-20 nm can be obtained (70). Moreover, since QDs feature a narrow spectral emission compared to organic dyes or fluorescent proteins, they are especially suitable for multi-color SPT (71). This is particularly advantageous when addressing how different multi-colored labeled proteins interact in real time at the nanoscale. Nevertheless, it should be realized that SPT experiments must be performed at sub-labeling conditions (typically two orders of magnitudes lower labeling than for super-resolution imaging) so that individual trajectories can be re-connected in time. As consequence, only a sub-set of molecules can be investigated in a dynamic fashion and a large set of data are necessary to derive statistically relevant information on the processes of interest.

Cell membrane: organization, dynamics and function

The cell membrane represents the ultimate barrier between the interior of a cell and the extracellular environment. Thus, any outside-in or inside-out intercommunication between the cell and its environment has to be triggered or terminated on the cell surface. The main constituents of cell membranes are phospholipids which organize in a double layer exposing their polar residues to the aqueous milieu. Components of the cell membrane such as transmembrane proteins would then have their non-polar aminoacids buried into the double lipid bilayer (72) while their polar residues exposed to water. The seminal experiment carried out by Frye and Edidin (73) showed that the behavior of the lipid bilayer of cell membranes correspond to a fluid rather than a solid. This led to the concept that cell membranes are essentially a fluid mosaic where transmembrane proteins could diffuse laterally in a random behavior. However, thanks to the application of advanced biophysical techniques such as FRAP, SPT and optical laser trap (74), it started to become clear that the lateral diffusion of membrane proteins was hindered by obstacles leading to the hypothesis of membrane compartmentalization about 20 years ago. This constitutes an excellent example of how our understanding about biology is constantly reshaped by the implementation of physical techniques.

The advent of super-resolution fluorescence microscopy combined with high-temporal fluorescence imaging techniques such as SPT and FCS has led to the more recent concept that compartmentalization at different temporal and spatial scales is a general organizing principle on the cell membrane (36). The observation that many, if not most, membrane components such as proteins or lipids are clustered at the plasma membrane at different scales has been consistently reported in the literature for many different proteins, lipids and in many different cells, specially leukocytes. It has been reported that nanoclusters can be organized on the nano- as well as on the mesoscale to form nano- and microdomains that are capable of supporting cell adhesion, pathogen binding and immune cell-cell recognition amongst many other cell functions. Hence, there has to be one or many conserved mechanisms responsible for membrane compartmentalization.

One of the most prominent concepts for membrane compartmentalization refers to the ‘lipid raft hypothesis’. The raft model originated from a study more than 25 years ago (75) and has been extensively reviewed since then (76, 77). The lipid raft notion proposes the existence of small plasma membrane compartments that are enriched in cholesterol and sphingolipids, and populated by ‘raftophilic’ proteins such as, for example, glycosylphosphatidyl-anchored proteins (GPI-APs). Persistent controversies have led to a provisional contemporary definition that emphasizes the small and transient nature of putative lipid rafts (78). Yet, when considering the current, general view about the nature of lipid rafts, it must be borne in mind that membranes are rich in proteins (79) and that any preferential residence of membrane proteins in regions populated by raft lipids most likely occurs only on a very small spatial and temporal scale (61). At present, the existence of relatively large, and predominantly ‘lipid raft’ domains is expected to be the exception rather than the rule.

Another prominent concept for plasma membrane compartmentalization is based on the meshwork of filamentous proteins including F-actin and spectrin that immediately underlie the plasma membrane. This model originated over three decades ago on the basis of lateral diffusion studies of proteins in the membranes of red blood cells (80) and was later expanded by work from Akihiro Kusumi's group, who termed it the membrane cytoskeleton ‘fence’ (81). They also coined the term ‘anchored transmembrane picket’, which refers to the more or less regular array of transmembrane proteins (posts) that are anchored to the underlying membrane-associated cytoskeletal fence serving to compartmentalize the membrane. Thus, long-range diffusion of both transmembrane and lipid-anchored proteins is restricted because it is rate-limited by fluctuations in the cytoskeletal ‘fence–picket’ structure that permits the inter-compartmental barriers to be traversed by the diffusing molecule. By contrast, short-range diffusion within each compartment is much more rapid.

Other notions have also been put forth with regard to factors that govern plasma membrane compartmentalization on different length and time scales, such as lipid shells (82), tetraspanin-enriched microdomains (83) and galectin lattices (84). Moreover, recent evidence suggests that these possible local organizers are not independent from each other but, rather, act in a synergistic manner that remains to be precisely defined (85, 84).

The term 'microdomain' is generally employed to describe membrane compartmentalization that occurs either naturally or is ligand induced. However, the size of such domains can vary from a few nanometers to several micrometers, most probably owing to their different molecular composition and different capacities to coalesce with or segregate from each other. A plausible hypothesis is that plasma membrane compartmentalization is based on a hierarchical organization of molecules that ranges from classic protein oligomerization to nanometer-sized or micrometer-sized clusters, which may provide multi-scale regulation of membrane protein function.

Some examples of protein nanoclustering on the cell membrane

GPI-APs

Some of the smallest documented nanoclusters are those that contain GPI-APs. These extracellular, lipid-linked proteins constitute a diverse set of proteins tethered to the outer leaflet of the plasma membrane that exhibits specific sorting and signaling properties. GPI-APs are regulated by alterations in cholesterol and sphingolipid levels in cell membranes and, as such, have been considered to be classic lipid-raft markers (86). The first studies discussing the unusual nature of GPI-AP nanoclustering were reported by two different groups using complementary approaches; i.e. chemical crosslinking (87) and fluorescence resonance energy transfer (FRET) (88). Later, using a combination of homo- and hetero-FRET techniques, it was shown that GPI-APs co-exist on the cell membrane as mixtures of monomers together with a fraction (20–40%) that includes cholesterol-sensitive oligomers (<5 nm) composed of at most four molecules; this was shown for a diverse set of GPI-AP species (89). Surprisingly, the relationship between monomers and nanoclusters did not obey the mass-action law that would be expected for a classic chemical equilibrium, because the percentages of GPI-APs nanoclusters and their molecular density were concentration-independent (90). Importantly, GPI-AP nanoclustering has been more recently confirmed by super-resolution microscopy techniques including NSOM (49) and PALM (91).

SPT and FCS studies on nanoscale volumes (61) have provided further evidence for the existence of small GPI-AP nanoclusters in living cell membranes – although, as recently pointed out, an entirely consistent picture has not yet emerged owing to the high number of different techniques employed (92).

Of considerable interest is the nature of the factors that regulate and stabilize nanoclusters of lipid-anchored proteins. In general, lipid-linked protein nanoclusters might be stabilized by *cis* associations of their protein ectodomains, cytosolic domains, lipid anchors or a combination of these. For example, Akihiro Kusumi's group recently showed that ectodomain interactions are the primary factor in transiently stabilizing homodimers of the GPI-AP CD59, with cholesterol and other lipids having secondary stabilizing roles (93). Furthermore, in supported lipid bilayers, Ras GTPases dimerize using a specific motif in their cytosolic domains (94). These studies suggest that protein–protein interactions among identical lipid-linked proteins play a significant role with respect to the stability of lipid-linked protein nanoclusters. Furthermore, it has been also proposed that dynamic, short actin filaments form aster-like aggregates under the plasma membrane that actively drive lipid-anchored proteins into nanoclusters (95) (Fig. 1.5A). The observation that GPI-AP nanoclusters are found to be spatially separated by a characteristic distance of less than 250 nm (49), further indicates that the assembly of actin asters close to the inner leaflet of the plasma membrane occurs at this spatial scale (Fig. 1.5B). Recently, it has been proposed that a combination of transbilayer coupling of long acyl chain lipids, actin dependent immobilization of inner leaflet phosphatidylserine and the proper amount of cholesterol on the cell membrane might be the mechanism driving GPI-AP nanoclustering (96).

The lymphocyte function-associated antigen-1

The main integrin receptor involved in leukocyte adhesion is the lymphocyte function-associated antigen-1 (LFA-1, officially known as ITGAL), which forms nanoclusters of ~70 nm on monocytes prior to ligand binding (97). The integrity of these nanoclusters is independent of cholesterol or the actin cytoskeleton and the clusters contain on average six LFA-1 molecules (97). By using NSOM, a first level of hierarchy for LFA-1 organization was defined because ligand-independent LFA-1 nanoclusters resided within 50–100 nm of GPI-AP nanodomains (49) (Fig. 1.6). Upon ligand-induced LFA-1 activation, a higher level of hierarchy that is associated with function was observed (49). Indeed, coalescence of the two nanodomain types and further recruitment of GPI-APs to these sites resulted in the formation of stable cell adhesion nanoplatforms (49) (Fig. 1.6). Although there is no clear explanation yet with regard to what keeps LFA-1 in nanoclusters, it is tempting to speculate that LFA-1 and GPI-AP nanoclusters are somehow interconnected by the actin cytoskeleton to the sub-membranous actin asters described above (95). More recently, using a combination of NSOM and SPT, the importance of the actin cytoskeleton was demonstrated for inside–out activation of LFA-1, its stable ligand binding and firm cell adhesion (67). Although LFA-1 nanoclustering in resting monocytes was observed prior to ligand activation, it is worth mentioning that other integrins, such as β_1 and β_3, form nanoclusters upon ligand activation (98, 99). These nascent nanoclusters are thought to play a key role in the initiation of cell adhesion (99) and in the formation of focal adhesion complexes (98, 49, 99).

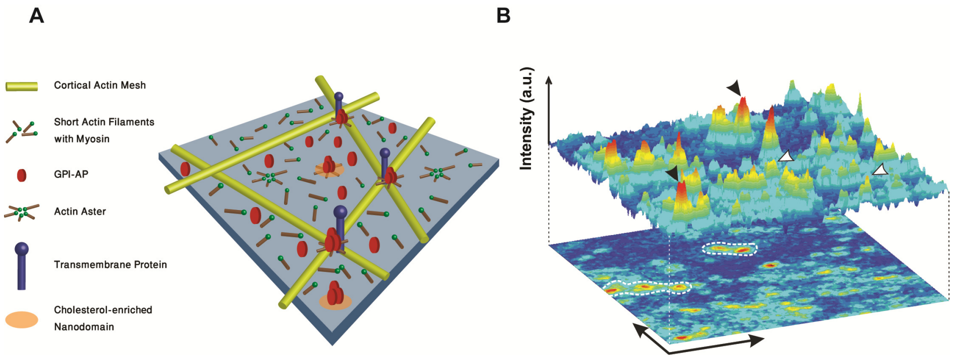

Figure 1.5 Nanoscale organization of GPI-APs on the cell membrane. (**A**) The organization of GPI-APs on plasma membranes as co-existence between monomers and small nanoclusters containing a few molecules. Nanocluster formation appears to be driven by cortical actin (hypothetical actin asters) and maintained by weak interactions with cholesterol (95). These small nanoclusters can be further stabilized by cortical actin through asters and/or proximal transmembrane proteins that act as 'posts' attached to the cortical actin. The physical separation between GPI-AP nanoclusters has been observed to be within 200–250 nm (49). (**B**) (Top) 3D intensity projection of a super-resolution NSOM image showing the co-existence of nanoclusters (black arrowheads) and monomers (white arrowheads) of GPI-APs. (Bottom) Areas encircled by a dashed line on the 2D image illustrate that nanoclusters prefer to concentrate at specific sites as hotspots that are typically separated by less than 250 nm. This characteristic separation might reflect the physical dimensions of the actin meshwork and/or spatial distribution of actin asters (95, 49). a.u., arbitrary units.

T-cell receptors, linkers for activation of T cells and B-cell receptors

Several other receptors involved in the immune system have also been shown to form nanoclusters (100). For instance, there is accumulating evidence that T-cell receptors (TCRs) form nanoclusters on the surface of unstimulated T cells. Initial biochemical and EM experiments carried out in Alarcon's group showed that monomers and TCR nanoclusters co-exist on resting T cells (101). Another study confirmed this by using the two-color coincidence-detection technique but found a smaller population of nanoclusters compared to monomers (102). More recently, TCR nanoclustering has been demonstrated by EM and PALM on fixed cells (37). Although the molecular mechanisms for the formation of TCR nanoclusters are still highly debated, nanocluster

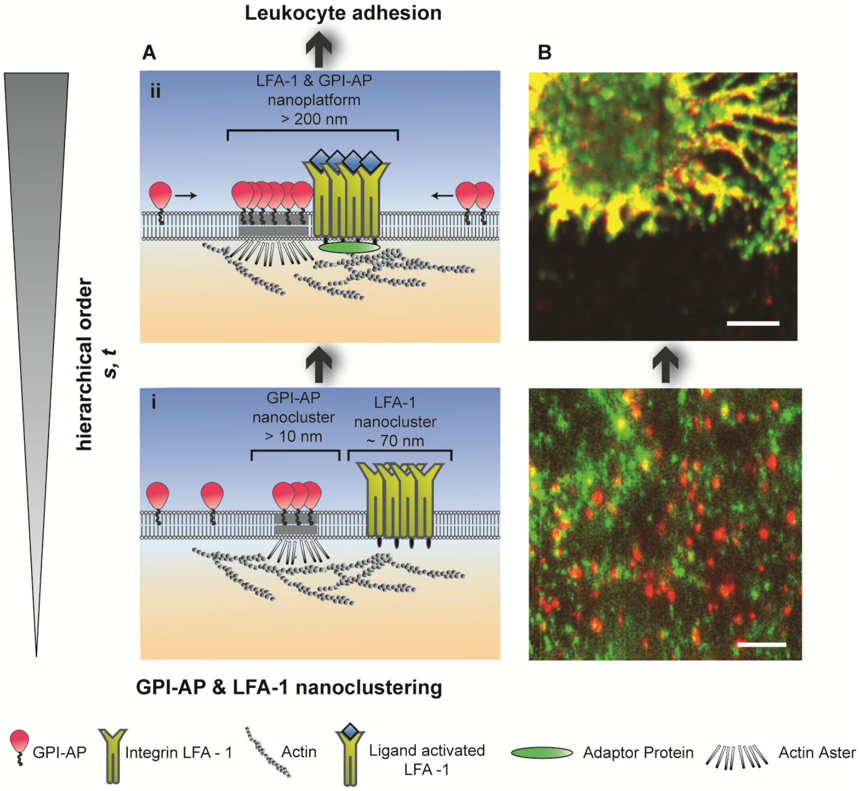

Figure 1.6 Hierarchical organization of GPI-APs and the cell adhesion integrin receptor LFA-1. The inverted triangle at the left indicates the increase in hierarchical order in space and time from bottom to top of each panel. (**A**) Bottom panel: GPI-AP nanoclusters (containing two to four molecules in total) and pre-formed LFA-1 nanoclusters (six to ten molecules in total) have been observed in close proximity from each other (50–150 nm) before LFA-1 is activated through ligand binding. Top panel: Activation of LFA-1 through ligand binding, correlates with an increase in the number of GPI-AP molecules in each nanocluster that is likely to be mediated by local rearrangements of the cytoskeleton through adaptor proteins (green). Furthermore, incorporation (arrows) of mobile monomeric GPI-APs and diffusible LFA-1 nanoclusters (67) can further strengthen the nanoclusters and lead to the assembly of LFA-1- and GPI-AP-containing nanoplatforms that are adhesion competent. (**B**) Bottom panel: Representative super-resolution NSOM images of GPI-AP (green) and LFA-1 nanoclusters (red) in resting monocytes show that LFA-1 and GPI-AP are not associated but in close proximity to each other. Scale bar: 1 µm. Top panel: Ligand activation of LFA-1 leads to aggregation of GPI-APs and LFA-1 (visualized by the substantial increase in yellow areas, which indicates spatial colocalization at the nanoscale) into adhesion-competent nanoplatforms. Scale bar: 5 µm. Images have been taken from (49).

stability appears to depend on cholesterol and sphingomyelin (103, 101). Because T cells can regulate the extent of TCR nanoclustering depending on their activity, i.e. naïve versus memory T cells, it has been suggested that nanoclustering facilitates a quick memory response upon T-cell activation (104).

The adaptor proteins linker for activation of T-cells 1 and 2 (LAT1 and LAT2, hereafter referred to as LAT) are members of the TRAP family (105) and also form nanoclusters on resting T cells, although the size of these nanoclusters and their participation in T-cell signaling are still debated. Lillemeier et al. showed that TCR and LAT exist as separate and discrete nanoclusters (also termed 'protein islands' by the authors) of 70–140 nm in diameter that concatenate (without mixing) during activation (37) (Fig. 1.7A). By contrast using similar super-resolution approaches – another study showed that TCR and LAT nanoclusters are highly mixed, and that LAT nanoclusters are composed of only a few molecules (106). These nanoclusters might not participate in early T-cell signaling events because sub-synaptic vesicles of LAT were seen to dock to the plasma membrane to TCR-activation sites (55) (Fig. 1.7B), a process that is dependent on the vesicle (v)-SNARE protein VAMP7 (107). The reasons for these contrasting results are not yet clear but they might be related to differences in the TCR activation times used by the different research groups.

The multi-chain high-affinity IgE ε receptor subunit β (FcεRI; also known as MS4A2) and the B cell receptor are other examples of receptors that pre-cluster prior to antigen binding (108-110). For instance, by using a combination of (dSTORM) and SPT, BCR and its co-receptor CD19 were found to exist in spatially distinct preformed nanoclusters in resting B cells (111). Although the actin cytoskeleton regulates BCR, CD19 mobility appears restricted by the tetraspanin CD81, indicating that both CD19 and CD81 can form scaffolds to support BCR signaling (111).

Nanocluster biogenesis, formation and stability

The full intracellular molecular complement of membrane nanoclusters (e.g. individual protein monomers, preformed protein homo-oligomers, preformed protein hetero-oligomers and/or particular lipid components) is typically unknown. Of interest is whether a given nanocluster arrives at the plasma membrane as an almost fully assembled entity – as appears to be the case for LAT (55) – with only a few factors to be subsequently recruited and/or eliminated or, by contrast, almost completely unassembled. It is unlikely that most membrane nanoclusters are composed solely of close-packed, identical proteins, although the idea is conceptually attractive. Instead, the current evidence strongly suggests that a specific complement of lipids and (most probably) other proteins will be present in nanoclusters. Indeed, at least in the case of LFA-1 (49) and BCR (111), nanoclusters are not fully packed with their respective receptors.

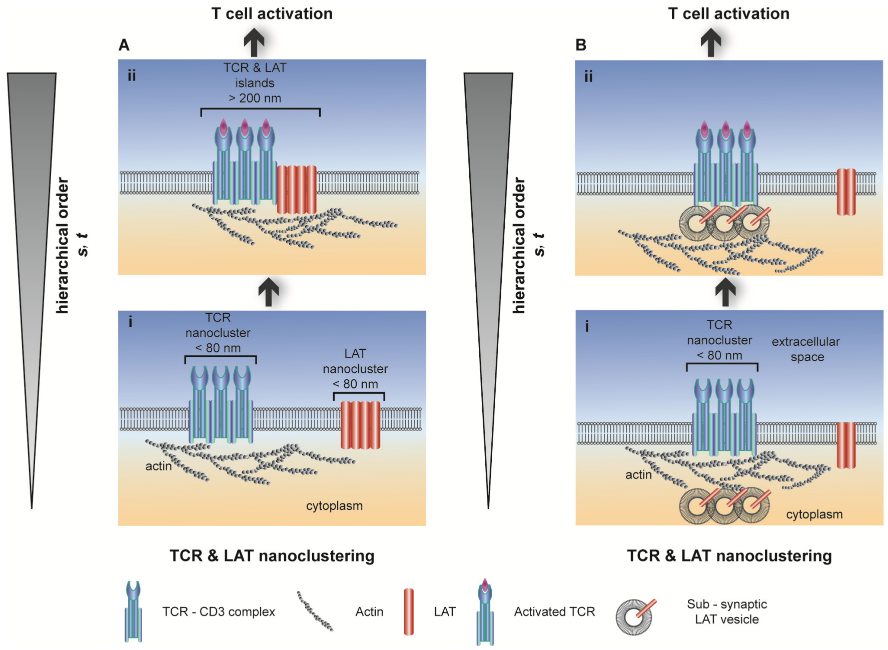

Figure 1.7 Two possible pathways for the hierarchical organization of TCR and LAT molecules at T cells. The inverted triangle to the left indicates the increase in hierarchical order in space and time from bottom to top of each panel. (**A**) One possible pathway considered in the field, termed the 'protein island' model. TCR–CD3 [comprising TCR and the T-cell co-receptor cluster of differentiation 3 (CD3), also known as Cde3] complexes and LAT molecules are already present as small preassembled nanoclusters on the surface of resting T cells (bottom panel). After antigen recognition and TCR activation, TCR-CD3 and LAT nanoclusters concatenate, but do not mix (top panel). The actin cytoskeleton is thought to play a main role in this process (37). Evidence for the protein island model comes from EM and PALM images before and after TCR activation. (**B**) An alternative assembly pathway of TCR and LAT nanoclusters, involving sub-synaptic LAT vesicles. TCR-CD3 complexes, as well as some LAT molecules, exist as small nanoclusters on the surface of resting T cells (bottom panel). LAT can also be found in sub-synaptic vesicles (top panel). After TCR activation, only LAT molecules within the sub-synaptic vesicles in close proximity to the cell membrane participate in signal transduction (55). Evidence for the involvement of LAT sub-synaptic vesicles comes from PALM images in living cells, which show LAT recruitment in close proximity to the cell membrane. These LAT nanoclusters appear and disappear quickly over time, suggesting that vesicles dock and undock at the membrane without undergoing any appreciable lateral movement (55).

The mechanism by which nanocluster precursors undergo initial reorganization after their delivery to the plasma membrane is a key issue. One might expect at least passive reorganization to occur in response to the differences in chemical composition between the intracellular and plasma membrane environments. These arise from at least three specific characteristics of plasma membranes: (1) molecular components have specific orientations and cannot be treated as soluble proteins with the freedom to reorient in three dimensions; (2) the environment contains additional structural features, i.e. the outer and inner membrane environments are considerably different; and (3) the membrane is very crowded. Involvement of an active rather than passive process in the formation of nanoclusters and their stabilization is also possible (95).

If the mechanisms of nanocluster formation involve at least the partial self-association at the plasma membrane, then how are these associations limited to the nanoscale? The limiting factors could be of biochemical nature (i.e. they might constitute specific molecular interactions), reflect cell biological aspects (e.g. transmembrane pickets attached to the cytoskeleton) (112) or result from physical effects (e.g. kinetics trapping or the entropic costs associated with nanocluster existence). Importantly, at least in several cases, there is no particular size limit; instead nanoclusters of varying sizes simultaneously coexist (51, 113, 114, 55).

Elucidating the factors that contribute to nanocluster stability is crucially important in understanding nanocluster function and regulation. Generally speaking, nanoclusters could merge, partially disassemble, change their biochemical composition or completely dissolve. A dynamic equilibrium may also exist between nanoclusters and their components in the nearby membrane environment. Another characteristic of nanoclusters is their lateral mobility within the membrane plane. Examples, of functions that require nanocluster mobility are the rearrangement of the relative spatial distributions of TCR and LAT nanoclusters after T cell activation (37), and rearrangement and further recruitment of GPI-APs to activated LFA-1 nanoclusters (49). Finally, the role of the membrane-associated actomyosin cell cortex has only just began to be investigated in detail, both structurally and functionally (95, 113, 112, 115, 116). Determination of its actual organization and structural association with membrane components should be an area of intense investigation in the future.

Role of non-clustered components

Although the forces that drive and limit nanocluster assembly are still under discussion, it is important to note that clustering is rarely complete and that, in many cases, nanoclusters co-exist with randomly distributed non-clustered components, as shown for TCR, LAT, GPI-APs, CD71 (49) and CD36 (117), suggesting that such co-existence has a functional or regulatory role (Fig. 1.8). For example, nanoclusters could act as pre-assembled units that have the potential to become activated upon ligand binding because they spatially concentrate receptors and commonly exhibit restricted diffusion or are even spatially trapped. Yet, they might exist below a functional threshold because of their small size and, as such, are not able to stably bind their ligands. Alternatively, binding of ligands to such small nanoclusters might not be sufficient to elicit a downstream response. Non-clustered components, typically characterized by faster and unconstrained diffusion, might modulate nanocluster function by being incorporated into pre-existing nanoclusters, thereby acting as switches that provide the necessary threshold of nanocluster assembly in order to initiate their function. According to this hypothesis, dynamic pre-formed nanoclusters may not be functional when their size is below a specific threshold. Non-clustered receptors could provide a positive feedback to create larger domains as a way to trigger nanocluster assembly and hierarchical organization in a functional context. Such a positive feedback would, in principle, come into play upon nanocluster activation, and be mediated by lateral diffusion and encounter with nanoclusters, as recently suggested for TCRs (100).

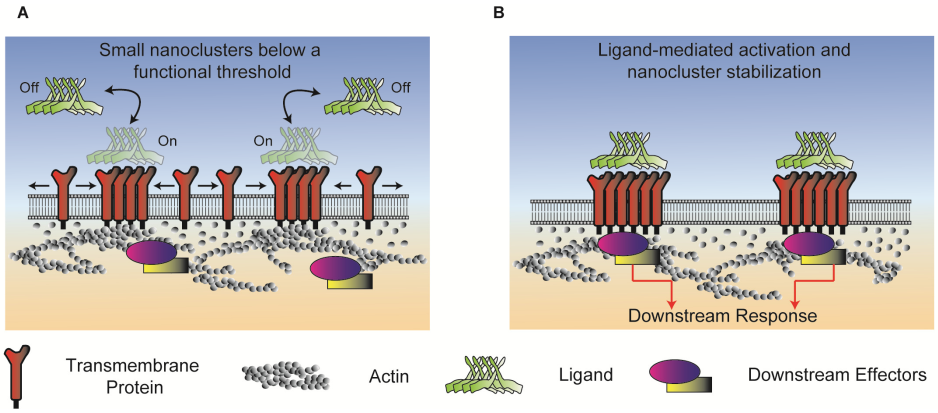

Figure 1.8 Co-existence of transmembrane protein monomers and nanoclusters at the cell membrane. (**A**) Monomers and small inactive nanoclusters co-exist within the cell membrane. Small nanoclusters generally diffuse only slowly or, as shown here, might be anchored to the actin cytoskeleton. Monomeric species, by contrast, have greater mobility. At resting condition, i.e. in their inactivated non-ligand-bound state, it is possible that the size of the nanoclusters is below a functional threshold, at which they cannot stably bind their ligands (the on–off arrows indicate an equilibrium between extracellular and bound ligands). Alternatively, binding of ligands to small nanoclusters might not be sufficient to elicit a response to downstream effectors. (**B**) Upon ligand binding, a pre-existing small nanocluster can incorporate further monomers. Nanocluster activation through ligand binding and further recruitment of protein monomers stabilize the – now – larger cluster and render it functional, resulting in a downstream response. How this process is mediated in unknown but it might require the assistance of the local actin cytoskeleton and/or other signaling molecules, or involve stable conformational changes of the bound receptors that are transmitted to the monomer species.

Why nanoclusters?

The ubiquitous presence of protein nanoclusters in mammalian plasma membranes prompts the crucial question of why nature has chosen this feature. Possible answers might come from elucidating why many soluble proteins are found in oligomeric states. This fundamental question has been addressed in several reviews that discuss plausible hypotheses, many of which may also be applicable to membrane protein nanoclusters (118-120). One important feature of soluble, oligomeric proteins is that they present the possibility of allosteric regulation; thus membrane protein nanoclusters might also be subject to this type of regulation. Another potential function of oligomerization of soluble proteins is to provide multiple, identical, ligand-binding sites in close proximity. For multivalent ligands, nanoclustering might increase the effective ligand-binding affinity (121). Furthermore – compared with non-clustered receptors – in the case of monovalent ligands, oligomerization of their receptors can result in a higher dwell time of the ligand because ligand rebinding is facilitated (122). Moreover, the time of ligand engagement to the nanocluster might be regulated by altering the density of clustered ligand-binding sites because ligand-rebinding probability increases with the square of the binding-site density.

With respect to signal transduction, Hancock and co-workers (123, 124) have proposed that nanoclustering in the plasma membrane offers a general way to ‘digitalize’ analog input signals according to their strength by increasing the number of nanoclusters, because each of these provides a discrete switch-like output because of the short lifetime of nanoclusters (125). For example, in response to EGF stimulation, ligation of the EGF receptor activates K-Ras, thereby generating nanoclusters that provide digital inputs to the Ras–Raf–MEK–ERK kinase signaling cascade. This allows the pathway to be sensitive to small amounts of the activating ligand. The ‘quantal’ outputs from each signaling nanocluster are ‘counted’, i.e. integrated, in the cytoplasm by the kinase cascade to generate the bulk, analog cellular response.

A number of recent studies have demonstrated that membrane protein nanoclusters and their functional remodeling is an emerging theme in eukaryotic plasma membrane organization. It is reasonable to expect that, as the field progresses – particularly in light of the increasing availability of super-resolution microscopy – even more examples will be discovered. The development of technologies that permit simultaneous, multiplexed observation of different nanocluster types in living cells might, in the near future, give rise to a new field of systems nanobiology to specifically address the structural and functional properties of membrane protein nanoclusters. Although each imaging technique has potential drawbacks, the convergence of observations obtained with different approaches strongly suggests that nanoclustering will be increasingly recognized as a predominant feature. One of the challenges that lie ahead is to determine with certainty why nanoclustering is so prevalent.

Concept of this thesis

In this thesis, we address the lateral behavior of the membrane receptor DC-SIGN and of the antigen presenting protein CD1d. By combining multiple color-SPT and STED nanoscopy, we aim to tackle how these two transmembrane proteins are organized on the surface of antigen presenting cells. Moreover, we try to connect the spatiotemporal behavior of these two proteins with their biological function within the context of the human immune system. In Chapter 1, a review is presented about the latest findings of protein nanoclustering on the cell membrane together with the concepts of state-of-the-art biophysical techniques featuring high temporal and spatial resolution. In Chapter 2, the biophysical techniques and the quantitative methodology used throughout this thesis are presented. In Chapter 3, the influence of the neck region of DC-SIGN on its degree of nanoclustering and its virus-binding capabilities is addressed. In Chapter 4, we study the influence of the glycosylation network on the meso-scale spatiotemporal behavior of DC-SIGN. In Chapter 5, we try to link the weak ergodicity breaking of DC-SIGN with its molecular structure, nanoclustering degree and biological function. In Chapter 6, by combining multi-color SPT and STED nanoscopy, the spatiotemporal behavior of CD1d on the cell membrane is addressed and linked to CD1d-mediated iNKT cell activation. Finally, in Chapter 7, we discuss the conclusions of the thesis and highlight developments and experiments for the near-future.

References

1. Parkin J, Cohen B (2001) An overview of the immune system. *Lancet* **357**, 1777-1789.

2. Litman GW, Cannon JP, Dishaw LJ (2005) Reconstructing immune phylogeny: new perspectives. *Nat. Rev. Immunol.* **5**, 866-879.

3. O'Neill LA, Golenbock D, Bowie AG (2013) The history of Toll-like receptors - redefining innate immunity. *Nat. Rev. Immunol.* **13**, 453-460.

4. DiLillo DJ, Horikawa M, Tedder TF (2011) B-lymphocyte effector functions in health and disease. *Immunol. Res.* **49**, 281-292.

5. Banchereau J, Steinman RM (1998) Dendritic cells and the control of immunity. *Nature* **392**, 245-252.

6. Steinman R, Kaplan G, Witmer M, Cohn Z (1979) Identification of a novel cell type in peripheral lymphoid organs of mice. V. Purification of spleen dendritic cells, new surface markers, and maintenance in vitro. *J. Exp. Med.* **149**, 1-16.

7. Steinman RM (2012) Decisions about dendritic cells: past, present, and future. *Ann. Rev. Immunol.* **30**, 1-22.

8. Steinman RM, Cohn ZA (1973) Identification of a novel cell type in peripheral lymphoid organs of mice I. Morphology, quantitation, tissue distribution. *J. Exp. Med.* **137**, 1142-1162.

9. Steinman RM, Cohn ZA (1974) Identification of a novel cell type in peripheral lymphoid organs of mice II. Functional properties in vitro. *J. Exp. Med.* **139**, 380-397.

10. Delamarre L, Holcombe H, Mellman I (2003) Presentation of exogenous antigens on major histocompatibility complex (MHC) class I and MHC class II molecules is differentially regulated during dendritic cell maturation. *J. Exp. Med.* **198**, 111-122.

11. Neefjes J, Jongsma ML, Paul P, Bakke O (2011) Towards a systems understanding of MHC class I and MHC class II antigen presentation. *Nat. Rev. Immunol.* **11**, 823-836.

12. Rodriguez A, Regnault A, Kleijmeer M, Ricciardi-Castagnoli P, Amigorena S. (1999), Selective transport of internalized antigens to the cytosol for MHC class I presentation in dendritic cells. *Nat. Cell Biol.* **1**, 362-368.

13. Palucka K, Banchereau J (2012) Cancer immunotherapy via dendritic cells. *Nat. Rev. Cancer* **12**, 265-277.

14. Palucka K, Banchereau J, Mellman I (2010) Designing vaccines based on biology of human dendritic cell subsets. *Immunity* **33**, 464-478.

15. Trombetta ES, Mellman I (2005) Cell biology of antigen processing in vitro and in vivo. *Annu. Rev. Immunol.* **23**, 975-1028.

16. Lämmermann T, Bader BL, Monkley SJ, Worbs T, Wedlich-Söldner R, Hirsch K*, et al.* (2008) Rapid leukocyte migration by integrin-independent flowing and squeezing. *Nature* **453**, 51-55.

17. Weber M, Hauschild R, Schwarz J, Moussion C, de Vries I, Legler DF*, et al.* (2013) Interstitial dendritic cell guidance by haptotactic chemokine gradients. *Science* **339**, 328-332.

18. Banchereau J, Briere F, Caux C, Davoust J, Lebecque S, Liu Y-J*, et al.* (2000) Immunobiology of dendritic cells. *Ann. Rev. Immunol.* **18**, 767-811.

19. Steinman RM, Hawiger D, Nussenzweig MC (2003) Tolerogenic dendritic cells*. *Ann. Rev. Immunol.* **21**, 685-711.

20. Trombetta ES, Ebersold M, Garrett W, Pypaert M, Mellman I (2003) Activation of lysosomal function during dendritic cell maturation. *Science* **299**, 1400-1403.

21. Figdor CG, van Kooyk Y, Adema GJ (2002) C-type lectin receptors on dendritic cells and Langerhans cells. *Nat. Rev. Immunol.* **2**, 77-84.

22. van Kooyk Y, Geijtenbeek TB (2003) DC-SIGN: escape mechanism for pathogens. *Nat. Rev. Immunol.* **3**, 697-709.

23. Khoo U-S, Chan KY, Chan VS, Lin CS (2008) DC-SIGN and L-SIGN: the SIGNs for infection. *J. Mol. Med.* **86**, 861-874.

24. Serrano-Gómez D, Sierra-Filardi E, Martínez-Nuñez RT, Caparrós E, Delgado R, Muñoz-Fernández MA*, et al.* (2008) Structural requirements for multimerization of the pathogen receptor dendritic cell-specific ICAM3-grabbing non-integrin (CD209) on the cell surface. *J. Biol. Chem.* **283**, 3889-3903.

25. Gringhuis SI, den Dunnen J, Litjens M, van der Vlist M, Geijtenbeek TB (2009) Carbohydrate-specific signaling through the DC-SIGN signalosome tailors immunity to Mycobacterium tuberculosis, HIV-1 and Helicobacter pylori. *Nat. Immunol.* **10**, 1081-1088.

26. Cambi A, Beeren I, Joosten B, Fransen JA, Figdor CG (2009) The C-type lectin DC-SIGN internalizes soluble antigens and HIV-1 virions via a clathrin-dependent mechanism. *Eur. J. Immunol.* **39**, 1923-1928.

27. Cambi A, Lidke DS, Arndt-Jovin DJ, Figdor CG, Jovin TM (2007) Ligand-conjugated quantum dots monitor antigen uptake and processing by dendritic cells. *Nano Lett.* **7**, 970-977.

28. Cambi A, de Lange F, van Maarseveen NM, Nijhuis M, Joosten B, van Dijk EM*, et al.* (2004) Microdomains of the C-type lectin DC-SIGN are portals for virus entry into dendritic cells. *J. Cell Biol.* **164**, 145-155.

29. De Libero G, Mori L (2005) Recognition of lipid antigens by T cells. *Nat. Rev. Immunol.* **5**, 485-496.

30. Blumberg R, Terhorst C, Bleicher P, McDermott F, Allan C, Landau S*, et al.* (1991) Expression of a nonpolymorphic MHC class I-like molecule, CD1D, by human intestinal epithelial cells. *J. Immunol.* **147**, 2518-2524.

31. Dutronc Y, Porcelli S (2002) The CD1 family and T cell recognition of lipid antigens. *Tissue Antigens* **60**, 337-353.

32. Salio M, Speak AO, Shepherd D, Polzella P, Illarionov PA, Veerapen N*, et al.* (2007) Modulation of human natural killer T cell ligands on TLR-mediated antigen-presenting cell activation. *Proc. Natl. Acad. Sci. U S A* **104**, 20490-20495.

33. Taniguchi M, Tashiro T, Dashtsoodol N, Hongo N, Watarai H (2009) The specialized iNKT cell system recognizes glycolipid antigens and bridges the innate and acquired immune systems with potential applications for cancer therapy. *Int. Immunol.* dxp104.

34. Cerundolo V, Barral P, Batista FD (2010) Synthetic iNKT cell-agonists as vaccine adjuvants—finding the balance. *Curr. Opin. Immunol.* **22**, 417-424.

35. Cerundolo V, Silk JD, Masri SH, Salio M (2009) Harnessing invariant NKT cells in vaccination strategies. *Nat. Rev. Immunol.* **9**, 28-

36. Garcia-Parajo MF, Cambi A, Torreno-Pina JA, Thompson N, Jacobson K (2014) Nanoclustering as a dominant feature of plasma membrane organization. *J. Cell Sci.* **127**, 4995-5005.

37. Lillemeier BF, Mörtelmaier MA, Forstner MB, Huppa JB, Groves JT, Davis MM (2010) TCR and Lat are expressed on separate protein islands on T cell membranes and concatenate during activation. *Nat. Immunol.* **11**, 90-96.

38. Hell SW (2007) Far-field optical nanoscopy. *Science* **316**, 1153-1158.

39. Saka SK, Honigmann A, Eggeling C, Hell SW, Lang T, Rizzoli SO (2014) Multi-protein assemblies underlie the mesoscale organization of the plasma membrane. *Nat. Commun.* **5**.

40. Pertsinidis A, Zhang Y, Chu S (2010) Subnanometre single-molecule localization, registration and distance measurements. *Nature* **466**, 647-651.

41. Yildiz A, Forkey JN, McKinney SA, Ha T, Goldman YE, Selvin PR (2003) Myosin V walks hand-over-hand: single fluorophore imaging with 1.5-nm localization. *Science* **300**, 2061-2065.

42. Betzig E, Patterson GH, Sougrat R, Lindwasser OW, Olenych S, Bonifacino JS*, et al.* (2006) Imaging intracellular fluorescent proteins at nanometer resolution. *Science* **313**, 1642-1645.

43. Rust MJ, Bates M, Zhuang X (2006) Sub-diffraction-limit imaging by stochastic optical reconstruction microscopy (STORM). *Nat. Methods* **3**, 793-796.

44. Thompson RE, Larson DR, Webb WW (2002) Precise nanometer localization analysis for individual fluorescent probes. *Biophys. J.* **82**, 2775-2783.

45. Hell SW (2003) Toward fluorescence nanoscopy. *Nat. Biotechnol.* **21**, 1347-1355.

46. Hell SW, Wichmann J (1994) Breaking the diffraction resolution limit by stimulated emission: stimulated-emission-depletion fluorescence microscopy. *Opt. Lett.* **19**, 780-782.

47. Klar TA, Jakobs S, Dyba M, Egner A, Hell SW (2000) Fluorescence microscopy with diffraction resolution barrier broken by stimulated emission. *Proc. Natl. Acad. Sci. U S A* **97**, 8206-8210.

48. Betzig E, Trautman JK (1992) Near-field optics: microscopy, spectroscopy, and surface modification beyond the diffraction limit. *Science* **257**, 189-195.

49. van Zanten TS, Cambi A, Koopman M, Joosten B, Figdor CG, Garcia-Parajo MF (2009) Hotspots of GPI-anchored proteins and integrin nanoclusters function as nucleation sites for cell adhesion. *Proc. Natl. Acad. Sci. U S A* **106**, 18557-18562.

50. van Zanten TS, Gómez J, Manzo C, Cambi A, Buceta J, Reigada R*, et al.* (2010) Direct mapping of nanoscale compositional connectivity on intact cell membranes. *Proc. Natl. Acad. Sci. U S A* **107**, 15437-15442.

51. de Bakker BI, de Lange F, Cambi A, Korterik JP, van Dijk EM, Van Hulst NF*, et al.* (2007) Nanoscale Organization of the Pathogen Receptor DC-SIGN Mapped by Single-Molecule High-Resolution Fluorescence Microscopy. *ChemPhysChem* **8**, 1473-1480.

52. García-Parajó MF, de Bakker BI, Koopman M, Cambi A, de Lange F, Figdor CG*, et al.* (2005) Near-field fluorescence microscopy. *Nanobiotechnol.* **1**, 113-120.

53. Koopman M, Cambi A, de Bakker BI, Joosten B, Figdor CG, van Hulst NF*, et al.* (2004) Near-field scanning optical microscopy in liquid for high resolution single molecule detection on dendritic cells. *FEBS Lett.* **573**, 6-10.

54. Manzo C, Torreno-Pina JA, Joosten B, Reinieren-Beeren I, Gualda EJ, Loza-Alvarez P*, et al.* (2012) The neck region of the C-type lectin DC-SIGN regulates its surface spatiotemporal organization and virus-binding capacity on antigen-presenting cells. *J. Biol. Chem.* **287**, 38946-38955.

55. Williamson DJ, Owen DM, Rossy J, Magenau A, Wehrmann M, Gooding JJ*, et al.* (2011) Pre-existing clusters of the adaptor Lat do not participate in early T cell signaling events. *Nat. Immunol.* **12**, 655-662.

56. Axelrod D, Ravdin P, Koppel D, Schlessinger J, Webb W, Elson E*, et al.* (1976) Lateral motion of fluorescently labeled acetylcholine receptors in membranes of developing muscle fibers. *Proc. Natl. Acad. Sci. U S A* **73**, 4594-4598.

57. Lippincott-Schwartz J, Altan-Bonnet N, Patterson GH. (2003) Photobleaching and photoactivation: following protein dynamics in living cells. *Nat. Cell Biol.* S7-14.

58. Reits EA, Neefjes JJ (2001) From fixed to FRAP: measuring protein mobility and activity in living cells. *Nat. Cell Biol.* **3**, E145-E147.

59. Haustein E, Schwille P (2007) Fluorescence correlation spectroscopy: novel variations of an established technique. *Annu. Rev. Biophys. Biomol. Struct.* **36**, 151-169.

60. Kim SA, Heinze KG, Schwille P (2007) Fluorescence correlation spectroscopy in living cells. *Nat. Methods* **4**, 963-973.

61. Eggeling C, Ringemann C, Medda R, Schwarzmann G, Sandhoff K, Polyakova S*, et al.* (2009) Direct observation of the nanoscale dynamics of membrane lipids in a living cell. *Nature* **457**, 1159-1162.

62. Manzo C, van Zanten TS, Garcia-Parajo MF (2011) Nanoscale fluorescence correlation spectroscopy on intact living cell membranes with NSOM probes. *Biophys. J.* **100**, L8-L10.

63. Kusumi A, Sako Y, Yamamoto M (1993) Confined lateral diffusion of membrane receptors as studied by single particle tracking (nanovid microscopy). Effects of calcium-induced differentiation in cultured epithelial cells. *Biophys. J.* **65**, 2021-2040.

64. Saxton MJ, Jacobson K (1997) Single-particle tracking: applications to membrane dynamics. *Annu. Rev. Biophys. Biomol. Struct.* **26**, 373-399.

65. Suzuki KG, Fujiwara TK, Sanematsu F, Iino R, Edidin M, Kusumi A (2007) GPI-anchored receptor clusters transiently recruit Lyn and Gα for temporary cluster

immobilization and Lyn activation: single-molecule tracking study 1. *J. Cell Biol.* **177**, 717-730.

66. Saxton MJ (1997) Single-particle tracking: the distribution of diffusion coefficients. *Biophys. J.* **72**, 1744.

67. Bakker GJ, Eich C, Torreno-Pina JA, Diez-Ahedo R, Perez-Samper G, van Zanten TS*, et al.* (2012) Lateral mobility of individual integrin nanoclusters orchestrates the onset for leukocyte adhesion. *Proc. Natl. Acad. Sci. U S A* **109**, 4869-4874.

68. Dahan M, Levi S, Luccardini C, Rostaing P, Riveau B, Triller A (2003) Diffusion dynamics of glycine receptors revealed by single-quantum dot tracking. *Science* **302**, 442-445.

69. Pinaud F, Clarke S, Sittner A, Dahan M (2010) Probing cellular events, one quantum dot at a time. *Nat. Methods* **7**, 275-285.

70. Sergé A, Bertaux N, Rigneault H, Marguet D (2008) Dynamic multiple-target tracing to probe spatiotemporal cartography of cell membranes. *Nat. Methods* **5**, 687-694.

71. Andrews NL, Lidke KA, Pfeiffer JR, Burns AR, Wilson BS, Oliver JM*, et al.* (2008) Actin restricts Fcϵ RI diffusion and facilitates antigen-induced receptor immobilization. *Nat. Cell Biol.* **10**, 955-963.

72. Singer S, Nicolson GL (1972) The fluid mosaic model of the structure of cell membranes. *Science* **175**, 720-731.

73. Frye L, Edidin M (1970) The rapid intermixing of cell surface antigens after formation of mouse-human heterokaryons. *J. Cell Sci.* **7**, 319-335.

74. Jacobson K, Sheets ED, Simson R (1995) Revisiting the fluid mosaic model of membranes. *Science* **268**, 1441.

75. van Meer G, Stelzer E, Wijnaendts-van-Resandt RW, Simons K (1987) Sorting of sphingolipids in epithelial (Madin-Darby canine kidney) cells. *J. Cell Biol.* **105**, 1623-1635.

76. Lingwood D, Simons K (2010) Lipid rafts as a membrane-organizing principle. *Science* **327**, 46-50.

77. Simons K, Toomre D (2000) Lipid rafts and signal transduction. *Nat. Rev. Mol. Cell Biol.* **1**, 31-39.

78. Pike LJ (2006) Rafts defined: a report on the Keystone Symposium on Lipid Rafts and Cell Function. *J. Lipid Res.* **47**, 1597-1598.

79. Jacobson K, Mouritsen OG, Anderson RG (2007) Lipid rafts: at a crossroad between cell biology and physics. *Nat. Cell Biol.* **9**, 7-14.

80. Sheetz M. Membrane skeletal dynamics: role in modulation of red cell deformability, mobility of transmembrane proteins, and shape. Semin. Hematol.; 1983; 1983. p. 175-188.

81. Kusumi A, Nakada C, Ritchie K, Murase K, Suzuki K, Murakoshi H*, et al.* (2005) Paradigm shift of the plasma membrane concept from the two-dimensional continuum fluid to the partitioned fluid: high-speed single-molecule tracking of membrane molecules. *Annu. Rev. Biophys. Biomol. Struct.* **34**, 351-378.

82. Anderson RG, Jacobson K (2002) A role for lipid shells in targeting proteins to caveolae, rafts, and other lipid domains. *Science* **296**, 1821-1825.

83. Yáñez-Mó M, Barreiro O, Gordon-Alonso M, Sala-Valdés M, Sánchez-Madrid F (2009) Tetraspanin-enriched microdomains: a functional unit in cell plasma membranes. *Trends Cell Biol.* **19**, 434-446.

84. Lajoie P, Goetz JG, Dennis JW, Nabi IR (2009) Lattices, rafts, and scaffolds: domain regulation of receptor signaling at the plasma membrane. *J. Cell Biol.* **185**, 381-385.

85. Delaguillaumie A, Harriague J, Kohanna S, Bismuth G, Rubinstein E, Seigneuret M*, et al.* (2004) Tetraspanin CD82 controls the association of cholesterol-dependent microdomains with the actin cytoskeleton in T lymphocytes: relevance to co-stimulation. *J. Cell Sci.* **117**, 5269-5282.

86. Mayor S, Riezman H (2004) Sorting GPI-anchored proteins. *Nat. Rev. Mol. Cell Biol.* **5**, 110-120.

87. Friedrichson T, Kurzchalia TV (1998) Microdomains of GPI-anchored proteins in living cells revealed by crosslinking. *Nature* **394**, 802-805.

88. Varma R, Mayor S (1998) GPI-anchored proteins are organized in submicron domains at the cell surface. *Nature* **394**, 798-801.

89. Sharma P, Varma R, Sarasij R, Gousset K, Krishnamoorthy G, Rao M*, et al.* (2004), Nanoscale organization of multiple GPI-anchored proteins in living cell membranes. *Cell* **116**, 577-589.

90. Mayor S, Rao M (2004) Rafts: scale-dependent, active lipid organization at the cell surface. *Traffic* **5**, 231-240.

91. Sengupta P, Jovanovic-Talisman T, Skoko D, Renz M, Veatch SL, Lippincott-Schwartz J (2011) Probing protein heterogeneity in the plasma membrane using PALM and pair correlation analysis. *Nat. Methods* **8**, 969-975.

92. Klotzsch E, Schütz GJ (2013) A critical survey of methods to detect plasma membrane rafts. *Philos. Trans. R. Soc. Lond. B Biol. Sci.* **368**, 20120033.

93. Suzuki KG, Kasai RS, Hirosawa KM, Nemoto YL, Ishibashi M, Miwa Y*, et al.* (2012) Transient GPI-anchored protein homodimers are units for raft organization and function. *Nat. Chem. Biol.* **8**, 774-783.

94. Lin W-C, Iversen L, Tu H-L, Rhodes C, Christensen SM, Iwig JS*, et al.* (2014) H-Ras forms dimers on membrane surfaces via a protein–protein interface. *Proc. Natl. Acad. Sci. U S A* **111**, 2996-3001.

95. Gowrishankar K, Ghosh S, Saha S, Rumamol C, Mayor S, Rao M (2012) Active remodeling of cortical actin regulates spatiotemporal organization of cell surface molecules. *Cell* **149**, 1353-1367.

96. Raghupathy R, Anilkumar AA, Polley A, Singh PP, Yadav M, Johnson C*, et al.* (2015) Transbilayer Lipid Interactions Mediate Nanoclustering of Lipid-Anchored Proteins. *Cell* **161**, 581-594.

97. Cambi A, Joosten B, Koopman M, de Lange F, Beeren I, Torensma R*, et al.* (2006) Organization of the integrin LFA-1 in nanoclusters regulates its activity. *Mol. Biol. Cell* **17**, 4270-4281.

98. Rossier O, Octeau V, Sibarita J-B, Leduc C, Tessier B, Nair D*, et al.* (2012) Integrins β1 and β3 exhibit distinct dynamic nanoscale organizations inside focal adhesions. *Nat. Cell Biol.* **14**, 1057-1067.

99. Yu C-h, Luo W, Sheetz MP (2012) Spatial-temporal reorganization of activated integrins. *Cell adhesion & migration* **6**, 280-284.

100. Schamel WW, Alarcón B (2013) Organization of the resting TCR in nanoscale oligomers. *Immunol. Rev.* **251**, 13-20.

101. Schamel WW, Arechaga I, Risueño RM, van Santen HM, Cabezas P, Risco C*, et al.* (2005) Coexistence of multivalent and monovalent TCRs explains high sensitivity and wide range of response. *J. Exp. Med.* **202**, 493-503.

102. James JR, White SS, Clarke RW, Johansen AM, Dunne PD, Sleep DL*, et al.* (2007) Single-molecule level analysis of the subunit composition of the T cell receptor on live T cells. *Proc. Natl. Acad. Sci. U S A* **104**, 17662-17667.

103. Molnár E, Swamy M, Holzer M, Beck-García K, Worch R, Thiele C*, et al.* (2012) Cholesterol and sphingomyelin drive ligand-independent T-cell antigen receptor nanoclustering. *J. Biol. Chem.* **287**, 42664-42674.

104. Kumar R, Ferez M, Swamy M, Arechaga I, Rejas MT, Valpuesta JM*, et al.* (2011) Increased sensitivity of antigen-experienced T cells through the enrichment of oligomeric T cell receptor complexes. *Immunity* **35**, 375-387.

105. Hořejší V, Zhang W, Schraven B (2004) Transmembrane adaptor proteins: organizers of immunoreceptor signalling. *Nat. Rev. Immunol.* **4**, 603-616.

106. Sherman E, Barr V, Manley S, Patterson G, Balagopalan L, Akpan I*, et al.* (2011) Functional nanoscale organization of signaling molecules downstream of the T cell antigen receptor. *Immunity* **35**, 705-720.

107. Larghi P, Williamson DJ, Carpier J-M, Dogniaux S, Chemin K, Bohineust A*, et al.* (2013) VAMP7 controls T cell activation by regulating the recruitment and phosphorylation of vesicular Lat at TCR-activation sites. *Nat. Immunol.* **14**, 723-731.

108. Veatch SL, Chiang EN, Sengupta P, Holowka DA, Baird BA (2012) Quantitative nanoscale analysis of IgE-FcεRI clustering and coupling to early signaling proteins. *J. Phys. Chem. B* **116**, 6923-6935.

109. Wilson BS, Pfeiffer JR, Surviladze Z, Gaudet EA, Oliver JM (2001) High resolution mapping of mast cell membranes reveals primary and secondary domains of FcϵRI and LAT. *J. Cell Biol.* **154**, 645-658.

110. Yang J, Reth M (2010) Oligomeric organization of the B-cell antigen receptor on resting cells. *Nature* **467**, 465-469.

111. Mattila PK, Feest C, Depoil D, Treanor B, Montaner B, Otipoby KL*, et al.* (2013) The actin and tetraspanin networks organize receptor nanoclusters to regulate B cell receptor-mediated signaling. *Immunity* **38**, 461-474.

112. Kusumi A, Suzuki KG, Kasai RS, Ritchie K, Fujiwara TK (2011) Hierarchical mesoscale domain organization of the plasma membrane. *Trends Biochem. Sci.* **36**, 604-615.

113. Gudheti MV, Curthoys NM, Gould TJ, Kim D, Gunewardene MS, Gabor KA*, et al.* (2013) Actin mediates the nanoscale membrane organization of the clustered membrane protein influenza hemagglutinin. *Biophys. J.* **104**, 2182-2192.

114. Itano MS, Steinhauer C, Schmied JJ, Forthmann C, Liu P, Neumann AK*, et al.* (2012) Super-resolution imaging of C-type lectin and influenza hemagglutinin nanodomains on plasma membranes using blink microscopy. *Biophys. J.* **102**, 1534-1542.

115. Luo T, Mohan K, Iglesias PA, Robinson DN. (2013) Molecular mechanisms of cellular mechanosensing. *Nat. Mater.* **12**, 1064-1071.

116. Xu K, Zhong G, Zhuang X. (2013) Actin, spectrin, and associated proteins form a periodic cytoskeletal structure in axons. *Science* **339**, 452-456.

117. Jaqaman K, Kuwata H, Touret N, Collins R, Trimble WS, Danuser G*, et al.* (2011) Cytoskeletal control of CD36 diffusion promotes its receptor and signaling function. *Cell* **146**, 593-606.

118. Ali MH, Imperiali B (2005) Protein oligomerization: how and why. *Bioorg. Med. Chem.* **13**, 5013-5020.

119. Hashimoto K, Nishi H, Bryant S, Panchenko AR (2011) Caught in self-interaction: evolutionary and functional mechanisms of protein homooligomerization. *Phys. Biol.* **8**, 035007.

120. Lynch M (2013) Evolutionary diversification of the multimeric states of proteins. *Proc. Natl. Acad. Sci. U S A* **110**, E2821-E2828.

121. Cebecauer M, Spitaler M, Sergé A, Magee AI (2010) Signalling complexes and clusters: functional advantages and methodological hurdles. *J. Cell Sci.* **123**, 309-320.

122. Lagerholm BC, Thompson NL (1998) Theory for ligand rebinding at cell membrane surfaces. *Biophys. J.* **74**, 1215-1228.

123. Harding AS, Hancock JF (2008) Using plasma membrane nanoclusters to build better signaling circuits. *Trends Cell Biol.* **18**, 364-371.

124. Tian T, Harding A, Inder K, Plowman S, Parton RG, Hancock JF (2007) Plasma membrane nanoswitches generate high-fidelity Ras signal transduction. *Nat. Cell Biol.* **9**, 905-914.

125. Murakoshi H, Iino R, Kobayashi T, Fujiwara T, Ohshima C, Yoshimura A*, et al.* (2004) Single-molecule imaging analysis of Ras activation in living cells. *Proc. Natl. Acad. Sci. U S A* **101**, 7317-7322.

Chapter 2

Quantitative methodology for STED nanoscopy and multi-color single particle tracking

As discussed in Chapter 1, the study of the spatiotemporal behavior of membrane receptors of antigen presenting cells represents a crucial step in understanding immune reactions at the molecular level. Super-resolution techniques and single particle tracking have allowed for the first time the direct visualization of transmembrane proteins at the nanoscale. In this thesis, we combine STED nanoscopy and multi-color single-particle tracking to address the lateral behavior of DC-SIGN and CD1d. In this chapter, we present a methodological framework that allows us to quantify STED nanoscopy images and multi-color single-particle data.

This work has been partially published as **1.** C. Manzo , T.S. van Zanten, S. Saha, J.A. Torreno-Pina, S. Mayor, M.F. Garcia-Parajo, "PSF decomposition of nanoscopy images via Bayesian analysis unravels distinct molecular organization of the cell membrane", *Scientific Reports* **4**, 4354 (2014) and **2.** G.J. Bakker, C. Eich, J.A. Torreno-Pina, R. Diez-Ahedo, G. Perez-Samper, T.S. van Zanten, C.G. Figdor, A. Cambi, M.F. Garcia-Parajo, "Lateral mobility of individual integrin nanoclusters orchestrates the onset for leukocyte adhesion", *P.N.A.S.* **109**, 4869 (2012).

Introduction

As extensively described in Chapter 1, in the last ten years a group of super-resolution optical techniques have been developed to obtain lateral nanometric resolution of fixed samples at highly dense molecular densities. Moreover, we also discussed several approaches to derive dynamic information on living cells at the single molecule level. In this thesis, we have combined stimulated emission depletion (STED) microscopy together with single particle tracking (SPT) using quantum dots (QDs) to investigate the spatiotemporal organization of different receptors on cells of the immune system. We take advantage of the high spatial resolution of STED to map the lateral distribution of receptors on fixed cells. In addition, multi-color SPT is used to infer how the lateral organization of these receptors changes over time and how receptors dynamically interact with other cellular membrane components.

In this chapter we explain the methodological approach followed in the thesis. In particular, we describe the two different experimental configurations, i.e., STED & SPT as well as the specific sample preparation conditions of both techniques. Moreover, we also explain the different algorithms used for every experimental condition to be able to analyze the data in a rigorous manner.

STED nanoscopy: from principles to imaging and data analysis

STED nanoscopy relies on the off-switching of an excited fluorophore using stimulated emission, a process theoretically discovered by Albert Einstein about hundred years ago (1). The off-switching is based on the principle that fluorophores can be de-excited by stimulating their decay from an excited state (S_1) to the ground state (S_0) using light without the emission of fluorescence photons (2). Hence, and in contrast to spontaneous fluorescence emission, stimulated emission is not a stochastic process. STED nanoscopy breaks diffraction by off-switching excited fluorophores within a predefined area of the sample via stimulated emission. This concept is engineered by overlapping a red-shifted doughnut-shaped STED beam with a Gaussian-shaped excitation laser creating a mask with an effective sub-diffraction sized area in the center of both beams (2) (Fig. 2.1).

The choice of the fluorophore to be used is a critical step when performing STED nanoscopy. For instance, the fluorophore in the excited state can absorb a photon from the STED beam and instead of undergoing stimulated emission, the fluorophore can be further excited into higher singlet ($S_{n>1}$) or triplet ($T_{n>1}$) states which can lead to its photobleaching (3, 4). Hence, fluorophores bearing little absorption from S_1 to $S_{n>1}$ or $T_{n>1}$ states at the STED wavelength are ideally suited for STED nanoscopy (5). Another limitation in choosing a dye and a corresponding STED beam wavelength is the potential spectral overlap between the absorption and emission spectrum of the fluorophore. If there is a strong overlay of both spectra, the STED beam can excite fluorophores from higher vibrational states of S_0 to the S_1 state leading to anti-Stokes emission (6). This process can lead to background fluorescence of the dyes below the STED beam area and a concomitant reduction in the lateral resolution of the STED nanoscope. This effect is in practice solved by red-shifting the wavelength of the STED beam to the far-red edge of the fluorescence emission spectrum. Hence, although STED represents a very powerful working principle, the right combination of the STED beam wavelength with the proper fluorophore is a crucial step when performing STED super-resolution imaging.

Since STED relies on the off-switching of excited fluorophores via stimulated emission, its lateral resolution depends ultimately on the intensity *I* of the STED beam as given in the following formula (1):

$$\Delta r \approx \frac{\lambda}{2n\sin\alpha\sqrt{(1+{}^{I}/_{I_s})}} \tag{1}$$

where *n* is the refractive index of the medium between the sample and the objective, α is the one-half angular aperture of the objective and λ is the wavelength of the excitation light. I_s is the STED beam intensity value at which the fluorescence of the excited dye is depleted to 50% (1). Thus, only when the STED beam intensity favors stimulated emission over spontaneous emission, the excited fluorophores are switched off (1). Since the rate of fluorescence spontaneous emission (τ) is typically as high as 10^9 s^{-1} and the cross-section for stimulated emission (σ_{STED}) is 10^{-16} cm^2 (6), STED beams with very high excitation densities (~GW/cm^2) are required to induce stimulated emission. To maximize the optimization of the depletion process while trying to minimize the amount of STED beam intensity needed, STED nanoscopy is best performed using pulsed lasers (3). By fine-tuning the arrival time and duration of the pulse of the excitation and STED beam, stimulated emission can be favored over other competing transitions of the excited fluorophores efficiently. The STED pulse should ideally arrive after the excitation pulse and be shorter than the vibrational relaxation of electrons in the excited state S_1, typically 10^{-12} to 10^{-14} s (7). For example, STED nanoscopy have been performed by time-delaying a 250 ps STED pulse with respect to a 80 ps excitation pulse (3, 8, 9, 10).

Although pulsed-STED offers a lateral resolution close to the molecular level, its com-

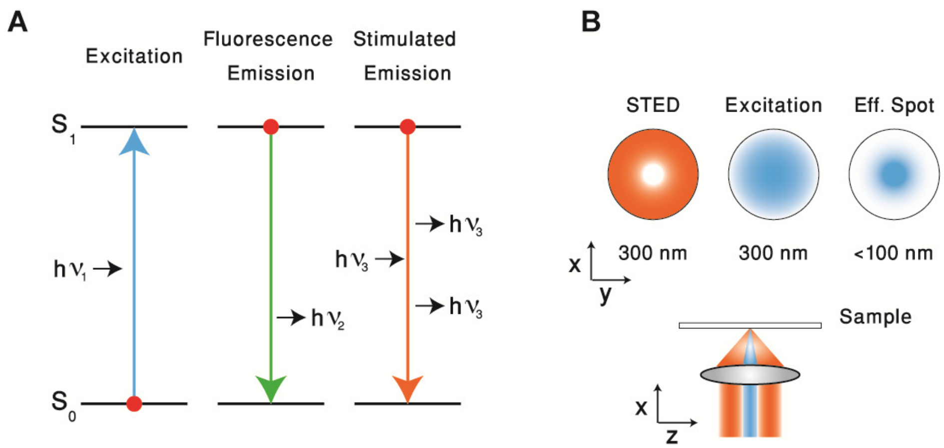

Figure 2.1 Schematic of the working principle of stimulated emission and STED nanoscopy. (**A**) The fluorophore (represented as a red dot) is excited from the ground state (S_0) to the excited state (S_1) by the incidence of a photon (left). From the excited state, the fluorophore can decay via spontaneous emission to the ground state (center) emitting a fluorescence photon with lower energy than the excitation one ($\upsilon_1 > \upsilon_2$). Alternatively, the fluorophore can decay to the ground state via stimulated emission induced by an incoming red-shifted photon ($\upsilon_1 > \upsilon_2 > \upsilon_3$). The additional emitted photon via stimulated emission has the same wavelength, phase and polarization than the incident one. (**B**) A diffraction-limited excitation laser (blue) is overlapped with a doughnut-shaped STED beam (red). Fluorophores located under the STED beam area are switched off via stimulated emission while fluorophores located in the central region with an effective sub-diffraction area are allowed to emit fluorescence.

plicated pulse optimization and synchronization represents a limitation when developing a STED microscope in the lab. Continuous wave (CW) STED represents a simplified version of a STED microscope where the fluorophore is continuously illuminated and excited (10). However, this continuous illumination of the dye requires higher STED beam intensities to enhance stimulated emission over other competing transitions. Hence, due to this higher STED beam intensity, the probability of photobleaching of the fluorophore in CW-STED increases compared to pulsed-STED. Nevertheless, photobleaching can be reduced on CW-STED by reducing the pixel integration time and faster-scanning of the sample. Although the achievable resolution of CW-STED is typically lower than with pulsed-STED, it offers a good compromise between set-up simplicity and a reasonable resolution (somewhere between 80-100nm).

In this thesis, we have performed STED nanoscopy using a commercial Leica CW-STED setup (TCS-SP5). A fully motorized Leica DMI6000B microscope equipped with a 100x 1.4 N.A. oil objective (HCX PL APO CS, Leica) was used to visualize the sample. We chose to use AlexaFluor 488nm (AF488) for all the experiments reported in this thesis given its good performance in CW-STED set-ups (11). AF488 fluorophores were excited with the 488nm line of an ArKr laser with a laser intensity of ~1 µW in the focal plane. To achieve the highest lateral resolution possible by the setup, the STED laser beam intensity was set to 100% of its power, ~100-130 mW in the focal plane. Co-alignment of the excitation and the STED beam was automatically performed several times to ensure optimal alignment, depletion efficiency and maximal lateral resolution by the setup. 1024x1024 pixel STED images were acquired with a bit depth of 12 bits. The fluorescence intensity coming from the sample was detected either by an avalanche photo diode module (APD) or with a photomultiplier tube (PMT). Line accumulation and image averaging depended on the labeling conditions of the sample. However, to be able to compare different imaging conditions, STED imaging of individual fluorescent labeled Abs was performed every time under the exact same imaging conditions as the sample. STED resolution was ≈100 nm or ≈85 nm when fitting the point-spread function of the fluorescence spots with a Gaussian or with a Lorentzian function, respectively.

Sample preparation for STED imaging. The main goal of super-resolution imaging is to map the entire population of receptor proteins on the cell membrane. Thus, a high concentration of labeling probes such as fluorophore labeled antibodies (Abs), has to be applied so that ideally all target proteins on the cell membrane can be fluorescently labeled, imaged and quantified. The general procedure for receptor labeling used throughout this thesis has been the following: typically, adherent cells such as Chinese Hamster Ovary (CHO) cells or immature Dendritic Cells (imDCs) were directly cultured on glass coverslips so that no further substrate treatment was needed to ensure cell spreading and adhesion. Non adherent cells such as the human myelomonocytic cell line THP-1 were incubated onto PLL-coated (10 µg/ml) glass coverslips for 30 min at 37ºC. After cell adhesion, cells were fixed in 2% Paraformaldehyde (PFA) for 15 min and subsequently blocked with a solution containing 3% BSA + 20 mM Glycine in PBS buffer for 15 min (12). Fc receptors were blocked in order to avoid non-specific binding of Antibodies (Abs) to the cells by blocking them with a 2% HS. In 2 separated steps, primary mouse anti-human Abs and goat anti-mouse AlexaFluor488 (AF488) labeled secondary Abs were added at a concentration of ≈5 µg/ml (≈30 nM) and incubated for 30 min at room temperature. Isotype controls were always performed in order to check that all the labelings were specific. After the sample preparation was completed, cells were kept in a 1% PFA solution in PBS buffer till imaging.

Analysis of STED nanoscopy images

In this thesis, we have followed two different methodologies to analyze STED nanoscopy images with the aim of obtaining the nanoclustering degree of membrane receptors. The two methodologies extract the nanocluster stoichiometry based on the comparison between the fluorescence intensity signals of an individual nanocluster with the intensity fluorescence signal of individual Abs spread on glass. The choice of each methodology depended on the receptor density on the cell membrane. If, due to a low receptor density and a concomitant nearest-neighbor distance (*nnd*) larger than the lateral resolution of the STED microscope, individual spots could be visually identified, manual Gaussian fitting of each spot was performed. On the contrary, if the receptor density prevented the identification of individual spots on the raw STED image, an algorithm based on the decomposition of intensity peaks with PSFs obtained from single markers was used.

Gaussian fitting of single membrane protein nanoclusters. To extract quantitative information about the lateral organization of receptors with a low protein density on the cell membrane, we fitted the intensity profile of each individual nanocluster with a 2D Gaussian curve (12, 13):

$$I(x,y) = I_0 e^{-\left(\left(\frac{(x-x_0)^2+(y-y_0)^2}{2\sigma^2}\right)\right)} \tag{2}$$

where x_0 and y_0 are the peak location coordinates, I_0 is the peak intensity and σ the standard deviation in both dimensions.

By extracting the centroid position, the FWHM and the intensity from the fit, the lateral position, the size and the nanoclustering degree, i.e. number of molecules per cluster, of each individual spot could be obtained, respectively. This is a valid approach because the total intensity profile of any given nanocluster is directly proportional to the number of AF488-labeled Abs attached to it as long as the number of molecules per cluster is relatively small so that self-quenching does not occur. Hence, by comparing the fluorescence intensity of each protein nanocluster on the cell membrane with the fluorescence intensity of individual AF488-labeled Abs spread on the glass coverslip, we estimated the number of proteins per nanocluster. Specifically, the total intensity of each individual nanocluster was extracted by averaging the background-corrected intensity values over all pixels located within the FWHM of each spot. Moreover, the total intensity of spots on glass corresponding to single Abs was determined using the same approach. By dividing the mean fluorescence intensity of all the individual nanoclusters by the mean intensity value of all the spots on glass, the nanoclustering degree of membrane receptors could be estimated.

PSF decomposition of nanoscopy images via Bayesian analysis. As mentioned above, manual Gaussian fitting can only be applied when the identification of individual spots on the cell membrane is feasible due to a low protein density. For highly dense STED nanoscopy images, a more advanced algorithm based on Bayesian inference was developed by Dr. Carlo Manzo in our lab (14). The concept of this algorithm is the progressive reconstruction of a high fidelity synthetic super-resolution image by quantifying the fluorescence intensity of each local intensity peak of the raw STED image using the fluorescence intensity of individual markers as a reference. The method only requires two input parameters: the width of the PSF and the intensity distribution of individual receptor markers. Both quantities can be evaluated from images of sparse immobilized fluorescent markers on glass or on the cell membrane. The fact that the algorithm only requires these 2 parameters allows a high throughput quantification of super-resolution images and a very user-friendly approach. Moreover, since this method is based on the fluorescence intensity of the sample, it represents a particularly suitable data analysis methodology for low intensity STED nanoscopy or circular aperture-based NSOM since both techniques offer a low probability of fluorophore photobleaching while achieving nanoscopic resolution.

The algorithm relies on the progressive full reconstruction of a synthetic image by detecting, reconstructing and correspondingly subtracting all the local peak intensity values within a sub-region of the raw unprocessed image. After peak subtraction of the reconstructed sub-region, the deflated image undergoes a new iteration of the algorithm. This process continues *n* cycles for *n* sub-regions until a final faithfully reconstructed synthetic super-resolution image is obtained (Fig. 2.2). The schematic of the algorithm is the following: First, the algorithm is applied on the STED raw image (RAW in Fig. 2.2) without filtering or preprocessing (Fig. 2.2A). The first step consists in determining an image sub-region having the highest probability of containing features that can be associated to marker fluorescence emission and not to noise (Fig. 2.2B). After having identified that fixed size sub-region (white box in Fig. 2.2A or red box in Fig. 2.2B), the raw intensity map of the sub-region is attempted to be reconstructed (REC in Fig. 2.2C) as the sum of *n* PSFs, each PSF being two-dimensional Gaussian functions obtained from individual markers spread on glass. This reconstruction is performed by minimizing the Bayesian Inference Criterion (BIC) (14). Importantly, BIC introduces a penalty for the addition of further PSFs, thus preventing overestimation of the particle number when reconstructing the sub-region raw image. When the algorithm has faithfully reconstructed the intensity map contained within the sub-region (Fig. 2.2C, right), the algorithm adds the reconstructed intensity map to the synthetic final super-resolution image (Fig. 2.2D, left) while subtracting the corresponding region from the entire raw STED image (SUB in Fig. 2.2D, right). The resulting subtracted image is passed again through the algorithm and a new iteration starts. This cycle is repeated *n* times till the full raw STED image has been reconstructed by PSFs extracted from markers. After full reconstruction of the synthetic image, the algorithm minimizes false detected peaks in the entire image by doing a global BIC analysis on all the detected PSFs. This final step prevents overestimation of the detected number of particles yielding a high fidelity reconstructed synthetic super-resolution image.

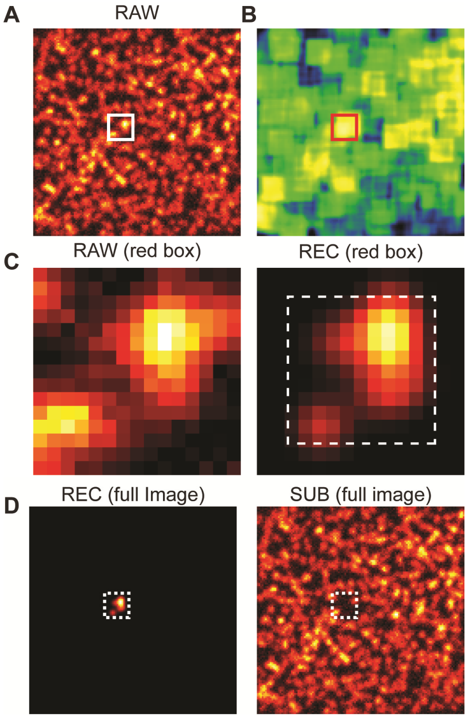

Figure 2.2 Schematic of the PSF decomposition algorithm via Bayesian Analysis. (**A**) A fixed size sub-region from the raw image having the highest likelihood (**B**) to contain intensity values corresponding to the intensity of single markers is searched and selected (white box in **A** or red box in **B**) for further calculation. (**C**) The raw intensity peaks in the sub-region (left) are reconstructed as a sum of PSFs (REC, right) determined from single markers using a BIC routine (see main text for details). (**D**) The reconstructed sub-region is added to a null synthetic image (left) and the corresponding area (right) in the raw STED image is subtracted. The algorithm is repeated until the entire raw fluorescence image is depleted and a full reconstructed (synthetic) image is generated.

Evaluation of the performance of the algorithm. Besides molecular density, other factors such as the width of the PSF, background noise and marker brightness distribution significantly affect particle localization accuracy of the algorithm. While PSF width and noise depends on instrumental settings, marker brightness distribution is related to the labeling marker. For STED nanoscopy, receptors are typically labeled with antibodies containing one or more organic fluorophores. The brightness intensity distribution accounts for the fluorophore quantum yield, mean and variance of the number of fluorophores per antibody and the intrinsic stochasticity of fluorophore emission. Since the algorithm takes advantage of such a distribution to infer on particle localization, its impact on the algorithm performance was evaluated. For this, synthetic images were generated at different molecular densities while varying the FWHM of the PSF, signal-to-noise ratio (SNR, calculated as 20 times the logarithm of the mean brightness over the background noise standard deviation), average intensity (I) and width (σ_I^2) of the marker brightness distribution. The analysis of simulated data (Fig.

2.3) shows the algorithm capability to reconstruct raw images in a wide range of molecular densities (up to 200 μm^{-2}) at moderate super-resolution conditions (FWHM = 90 nm) typically afforded by our commercial STED microscope. At densities larger than ~500 μm^{-2} (Fig. 2.3, lower panels), the finite width of the intensity distribution increases the probability that different molecules separated by distances shorter than the resolution are identified as a single one, affecting the particle localization accuracy and the number of positive detections.

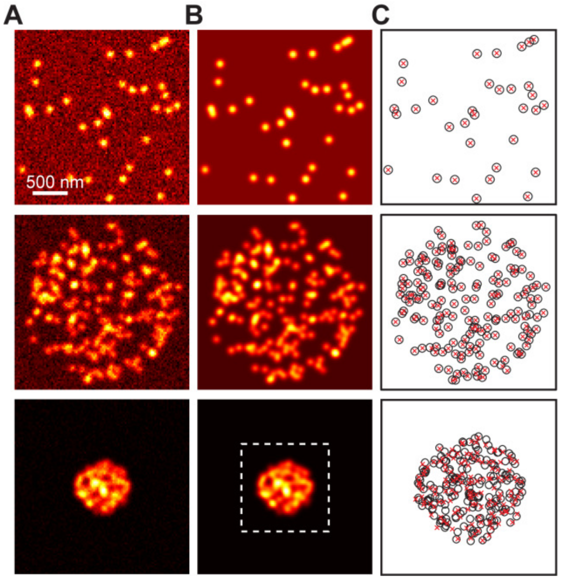

Figure 2.3 Simulated images were generated using standard experimental imaging conditions, i.e., resolution = 90 nm, signal-to-noise ratio = 15 dB, average intensity of 100 counts and standard deviation of the intensity of 15 counts. (**A**) Representative synthetic images at three different densities (5, 50, 500 μm^{-2}, from top to bottom). (**B**) Corresponding images reconstructed by the PSF decomposition via Bayesian algorithm. (**C**) Particle localizations retrieved by the algorithm (red crosses) compared with the original particle locations used in the simulations (open circles).

For a quantitative assessment of the algorithm performance, we then calculated the recall fraction R_f, i.e. the ratio between the number of particles correctly identified with localizations and the number of simulated ones, the localization error L_{err} and the relative intensity error I_{err} (Fig. 2.4). We first evaluated the effect of the instrumental resolution on particle identification and localization (Fig. 2.4A). Notably, the method yields a high R_f, small L_{err} and I_{err} at receptor densities <200 μm^{-2} for all the investigated resolutions. For densities beyond this value, R_f decays in a resolution-dependent way towards a constant offset (~0.4), together with a concomitant increase in L_{err} and I_{err}. Notice that for extremely high densities (>1000 μm^{-2}) there is an apparent decrease in L_{err} due to the false identification of closely spaced particles as a single one.

Quantification of receptor spatial organization from reconstructed STED images. We determined the cluster size and number of particles per cluster using the pair-correlation function. The pair-correlation function *g(r)* was calculated similarly as previously detailed (15) on reconstructed images obtained by convoluting the particle localizations with 2D Gaussian functions having width equal to the localization accuracies Δr_i. Each curve represents the average of at least 30 pair correlations obtained over 3x3 μm^2 regions of interest.

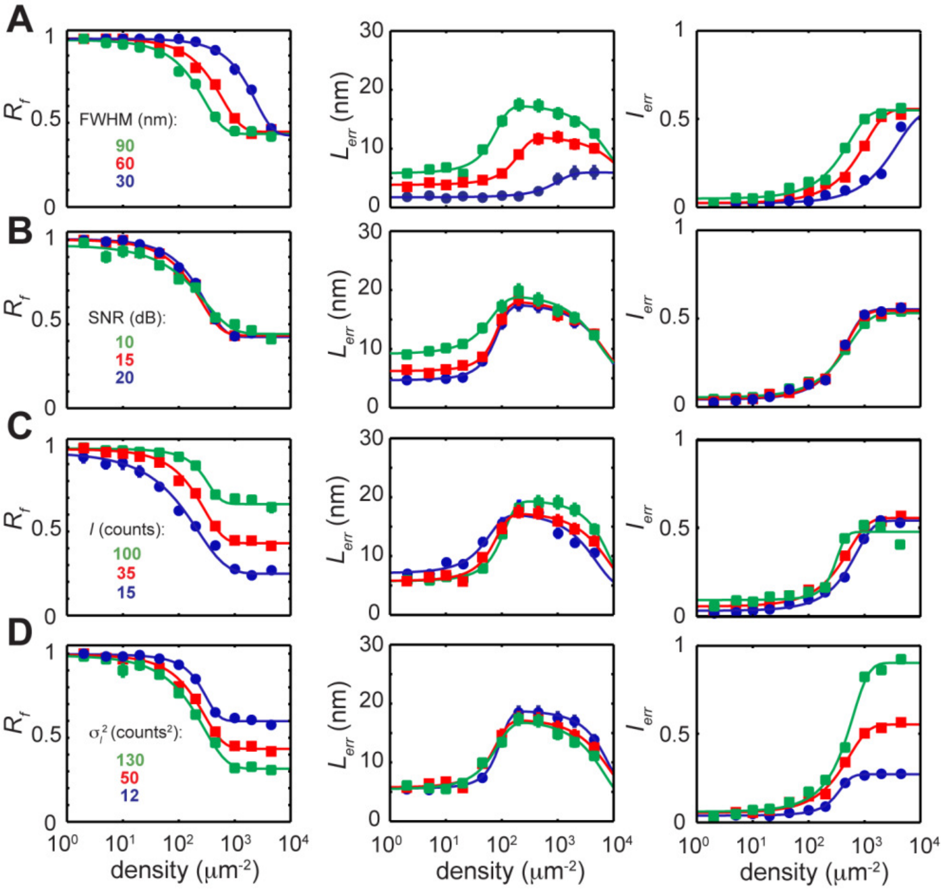

Figure 2.4 The recall fraction R_f, localization error L_{err} and intensity relative error I_{err} were evaluated as a function of molecular density for different experimental settings. (**A**) For varying image resolution, i.e, FWHM, with SNR = 15 dB, I = 35 counts,σ_I^2 = 50 counts^2. (**B**) For varying SNR, with FWHM = 90 nm, I = 35 counts, σ_I^2 = 50 counts^2. (**C**) For varying mean intensity value I, with FWHM = 90 nm, SNR = 15 dB, σ_I^2 = 50 counts^2 and (**D**) for varying width of the intensity distribution σ_I^2, with FWHM = 90 nm, SNR = 15 dB and I = 35 counts.

Fitting of the *g(r)* curves was performed according to:

$$g(r) = \frac{1}{4\pi\langle\Delta r_i\rangle^2\rho}\exp\left(-\frac{r^2}{4\langle\Delta r_i\rangle^2}\right) + g_{rec}\otimes g_{\langle\Delta r_i\rangle} \tag{3}$$

where the first term accounts for the average particle localization accuracy $\left\langle \Delta r_i \right\rangle$ and with ρ indicating the protein density. The second term represents the convolution of the receptor correlation with a Gaussian function having width equal to the average localization accuracy. The cluster radius r_{clust} was calculated as the value at which g_{rec} decays at *1/e*. From these quantities, the average number of particle per cluster N_{clust} was calculated as described by Sengupta et al (15). The errors on the fitting parameters were calculated as the 95.4% confidence interval (14). Errors on the derived quantities were obtained through statistical error propagation.

Single Particle Tracking: from principles to tracking and data analysis

Although super-resolution techniques are able to break the diffraction limit allowing nanoscopic imaging, their poor temporal resolution constitutes a major limitation when studying the behavior of dynamic processes on the cell membrane of a living cell. Single Particle Tracking (SPT) represents an alternative imaging technique to nanoscopy offering both single molecule sensitivity and micro- to millisecond time resolution (16, 17, 18). In SPT, fluorescently labeled diffusing molecules are temporally imaged and their position tracked for a given period of time. One key difference between super-resolution techniques and SPT is the amount of fluorophores use to label the sample. Since in super-resolution imaging the mapping of the entire population is desired, a high concentration of labeling molecules is used. In contrast, in SPT only a few molecules from the entire population are labeled with the desired fluorophore. This is due to the fact that for tracking an individual molecule in time it is necessary to be able to distinguish it from other identical molecules throughout the entire experiment. This would not be feasible on a sample with high labeling density since intercrossing of different diffusing molecules would prevent their precise identification in every frame of the movie.

In analogy to super-resolution imaging, the choice of the fluorophore when performing SPT experiments constitutes a critical step. Traditional organic dyes or fluorescent proteins suffer mainly from limited brightness and photostability (19). The first limits the localization accuracy of the dye since it depends on the number of emitted photons N, $\sigma \sim \mathrm{FWHM}/\sqrt{N}$ (20). Moreover, photobleaching prevents the recording of long trajectories limiting the access to information on a long temporal scale (21). Quantum dots (QDs) are labeling probes that offer exceptional brightness and photostability due to their high extinction coefficient when compared to organic dyes (22, 23, 21). Moreover, the possibility of biofunctionalizing their surface with a range of different biocompatible molecules such as proteins allows a wide applicability in bioimaging (21). The conjugation of streptavidine coated QDs with biotinylated Fab fragments or antibodies constitute a canonical example of their use as imaging probes in live cell fluorescence imaging. Since QDs have an absorption spectrum covering a wide range of wavelengths and a very narrow fluorescence emission spectrum (21), they can be easily combined with other QDs, organic dyes or autofluorescent proteins to perform multicolor imaging in real time.

In this thesis, we have performed multicolor SPT experiments by labeling membrane receptors with a combination of different QDs. Moreover, we have also addressed how membrane receptors diffuse with respect to other cellular components such as the actin cytoskeleton and clathrin coated pits by combining single QD tracking with fluorescent proteins. Moreover, we have used a range of different analysis methods in order to gain access to the spatiotemporal behavior of membrane receptors. Overall, the SPT data presented in this thesis constitutes a perfect complementary approach to the results of STED super-resolution imaging. By combining these two imaging techniques, the temporal as well as the spatial organization of membrane receptors could be obtained.

Fluorescence imaging was performed using a home-made single molecule sensitive microscope working under wide-field geometry (Chapter 3, 4 and 5) or under total-internal reflection (TIR) geometry (Chapter 6). Continuous excitation of the QDs was provided by the 488-nm line of an Ar^+ laser ($0.3 kW/cm^2$) (Fig. 2.5). Circular polarization of the light was achieved by passing the laser beam through a quarter-wave plate. The diameter of the excitation beam was magnified three times using a telescope and then focused in the back focal plane of the objective of a commercial inverted IX71 Olympus microscope. To achieve TIR geometry, a mirror was accurately shifted laterally with respect to the objective by a linear translation stage. Fluorescence was collected using a 1.4 NA oil immersion objective (Olympus). Fluorescence emission was then guided into an EM-CCD camera (C9100-13, Hamamatsu) after suitable filtering. The arriving photons were integrated from a 256x256 or 128x128 pixel array with a frame rate of 60 Hz and 100 Hz, respectively. The total size of the chip of the CCD camera is 512x512 pixel with a image size of 16x16 μm. The data were not binned after integration (1x1 bin). The bit depth was 16 bits. The FWHM of the PSF of the microscope with these conditions was ≈360 nm. Since the commercial tube lens of the microscope produced an image with a pixel size of 270 nm, the image was magnified by a factor of two (135 nm pixel size) or three (90 nm pixel size) times with a telescope in order to achieve a pixel size equal to the standard deviation of the FWHM. This guarantees a proper fitting of the PSF with a Gaussian function.

Dual-color SPT were always performed on the basis that one of the fluorescence emission channels was efficiently collecting the emission of QD655. The second chan-

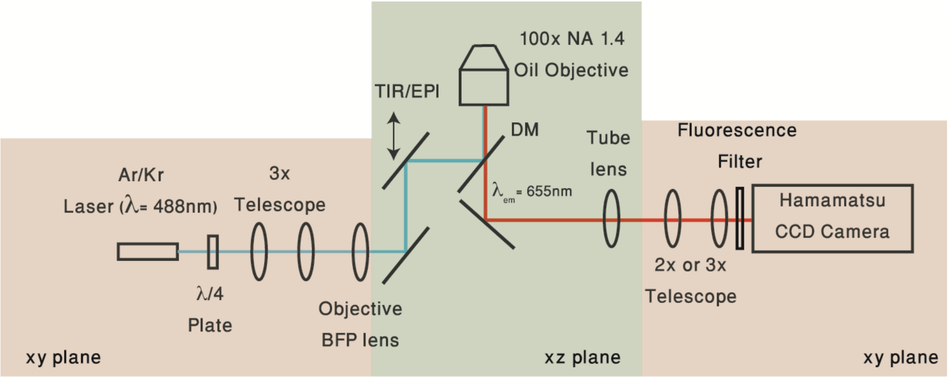

Figure 2.5 QD655 were imaged and detected using wide-field or TIR geometry on an inverted single-molecule sensitive fluorescence microscope. The sample was illuminated by a 488 nm excitation line focused on the back focal plane of the objective. Fluorescence emission was collected through the objective and focused after magnification and bandpass filtered (655±25 nm) on a CCD Camera.

nel contained fluorescence emission coming from either Green Fluorescent Protein (GFP; λ_{em}=509 nm), Yellow Fluorescent Protein (YFP; λ_{em}=527 nm) or QD585 (λ_{em}=585 nm). In all cases, the excitation light was also the 488 nm-line of the Ar+ laser (Fig. 2.6 and 2.7). This simplified the alignment of the excitation path since only a laser beam was used for multicolor excitation. The intensity of the 488 nm-line was adjusted depending on the conditions of each experiment, such as the expression levels of Clathrin-YFP or Lifeact-GFP. The dual-color fluorescence emission was split using a dichroic mirror with a cutoff wavelength of 600 nm and narrowband filtered (525±25 nm for GFP/YFP, 560±40 nm for QD585 and 655±25 nm for QD655) before reaching the camera (Fig. 2.6 and 2.7). QD655 and QD585 were simultaneously used when tracking homo protein interactions (DC-SIGN or CD1d) on the cell membrane (see Chapters 4 and 6 for details). In this case, both fluorescence channels were recorded by the same full chip of the Hamamtsu EM-CCD Camera at a frame rate of 30 Hz. When tracking DC-SIGN or CD1d with respect to global static cellular structures such as clathrin coated pits (YFP-tagged) or the actin cytoskeleton labeled with lifeact-GFP (24), the fluorescence emission from the fluorescent proteins was projected onto a second 12 bit CCD I-PentaMAX (Roper Scientific) Camera at a frame rate of 10 Hz.

To accurately overlay different fluorescence emission channels, images of multi-fluorophore fluorescent beads (0.2 µm Tetraspeck, Invitrogen), having emission spectra covering the two detection channels were obtained to determine the spatial transformation leading to the overlay of the two spectral channels. To calculate the

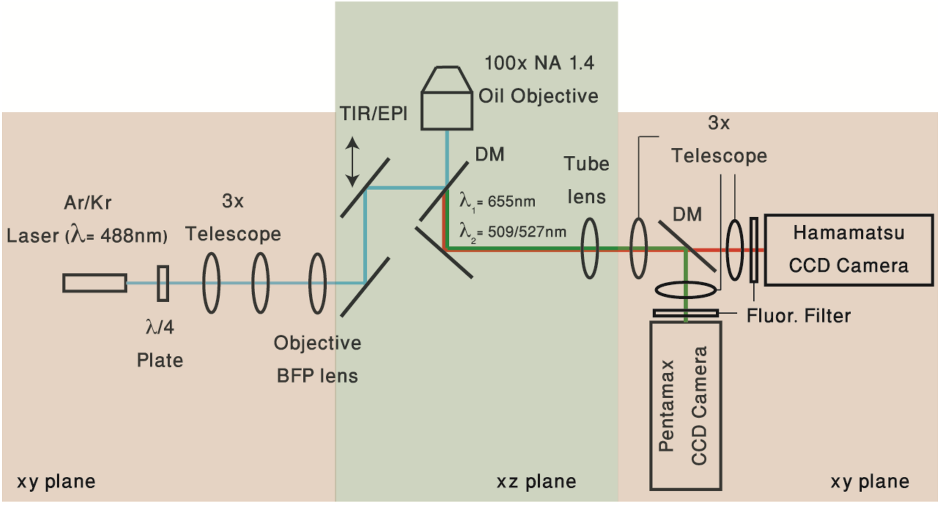

Figure 2.6 QD655 and GFP or YFP transfected proteins were imaged and detected using TIR geometry on an inverted single-molecule sensitive fluorescence microscope with two CCD Cameras. The sample was illuminated by a single 488 nm excitation line focused on the back focal plane of the objective. Dual-color fluorescence emission was collected through the objective, magnified, split by a dichroic mirror (DM) and focused on two different CCD Cameras after narrow band filtering.

spatial transformation, at least 10 beads appearing on both channels were manually selected, their centroid positions calculated with subpixel accuracy and stored in two coordinate lists. The transformation matrix was inferred from the coordinate lists according to an affine transformation, correcting for displacement and small chromatic aberrations. Physiological conditions (37ºC, 5% CO_2) were maintained during the experiments using a culture dish incubator (DH-35iL, Warner Instruments) equipped with a temperature controller (TC-324B, Warner Instruments) and a digital CO_2 controller (DGTCO2BX, Okolab).

Sample preparation for multicolor single particle tracking. In contrast to super-resolution imaging of fully protein labeled cell membranes, the key property of any single-molecule localization based imaging of diffusing particles is that a very low amount of dye is required. The concentration of labeling probe attached to an Ab for single-molecule detection of membrane receptors is typically 2 orders of magnitude (≈200-500 pM) lower than for nanoscopy imaging (≈30 nM). Moreover, in the case that fluorescently labeled ligands are used to map membrane receptors, higher concentrations (≈2 nM) have to be used due to the higher dissociacion constants of ligand-receptor complexes compared to Ab-receptor complexes.

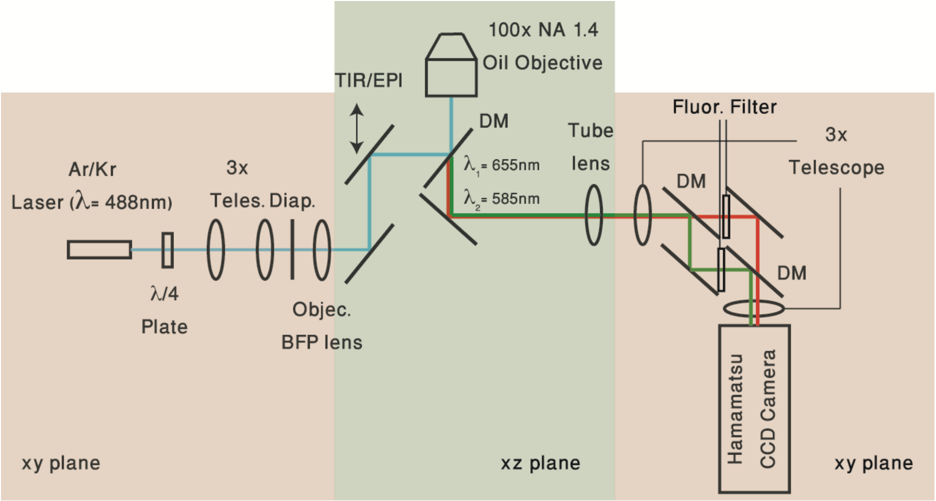

Figure 2.7 QD655 and QD585 were simultaneously imaged and detected using TIR/EPI geometry on an inverted single-molecule sensitive fluorescence microscope. The sample was illuminated by a single 488 nm excitation line focused on the back focal plane of the objective. After adjusting the separation of the two color fields of view by a diaphragm in the excitation path, dual-color fluorescence emission was collected through the objective, magnified, split by a dichroic mirror (DM) and focused on the same CCD Camera allowing simultaneous imaging of two different QDs.

Single particle tracking analysis. Trajectories of individual QDs with at least 200 points (DC-SIGN data, Chapter 3, 4 and 5) or 100 points (CD1d data, Chapter 6) were reconnected with Matlab routines based on the multiple-target-tracing (MTT) algorithm described by Serge et al. (25). This method relies on past statistical history in order to achieve a more efficient reconnection of trajectories. Importantly, although this method could provide reconnection of QDs trajectories with “off” times, only trajectories with QDs emitting above a certain signal-to-background level (Probability of false alarm for peak detection: $PFA_{peak}<10^{-6}$) in every frame of the trajectory were selected for analysis in this thesis. To validate the performance of the detection and reconnection algorithm, reconnected trajectories were always overlaid onto the corresponding original raw video and visually inspected with a custom-made software in ImageJ.

As a general approach throughout this thesis, individual trajectories were analyzed by calculating their mean-squared-displacement (MSD) according to the following formula (16):

$$MSD(n \cdot \Delta t) = \frac{1}{N-n-1}\sum_{j=1}^{N-n-1}[x(j\Delta t + n\Delta t) - x(j\Delta t)]^2 + [y(j\Delta t + n\Delta t) - y(j\Delta t)]^2 \quad (4)$$

where Δt is the time lag, N is the total number of frames of the trajectory, n represents the time increment and x,y represent the 2D particle position. Short-range diffusion coefficients were extracted from the linear fit to the 2nd- 4th point of the MSD curve using the following equation:

$$MSD = 4D_{2-4}t + \Delta_0 \tag{5}$$

where D_{2-4} is the instantaneous diffusion coefficient and Δ_0 is the MSD offset at zero time increment. To validate the correct performance of the MTT algorithm in terms of detecting and reconnecting individually diffusing QDs, manual tracking for every condition was performed and the distribution of the D_{2-4} values of both cases were compared.

The offset is related to the localization accuracy by the following formula (26):

$$\left\langle (\Delta x)^2 \right\rangle = \Delta_0 / 2d \tag{6}$$

where d accounts for the space Euclidean dimension (in this case, d=2). Using the given formula, we obtained a localization accuracy of 18-20 nm for quantum dots under the different experimental conditions used throughout this thesis.

The smallest detectable diffusion coefficient was obtained after imaging immobilized QDs on a coverslip using either EPI (DC-SIGN experiments reported in Chapters 3,4 and 5) or TIRF (CD1d experiments reported in Chapter 6) configurations at the same frame rate as in the corresponding experiments, 60Hz and 100Hz, respectively. 95% of the immobile QDs displayed diffusion coefficients $<10^{-3}$ μm^2/s or $<6\cdot10^{-4}$ μm^2/s under TIRF (100Hz) or EPI (60Hz) geometry, respectively. Hence, these values were selected as the thresholds for discriminating immobile vs. mobile trajectories. To avoid any overestimation of the immobile fraction due to non-specific interaction of QDs with the coverslip, only trajectories classified as mobile were used for the trajectory analysis under TIR geometry. In case of EPI illumination, the microscope was focused slightly above the focal plane of the coverslip avoiding the detection of off-focus QDs immobilized on glass by the MTT algorithm.

An alternative to MSD based analysis was used to detect transient confinement zones (TCZ) based on Simson et al. (27). The algorithm calculates the probability that a diffusing particle would stay within a zone of a given radius for a particular amount of time. If the particle stays within that zone for a longer period of time compared to a particle diffusing with purely Brownian motion, the algorithm then classifies that region as a confinement zone. By comparing the performance of the software with simulated trajectories showing purely Brownian motion, the input parameters of the software and its performance can be addressed. Overall, this algorithm constitutes an efficient approach to study whether a diffusing molecule stays temporally trapped within certain regions of the explored area or volume (28, 29).

Dual Color trajectory analysis of QDs. After successfully overlaying the two fluorescence emission channels (Fig. 2.8A), individual trajectories were manually reconnected. The position of each QD at every frame was determined by fitting the PSF of every individual QD with a Gaussian function. After reconnecting every trajectory, the interparticle distance between both QDs per frame was calculated (Fig. 2.8B,C). To quantify whether the interparticle interactions corresponded to purely Brownian stochastic encounters or to specific protein-protein interactions, the distribution of the interparticle distances were compared to Monte-Carlo simulations of Brownian diffusing particles with the same initial interparticle distances and diffusion coefficients than the experimental data (see Chapters 4 and 6).

Membrane exploration or cartography maps

SPT allows the characterization of the lateral behavior of individual diffusing proteins on the cell membrane at the nanoscale with ms time resolution. However, SPT requires reconnection of trajectories which can be challenging even using automated reconnection algorithms such as MTT. Very low densities of fluorophores, e.g., are required in order to discriminate properly between trajectories. This prevents the simultaneous recording of a large amount of long trajectories (>100 points) in a single cell making traditional SPT a low throughput technique. In the recent years, some single-molecule based techniques have tried to exploit high-density single particle tracking following different approaches: single particle tracking-PALM, hyperspectral imaging and MTT (30, 31, 25). Although the global mapping of the cell membrane has been possible with these approaches by creating, e.g., diffusion maps (30), all these techniques still rely on the limiting factor of reconnecting trajectories. Moreover, although diffusion coefficient-based analysis provides information on the diffusing receptor and its interaction with the environment, it is much harder to extract information over potential confinement in mesoscale areas of the cell membrane using this approach.

In this thesis, we have developed a methodology based on the localization of single QDs over a micron size area on the cell membrane of living cells for a precise period of time.

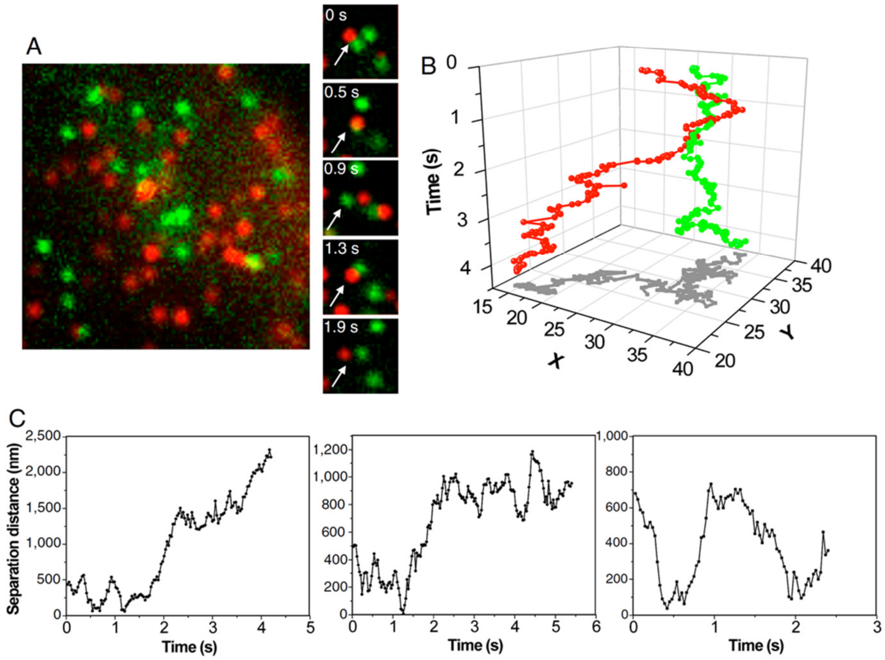

Figure 2.8 Dual color QD tracking analysis was based on the interparticle distance between individual QDs per frame. (**A**) Still frame of a movie showing individual receptor nanoclusters labeled with either green (585) or red (655) QDs; and sample time series of two QDs (red and green) spatially close in time (see white arrows). (**B**) Full reconstruction of the 2D green and red trajectories in time of the two QDs shown in A. High labeling conditions have been used to increase the probability of observing such events. (**C**) Examples of separation distances obtained for three pairs of seemly closed QDs, showing large and random variations in the relative positions between QDs.

We essentially recorded the highest possible amount of localization of *diffusing* QDs during a movie. However, we did not reconnect any trajectories but instead analyzed the spatial distribution of all the localizations obtained during the full video after collapsing them into one single final image (Figure 2.9). This methodology offers the great advantage of accessing not only the nano- but also importantly, the mesoscale distribution of the transmembrane protein of interest without the need of reconnecting very long trajectories. This has a great impact in the amount of time needed to collect data, making membrane exploration maps a high throughput technique. In addition, the setup required for performing membrane exploration maps with QDs is greatly simplified with respect to the setups needed to perform spt-PALM or QD hyperspectral imaging. Moreover, by combining cartography maps of different colors, the different lateral organization of molecules at multiple temporal and spatial scales of interest can be obtained with high throughput (Chapter 4).

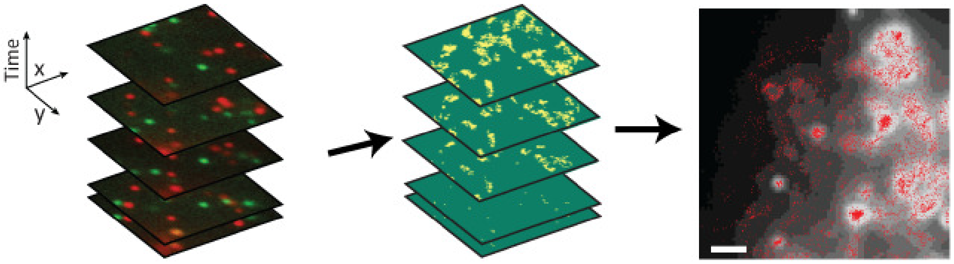

Figure 2.9 Cartography maps are generated by localizing all QDs in every frame of the movie and collapsing all the detected localizations in one single frame. This can be done by dual-color or by high-density single color SPT techniques.

Discussion

In this thesis, we have combined several state-of-the-art single-molecule sensitive fluorescence technologies to gain access to the spatiotemporal behavior of the membrane receptors such as CD1d and DC-SIGN. By using STED nanoscopy, we could identify that these receptors do not organize in a random manner but in nanoclusters on the cell membrane. To gain access to the temporal behavior of CD1d and DC-SIGN, multi-color single particle tracking was developed allowing us to study how these transmembrane proteins interact not only with each other but also with surrounding cellular components. Thus, by combining both multicolor SPT and STED nanoscopy, we could characterize the composition of each individual nanocluster and how these nanoclusters diffuse laterally in space and time.

To quantify the nanoclustering degree of DC-SIGN or CD1d from the STED nanoscopy images, two different types of analysis were applied. The relative low protein density of DC-SIGN on the cell membrane allowed the fitting of every single nanocluster on the cell membrane with a Gaussian function. By extracting the characteristic parameters of the fit, the size and composition of every individual DC-SIGN nanocluster could be estimated. On the other hand, the high density of CD1d molecules on the cell membrane prompted us to develop an algorithm that could reconstruct the spatial organization of highly dense CD1d STED images. The algorithm works on the basis that a nanoscopic image can be reconstructed, using the Bayesian Information Criterion, by the sum of multiple PSFs with an intensity distribution that can be experimentally determined from single markers.

The lateral behavior of CD1d and DC-SIGN was accessible using single or multi-color single particle tracking. By simultaneous recording of DC-SIGN vs DC-SIGN or CD1d vs CD1d, potential homo-interaction between diffusing nanoclusters could be studied. Moreover, dual color imaging of DC-SIGN on top of clathrin, or CD1d on top of actin, are examples of the possibility of addressing the potential influence of other cell components on the lateral behavior of diffusing transmembrane proteins. This technique offers a unique possibility to test the influence of a cell component on the molecule of interest in a minimally invasive manner. This is in strong contrast to traditional biochemical approaches which rely on very perturbing methods such as drug treatments or gene knockdowns/knockouts of the cellular component of interest.

Membrane exploration maps were developed in order to combine information about the spatial organization with temporal resolution in a single experiment. Not only the areas covered by a diffusing molecule over time can be obtained by collapsing all the localizations of a video into one single frame but also importantly, how efficiently those areas are being explored. Moreover, the nano- and microscale spatiotemporal behavior can be extracted without the need of extensive data collection. By expanding membrane exploration maps to multi-color imaging, detailed information on how the collective spatiotemporal behavior of a transmembrane protein depends on the organization of another one can be extracted. This is a particularly powerful approach to study components of the cell membrane because they can easily be simultaneously fluorescently labeled and imaged in real time.

In summary, in this Chapter we have described the development of the tools needed to study the spatiotemporal behavior of transmembrane proteins with high temporal and spatial resolution. By combining STED nanoscopy with multi-color SPT, we have successfully characterized how CD1d and DC-SIGN are distributed on the cell membrane and how they interact with other cell membrane components. Overall, this Chapter presents a palette of imaging techniques and analysis tools that allows to extract biologically relevant information that could have not be obtained using standard traditional biochemical approaches.

References

1.Hell SW (2007) Far-field optical nanoscopy. *Science* **316**, 1153-1158.
2.Hell SW (2003) Toward fluorescence nanoscopy. *Nat. Biotechnol.* **21**, 1347-1355.

3.Donnert G, Keller J, Medda R, Andrei MA, Rizzoli SO, Lührmann R*, et al.* (2006) Macromolecular-scale resolution in biological fluorescence microscopy. *Proc. Natl. Acad. Sci. U. S. A.* **103**, 11440-11445.

4.Song L, Varma C, Verhoeven J, Tanke HJ (1996) Influence of the triplet excited state on the photobleaching kinetics of fluorescein in microscopy. *Biophys. J.* **70**, 2959.

5.Hotta J-i, Fron E, Dedecker P, Janssen KP, Li C, Müllen K*, et al.* (2010) Spectroscopic rationale for efficient stimulated-emission depletion microscopy fluorophores. *J. Am. Chem. Soc.* **132**, 5021-5023.

6.Vicidomini G, Moneron G, Eggeling C, Rittweger E, Hell SW (2012) STED with wavelengths closer to the emission maximum. *Opt. Express* **20**, 5225-5236.

7.Lakowicz JR. *Principles of Fluorescence Spectroscopy*, 3rd Edition edn. Springer, 2006.

8.Eggeling C, Willig KI, Barrantes FJ (2013) STED microscopy of living cells–new frontiers in membrane and neurobiology. *J. Neurochem.* **126**, 203-212.

9.Nägerl UV, Willig KI, Hein B, Hell SW, Bonhoeffer T (2008) Live-cell imaging of dendritic spines by STED microscopy. *Proc. Natl. Acad. Sci. U. S. A.* **105**, 18982-18987.

10.Willig KI, Harke B, Medda R, Hell SW (2007) STED microscopy with continuous wave beams. *Nat. Methods* **4**, 915-918.

11.Moneron G, Medda R, Hein B, Giske A, Westphal V, Hell SW (2010) Fast STED microscopy with continuous wave fiber lasers. *Opt. Express* **18**, 1302-1309.

12.van Zanten TS, Cambi A, Koopman M, Joosten B, Figdor CG, Garcia-Parajo MF (2009) Hotspots of GPI-anchored proteins and integrin nanoclusters function as nucleation sites for cell adhesion. *Proc. Natl. Acad. Sci. U. S. A.* **106**, 18557-18562.

13.van Zanten TS, Gómez J, Manzo C, Cambi A, Buceta J, Reigada R*, et al.* (2010) Direct mapping of nanoscale compositional connectivity on intact cell membranes. *Proc. Natl. Acad. Sci. U. S. A.* **107**, 15437-15442.

14.Manzo C, van Zanten TS, Saha S, Torreno-Pina JA, Mayor S, Garcia-Parajo MF (2014) PSF decomposition of nanoscopy images via Bayesian analysis unravels distinct molecular organization of the cell membrane. *Sci. Rep.* **4**.

15.Sengupta P, Jovanovic-Talisman T, Skoko D, Renz M, Veatch SL, Lippincott-Schwartz J (2011) Probing protein heterogeneity in the plasma membrane using PALM and pair correlation analysis. *Nat. Methods* **8**, 969-975.

16.Kusumi A, Sako Y, Yamamoto M (1993) Confined lateral diffusion of membrane receptors as studied by single particle tracking (nanovid microscopy). Effects of calcium-induced differentiation in cultured epithelial cells. *Biophys. J.* **65**, 2021-2040.

17.Saxton MJ, Jacobson K (1997) Single-particle tracking: applications to membrane dynamics. *Annu. Rev. Biophys. Biomol. Struct.* **26**, 373-399.

18.Suzuki KG, Fujiwara TK, Sanematsu F, Iino R, Edidin M, Kusumi A (2007) GPI-anchored receptor clusters transiently recruit Lyn and Gα for temporary cluster immobilization and Lyn activation: single-molecule tracking study 1. *J. Cell Biol.* **177**, 717-730.

19.Schmidt T, Schütz G, Baumgartner W, Gruber H, Schindler H (1996) Imaging of single molecule diffusion. *Proc. Natl. Acad. Sci. U. S. A.* **93**, 2926-2929.

20.Thompson RE, Larson DR, Webb WW (2002) Precise nanometer localization analysis for individual fluorescent probes. *Biophys. J.* **82**, 2775-2783.

21.Pinaud F, Clarke S, Sittner A, Dahan M (2010) Probing cellular events, one quantum dot at a time. *Nat. Methods* **7**, 275-285.

22.Dahan M, Levi S, Luccardini C, Rostaing P, Riveau B, Triller A (2003) Diffusion dynamics of glycine receptors revealed by single-quantum dot tracking. *Science* **302**, 442-445.

23.Michalet X, Pinaud FF, Bentolila LA, Tsay JM, Doose S, Li JJ*, et al.* (2005) Quantum dots for live cells, in vivo imaging, and diagnostics. *Science* **307**, 538-544.

24.Riedl J, Crevenna AH, Kessenbrock K, Yu JH, Neukirchen D, Bista M*, et al.* (2008) Lifeact: a versatile marker to visualize F-actin. *Nat. Methods* **5**, 605-607.

25.Sergé A, Bertaux N, Rigneault H, Marguet D (2008) Dynamic multiple-target tracing to probe spatiotemporal cartography of cell membranes. *Nat. Methods* **5**, 687-694.

26.Bakker G-J (2011) LFA-1 dynamics on the membrane of leukocytes. *PhD Thesis, University of Twente, Enschede, The Netherlands*.

27.Simson R, Sheets ED, Jacobson K (1995) Detection of temporary lateral confinement of membrane proteins using single-particle tracking analysis. *Biophys. J.* **69**, 989-993.

28.Dietrich C, Yang B, Fujiwara T, Kusumi A, Jacobson K (2002) Relationship of lipid rafts to transient confinement zones detected by single particle tracking. *Biophys. J.* **82**, 274-284.

29.Thompson MA, Casolari JM, Badieirostami M, Brown PO, Moerner W (2010) Three-dimensional tracking of single mRNA particles in Saccharomyces cerevisiae using a double-helix point spread function. *Proc. Natl. Acad. Sci. U. S. A.* **107**, 17864-17871.

30.Cutler PJ, Malik MD, Liu S, Byars JM, Lidke DS, Lidke KA (2013) Multi-color quantum dot tracking using a high-speed hyperspectral line-scanning microscope. *PLoS One* **8**, e64320.

31.Manley S, Gillette JM, Patterson GH, Shroff H, Hess HF, Betzig E*, et al.* (2008) High-density mapping of single-molecule trajectories with photoactivated localization microscopy. *Nat. Methods* **5**, 155-157.

Chapter 3

The neck region regulates the spatiotemporal organization and virus-binding capability of DC-SIGN

As discussed in Chapter 1, the study of the spatiotemporal behavior of transmembrane proteins is crucial to understand their biological function. In this Chapter, by combining biochemical and advanced biophysical techniques, including optical super-resolution and single particle tracking, we demonstrate that DC-SIGN forms nanoclusters on the cell membrane of antigen presenting cells. Moreover, its intrinsic nanoclustering capacity strictly depends on its molecular structure. DC-SIGN nanoclusters exhibited free, Brownian diffusion on the cell membrane. Truncation of the extracellular neck region, known to abrogate tetramerization, significantly reduced nanoclustering and concomitantly increased lateral diffusion. Importantly, DC-SIGN nanocluster dissolution exclusively compromised binding to nanoscale size pathogens. Monte Carlo simulations revealed that heterogeneity on nanocluster density and spatial distribution confers broader binding capabilities to DC-SIGN. As such, our results underscore a direct relationship between spatial nanopatterning, driven by intermolecular interactions between the neck regions, and receptor diffusion, to provide DC-SIGN with the exquisite ability to dock pathogens at the virus length-scale. Insight on how virus receptors are organized prior to virus binding and how they assemble into functional platforms for virus docking is helpful to develop novel strategies to prevent virus entry and infection.

This work has been published as C. Manzo*, J.A. Torreno-Pina*, B. Joosten, I. Reinieren-Beeren, E.J. Gualda, P. Loza-Alvarez, C.G. Figdor, M.F. Garcia-Parajo, A. Cambi, "The neck region of the C-type lectin DC-SIGN regulates its surface spatiotemporal organization and virus-binding capacity on antigen-presenting cells", *Journal of Biological Chemistry* 287, 38946 (2012). * Equally contributing authors.

Introduction

As briefly described in Chapter 1, dendritic cells (DCs) constitute a specific group of professional antigen presenting leukocytes that link the innate and adaptive branches of the immune response by virtue of their capacity to recognize pathogen-specific structures (1). Immature DCs (imDCs) migrate from the blood into tissues where they detect foreign antigens. Upon antigen recognition, imDCs are activated and migrate to the lymph nodes, where they present antigen-derived peptides to naive T lymphocytes and induce an effective immune response (2-4). For efficient pathogen recognition, imDCs are equipped with a large number of lectin and lectin-like receptors (CLR) on the cellular membrane that bind to high mannose structures present on the surfaces of a broad range of pathogens including viruses, bacteria, yeast and parasites (5,6). Since DCs can be manipulated *ex-vivo*, numerous efforts have been undertaken for exploiting the extraordinary binding capabilities of CLRs to target antigens directly to DCs *in vivo*, potentially increasing the effectiveness of antitumor and antiviral vaccines (7,8).

Dendritic cell-specific ICAM-3-grabbing nonintegrin (DC-SIGN; CD209) is a type II membrane CLR abundantly expressed *in-vivo* on myeloid DC and macrophage populations (9,10) as well as on *in-vitro* generated monocyte-derived DCs and activated macrophages (10-12). DC-SIGN is responsible for the binding and uptake of a multitude of pathogens, such as HIV-1 (13), Ebola virus (14), hepatitis C virus (15), *Candida albicans* (16) and *Mycobacterium tuberculosis* (17) via mannan- and Lewis X oligosaccharides-dependent interactions. More recently, it is been shown that upon recognition of mannan or Lewis X carbohydrates, DC-SIGN associates with distinct signaling molecules to induce differential production of cytokines that in turn lead to enhancement or suppression of proinflammatory responses (18). The mechanisms by which these diverging signaling pathways are generated remain a mystery although it has been suggested that the molecular structure of DC-SIGN might be altered upon binding to the two different carbohydrates.

Structurally, DC-SIGN is a tetrameric transmembrane protein with each sub-unit comprising a long extracellular part with a carbohydrate-recognition domain (CRD), a 7-and-a-half tandem repeat of 23 amino acids forming the neck region, and a transmembrane part followed by a cytoplasmic tail containing recycling and internalization motifs (19-20). Analysis of recombinant molecules, hydrodynamic and surface force measurements revealed that the neck region of DC-SIGN is responsible for its tetramerization (21-23) enabling the formation of CRD multi-binding sites and increasing the interaction strength with specific ligands (23). Based on these results it has been proposed that the neck configuration is likely to play a significant role in pathogen capture (23).

Using transmission electron microscopy (TEM) and near-field optical nanoscopy, it was previously shown that DC-SIGN forms nanoclusters on the membrane of fixed immature (im)DCs far beyond mere tetramerization (11,24,25). These results have been recently validated on living imDCs (26) and on several cell lines transfected with DC-SIGN (26,27). Importantly, tight spatial ordering of DC-SIGN in nanoclusters resulted crucial for binding and internalization of HIV-1 (11). However, how DC-SIGN achieves such a refined level of spatial control is largely unknown. Although DC-SIGN has been shown to partially associate to lipid rafts, cholesterol extraction did not alter the integrity of the nanoclusters (11). Similarly, DC-SIGN nanocluster formation and/or stability do not require interactions with the cortical cytoskeleton (27) neither association with tetraspanins (27). Recently, it has been hypothesized that large DC-SIGN domains, i.e., *microclusters* could be formed and stabilized through interactions between the CRDs and yet unidentified extracellular components, as deletion of the CRD moiety abrogated DC-SIGN microclustering (28). However, since these experiments were performed using diffraction limited confocal microscopy, it is not clear whether the *nanoclustering* capacity of DC-SIGN also requires the presence of the CRD. Thus, despite the importance of DC-SIGN nanoclustering in pathogen recognition, the studies performed so far have not provided yet conclusive evidences to explain the origin for this well-defined organization.

This chapter addresses the mechanisms leading to DC-SIGN nanoclustering by combining biochemical assays, super-resolution optical nanoscopy, single particle tracking and Monte Carlo simulations of different DC-SIGN mutants. Moreover, we correlate DC-SIGN nanoclustering with viral binding capacity. Our results reveal that homophilic interactions mediated by the neck region of DC-SIGN are responsible for its nanoclustering and enhanced virus-binding ability.

Results

Mutated DC-SIGN forms are functional but have impaired virus-binding capacity. Previously it was shown that DC-SIGN expressed in CHO cells serve as a valid model system to study binding, internalization and trafficking of different antigens targeted to DC-SIGN, recapitulating its essential activities on imDCs (33,34). We thus used 3 different DC-SIGN mutants where specific regions of the molecule were deleted (Fig. 3.1A). Moreover, the DC-SIGN mutants were stably transfected in CHO cells to investigate their effect on pathogen binding (Fig. 3.1A). The mutants are denoted as ΔCRD (lacking the CRD domain), ΔRep (lacking the tandem repeats in the extracellular neck region) and Δ35 (lacking the first 35 amino acids from the N terminal in the cytoplasmatic tail). We evaluated the functionality and binding capability of the stable transfectants to soluble ligands, virus-sized and micron-sized objects. Whereas wt-DC-SIGN, ΔRep- and Δ35- bind to fluorescent soluble mannan, the lack of the CRD unexpectedly prevents binding, consistent with the fact that DC-SIGN-mediated interactions occur through the CRD (20) (Fig. 3.1B). Addition of blocking-antibodies or competing soluble mannan significantly reduces the binding in all cases, showing DC-SIGN specificity. These results confirm that wt-DC-SIGN, ΔRep- and Δ35- are all functional on CHO cells, and furthermore show that the CRD is available for binding even in the absence of the neck region.

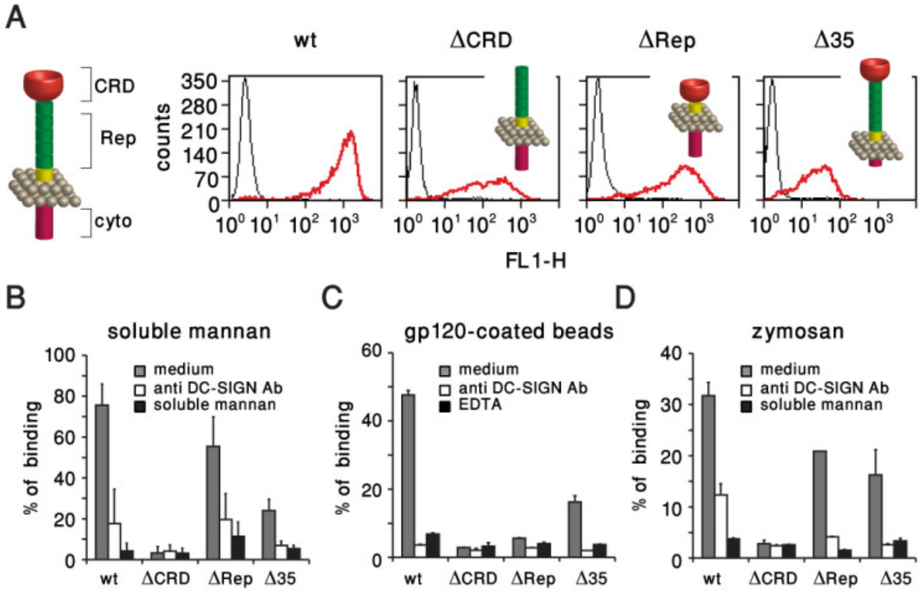

Figure 3.1 Mutated DC-SIGN forms are functional but have impaired virus-binding capacity. (**A**) Schematics of wt-DC-SIGN and cell surface expression levels of wt-DC-SIGN and mutants on stably transfected CHO cells as determined by FACS analysis. The black histogram represents the isotype control, and the red histogram indicates the specific staining with anti-DC-SIGN Ab (anti-AU1). (**B**-**D**) Binding of soluble fluorescent Alexa-647-mannan (**B**), gp120-coated fluorescent nanobeads (40 nm Ø) (**C**) and micron-sized FITC-zymosan (**D**) to CHO cells expressing wt-DC-SIGN or mutants were measured by FACS. Specificity was determined by measuring binding in presence of anti-DC-SIGN blocking Ab (AZN-D1) or Ca^{2+} chelating agent EDTA or soluble non-fluorescent mannan. One representative experiment out of 3 is shown. Values represent average of duplicates experiments with corresponding SD.

To investigate the DC-SIGN capability for virus docking, we carried out binding assays with gp120-coated nanobeads (40 nm in diameter, Fig. 3.1C) having comparable size to HIV-1 (35). Interestingly, significant binding is only observed on wt-DC-SIGN and

Δ35-. While a lack of binding is expected for ΔCRD-DC-SIGN, the complete absence of binding of ΔRep-DC-SIGN indicates a key role for the neck region in securing interactions with nanometric-size particulate antigens. This was further confirmed by using real HIV-1 virus particles, which were bound by CHO cells expressing wt-DC-SIGN and not by ΔRep-DC-SIGN (Fig. 3.2), thus validating the use of nanobeads as virus-like particles and in agreement with previous studies (30,34). To further investigate the binding capability to large objects, we performed similar experiments using micron-sized zymosan particles (yeast cell walls, Fig. 3.1D). High binding was retrieved for wt-DC-SIGN and all the mutants, except for ΔCRD-DC-SIGN, in similar fashion as found for the soluble ligand. Notice that the somewhat lower binding of Δ35-DC-SIGN in all cases is due to its lower expression level as compared to wt-, ΔCRD- and ΔRep- (Fig. 3.1A). These results show that whereas binding of DC-SIGN and its mutants to soluble ligands and large particles occur with similar efficiency, the neck region of DC-SIGN is crucial to ensure binding of small virus-size particles.

The cytoplasmic tail impacts on DC-SIGN clathrin-dependent internalization. It has been previously shown that DC-SIGN-mediated endocytosis of virus-like particles occurs via clathrin (33,34). Therefore we sought to investigate the effect of structural mutations on DC-SIGN mediated endocytosis by comparing the amount of Ab on the cell membrane before and after internalization. The percentage of internalized mAb was calculated by measuring the mean fluorescence (MF) of the samples using flow cytometry and by applying the following formula: ((MF@37°C – MF@4°C) / MF@4°C) x100 (Fig. 3.3A). Truncation of the neck region (ΔRep-DC-SIGN) does not affect antigen internalization compared to wt-DC-SIGN (Fig. 3.3A). In contrast, deletion of the cytoplasmatic tail (Δ35-DC-SIGN) significantly reduced internalization (Fig. 3.3A), supporting previous findings obtained on Δ35-DC-SIGN expressed on Raji cells and incubated with HIV-1 virions (36). Subsequently, we used confocal imaging to determine the degree of colocalization of anti-DC-SIGN mAbs and clathrin before and 10 min after endocytosis triggering (Fig. 3.3B). Colocalization with clathrin was not observed for wt-DC-SIGN or the two mutants investigated (ΔRep-DC-SIGN and Δ35-DC-SIGN) in the basal state. Triggering of endocytosis by shifting the temperature to 37ºC for 10 min induced significant colocalization with clathrin for wt-DC-SIGN and ΔRep-DC-SIGN but not for Δ35-DC-SIGN, as quantified using the Pearson correlation coefficient (Fig. 3.3C). Our data thus show that the cytosplasmic tail of DC-SIGN is crucial for clathrin-dependent endocytosis whereas the neck region has no major influence on internalization.

The neck region is required for DC-SIGN nanoclustering. It is known that DC-SIGN forms nanoclusters on the cell surface of imDCs and of several cell lines (11,24-27). To

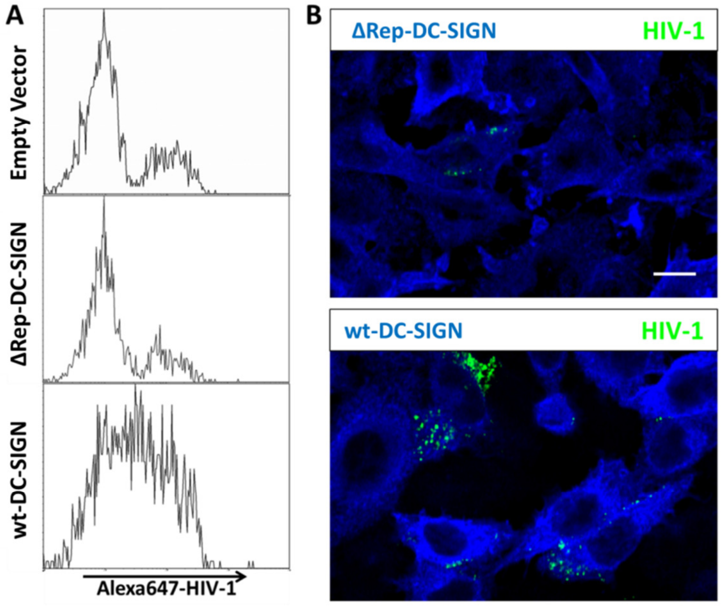

Figure 3.2 The lack of the neck region prevents binding of real HIV-1 particles. (**A**) CHO cells transfected with empty vector, ΔRep-DC-SIGN or wt-DC-SIGN were incubated with Alexa647-labeled HIV-1 (400 ng HIV-1 p24 Ag/100.000 cells) for 30 min at 37ºC or 30 min at 37ºC. After washing unbound virus, cells were analyzed by flow cytometry. Cells that have bound fluorescent virus particles became fluorescent, as indicated by the shift of the mean fluorescence histogram towards higher values on the x axis. The cell counts are shown on the y axis. One representative experiment out of two is shown. (**B**) To visualize the difference in HIV-1 binding, CHO cells were incubated with the Alexa647-labelled HIV-1 particles, as described in A, and after removing unbound virus the samples were fixed with 4% PFA for 1 hr at RT and subsequently labeled for DC-SIGN. Samples were then fixed again and analyzed by confocal microscopy. One representative field of view is shown. Scale bar, 10 µm.

investigate whether a potential relationship might exist between the molecular structure of DC-SIGN and its nanoclustering capacity we analyzed TEM images on whole-mount samples of CHO cells (Fig. 3.4). TEM images of immunogold-labeled wt-DC-SIGN showed a non-homogeneous receptor distribution over the cell membrane, characterized by regions of closely grouped particles (Fig. 3.4A). Similar nanoclustered organization was found for the Δ35 and the ΔCRD mutants (Fig. 3.4 C,D respectively). In contrast, a significantly more disperse distribution was observed for the ΔRep mutant (Fig. 3.4 B). To quantitatively analyze the images we developed a cluster-searching algorithm that discriminates between isolated and clustered receptors by recursively comparing the inter-particle distances to a threshold value of 80 nm (Fig. 3.5). Briefly, gold particle positions were automatically detected by means of maximum-likelihood based routine (51). Then, the classification of particles into clusters was performed by means of a threshold-based algorithm. If the interparticle distance between 2 particles is below a given threshold value *th*, the particles are assigned to the same cluster (Fig. 3.5A). For a proper choice of the threshold, we generated simulated images of randomly positioned particles, using a particle density similar to that of the experimental data data (17 particles/μm^2), and retrieved the nearest neighbor distribution (*nnd*) from the simulated images (Fig. 3.5B). To determine the threshold value, we compared the *nnd* of randomly positioned particles with the *nnd* distribution obtained from the experimental data. The curves of the experimental and the simulated data intersect at a distance of 80 nm. Therefore, we used the value *th*=80 nm to rigorously define our threshold and minimize the false-positive cluster identifications (Fig. 3.5B).

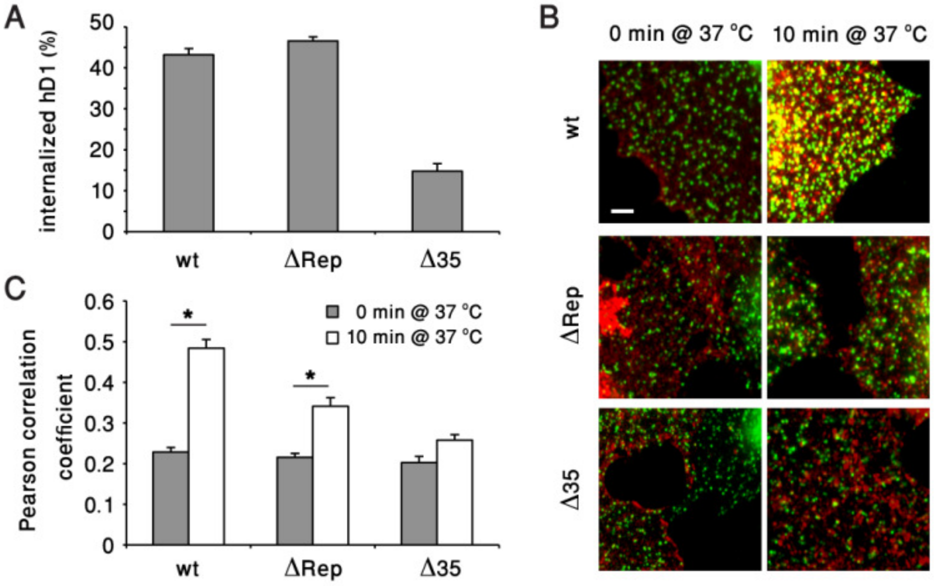

Figure 3.3 The cytoplasmic tail impacts on DC-SIGN clathrin-dependent internalization. (**A**) CHO cells stably transfected with DC-SIGN constructs were incubated with anti-DCSIGN mAb hD1 at 4ºC, washed and incubated for 30 min at 37ºC to induce endocytosis. (**B**) CHO transfectants were incubated with hD1 at 4ºC, washed and shortly incubated with isotype specific Alexa-647 (red) conjugated secondary Abs at 4ºC. After washing, cells were kept on ice (0 min @ 37ºC) or shifted for 10 min at 37ºC to induce endocytosis (10 min @ 37ºC). After fixation and permeabilization, clathrin (green) was labeled. The pictures are enlarged areas taken from representative cells. Scale bar, 5 μm. (**C**) Pearson colocalization coefficient plot of DC-SIGN and clathrin. Values ± SEM are average of multiple images from several cells in at least three different experiments. (* = p<0.01, T-test).

Fig. 3.5C shows the histogram of the nearest neighbor distribution for wt-DC-SIGN, Δ35-, and ΔCRD- showing a similar distribution peaked around ~6 pixels with a slowly decaying tail, whereas ΔRep- shows a significant deviation in the ~20-60 pixels region due to the higher number of isolated particles. Moreover, the distribution of ΔRep-DC-SIGN shows a broad distribution peaked around 30 pixels due to isolated particles (Fig.

3.5C, inset) very similar to the nearest neighbor distribution of simulated random-distributed particles. This already suggests that DC-SIGN nanoclustering is strongly dependent on its neck region. Fig. 3.5D shows a linear relationship between the cluster size and the number of particles per cluster suggesting a homoprotein-protein interaction as the mechanism responsible for DC-SIGN nanoclustering.

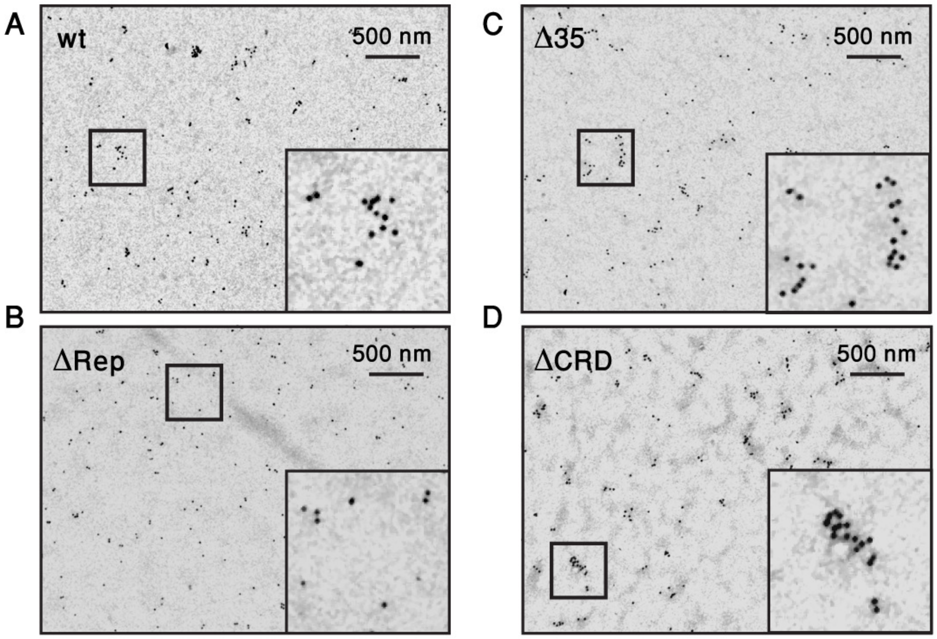

Figure 3.4 DC-SIGN nanoclustering is only affected by truncation of the neck region. (**A**-**D**) Representative TEM images of whole-mount, immunogold labeled CHO cells expressing wt-DC-SIGN (**A**) and the different mutants: ΔRep- (**B**), Δ35- (**C**), and CRD- (**D**). The insets show zoomed regions (black boxes) of the images, evidencing similar cluster capability for wt-DC-SIGN, Δ35-, and ΔCRD- and reduced clustering of ΔRep-.

Figure 3.6 shows once more representative TEM images of wt-DC-SIGN and the ΔRep mutant highlighting their markedly different spatial distribution. Quantification of the wt-DC-SIGN, ΔCRD- and Δ35- gold particle distributions showed that the large majority (~80%) of receptors are organized in nanoclusters and that this percentage drops to ~60% for ΔRep-DC-SIGN (Fig. 3.6B). Since two particles closer than 80 nm from each other are already defined as a cluster by the algorithm (Fig. 3.5), we further inquired whether the degree of clustering of wt-DC-SIGN differed from that of the mutants. For this, we calculated the distribution of the number of particles per nanocluster (n_{clust}). The cluster probability distributions are similar for wt-DC-SIGN, ΔCRD- and Δ35-, indicating that the CRD and the cytoplamic tail of DC-SIGN do not

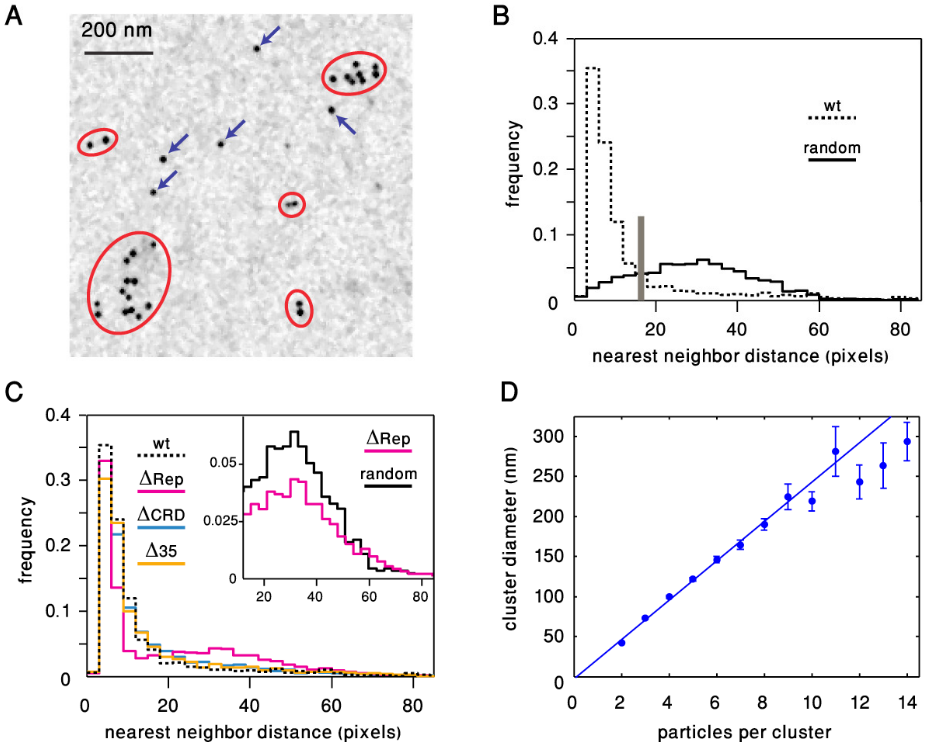

Figure 3.5 Quantification of the degree of nanoclustering from TEM images. (**A**) Zoomed-in region of a TEM image of wt-DC-SIGN showing the result of the cluster-searching algorithm. (**B**) Histograms of the nearest neighbor distribution for wt-DC-SIGN (dotted line) and simulated random-distributed particles (continuous line) are shown. The distance at which the two histograms intersect is selected as the threshold value (vertical gray line). (**C**) Histogram of the nearest neighbor distribution for wt-DC-SIGN and the different mutants (ΔRep-, Δ35-, and ΔCRD-). Inset: zoom-in of the distribution of ΔRep-DC-SIGN and comparison with the nearest neighbor distribution of simulated random-distributed particles. Pixel size is 4.451nm. (**D**) Plot of the cluster diameter versus the number of particles (circles) and corresponding linear fit (line). Error bars represent the standard error.

play a role in DC-SIGN nanoclustering (Fig. 3.6C). In remarkable contrast, the large majority of the ΔRep-DC-SIGN nanoclusters contain at the most 2-3 particles. Beyond these values, the distribution of cluster sizes decays very rapidly, significantly overlapping with that of simulations of random organization. Indeed, the probability of finding clusters of 4 particles is nearly six-fold lower in the case of ΔRep-DC-SIGN with respect to wt-DC-SIGN (and the other mutants) and ten-fold lower for clusters larger than 8 particles (Fig. 3.6C). Altogether these data demonstrate that deletion of the neck region severely reduces the aggregation state of DC-SIGN at the nanoscale, indicating that the neck region is crucial to maintain nanocluster integrity.

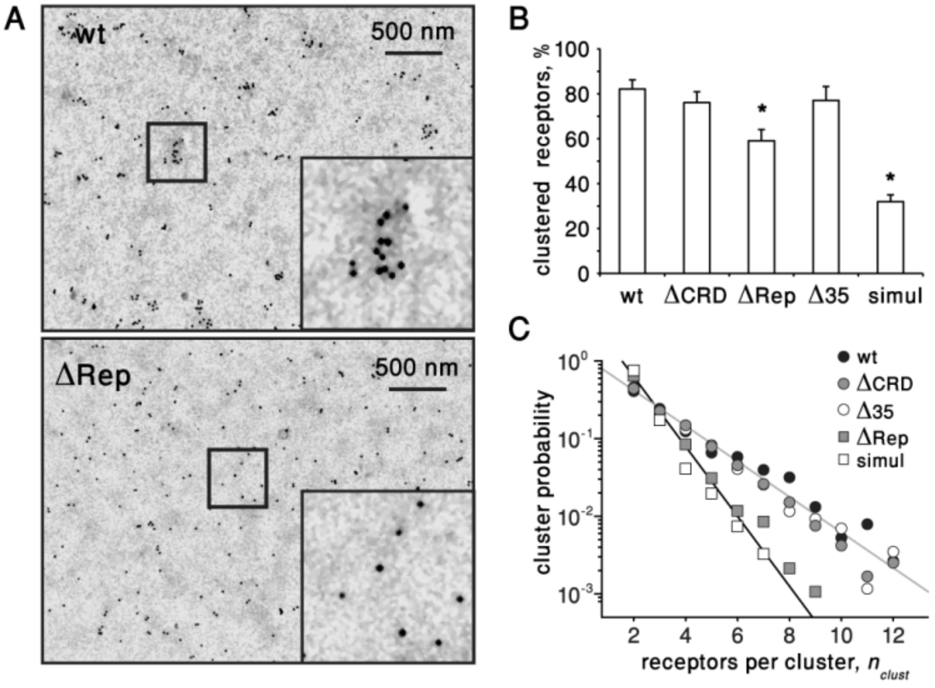

Figure 3.6 Truncation of the neck region affects DC-SIGN nanoclustering. (**A**) Representative TEM images of whole-mount, immunogold labeled CHO cells expressing wt-DC-SIGN (top) and ΔRep-DC-SIGN (bottom). Anti-AU1 mAb and 10 nm Ø gold particles were used to specifically stain DC-SIGN. Results are representatives of multiple cells in several independent experiments. (**B**) The digital images of electron micrographs were processed to extract the percentage of DC-SIGN molecules organized in nanoclusters for wt-DC-SIGN and the different mutants (ΔCRD-, ΔRep- and Δ35-). The results are compared to simulations of random organization with similar surface density as in the experiments. T-test was used to compare the data of wt-DC-SIGN to ΔCRD- and Δ35- that of ΔRep- (* = $p < 10^{-5}$). (**C**) Probability distribution of the number of particles per nanocluster from multiple TEM images over at least 3 independent experiments compared to simulation of random distribution with same surface density as in the experiments. Lines are guides for the eye. At least 10 different TEM images over different cells at each condition.

To exclude the possibility that the observed difference in nanoclusters results from the Ab chosen, anti-AU1 as well as anti-DC-SIGN AZN-D1 and DCN46 antibodies were also used for labeling. More specifically, while anti-AU1 Ab was used to label all DC-SIGN molecules (as all constructs bear the AU1 tag), the anti-CRD Ab AZN-D1 was used to label all DC-SIGN molecules except the ΔCRD mutant, while the anti-neck Ab DCN46 was applied to label all DC-SIGN molecules except the ΔRepeat mutant (31). As shown in Figure 3.7, when anti-AU1, AZN-D1 and DCN46 labeling were compared for wt-DC-SIGN, no significant differences in the nanoclustered organization of the receptor were observed.

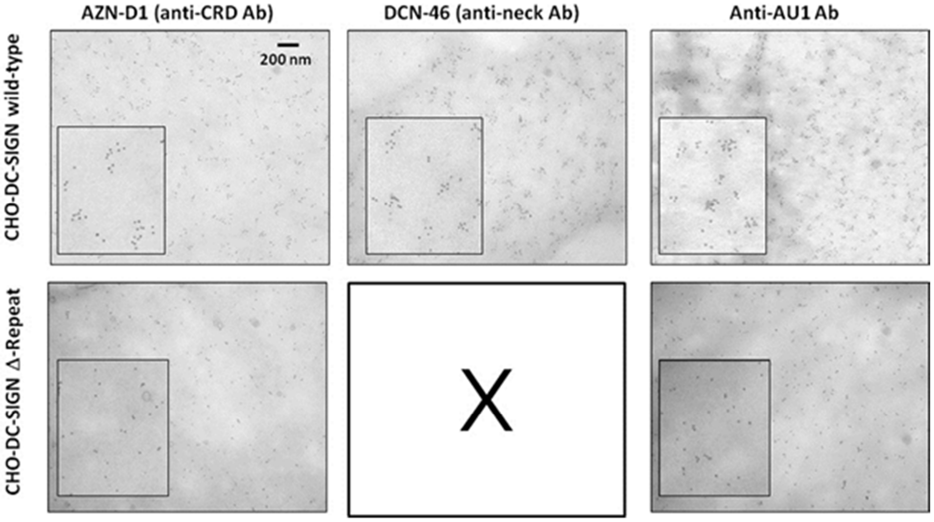

Figure 3.7 The nanoclustered organization of DC-SIGN is not determined by the chosen antibody. AZN-D1 is an anti-CRD Ab, DCN46 is an anti-neck Ab and anti-AU1 is an Ab against the short AU1 tag fused at the C-terminal of each DC-SIGN construct. Representative TEM images of whole-mount, immunogold labeled CHO cells expressing wt-DC-SIGN (top) and ΔRep-DC-SIGN (bottom) obtained by using the different Abs and 10 nm Ø gold particles are shown. The insets show enlarged parts of the images. ΔRep-DC-SIGN cannot be labelled with the anti-neck Ab DCN46 since this mutant lacks the entire neck domain. Results are representatives of multiple cells in several independent experiments.

Super-resolution optical nanoscopy reveals differences in the spatial organization of DC-SIGN that depend on its molecular structure. Although TEM images show the presence of DC-SIGN nanoclustering on CHO cells, in a similar fashion as already reported for imDC (11), steric hinderance between Abs and/or gold beads can induce non-saturated receptor labeling, potentially leading to an underestimation of nanoclustering. Therefore, to confirm wt-DC-SIGN nanoclustering and its abrogation for ΔRep-DC-SIGN, we performed extensive nanoscale imaging on fully intact CHO cells and imDCs using stimulated emission depletion (STED) as well as near-field scanning optical microscopy (NSOM). Representative confocal and STED images of wt-DC-SIGN on the membrane of fixed CHO cells are shown in Figs. 3.8A,B. With an optical resolution of 95nm, STED nanoscopy reveals individual DC-SIGN spots well separated on the cell membrane and significantly brighter than those on the glass substrate, which arise from sparsely and non-specifically attached individual antibodies.

Similar results were obtained when imaging DC-SIGN on monocyte-derived imDCs using a combined single molecule confocal/NSOM set-up at an optical resolution of 90 nm (Fig. 3.9A,B) (24,25). In contrast, significantly weaker florescent spots were retrieved when performing STED imaging of ΔRep-DC-SIGN on CHO cells (Fig. 3.8C,D).

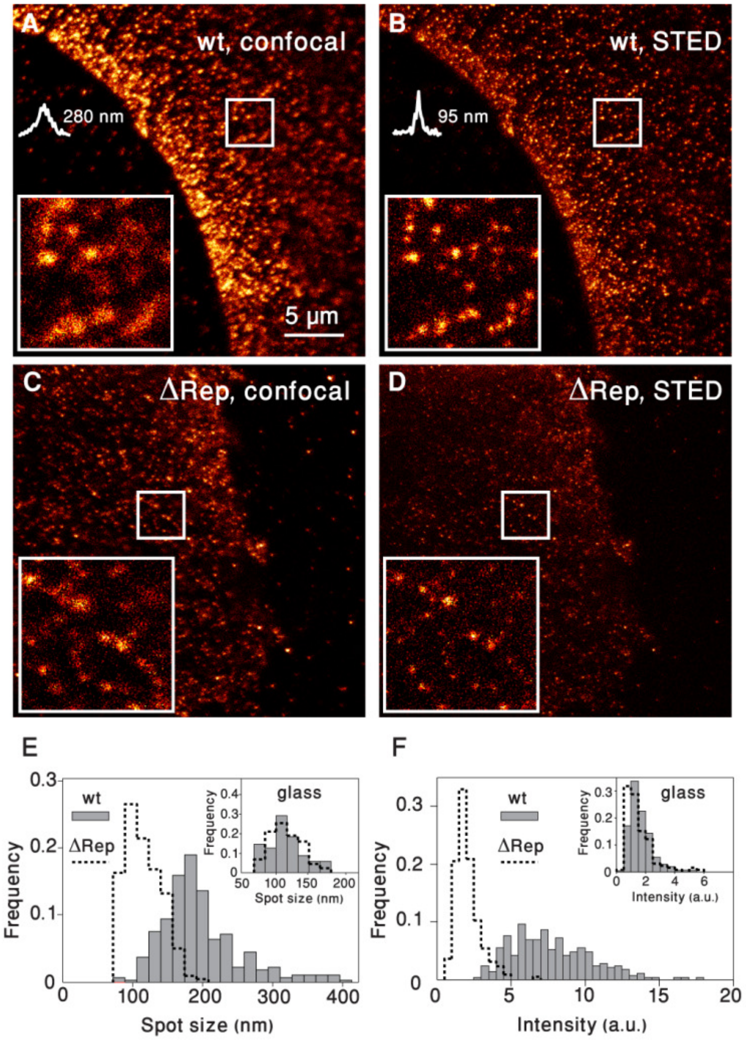

Figure 3.8 Super-resolution optical nanoscopy confirms loss of nanoclustering for ΔRep-DC-SIGN. (**A**-**D**) Confocal (**A**, **C**) and counterpart STED (**B**, **D**) images of wt-DC-SIGN (**A**, **B**) and ΔRep- (**C**, **D**) on CHO cells. The insets highlight the increased resolution of STED compared to diffraction-limited confocal microscopy. (**E**) Normalized distribution of the spot sizes obtained for wt-DC-SIGN (gray bars) compared to that of ΔRep- (dotted). The average spot sizes are 186 (55) nm and 108 (24) nm for wt-DC-SIGN and ΔRep- respectively. The inset shows the spot sizes obtained from individual Abs non-specifically attached to glass and are used to illustrate the spatial resolution of STED (*ca.* 100nm). (**F**) Normalized intensity distribution of fluorescent spots obtained for wt-DC-SIGN (gray bars) compared to that of ΔRep- (dotted). The inset shows the corresponding intensity of spots found on glass. 266 and 198 spots wt-DC-SIGN and ΔRep- respectively from multiple STED images.

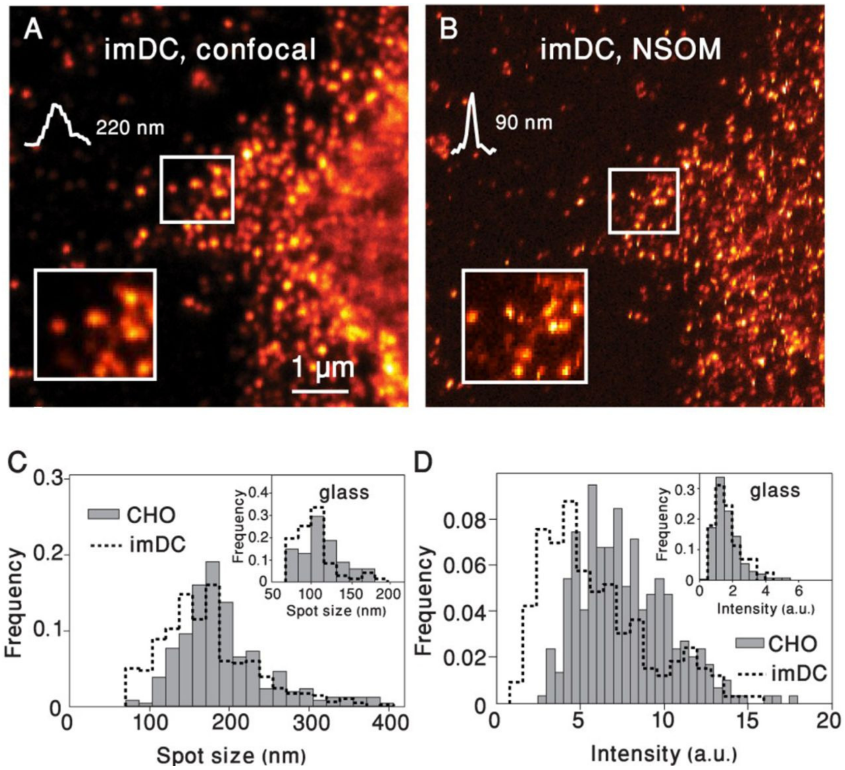

Figure 3.9 Near-field Scanning Optical Microscopy (NSOM) confirms DC-SIGN nanoclustering on imDC. (**A**-**B**) Confocal (**A**) and counterpart NSOM (**B**) images of DC-SIGN on imDC. The insets highlight the increased resolution of NSOM compared to diffraction-limited confocal microscopy. (**C**) Normalized distribution of the spot sizes obtained for DC-SIGN on imDC (dotted) compared to that of CHO cells expressing wt-DC-SIGN (gray bars). The inset shows the spot sizes obtained from individual Abs nonspecifically attached to glass and are used to illustrate the spatial resolution of NSOM (*ca.* 100nm). (**D**) Normalized intensity distribution of fluorescent spots obtained for DC-SIGN on imDC (dotted) compared to that of CHO cells expressing wt-DC-SIGN (gray bars). The inset shows the corresponding intensity of spots found on glass.

The physical size of the spots was determined from multiple super-resolution images by directly measuring their full-width-at-half-maximum (FWHM) (Fig. 3.8E). In full agreement with the TEM data, the size distribution of ΔRep-DC-SIGN spots markedly shifted towards smaller diameters compared to wt-DC-SIGN, being similar in size to the STED resolution (Fig. 3.8E, inset), consistent with a strong reduction of nanoclustering or its complete abrogation. On the other hand, fluorescent spots of wt-DC-SIGN on CHO cells and endogenous DC-SIGN on imDCs exhibited similar average sizes (*ca.*

180 nm) and comparable size distributions (Fig. 3.9C,D). Brightness analysis (see Chapter 2) to estimate the number of molecules per fluorescent spot confirmed nanoclustering of wt-DC-SIGN with a mean value of 7.5 (*s.d.*=2.7) molecules/nanocluster. This value reduced to 1.8 (*s.d.*=0.8) in the case of ΔRep-DC-SIGN. Collectively, these results confirm that the neck region of DC-SIGN crucially affects its nanocluster capacity. Since the neck region is also imperative for DC-SIGN tetramerization (21,37), our data indicate that inter-molecular interactions mediated by the neck region of DC-SIGN regulate different hierarchical levels of receptor spatial organization on the cell membrane. Together with the reduced binding capability to virus-sized particles observed for ΔRep-DC-SIGN, our data establish a direct relationship between nanoclustering formation and the exquisite ability of DC-SIGN to dock pathogens at the virus length-scale.

DC-SIGN nanoclusters are mobile on CHO cells and imDCs. Recent reports on DC-SIGN expressed on NIH-3T3 cells and imDC showed an unusual stability of DC-SIGN in terms of dynamics (26-28). We decided to thoroughly investigate the lateral mobility of DC-SIGN on both CHO and imDCs using particle tracking (SPT) of quantum dots (QD) specifically labeling DC-SIGN, at high speed (60 frame/s) and 20 nm localization accuracy. To avoid potential artifacts due to interactions between the cell ventral membrane and the substrate, we performed QD-labeling of DC-SIGN (either using biotinylated anti-DC-SIGN DCN46 Fab, or anti-AU1 single-chain Ab) after cell stretching and recorded individual trajectories exclusively on the dorsal membrane. Clear mobility of wt-DC-SIGN nanoclusters and ΔRep-DC-SIGN was observed on CHO cells (Fig. 3.10A) in apparent contrast to the results obtained on NIH-3T3 cells (27,28).

To quantify the degree of mobility of DC-SIGN we built individual trajectories from multiple movies and generated plots of the mean-squared displacement (MSD) as a function of time lag. Apparent diffusion coefficients $D_{2\text{-}4}$ were calculated from the initial slopes by linear fit from the second to the fourth point, and included in a semi-log plot (Fig. 3.10B). The $D_{2\text{-}4}$ values of wt-DC-SIGN nanoclusters varied from 10^{-3}-10^{-1} $\mu m^2/s$, with a median value of $D_{2\text{-}4} = 6.5 \cdot 10^{-2}$ $\mu m^2/s$. On the other hand the $D_{2\text{-}4}$ distribution of ΔRep-DC-SIGN was significantly narrower and shifted to larger $D_{2\text{-}4}$ values, with a median value of $D_{2\text{-}4} = 1.23 \cdot 10^{-1}$ $\mu m^2/s$. Since the diffusion coefficient D depends on the size of the diffusing object R as $D \propto 1/R$, the higher $D_{2\text{-}4}$ values observed on ΔRep-DC-SIGN compared to those of wt-DC-SIGN are entirely consistent with nanocluster dissolution (38,39).

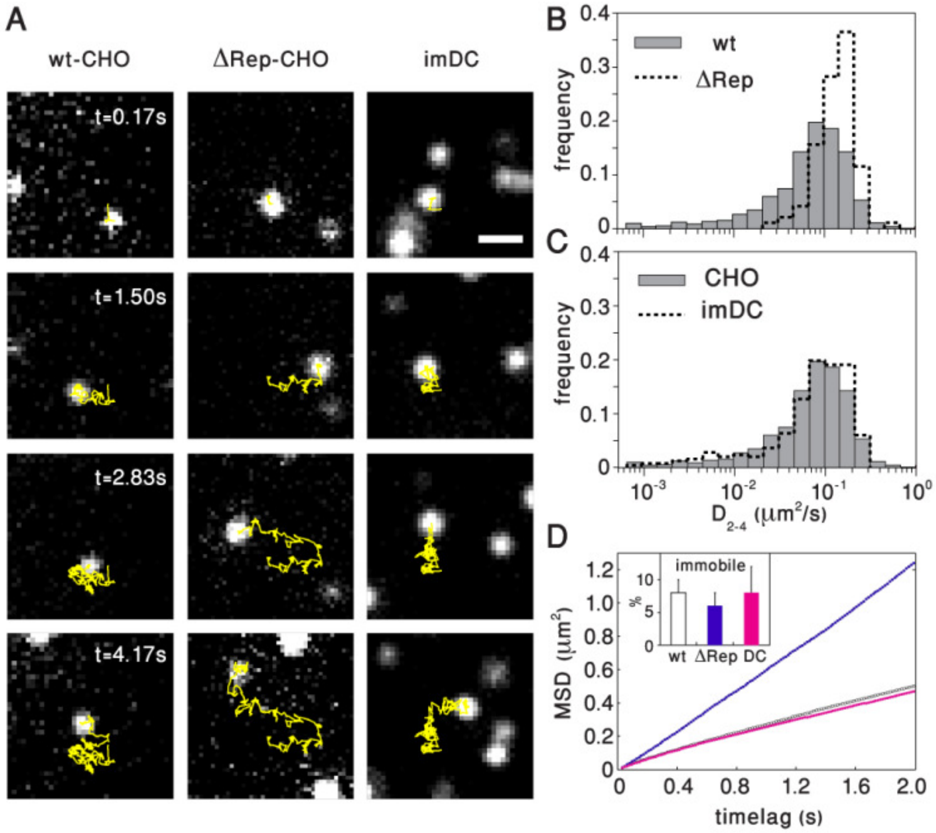

Figure 3.10 DC-SIGN nanoclusters are freely mobile on CHO cells and imDCs. (**A**) Selected sample time series of DC-SIGN-QD to illustrate the mobility of wt-DC-SIGN (left); ΔRep-DC-SIGN (middle); and DC-SIGN on imDC (right). Scale bar: 1μm. (**B**) Normalized semi-log distribution of $D_{2\text{-}4}$ values at short-time lags for wt-DC-SIGN (gray bars) and ΔRep-DC-SIGN (dotted). Each histogram contains at least 100 trajectories taken from >50 cells in multiple experiments. (**C**) Normalized semi-log distribution of $D_{2\text{-}4}$ values at short-time lags for wt-DC-SIGN (gray bars) and DC-SIGN on imDC (dotted). At least 250 trajectories per histogram from >40 cells in multiple experiments were analyzed. (**D**) Cumulative MSD plots of wt-DC-SIGN (black), ΔRep-DC-SIGN (blue) and DC-SIGN on imDC (magenta). The inset shows the percentage of trajectories with $D_{2\text{-}4} < 6 \cdot 10^{-4}$ μm²/s and classified as immobile.

To validate our results on CHO cells, we performed single QD tracking of endogenous DC-SIGN nanoclusters on monocyte-derived imDCs. Clear mobility was also observed on the dorsal membrane of imDCs (Fig. 3.10A), with comparable $D_{2\text{-}4}$ values as to those obtained for wt-DC-SIGN on CHO cells (Fig. 3.10C). Since $D_{2\text{-}4}$ does not report on the long-term diffusion behavior we then generated cumulative MSD plots of all trajectories at longer time lags for wt-DC-SIGN, ΔRep-DC-SIGN on CHO and DC-SIGN on imDCs (Fig 3.10D). In all the three cases, the plots are nearly linear indicating Brownian diffusion of DC-SIGN on both imDCs and CHO cells. As expected, the average *D* value of ΔRep-DC-SIGN, as extracted from the slope of the cumulative MSD plot, is higher than that of wt-DC-SIGN. Moreover, the immobile fraction ($D < 6 \cdot 10^{-4}$ $\mu m^2/s$) of DC-SIGN in the three cases accounted for < 10% of all trajectories analyzed. These results thus conclusively confirm lateral mobility of DC-SIGN nanoclusters within the cell membrane and further evidence a faster diffusion of ΔRep-DC-SIGN fully consistent with nanocluster dissolution at the cell membrane.

Monte Carlo simulations indicate that DC-SIGN nanoclustering enhances viral binding ability. Since the decreased capability of ΔRep-DC-SIGN to bind to virus-sized particles correlated with a loss of nanoclustering on the cell membrane, we wished to understand the impact of receptor organization, and in particular the role of DC-SIGN nanoclustering on viral binding. For this, we turned to Monte Carlo (MC) simulations where we considered different degrees of receptor organization and allowed pathogens of different sizes to land on the cell membrane. We first sought to investigate the role of receptor clustering as a function of pathogen size by choosing two extreme cases, i.e., pathogens with sizes comparable to those of viruses (r=50nm), and pathogens with sizes comparable to those of bacteria (r=500nm), (Fig. 3.11A).

As schematically depicted in Fig. 3.11A, pathogens are approximated as spheres of radius r and the membrane as a flat square region with lateral size $L >> r$. Receptor molecules are positioned on the membrane according to different spatial distributions, varying the degree of clustering, from completely random to fully clustered. In the simulations, the pathogen lands at a random position on the cell membrane and the number of DC-SIGN receptors (n) within the area projected by the pathogen is counted. From these data, the complementary cumulative distribution function (*ccdf*) is obtained and plotted versus n. The *ccdf* value for a given n represents the probability that at least n receptors are accessible to the pathogen at the moment of membrane contact. This quantity is important for pathogen binding since the larger the number of accessible receptors n, the more likely is for ligands on the pathogen surface to engage specific bonds with the membrane receptors.

First, we investigated the effect of receptor nanoclustering on virus binding (r=50nm), while keeping constant the total receptor density. As the percentage of clustering is increased, the *ccdf* decays at higher n, indicating an increased probability of having more accessible receptors around the virus contact point (Fig. 3.11B). Taking as a reference the value of n=4 (dashed vertical line), the corresponding *ccdf* varies over more than 2 orders of magnitude as a function of the clustering percentage, from $<10^{-4}$ for random organization, to $\sim 10^{-2}$ for total clustering. Importantly, a slight increase in clustering percentage from 60% to 80%, similarly to what is observed in the TEM images for ΔRep-DC-SIGN and wt- respectively, already produces a 5-fold probability enhancement.

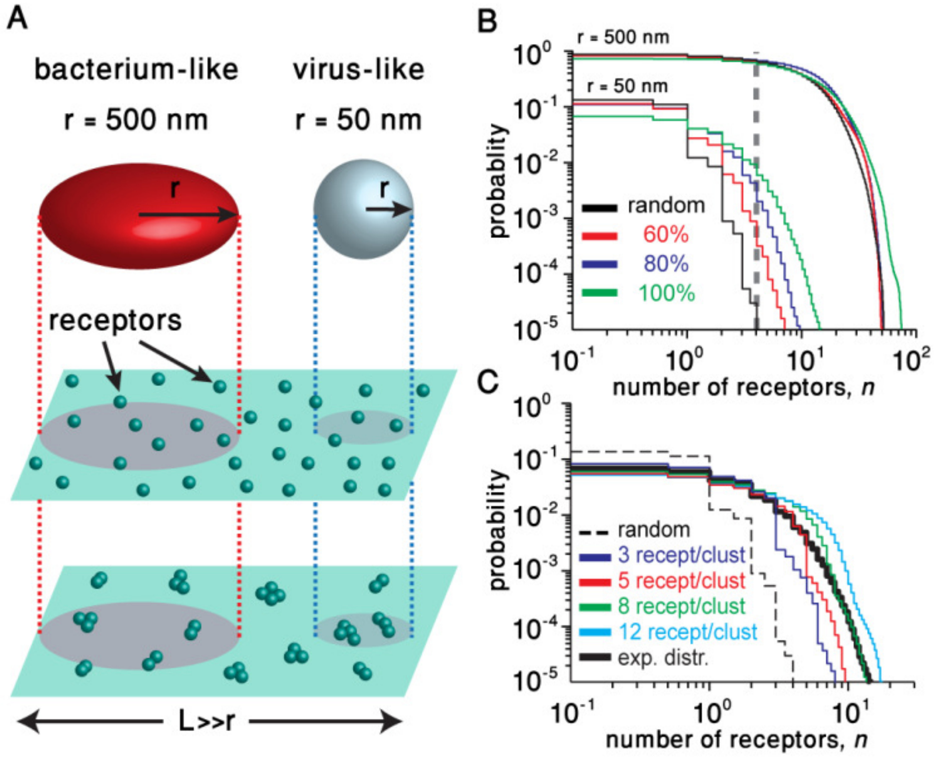

Figure 3.11 Monte Carlo simulations show the effect of nanoclustering on pathogen binding. (**A**) Schematics of the simulation of pathogen landing over a cell membrane containing receptors spatially distributed in a random or clustered fashion. (**B**) Complementary cumulative distribution function (*ccdf*) for having a given number of receptors at the pathogen-cell interface for two pathogen radii (50 and 500 nm) at different degrees of nanoclustering (Black: random distribution; red: 60% clustering; blue: 80% clustering; and green: full clustering). (**C**) *ccdf* for having a given number of receptors at the pathogen-cell interface for different cluster densities. The thick black line denotes the experimental distribution.

Although a qualitatively similar effect is also visible for larger pathogen-like particles (r=500 nm), the increased clustering induces a much smaller variation. Indeed, a change from random distribution to 80% clustering induces at most a 5-fold increase in the *ccdf* (n=30) and a significant change is only observed in case of total clustering for n>40. Our simulations thus confirm that nanoclustering has a crucial role for the docking of virus-size particles and provides a mechanistic explanation for the distinct binding capabilities of DC-SIGN by correlating pathogen size with DC-SIGN spatial organization.

Heterogeneity in cluster density confers broader binding capability to DC-SIGN. TEM and super-resolution images showed that DC-SIGN organizes in nanoclusters having a broadly distributed size and number of particles (Fig. 3.6C and 3.8E, F). To enquire whether this multi-dispersed distribution offers any advantage with respect to a mono-dispersed type of clustering, we performed MC simulations varying the number of receptors per cluster, given that the cluster size depends linearly on the number of receptors per cluster as shown in Fig. 3.5D.

Expectedly, the presence of clusters formed by a larger number of receptors progressively shifts the *ccdf* decay towards larger n (Fig. 3.11C). Interestingly, the *ccdf* obtained for the experimental distribution of n_{clust} (black curve) initially follows the same behavior as that simulated for $n_{\text{clust}} = 3$, to then decay similarly as $n_{\text{clust}} = 5$ and finally overlapping with the *ccdf* simulated for $n_{\text{clust}} = 8$. Therefore, these simulations show that the heterogeneity experimentally observed for the molecular density of DC-SIGN nanoclusters might serve to effectively broaden its binding capabilities to a variety of viruses having different sizes and/or binding affinities for DC-SIGN. Lateral mobility of nanoclusters, as observed in our experiments, will then further virus capture by increasing the probability of encountering events.

Discussion

It has been extensively documented that DC-SIGN forms stable tetramers both in-vitro and in living cells (21-23,37). Tetramers would allow establishing multivalent interactions via the CRDs increasing the adhesion energy of DC-SIGN to its ligands. Our results now show a higher level of spatial complexity of DC-SIGN at the cell membrane, and demonstrate for the first time a direct structural relationship between tetramer stability and nanoclustering formation sustained by the neck region of DC-SIGN. Furthermore, this particular arrangement resulted crucial for efficient binding of nanometer scale pathogens such as viruses, underscoring a physiological role for nanoclustering. Thus, our work provides a clear example of self-organization at the cell surface prior to ligand activation that is driven by the molecular structure of the receptor.

It has been proposed that the extended and flexible structure of the DC-SIGN neck region might play a role in favorably positioning the CRDs for efficient pathogen binding (21,22) and that neck-truncated molecules did not bind to HIV-1 because they are too short to emerge from the plasma membrane (30). Our binding assays show that the CRD of the neck-truncated mutant is fully available for binding to both soluble ligands and micron-size objects and that the impaired binding to virus-like particles is mostly due to the lack of nanocluster spatial organization of DC-SIGN. We also observed that DC-SIGN mediated internalization was independent of the neck region but highly affected by the cytosplamic tail of DC-SIGN. These results thus reflect different functional properties of DC-SIGN directly related to its molecular structure, i.e., whereas nanoclustering is important for pathogen binding, the cytoplasmic region determines internalization efficiency.

Recent work using diffraction-limited confocal imaging showed that on imDCs and fibroblast cell lines, DC-SIGN form immobile *micro*domains of dimensions larger than 600nm stabilized by interactions between the CRDs and the extracellular matrix (26-28). Deletion of the CRD abrogated *micro*clustering and resulted in DC-SIGN lateral diffusion on the cell membrane, as measured by fluorescence recovery after photobleaching using full Abs (28). In apparent contrast, we observed that truncation of the CRDs did not affect the *nano*clustering capacity of DC-SIGN and that nanoclusters are fully mobile, independent on the cell type and mutant investigated. Because of the limited spatial resolution of confocal microscopy, it might well be that nanoclusters (of sizes < 180 nm as observed in our super-resolution experiments) spatially proximal to each other appear as larger clusters when inspected by confocal microscopy. Indeed, recent work from the same group using super-resolution blink microscopy showed that the microdomains observed by diffraction limited optical techniques are in fact composed by discrete DC-SIGN nanodomains (40). In addition, receptor diffusion measurements on the cell membrane are highly influenced by the labeling conditions. Whereas the use of full Abs might induce cross-linking of close by receptors increasing clustering beyond the native state and reducing their overall mobility to the level of fixed cells (41,42), single chains or Fabs, as used in our experiments, guarantee that both nanoclustering as well as laterally mobility are minimally influenced. Additionally, possible Ab-induced receptor cross-linking could contribute to initiate DC-SIGN endocytosis via nascent clathrin-coated pits. These nascent endocytic complexes are likely to appear as immobile features at the observed time-scale.

In summary, we have shown that homophilic interactions mediated by the neck region of DC-SIGN are essential to coordinate its spatiotemporal organization on the cell membrane effectively broadening its binding capabilities to nanoscale-size pathogens. Since lateral mobility of receptors and ligands play a key role in facilitating mutual interactions, our results indicate that for a given number of receptors at the cell surface, tight spatial coordination in nanoclusters guarantees highly energetic interactions with ligands, while lateral mobility enhances the probability of ligand encountering for effective binding.

Interestingly, different DC-SIGN neck variants have been found to naturally occur on dendritic and myeloid cells (37) and polymorphisms in the DC-SIGN gene affecting the length of the neck region appeared correlated with altered susceptibility to HIV infection (43,44). Besides with HIV, DC-SIGN is known to interact with a plethora of viruses with different size and different properties. While DC-SIGN has been shown to solely act as attachment factor for viruses such as Ebola (45), Measles (46), and Hepatitis C (47), recent publications demonstrated the direct involvement of DC-SIGN in the entry of viruses such as arthropod-borne phleboviruses (48), coronavirus (49) and human Herpesvirus 8 (50). Clearly, DC-SIGN binds with equal efficiency to viruses of different sizes (from Dengue being about 50nm, HIV around 100nm and Measles virus 200-300nm). Furthermore, it has also been shown that DC-SIGN is able to bind to gp120-coated particles of 40nm in size as well as real HIV virions (11). In addition, Pohlmann and colleagues have reported that real HIV virus cannot bind to ΔRep-DC-SIGN (30), implying that 40nm and 100 nm are equally not bound by this mutant. Our work therefore demonstrates that the plasticity of DC-SIGN virus binding capacity is largely determined by its variable nanoclustering capacity, which is regulated by the neck region of the receptor. Furthermore, our simulations indicate that the number of receptors included in the clusters defines the effectiveness of the binding as long as the sizes of the viruses are comparable to the sizes of the DC-SIGN nanoclusters (i.e. from 80-400 nm with a mean size of 180nm). Thus, the inherent nanoclustering of DC-SIGN driven by the neck region, as observed in our measurements, could have important implications for DC-SIGN functionality under physiological settings and impact on our understanding of membrane receptor organization in relation to virus entry into the cells.

It has been previously shown that ligand binding via DC-SIGN neck region leads to prolonged antigen storage and enhanced cross-presentation capacity (43). Exploitation of the DC-SIGN neck region therefore represents an intriguing possibility for the development of novel targeted vaccination strategies, justifying the increasing interest in the contribution of the neck region to the immunobiology of DC-SIGN.

Materials & Methods

Cells and DNA constructs. CHO cell lines stably expressing wt-DC-SIGN, ΔCRD-, Δ35- and ΔRep- were established by LipofectaminTM 2000 transfection. Human imDCs were generated from buffy coats of healthy donors as previously reported (29). Plasmids used in this study were pcDNA-3 carrying the wt-DC-SIGN or deletion mutants. These constructs have a short C-terminal AU-1 tag and were constructed as already published (30).

Binding assays. Binding of CHO cells to soluble Alexa647-mannan was performed as follows: 50,000 cells were incubated with 50 µg/ml Alexa647-mannan in 20 mM Tris pH 8.0, containing 150 mM NaCl, 1 mM $CaCl_2$, 2mM $MgCl_2$, and 1% BSA (TSA-buffer) for 30 min on ice, in presence or absence of 20 µg/ml anti–DC-SIGN blocking mAb (AZN-D1) or 100 µg/ml unlabeled mannan. After thorough washing in PBS, the % of cells that had bound mannan was detected by flow cytometry using the FACSCalibur™ (Becton Dickinson). The values represent the mean ± the standard deviation of duplicates of one representative experiment out of three. Binding to gp120-coated beads was performed as already reported (11). Briefly, streptavidin-modified TransFluorSpheres (505/515 nm, 40-nm diam; Molecular Probes) were coated with recombinant biotinylated gp120 (HIV-1 III B, from ImmunoDiagnostics, Inc. Woburn, USA) and were added to 50,000 cells in a ratio of 20 beads/cell in TSA-buffer and the suspension was incubated for 30 min at 37ºC. When necessary, cells were pre-incubated with 20 µg/ml blocking mAb or 2 mM EDTA for 10 min at RT. Binding was determined by measuring the percentage of cells, which have bound fluorescent beads, by flow cytometry. Binding to FITC-conjugated zymosan was performed as already described (16). Briefly, CHO transfectants were incubated with FITC-labeled zymosan particles in the absence or the presence of mannan (100 µg/ml) or anti-DC-SIGN mAb AZN-D1 (20 µg/ml) in TSA buffer. After 30 min of incubation at 37ºC, cell-zymosan conjugates were analyzed by flow cytometry, and the percentage of CHO cells that had acquired a FITC+ signal was quantified by flow cytometry.

Antigen internalization assay. The internalization assay was performed as already reported (31). Briefly, CHO cell lines stably expressing wt-DC-SIGN or the deletion mutants were incubated with anti-DC-SIGN mAb hD1 (5 µg/ml) in serum-free medium for 20 min on ice. After washing the unbound mAb in ice-cold medium, half of the cells were further incubated for 15 min on ice to prevent internalization, while the other half was shifted to 37°C for 15 min to induce internalization. Subsequently, cells were placed back on ice to stop internalization, washed in ice-cold PBS containing 3% BSA, and incubated with PE-conjugated goat-anti-human antibodies for 20 min on ice to stain the mAb still present at the cell surface. Unbound Abs were washed away and cells were fixed in 1% formaldehyde. Isotype controls were always taken along.

Gold labeling of whole-mount samples. CHO transfectants were allowed to adhere and spread on glass coverslips covered by a thin layer of formvar for 1h at 37ºC and immediately fixed with 1% PFA for 15 min. After two washing steps with PBS and a subsequent incubation (60 min at RT) with blocking buffer (PBS, 0.1% glycine, 1% BSA, and 0.25% gelatin) to reduce specific background, the specimens were incubated for 30 min with primary antibodies (DCN46 Ab (Pharmingen) for wt-DC-SIGN, ΔCRD- and Δ35- or anti-AU1 Ab (Covance) for ΔRep-DC-SIGN in blocking buffer on ice, rinsed in PBS, and fixed in 1% PFA and 0.1% glutaraldehyde for 15 min. After two washing steps with PBS and blocking buffer, the samples were incubated with rabbit anti–mouse IgG (to detect mAb) for 30 min on ice. A final incubation with 10-nm diameter gold-labeled Protein A (to detect polyclonal antibodies) was performed, followed by final fixation in 1% glutaraldehyde in phosphate buffer for 20 min at RT.

TEM Sample preparation and imaging. After gold labeling and fixation, the samples were dehydrated by sequential passages through 30, 50, 70, 90%, and absolute ethanol. Next, the ethanol was substituted by liquid CO_2, and the samples were critical point dried. The formvar films were transferred from the glass onto copper grids, and the specimens were observed in a transmission electron microscope (model 1010; JEOL), operating at 60–80 kV. Gold particles were detected on the periphery and thinner parts of cells, where a good contrast could be achieved. Since the CHO cells widely spread, the membrane area available for analysis represented up to 60–70% of the whole labeled plasma membrane. For each cell at least four to six areas were analyzed at random.

TEM image analysis and quantification of clustering. The digital images of electron micrographs were processed by custom-written software based on Matlab (The Mathworks, Inc.). Gold particle positions were automatically detected by means of maximum-likelihood based routine (51). The classification of particles into clusters was performed by means of a threshold-based algorithm. The interparticle distance matrix M(i,j) is calculated for all the particles in an image. The routine finds the minimum of M(i,j) and compares it with a threshold value, *th*. If min(M)<*th*, the particles i^* and j^* with $(i^*, j^*)=\arg\{\min(M)\}$ are considered as belonging to a cluster. The search continues over the distances of all the remaining particles from i^* and j^*. If a third particle, k^* is found at a distance shorter than *th* from either i^* or j^*, then it is also included as part of the cluster. The search continues until no particles are found within a distance *th* from those composing the cluster. Then the algorithm moves to the next minimum of the matrix M and defines a new cluster. Once the particles are assigned to a given cluster, the area of the smallest ellipse inclosing all the particles is used to determine the cluster area, A_{clust}. The cluster size is calculated as $d_{clust}=2*(A_{clust}/\pi)^{1/2}$.

Near-field Scanning Optical Microscopy (NSOM). Cells were imaged with a custom-built confocal/NSOM microscope working in aqueous conditions (54). Custom built NSOM probes with an aperture of 80-100 nm were kept at a distance of ~10 nm above the sample using a shear-force feedback system, simultaneously yielding the sample topographic map. Typically, cells were first imaged in confocal mode. Subsequently, NSOM imaging was performed on a 7x7 μm area of a well-stretched region on the cell membrane. Scanning speed was 3-6 μm s^{-1}.

Binding to real HIV-1 particles. The AT-2-inactivated HIV-1 particles [HIV-1(MN)/H9 Cl.4 lot P3936 courtesy of Biological Products Section, AIDS and Cancer Virus Program, SAIC Frederick, Inc, National Cancer Institute at Frederick, Frederick, MD USA 21702] were already described (52). After conjugating the particles to Alexa647 dye, binding to the CHO cells was performed as already reported (53). Briefly, 400000 CHO cells transfected with empty vector or ΔRep-DC-SIGN or wt-DC-SIGN were left in suspension and incubated with Alexa647-conjugated HIV-1 virions (400 ng HIV-1 p24 Ag/100.000 cells) for 30 min at 37ºC. Unbound virus was discarded by washing 3 times with PBS buffer. Subsequently, fixation with 4% PFA for 1 hr at RT was performed and the samples were analyzed by flow cytometry (Fig. 3.2A). For the visualization of binding by confocal microscopy, 400000 adherent cells were allowed to interact with the fluorescent virus particles, as described above. Subsequently, after washing and fixation, the cells were stained with the anti-DC-SIGN mAb AZN-D1 and fluorescent secondary Ab and imaged by confocal microscopy (Fig. 3.2B).

Stimulated Emission Depletion (STED) Nanoscopy. Confocal and STED images were obtained in a sequential manner using a 100x oil immersion objective (HCX PL APO 100x/1.4 Oil, Leica Microsystems, Germany) of a commercial CW-STED SP-7 microscope (Leica Microsystems, Germany) as described in Chapter 2.

Single Particle Tracking. Single Particle Tracking experiments were performed on a custom built EPI single molecule sensitive fluorescence microscope with a Hamamtsu EM-CCD Camera at 60Hz and analyzed using the mean-square displacement as described on Chapter 2.

Fab/mAb preparation for single molecule dynamic measurements. Anti-human DC-SIGN Fab fragments were generated from DCN46 mAb by papain digestion (Pierce Biotechnology, Rockford, IL) according to the manufacturer's instructions. Fab fragments were further purified from remaining undigested IgG and Fc fragments on a NAb Protein A column (Pierce Biotechnology). Non-reducing 12.5% sodium dodecyl sulphate-polyacrylamide gel electrophoresis (SDS-PAGE) and staining with Coomassie brilliant blue were carried out to monitor Fab digestion and purification. Analysis of Fab fragment by gel filtration (Superdex 200 matrix) revealed a single homodisperse peak at an exclusion volume corresponding to a molecular weight ≈ 50 kDa. Where desired, purified Fab fragments were biotinylated with an EZ-Link Sulfo-NHS-Biotin reagent (Thermo Scientific) following the manufacturer's instructions. Non-reacted sulfo-NHS biotin was removed using PD SpinTrap G-25 columns (GE Healthcare Life Sciences).

Monovalent anti-human AU1 antibodies were generated from AU1 Ab (Covance) by reduction with Dithiothreitol (Invitrogen) according to manufacturer´s instructions. Biotinylation was then achieved by addition of Maleimide-PEG$_2$-Biotin (Thermo Scientific) to the reduced Abs. Non-reacted DTT or unbound biotin was removed by dialysis using Slide-A-Lyzer MINI Dyalisis Units (Thermo Scientific) overnight. A 4-12% Bis-Tris gel under denaturing and non-denaturing conditions was performed at every step to monitor the reaction.

Monte Carlo simulations. We performed Monte Carlo simulations of the random encounter of a pathogen-like object with the cell membrane. In our model, the cell membrane is approximated as a flat, square region (LxL=2048x2048 pixels, 4 nm per pixel) and the pathogen as a sphere (r = 50 and 500 nm). Receptors were positioned on the membrane according to different spatial distributions, with a given particle density (17 particles/µm^2) and periodic boundaries. Although the membrane is a dynamic surface, we only considered static distributions of receptors. This is a valid approximation since the simulations are focused on the initial moment of the cell-pathogen encounter, not including any dynamic process that may occur after the engagement. In each simulation run, the pathogen-like object encounters the membrane at a randomly drawn position. Receptor molecules were positioned on the membrane according to different spatial distributions, varying the degree of clustering, as well as the type of cluster distribution. Each type of receptor distribution was simulated 100 times and on each of such configurations we ran 100 simulation of pathogen landing. The number of receptors included inside the projected area of the pathogen was counted and recorded. The complementary cumulative probability distribution (*ccdf*) was then built and plotted against the minimum number of receptors, n.

References

1. Banchereau, J and Steinman, RM (1998) Dendritic cells and the control of immunity. *Nature*. **392**, 245-252.

2. Steinman, RM (1991) The Dendritic Cell System and Its Role in Immunogenicity. *Annu Rev Immunol*. **9**, 271-296.

3. Thery, C and Amigorena, S (2001) The cell biology of antigen presentation in dendritic cells. *Curr Opin Immunol*. **13**, 45-51.

4. Trombetta, ES and Mellman, I (2005) Cell biology of antigen processing in vitro and in vivo. *Annu Rev Immunol*. **23**, 975-1028.

5. Cambi, A and Figdor, CG (2003) Dual function of C-type lectin-like receptors in the immune system. *Curr Opin Cell Biol.*;15:539-546.

6. van Kooyk, Y and Geijtenbeek, TBH (2003) DC-sign: Escape mechanism for pathogens. *Nature Reviews Immunology*. **3**, 697-709.

7. Tacken, PJ, de Vries, IJM, Torensma, R, and Figdor, CG (2007) Dendritic-cell immunotherapy: from ex vivo loading to in vivo targeting. *Nature Reviews Immunology*. **7**, 790-802.

8. Bonifaz, LC, Bonnyay, DP, Charalambous, A, et al. (2004) In vivo targeting of antigens to maturing dendritic cells via the DEC-205 receptor improves T cell vaccination. *J Exp Med*. **199**, 815-824.

9. Geijtenbeek, TBH, Krooshoop, DJEB, Bleijs, DA et al. (2000) DC-SIGN-ICAM-2 interaction mediates dendritic cell trafficking. *Nat Immunol*. **1**, 353-357.

10. Soilleux, EJ, Morris, LS, Leslie, G, et al. (2002) Constitutive and induced expression of DC-SIGN on dendritic cell and macrophage subpopulations in situ and in vitro. *J Leukoc Biol*. **71**, 445-457.

11. Cambi, A, de Lange, F, van Maarseveen, NM, et al. (2004) Microdomains of the C-type lectin DC-SIGN are portals for virus entry into dendritic cells. *J Cell Biol*. **164**, 145-155.

12. Puig-Kroger, A, Serrano-Gomez, D, Caparros, E, et al. (2004) Regulated expression of the pathogen receptor dendritic cell-specific intercellular adhesion molecule 3 (ICAM-3)-grabbing nonintegrin in THP-1 human leukemic cells, monocytes, and macrophages. *J Biol Chem*. **279**, 25680-25688.

13. Geijtenbeek, TBH, Kwon, DS, Torensma, R, et al. (2000) DC-SIGN, a dendritic cell-specific HIV-1-binding protein that enhances trans-infection of T cells. *Cell*. **100**, 587-597.

14. Alvarez, CP, Lasala, F, Carrillo, J, Muniz, O, Corbi, AL, Delgado, R (2002) C-type lectins DC-SIGN and L-SIGN mediate cellular entry by Ebola virus in cis and in trans. *Journal of Virology*. **76**, 6841-6844.

15. Ludwig, IS, Lekkerkerker, AN, Depla, E, et al. (2004) Hepatitis C virus targets DC-SIGN and L-SIGN to escape lysosornal degradation. *Journal of Virology*. **78**, 8322-8332.

16. Cambi, A, Gijzen, K, de Vries, JM, et al. (2003) The C-type lectin DC-SIGN (CD209) is an antigen-uptake receptor for Candida albicans on dendritic cells. *Eur J Immunol*. **33**, 532-538.

17. Geijtenbeek, TBH, van Vliet, SJ, Koppel, EA et al. (2003) Mycobacteria target DC-SIGN to suppress dendritic cell function. *J Exp Med*. **197**, 7-17.

18. Gringhuis, SI, den Dunnen, J, Litjens, M, van der Vlist, M, Geijtenbeek, TBH (2009) Carbohydrate-specific signaling through the DC-SIGN signalosome tailors

immunity to Mycobacterium tuberculosis, HIV-1 and Helicobacter pylori. *Nat Immunol*. **10**, 1081-1088.

19. Feinberg, H, Mitchell, DA, Drickamer, K, Weis, WI (2001) Structural basis for selective recognition of oligosaccharides by DC-SIGN and DC-SIGNR. *Science*. **294**, 2163-2166.
20. Mitchell, DA, Fadden, AJ, Drickamer, K (2001) A novel mechanism of carbohydrate recognition by the C-type lectins DC-SIGN and DC-SIGNR - Subunit organization and binding to multivalent ligands. *J Biol Chem*. **276**, 28939-28945.
21. Feinberg, H, Guo, Y, Mitchell, DA, Drickamer, K, Weis, WI (2005) Extended neck regions stabilize tetramers of the receptors DC-SIGN and DC-SIGNR. *J Biol Chem*. **280**, 1327-1335.
22. Yu, QD, Oldring, AP, Powlesland, AS, et al. (2009) Autonomous Tetramerization Domains in the Glycan-binding Receptors DC-SIGN and DC-SIGNR. *J Mol Biol*. **387**, 1075-1080.
23. Menon, S, Rosenberg, K, Graham, SA et al. (2009) Binding-site geometry and flexibility in DC-SIGN demonstrated with surface force measurements. *Proc Natl Acad Sci U S A*. **106**, 11524-11529.
24. Koopman, M, Cambi, A, de Bakker, BI, et al. (2004) Near-field scanning optical microscopy in liquid for high resolution single molecule detection on dendritic cells. *FEBS Lett*. **573**, 6-10.
25. de Bakker, BI, de Lange, F, Cambi, A, et al. (2007) Nanoscale organization of the pathogen receptor DC-SIGN mapped by single-molecule high-resolution fluorescence microscopy. *Chemphyschem*. **8**, 1473-1480.
26. Neumann, AK, Thompson, NL, Jacobson, K (2008) Distribution and lateral mobility of DC-SIGN on immature dendritic cells - implications for pathogen uptake. *J Cell Sci*. **121**, 634-643.
27. Itano, MS, Neumann, AK, Liu, P, et al. (2011) DC-SIGN and Influenza Hemagglutinin Dynamics in Plasma Membrane Microdomains Are Markedly Different. *Biophys J*. **100**, 2662-2670.
28. Liu, P, Wang, X, Itano, MS, Neumann, AK, Jacobson, K, and Thompson, NL (2012) The Formation and Stability of DC-SIGN Microdomains Require its Extracellular Moiety. *Traffic*.;doi: 10.1111/j.1600-0854.2012.01337.x.
29. Geijtenbeek, TBH, Torensma, R, van Vliet, SJ, et al. (2000) Identification of DC-SIGN, a novel dendritic cell-specific ICAM-3 receptor that supports primary immune responses. *Cell*. **100**, 575-585.
30. Pohlmann, S, Leslie, GJ, Edwards, TG, et al. (2001) DC-SIGN interactions with human immunodeficiency virus: virus binding and transfer are dissociable functions. *J Virol*. **75**, 10523-10526.

31. Tacken, PJ, Ginter, W, Berod, L, Cruz, LJ, Joosten, B, Sparwasser, T, Figdor, CG, and Cambi, A (2011) Targeting DC-SIGN via its neck region leads to prolonged antigen residence in early endosomes, delayed lysosomal degradation, and cross-presentation. *Blood.***118**, 4111-4119.

32. Sierra-Filardi, E, Estecha, A, Samaniego, R, Fernández-Ruiz, E, Colmenares, M, Sánchez-Mateos, P, Steinman, RM, Granelli-Piperno, A, and Corbi, AL (2010) Epitope mapping on the dendritic cell-specific ICAM-3-grabbing non-integrin (DC-SIGN) pathogen-attachment factor *Mol. Immunol.* **47,** 840–848.

33. Cambi, A, Beeren, I, Joosten, B, Fransen, JA, and Figdor, CG (2009) The C-type lectin DC-SIGN internalizes soluble antigens and HIV-1 virions via a clathrin-dependent mechanism. *Eur J Immunol*. **39**, 1923-1928.

34. Cambi, A, Lidke, DS, Arndt-Jovin, DJ, Figdor, CG, and Jovin, TM (2007) Ligand-conjugated quantum dots monitor antigen uptake and processing by dendritic cells. *Nano Lett*. **7**, 970-977.

35. Zhu, P, Chertova, E, Bess, J, et al. (2003) Electron tomography analysis of envelope glycoprotein trimers on HIV and simian immunodeficiency virus virions. *Proc Natl Acad Sci U S A*. **100**, 15812-15817.

36. Smith, AL, Ganesh, L, Leung, K, Jongstra-Bilen, J, Jongstra, J, and Nabel, GJ (2007) Leukocyte-specific protein 1 interacts with DC-SIGN and mediates transport of HIV to the proteasome in dendritic cells. *J Exp Med*. **204**, 421-430.

37. Serrano-Gomez, D, Sierra-Filardi, E, Martinez-Nunez, RT, et al. (2008) Structural requirements for multimerization of the pathogen receptor dendritic cell-specific ICAM3-grabbing non-integrin (CD209) on the cell surface. *J Biol Chem*. **283**, 3889-3903.

38. Chung, I, Akita, R, Vandlen, R, Toomre, D, Schlessinger, J, and Mellman, I (2010) Spatial control of EGF receptor activation by reversible dimerization on living cells. *Nature*. **464**, 783-787.

39. Bakker, G.,J., Eich, C., Torreno-Pina, J.,A, et al. (2012) Lateral mobility of individual integrin nanoclusters orchestrates the onset for leukocyte adhesion. *Proc Natl Acad Sci U S A*. **109**, 4869-4874.

40. Itano, MS, Steinhauer, C, Schmied, JJ, et al. (2012) Super-Resolution Imaging of C-Type Lectin and Influenza Hemagglutinin Nanodomains on Plasma Membranes Using Blink Microscopy. *Biophys J*. **102**, 1534-1542.

41. Gaborski, TR, Clark, A, Waugh, RE, and McGrath, JL (2008) Membrane Mobility of beta 2 Integrins and Rolling Associated Adhesion Molecules in Resting Neutrophils. *Biophys J*. **95**, 4934-4947.

42. Ashby, MC, Maier, SR, Nishimune, A, and Henley, JM (2006) Lateral diffusion drives constitutive exchange of AMPA receptors at dendritic spines and is regulated by spine morphology. *J Neurosci*. **26**, 7046-7055.

43. Liu, HL, Hladik, F, Andrus, T, et al. (2005) Most DC-SIGNR transcripts at mucosal HIV transmission sites are alternatively spliced isoforms. *Eur J Hum Genet*. **13**, 707-715.

44. Khoo, US, Chan, KYK, Chan, VSF, and Lin, CLS (2008) DC-SIGN and L-SIGN: the SIGNs for infection. *J Mol Med*. **86**, 861-874.

45. Simmons, G, Reeves, JD, Grogan, CC, Vandenberghe, LH, Baribaud, F, Whitbeck, JC, Burke, E, Buchmeier, MJ, Soilleux, EJ, Riley, JL, Doms, RW, Bates, P and Pöhlmann, S (2003) DC-SIGN and DC-SIGNR bind ebola glycoproteins and enhance infection of macrophages and endothelial cells. *Virology*. **305**:115-23.

46. de Witte, L, Abt, M, Schneider-Schaulies, S, van Kooyk, Y and Geijtenbeek, TB (2006) Measles virus targets DC-SIGN to enhance dendritic cell infection.. *J Virol.* **80**:3477-86.

47. Lozach, PY, Amara, A, Bartosch, B, Virelizier, JL, Arenzana-Seisdedos, F, Cosset, FL and Altmeyer, R (2004) C-type lectins L-SIGN and DC-SIGN capture and transmit infectious hepatitis C virus pseudotype particles. *J Biol Chem.* **279**:32035-45.

48. Lozach, PY, Kühbacher, A, Meier, R, Mancini, R, Bitto, D, Bouloy, M and Helenius, A (2011) DC-SIGN as a receptor for phleboviruses. *Cell Host Microbe.* **10**:75-88.

49. Regan, AD & Whittaker, GR (2008) Utilization of DC-SIGN for entry of feline coronaviruses into host cells. *J Virol.* **82**:11992-6

50. Rappocciolo, G, Hensler, HR, Jais, M, Reinhart, TA, Pegu, A, Jenkins, FJ and Rinaldo, CR (2008) Human herpesvirus 8 infects and replicates in primary cultures of activated B lymphocytes through DC-SIGN. *J Virol.* **82**:4793-806.

51. Serge A, Bertaux N, Rigneault H, Marguet D (2008). Dynamic multiple-target tracing to probe spatiotemporal cartography of cell membranes. *Nat Methods* **5**:687-694.

52. Morcock, DR, Thomas, JA, Gagliardi, TD, Gorelick, RJ, Roser, JD, Chertova, EN, Bess, JW Jr, Ott, DE, Sattentau, QJ, Frank, I, Pope, M, Lifson, JD, Henderson, LE and Crise, BJ (2005) Elimination of retroviral infectivity by N-ethylmaleimide with preservation of functional envelope glycoproteins. *J Virol*. **79**: 1533-1542.

53. Cambi, A, Beeren, I, Joosten, B, Fransen, JA, and Figdor, CG (2009) The C-type lectin DC-SIGN internalizes soluble antigens and HIV-1 virions via a clathrin-dependent mechanism. *Eur J Immunol.* **39**:1923-1928.

54. van Zanten TS, Cambi A, Koopman M, Joosten B, Figdor CG, Garcia-Parajo MF (2009) Hotspots of GPI-anchored proteins and integrin nanoclusters function as nucleation sites for cell adhesion. *Proc Natl Acad Sci U S A*. **106**:18557-18562.

Chapter 4

Enhanced receptor-clathrin interactions induced by *N*-glycan-mediated membrane micropatterning

In Chapter 3, we have addressed the importance of the neck region in regulating DC-SIGN nanoclustering, lateral mobility and virus-binding capability. In this Chapter we have focused on the influence of another extracellular structural motif of DC-SIGN, its *N*-glycosylation motif, in regulating the spatiotemporal behavior of the receptor by interacting with extracellular sugars. Glycan-protein interactions are emerging as important modulators of membrane protein organization and dynamics, regulating multiple cellular functions. In particular, it has been postulated that glycan-mediated interactions regulate surface residence time of glycoproteins and endocytosis. How this precisely occurs is poorly understood. We applied single-molecule-based approaches to directly visualize the impact of glycan-based interactions on the spatiotemporal organization and interaction with clathrin of the N-glycosylated DC-SIGN. We find that cell surface glycan-mediated interactions do not influence the nanoscale lateral organization of DC-SIGN but restrict the mobility of the receptor to distinct micrometer-size membrane regions. Remarkably, these regions are enriched in clathrin, thereby increasing the probability of DC-SIGN-clathrin interactions beyond random encountering. N-glycan removal or neutralization leads to larger membrane exploration and reduced interaction with clathrin, compromising clathrin-dependent internalization of virus-like particles by DC-SIGN. Therefore, our data reveal that cell surface glycan-mediated interactions add another organization layer to the cell membrane at the microscale and establish a novel mechanism of extracellular membrane organization based on the compartments of the membrane that a receptor is able to explore. Our work underscores the important and complex role of surface glycans regulating cell membrane organization and interaction with downstream partners.

This work has been published as J.A. Torreno-Pina*, B.M. Castro*, C. Manzo, S.I. Buschow, A. Cambi, M.F. Garcia-Parajo, "Enhanced receptor-clathrin interactions induced by *N*-glycan-mediated membrane micropatterning", *Proc. Natl. Acad. Sci. U S A* **111**, 11037 (2014). * Equally contributing authors.

Introduction

Glycans are fundamental cellular components ubiquitously present in the extracellular matrix and cell membrane as glycoproteins or glycolipids. Glycan-binding proteins such as galectins, siglecs and selectins are mostly multivalent and thus thought to crosslink glycoproteins into higher order aggregates, creating a cell surface glycan-based connectivity also called glycan lattice or network (1-3) (Fig. 4.1). In the case of the galectins, there are 3 major groups that are classified according to their structure in mammals: proto-type, tandem-repeat type and chimera-type galectins (4). The first two type of galectins comprise 14 out of 15 different galectins which have been identified so far. Proto-type galectins contain 1-2 identical carbon recognition domains (CRD) whereas tandem-repeat galectins consist of two homologous CRDs that are interconnected by a protein residue. Galectin-3 has been classified as chimera-type galectin and has the unique properties of containing one CRD at the carboxy-terminus and a non-lectin region at the N-terminal region prone to multimerization. Galectins bind predominantly to glycoproteins containing *N*-acetyllactosamine residues (5). Moreover, different specificity among the galectin family is achieved through the different binding affinities to branched N-glycans (6).

Galectin-9 belongs to the family of tandem repeat-type galectins and consists of two homologous CRD which bind to *β*-galactoside (7). It is expressed in the extracellular milieu, the cytosol and in the nucleus (8). Galectin-9 has been associated to immunosuppressive activities such as exhausting activated T_H1 cells by binding to Tim-3 on their cell membrane (9). Moreover, the association of Galectin-9 to Tim-3 has been shown to reduce HIV- infection of activated CD4-T cells by down-regulating HIV coreceptors such as CCR5 (10). Another prominent binding molecule of Galectin-9 is the highly glycosylated glycoprotein CD44. It has been shown that Galectin-9 binding to CD44 prevents CD44-HA (hyaluronan) interactions imparing the infiltration of activated T cells into the airway in the context of allergic asthma in mice (11). Recently, it was also proposed that the co-binding of CD44 to Galectin-9 and TGF-β receptor promotes the expression of the iTreg master transcription factor Foxp3 and Galectin-9 in a feedforward loop (12). In the context of DC-SIGN, it has been shown that Galectin-9 and CD44 are recruited to the DC-SIGN highly enriched DC-phagosome, suggesting a multicomponent interaction on the cell membrane mediated by a glycan-based connectivity (13) regulating DC-SIGN mediated endocytosis. Thus, the interaction between Galectin-9 and CD44 serves as an excellent example of how glycoproteins interact and control downstream processes by means of a galectin-glycan lattice.

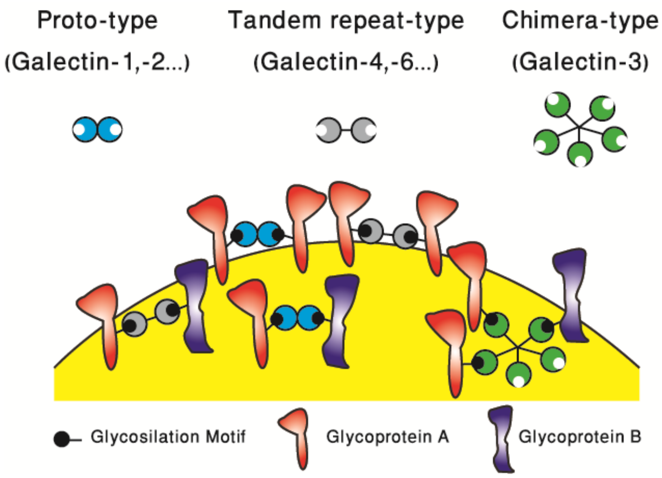

Figure 4.1 Galectins crosslink different glycosylated proteins on the cell membrane thereby creating a lattice that regulates the lateral behavior of membrane receptors. The different binding to multiple potential glycoproteins is ultimately defined by the specific glycan-protein affinities.

Based on their capability of modulating the lateral behavior of molecules on the cell membrane, several functions have been attributed so far to these galectin-glycan lattices such as regulating signaling thresholds of e.g. T-Cells or controlling cell membrane receptor residency time at the cell surface (14). In the context of T-Cell signaling, the galectin lattice has been proposed to have an opposing role to the actin cytoskeleton in laterally segregating CD45 and the T-Cell receptor (15). Moreover, it has been shown that the galectin lattice prevents TCR microclustering reducing the probability of T-Cell activation (15). On the other hand, how a glycan-based connectivity could coordinate cell membrane residency time of receptors was studied for the EGF receptor (16, 17). By means of FRAP, it has been suggested that cell surface glycan-based interactions restrict EGFR dynamics and localization into membrane regions away from endocytic platforms (16, 17). This could be seen as an example of how by concentrating specific glycoproteins or glycolipids while excluding other cell surface molecules, surface glycan-based connectivity can organize the plasma membrane into specialized domains that perform unique functions (1,3,18-20). Nevertheless, direct observation of glycan-mediated ligand crosslinking in living cells remains challenging (21, 22). Moreover, visualization of receptor interactions with the endocytic machinery under the influence of the glycan network has not yet been attained.

Clathrin-mediated endocytosis (CME) constitutes the primary pathway of cargo internalization in mammalian cells regulating the surface expression of receptors (23). Formation of clathrin-coated pits (CCPs) starts by nucleation of coat assembly at distributed positions in the inner surface of the plasma membrane where it continues to grow or dissolve rapidly unless coat stabilization occurs (24, 25). One event that clearly correlates with successful CCP stabilization is cargo loading (25). Recent studies show that cargo molecules diffuse randomly on the cell membrane until they meet growing CCPs, with the extent of cargo interactions regulating CCP maturation (26). As such, factors that affect cargo mobility within/at the cell surface will inevitably impact on CCP maturation and successful internalization. In the context of surface glycan-protein interactions, it has been shown that glycoproteins with an intact glycan-based connectivity exhibit reduced lateral mobility and this correlates with compromised endocytosis (3, 16, 17, 27-29). However, this has been shown in ensemble-type of measurement with poor spatial and temporal resolution.

This Chapter describes the application of super-resolution nanoscopy and dual-color single particle tracking (SPT) approaches to visualize the impact of glycan-based interactions on the spatiotemporal organization and clathrin interaction of DC-SIGN. DC-SIGN contains a single *N*-glycosylation site, organizes in nanoclusters at the cell membrane (30-33) and internalizes bound antigens via CPPs for subsequent processing and presentation to T-cells (34-37). Our work provides new insights on how surface glycan-mediated interactions tune spatiotemporal micropatterning of receptors on the cell membrane, potentially regulating interactions with the endocytic machinery and underscoring the importance and complex role of surface glycans on cell membrane organization and function.

Results

Glycan-based interactions do not affect DC-SIGN nanoclustering. It has been described that glycan-binding proteins crosslink surface glycoproteins into higher order oligomers (1, 2, 18, 19). Since DC-SIGN forms nanoclusters on the cell surface and has a single *N*-glycosylation site (30, 31-33), we first investigated the role of *N*-glycosylation on the nanoscale organization of DC-SIGN using stimulated emission depletion (STED) nanoscopy. We used CHO cells stably expressing wild-type DC-SIGN (wt-DC-SIGN) and a receptor variant presenting a point mutation within the DC-SIGN *N*-glycosylation motif (denoted as N80A), known to prevent receptor glycosylation (38). This cell system recapitulates DC-SIGN essential activities, such as antigen binding, internalization and trafficking (33, 35, 36). We first performed FACS analysis to confirm that the expression levels of wt-DC-SIGN and the N80A mutant were similar (Fig. 4.2).

STED images on fixed immuno-labeled cells expressing either wt-DC-SIGN or N80A

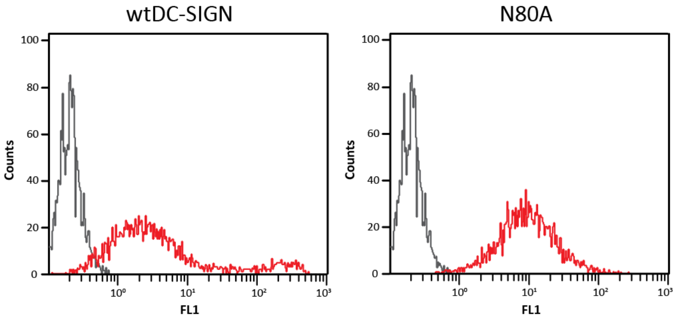

Figure 4.2 Cell surface expression levels of wt-DC-SIGN and N80A mutant on stably transfected CHO cells as determined by FACS analysis. The *black histogram* represents the isotype control and the *red histogram* indicates the specific staining with anti-DC-SIGN Ab (DCN46). Note that both cell lines have comparable expression levels of the receptor.

showed well-separated bright fluorescent spots (Fig. 4.3A, upper row). Spot size distributions were generated from multiple super-resolution images (Fig. 4.3B). As a control for impaired nanoclustering, we include the spot size distributions obtained for a DC-SIGN mutant lacking the neck region (ΔRep), known to abrogate nanoclustering as shown in the previous Chapter (33, 38). Interestingly, the spot size distributions for wt-DC-SIGN and N80A are similar, with average values around 160nm, in agreement with previously reported wt-DC-SIGN values (31, 33) and significantly larger than for ΔRep. We also generated fluorescence intensity distributions of DC-SIGN spots (Fig. 4.3C). Considering that antibodies typically bind to 1-2 antigens, an average of 5-10, 6-12 and 1-3 molecules/spot were obtained respectively for wt-DC-SIGN, N80A and ΔRep. These results thus show that glycosylation does not significantly affect DC-SIGN nanoscale organization on CHO cells.

Similar experiments were performed on imDCs (Fig. 4.3A lower row). Quantitative analysis confirms DC-SIGN nanoclustering on imDCs (Fig. 4.3B,C) with an average density of 3.5-7 molecules/nanocluster, in agreement with previous results (30-33). To test the effect of cell surface glycan-mediated interactions on DC-SIGN nanoclustering, we treated imDCs with lactose. Lactose impairs cell surface glycan-based connectivity promoted by galectins, by competing with their major ligands, branched *N*-linked protein glycans, dissociating bound galectins from the cell surface (16, 17, 39). Although lactose treatment highly reduced the surface levels of galectin-9 and -3 on imDCs (Fig. 4.4), it had no effect on DC-SIGN nanoclustering (Fig. 4.3B,C). These results indicate that DC-SIGN nanoscale organization is independent on the glycosylation state of the receptor and/or on glycan-based interactions at the cell surface.

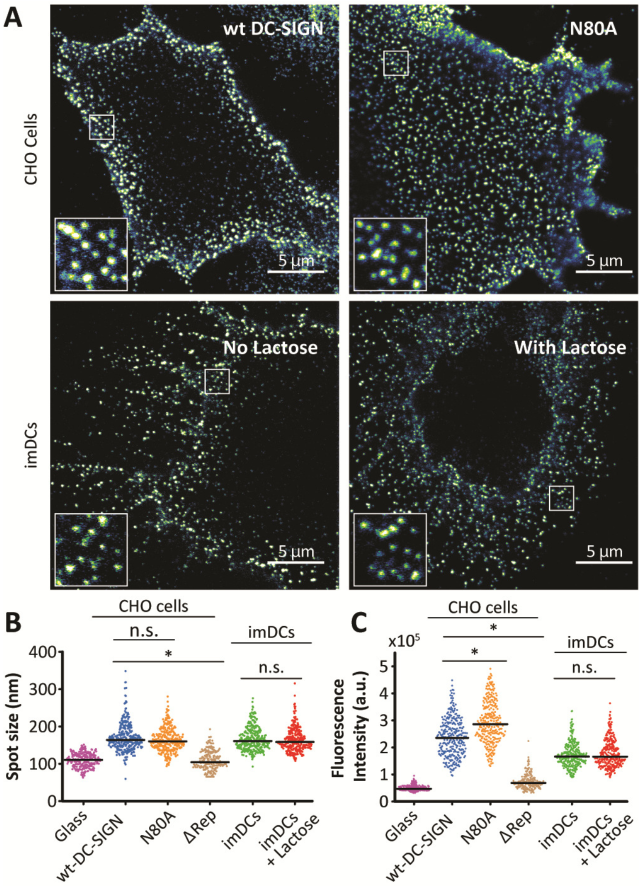

Figure 4.3 DC-SIGN nanoclustering is independent on its glycosylation motif. (**A**) Upper row: Representative STED images of wt-DC-SIGN (left) and N80A (right) on CHO cells. Lower row: DC-SIGN on imDCs (left) and on imDCs treated with 200 mM lactose (right). A magnified view of the receptor nanoclusters for each case is shown in the insets. Spot size (**B**) and normalized intensity distributions (**C**) of all fluorescent spots for each experimental condition, including data from the ΔRep mutant. 300 spots obtained from multiple STED images at each experimental condition. Data from individual Abs non-specifically attached to glass are also shown in (B) and (C) to illustrate the spatial resolution of STED (*ca.* 110nm) and sensitivity for single Abs detection respectively. Statistical significances were obtained with two-tailed Student's t -test. * $p < 0.05$; n.s. no significant.

DC-SIGN glycosylation does not influence nanocluster interactions in living cells. To capture potential effects of glycan-based interactions on DC-SIGN nanoclustering in living cells we applied dual-color SPT. We labeled DC-SIGN using two different quantum dots (QD) at concentrations such to increase the probability of capturing nanocluster interaction events in case they would occur, while allowing for the recording of individual trajectories (see also Chapter 2 for details). Examples of such 2 dimensional trajectories of spatially close QDs (green & red) for wt-DC-SIGN and the

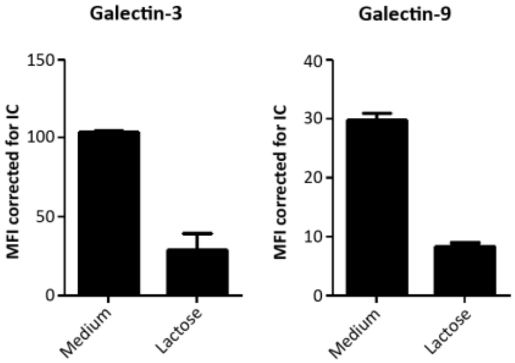

Figure 4.4 Mean fluorescence intensity (MFI) of imDCs labeled for cell surface galectin-3 (left) and galectin-9 (right) in the absence and presence of 25mM of lactose. The significant decrease in MFI after cells treatment with lactose indicates that galectins 3 and 9 surface levels of these cells have been highly reduced.

N80A mutant are shown in Fig 4.5. Fig. 4.6A also shows as example snapshots of two wt-DC-SIGN nanoclusters that are initially spatially close to each other, as a function of time. To calculate the separation distance between close QDs we exclusively focused on (green & red) QDs that were initially separated by a distance equal or below 400 nm (see also methods for a detailed explanation on how the interparticle distance separations were obtained). Two examples of the interparticle distance separation for wt-DC-SIGN & the N80A mutant are shown in Fig. 4.6B. In the case of interacting nanoclusters, dual color trajectories should exhibit correlated motion with separation distances between QDs close to or below 160nm which corresponds to the average nanocluster size as shown in Fig. 4.3. We then measured the times during which the separation distances remained below 160 nm and compared them to simulations of randomly encountering particles (40). We did this by generating in-silico close-by trajectories of randomly diffusing particles and determined the average times at which their mutual distances remained ≤ 160nm due to stochastic encountering. For generating these trajectories we took into account the diffusion coefficients of both wt-DC-SIGN and N80A mutant. The experimental and simulation results are shown in Fig. 4.6C and show that the average "interaction" times of wt-DC-SIGN and N80A nanoclusters are similar to those obtained from simulations of random encountering, demonstrating the absence of dynamic interactions between wt-DC-SIGN or N80A nanoclusters.

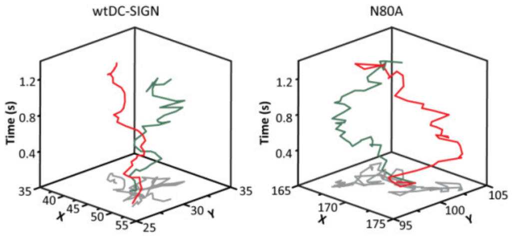

Figure 4.5 DC-SIGN nanoclusters trajectories do not show evidence for correlated motion. Representative 2D trajectories as a function of time for wt-DC-SIGN and N80A nanoclusters labeled with single chain DCN46-QD585 (green) or QD655 (red) on the upper surface of CHO cells.

Interestingly, the large majority of wt-DC-SIGN nanoclusters remained proximal to each other within a separation distance of ~1 μm, while larger values were observed for N80A (Fig. 4.6D, dashed line). To assess whether these observations bear physical si-

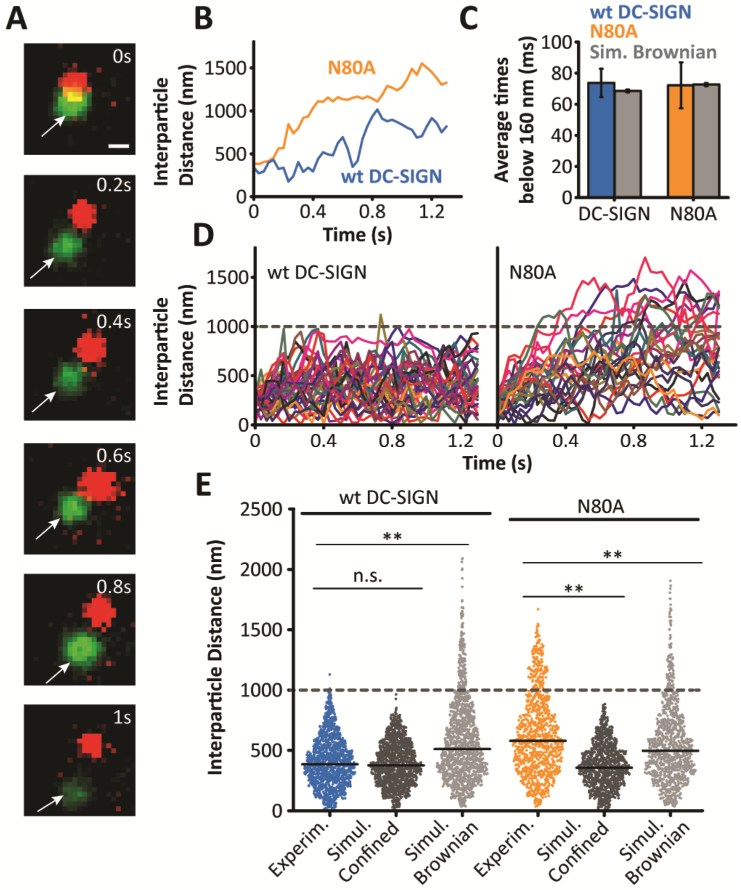

Figure 4.6 DC-SIGN glycosylation does not influence nanocluster interactions in living cells**.** (**A**) Sample time series of two DC-SIGN nanoclusters labeled with either green (585) or red (655) QDs, spatially close in time (white arrows). (**B**) Two examples of interparticle distances *vs*. time for two pairs of seemly closed QDs. Blue curve for two proximal wt-DC-SIGN nanoclusters, and orange curve for N80A. (**C**) Average times at which couples of QDs (green and red) remain below 160 nm. Experimental results are contrasted with simulations of Brownian diffusing particles (grey bars). Experimental data correspond to 32 and 26 pairs of QDs for wt-DC-SIGN and N80A respectively. Simulated data correspond respectively to 6400 and 5200 pairs of randomly coincident interactions for wt-DC-SIGN and N80A. (**D**) Interparticle distances *vs*. time for wt-DC-SIGN and N80A. (**E**) Interparticle distance distributions as obtained for wt-DC-SIGN and N80A and compared to simulated data of Brownian (light grey) or confined (to a 1 μm area, dark grey) particles. 1360 and 1040 occurrences for wt-DC-SIGN and N80A respectively, over 15 movies from different cells. $^{**}p < 0.01$; n.s. no significant.

gnificance, we generated interparticle distances histograms and compared the experimental data to simulations of freely- and confined-diffusion particles to a 1 µm region (Fig. 4.6E). As suspected, the experimental distribution for wt-DC-SIGN closely resembles the simulated distribution of confined diffusion, whereas the experimental distribution of N80A is closer to that of Brownian diffusion. wt-DC-SIGN confinement was also confirmed by direct analysis of long trajectories by means of their mean-square displacement (Fig. 4.7). These results indicate that *N*-glycosylation plays an important role in confining DC-SIGN nanoclusters at the meso-scale.

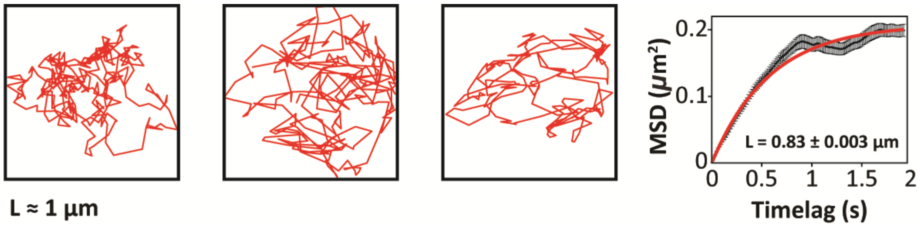

Figure 4.7 wt-DC-SIGN nanoclusters trajectories show restricted mobility within regions of ~1 µm. Three representative 2D trajectories of wt-DC-SIGN. The boxes around the trajectories are 1µm x 1µm in size and show wt-DC-SIGN diffusion in regions smaller than 1µm. Trajectories have been acquired at 60 frames/s. Trajectory length: 200 frames. The representative MSD plot on the right corresponds to one single trajectory exhibiting confinement to a region of 0.83 µm.

Glycan-based interactions enhance meso-scale compartmentalization of DC-SIGN. To directly visualize the micro-scale confinement of DC-SIGN, we generated dynamic membrane exploration maps using a method that combines nanometer-localization together with temporal information as obtained from SPT, and explained in detail in Chapter 2 (see also Fig. 4.8A). We found that glycosylated DC-SIGN nanoclusters are confined in meso-scale compartments, exploring only a fraction of the total cell membrane area (Fig. 4.8B, upper-row, left). Abrogation of DC-SIGN glycosylation relaxes the degree of confinement with receptors exploring larger surface areas (Fig. 4.8B, upper-row, right). Interestingly, comparable compartmentalization was obtained for DC-SIGN on untreated imDCs (Fig. 4.8B, lower-row, left), while treatment with lactose led to larger exploration regions (Fig. 4.8B, lower-row, right) qualitatively similar to those exhibited by N80A. To quantify these observations we analyzed the membrane exploration maps using a fixed grid box counting algorithm (Fig. 4.8C). A decrease on the normalized number of boxes containing at least one spatial localization event, with increasing box size was obtained for all cases (Fig. 4.8D). The curves were fitted using a double exponential decay indicating the existence of two spatially distinct compartments: a nanometer scale region, with values between 80-120 nm and a second meso-scale region with values between 1.3-1.6 μm (Table 1). Although the spatial scales of these two regions are similar for all cases, the relative occurrence of receptors being confined in meso-scale compartments differs significantly. Indeed, a larger percentage of receptors on cells with an intact glycan- based connectivity (wt-DC-SIGN-CHO or DC-SIGN on untreated imDCs) are confined at the meso-scale as compared to the case where these interactions are hindered (Fig. 4.8E).

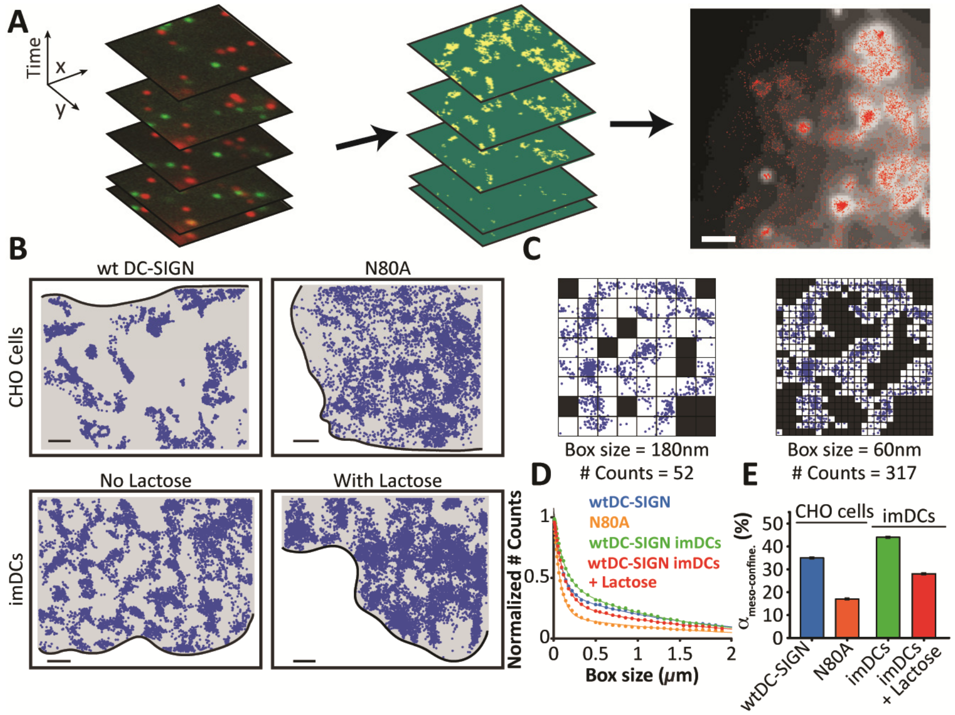

Figure 4.8 Membrane explorations maps reveal glycan-mediated confinement of DC-SIGN at the meso-scale. (**A**) Scheme illustrating how membrane exploration maps of DC-SIGN are generated from dual-color SPT movies at high labeling-densities, and example of such a map overlaid with the fluorescence image. (**B**) Representative membrane exploration maps for wtDC-SIGN and N80A on CHO cells (8000 localizations/map, 30 frames/s), and DC-SIGN on untreated and lactose-treated imDCs (10000 localizations/map, 30 frames/s). Each blue point corresponds to a localization event. Grey background corresponds to the cell surface area. Black contour lines delineate the edges of the membrane (scale bars – 400 nm). (**C**) Implementation of the fixed grid box-counting algorithm. Boxes of decreasing sizes are used and the # of boxes containing at least one localization event is recorded. (**D**) Normalized number of boxes containing at least one spatial localization event *vs.* box size. The solid lines are the fit to the data using a double exponential decay function. (**E**) Degree of meso-scale compartmentalization (expressed in %), as extracted from the weight coefficient of the second exponential decay (Table S1). Error bars represent the error on the fitting.

Cells	**CHO**		**imDCs**	
	wt-DC-SIGN	**N80A**	**No Lactose**	**With Lactose**
α	0.65 ± 0.03	0.83 ± 0.02	0.56 ± 0.02	0.72 ± 0.01
S_1 (nm)	87 ± 4	77 ± 3	116 ± 7	107 ± 4
(1- α)	0.35 ± 0.03	0.17 ± 0.02	0.44 ± 0.02	0.28 ± 0.01
S_2 (nm)	1540 ± 90	1610 ± 180	1310 ± 70	1540 ± 100

Table 1 Fitting parameters of the membrane exploration maps box counting analysis as obtained using Equation 1.

Collectively, these results demonstrate that glycan-based connectivity restricts DC-SIGN nanocluster mobility to micron-size regions of the membrane.

Glycan-based meso-scale compartments correlate with regions enriched in clathrin. Cell surface glycan-based interactions are thought to increase signaling and residence time of the EGFR by recruiting the receptor away from caveolae (16). Since DC-SIGN internalizes via CCPs (34, 35, 36) we investigated whether the glycan-based meso-scale confinement exhibited by DC-SIGN influences its interaction with clathrin. We performed SPT on CHO cells co-transfected with either wt-DC-SIGN or N80A, and clathrin light chain (CLC)-YFP (Fig. 4.9A) and generated membrane exploration maps of wt-DC-SIGN or N80A superimposed to the CLC-YFP signal (Fig. 4.9B). Some observations are derived from these dual color maps: *a)* a more restricted surface exploration of wt-DC-SIGN compared to N80A, consistent with the data shown in Fig. 4.8B; *b)* a non-homogeneous distribution of clathrin over the cell surface, with well-defined clathrin-rich and clathrin-poor regions; *c)* importantly, glycosylated DC-SIGN preferentially partitions into clathrin-rich regions compared to its de-glycosylated counterpart.

To quantify these observations we generated histograms of the normalized CLC-YFP signal associated to each wt-DC-SIGN or N80A localization (Fig. 4.9C). Clearly, the distribution of wt-DC-SIGN localizations is shifted to higher clathrin signal values confirming that wt-DC-SIGN resides closer to clathrin. To substantiate these results we calculated the difference between the normalized frequency of localizations of wt-DC-SIGN and N80A at each value of the normalized clathrin signal (Fig. 4.9D). For clathrin

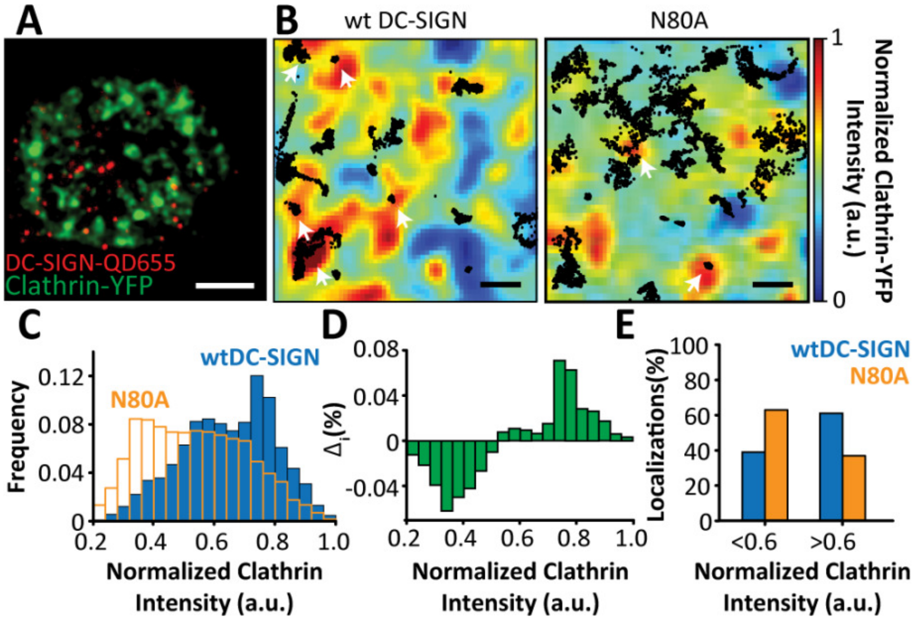

Figure 4.9 Glycan-based meso-scale compartments correlate with regions enriched in clathrin. (**A**) Still frame of a dual-color SPT movie taken in TIRF geometry showing individual DC-SIGN-QDs (red) overlaid with the clathrin-YFP signal (green) on the surface of a CHO cell (Video S2). Scale bar 5 µm. (**B**) Membrane exploration maps of wtDC-SIGN and N80A overlaid with the normalized CLC-YFP image. Black points correspond to individual localizations of wtDC-SIGN or N80A (≈12500 localizations/map). Arrows highlight localizations close to clathrin rich regions. Scale bars: 200 nm. (**C**) Distribution of the normalized CLC-YFP intensity associated to each localization of wtDC-SIGN (blue) or N80A (orange) on CHO cells extracted from the exploration maps. To avoid false co-localization of the receptors with clathrin due to background, only localizations associated to clathrin-YFP intensities ≥ 0.2 were considered. (**D**) Difference between the normalized frequency of localizations of wtDC-SIGN and N80A as function of the normalized clathrin signal. (**E**) Total percentages of wtDC-SIGN and N80A localizations associated to the normalized clathrin-YFP fluorescence signal for values < 0.6 and > 0.6 as extracted from C. At least 30000 localizations from 6 cells from different days at each experimental condition.

signals ≤ 0.55 the residuals are negative so that N80A localizations are dominant. Above 0.55 the residuals are positive and thus dominated by wt-DC-SIGN localizations. To account for the total percentage of localizations we separated the distributions in two subpopulations according to the clathrin signal, *i.e.*, clathrin-poor (signals < 0.6) and clathrin-rich (signals ≥ 0.6) regions. We found that ≈60% of wt-DC-SIGN localizations reside in clathrin-rich regions, whereas this percentage reduces to ≈40% for N80A localizations (Fig. 4.9E). These results thus show that DC-SIGN glycosylation enhances its meso-scale compartmentalization in regions of the cell membrane, which are enriched in clathrin.

Meso-scale compartmentalization influences nanoscale transient confinement of DC-SIGN. Next, we investigated the impact of DC-SIGN meso-scale compartmentalization on its nanoscale dynamic behavior. We performed SPT of DC-SIGN nanoclusters on CHO cells (wt-DC-SIGN and N80A), and on untreated and lactose-treated imDCs. In all cases DC-SIGN nanoclusters were mobile (Fig. 4.10A). Moreover, we analyzed the trajectories to detect regions of transient confinement zones using an algorithm which calculate the probability that a diffusing particle stays a given time within a zone of a fixed radius depending on the instantaneous mobility of the diffusing particle (41) (see methods for a detailed description). Fig. 4.10A shows example of trajectories where transient confinement zones have been detected. We then extracted all the detected transient confinement zones belonging to all the trajectories and analyzed using a cumulative probability analysis of the squared displacements yielding an immobile and a mobile fraction. We took only the mobile fraction for further analysis. By fitting the mean square displacement of the mobile fraction of the data with a confinement curve, we obtained not only an average value of the diffusion coefficient but also the size of the confinement zone (Fig. 4.10B). In addition, we determined the characteristic duration of the TCZs and the average number of TCZs/area by fitting the data in each case with single exponential curves (Fig. 4. 10C-D). The membrane explored area is calculated from ellipses gyration that characterize each trajectory (42) and determining their gyration radius $R_g^2=R_x^2+R_y^2$, where R_i is the maximum trajectory displacement in the x and y coordinates.

Although the average duration of the TCZs were roughly similar in all samples (Fig. 4.11A), the nanometer-scale TCZs sensed by DC-SIGN nanoclusters in unperturbed cells were larger in size compared to those found on the glycan-perturbed counterparts (Fig. 4.11B). Moreover, DC-SIGN diffusion coefficients inside TCZs were significantly larger in unperturbed cells compared to those obtained on N80A and on lactose-treated imDCs (Fig. 4. 11C). Finally, the TCZs surface density, *i.e.*, number of TCZs/area, was lower on cells with an intact DC-SIGN glycan-based connectivity compared to those where these interactions have been disturbed (Fig. 4. 11D), in nice correlation with the restricted surface exploration maps shown in Figure 4.8. Altogether, these results indicate that the meso-scale organization brought about by glycan-interactions influence the TCZs encountered by DC-SIGN and further support the existence of different mechanisms responsible for the occurrence of TCZs.

***N*- glycosylation enhances DC-SIGN clathrin interactions.** Based on our data, we further questioned whether: *a)* the detected TCZs might correspond to dynamic interactions of DC-SIGN with clathrin and *b)* glycan-based connectivity would impact on DC-SIGN-CCP interactions. To address these questions we analyzed DC-SIGN trajectories on double transfected cells (wt-DCSIGN or N80A and CLC-YFP) for the presence of TCZs and quantified their proximity to clathrin (Fig. 4.12A). Strikingly, ~ 80% of wt-DC-SIGN-TCZs were located inside or in the proximity to clathrin-rich areas, while this percentage decreased to ~ 40% for N80A (Fig. 4.12B).

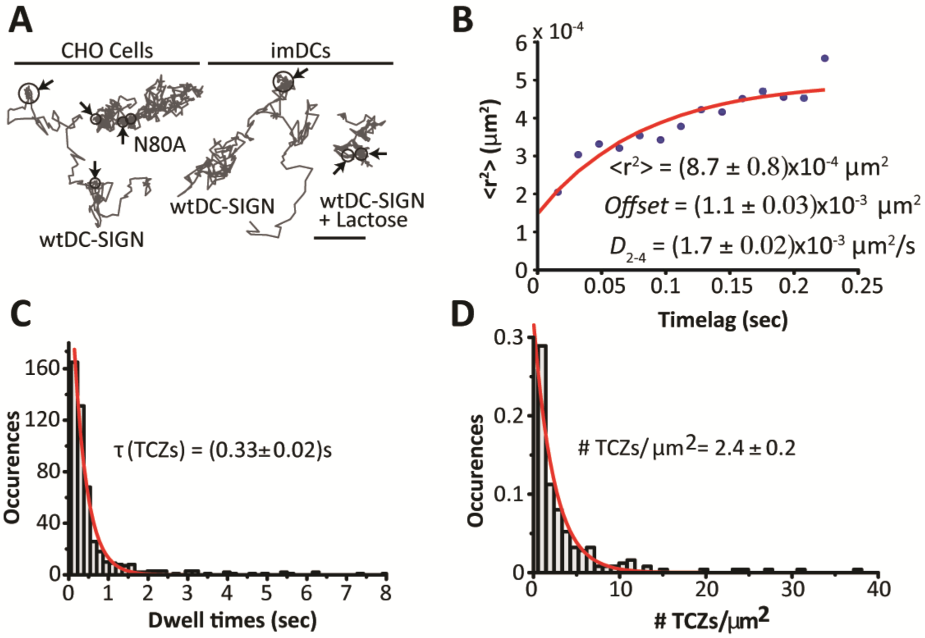

Figure 4.10 Representative analysis of detected transient confinement zones of DC-SIGN trajectories. **(A)** Representative trajectories of wt-DC-SIGN and N80A on CHO cells, and DC-SIGN on untreated and lactose-treated immature DCs. Regions of TCZs are detected and shown in circles and highlighted by arrows. Scale bar 400 nm. (**B**) Average MSD analysis of the mobile fraction of TCZs obtained by means of a cumulative probability analysis of r^2. The average diffusion coefficient *inside* TCZs is given by the fit parameter $D_{2\text{-}4}$. The average size of the TCZs was determined from the fit according to Equation 3. (**C**) Characteristic duration of the TCZs as extracted from the exponential fit (red line) of the histogram of the duration of each TCZs (**D**) Average number of TCZs/membrane area as retrieved from the exponential fit (red line) of the #TCZs/area histogram built from each trajectory containing at least one TCZ.

We further analyzed the TCZs with respect to their proximity to clathrin, both for wt-DC-SIGN and N80A. The majority of the N80A-TCZs occur outside clathrin with diffusion values (Fig. 4.12C) similar to those shown in Fig. 4.11C and D, indicating that these TCZs bear no relation to clathrin. In remarkable contrast, wt-DC-SIGN-TCZs inside clathrin showed similar characteristics as those found for DC-SIGN with intact glycan- based connectivity (compare Fig. 4.11C and D with 4.12C and D), revealing that dynamic interaction with clathrin leads to the transient arrest of DC-SIGN.

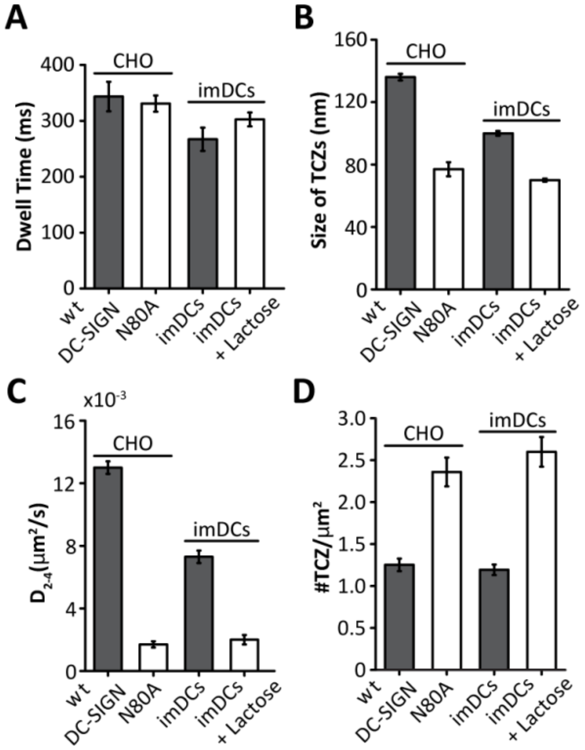

Figure 4.11 Meso-scale compartmentalization influences nanoscale transient confinement of DC-SIGN. (**A**) Average duration of TCZs. (**B**) Average size of the TCZs. (**C**) Average diffusion inside TCZs. (**D**) Average number of TCZs/area. Error bars correspond to the errors on the fitting. wt-DC-SIGN: 283 TCZ on 755 trajectories. N80A: 483 TCZ on 614 trajectories. ImDC: 293 TCZ on 171 trajectories. ImDC+lactose: 107 TCZ on 155 trajectories. Minimum of 50 cells from 10-20 separate experiments at each condition.

Regrettably, the poor transfection efficiency (<5%) and low cell viability of transfected imDCs prevented analogous studies on these cells. Importantly, these data imply that DC-SIGN-CCP interactions do not occur by random encounters between mobile receptors and CCPs. Instead, DC-SIGN micropatterning in regions enriched in clathrin, brought about by the glycan network, favors cargo-clathrin encounters. Interestingly, N80A-TCZs events proximal to clathrin showed similar diffusion as to those of wt-DC-SIGN- TCZ (Fig. 4.12C,D) indicating that glycosylation does not interfere on the dynamics of the interaction itself, but it affects the probability with which these interactions occur.

To investigate the consequences of DC-SIGN glycosylation on antigen internalization via clathrin-dependent endocytosis we used QDs conjugated with gp120, an HIV-1 envelope protein recognized and internalized by DC-SIGN, resulting in DC infection with HIV-1 virus (Fig. 4.12E and F). CHO cells expressing either wt-DC-SIGN or the N80A mutant and imDCs untreated or treated with lactose were incubated at 37 ºC with gp120-QDs. After particle binding and internalization, cells were fixed and labeled for clathrin and its degree of co-localization with gp120-coated QDs was determined. In all cases, internalization of single virus-like particles could be detected. However, the degree of co-localization between gp120-QDs and clahtrin was markedly different: cells with an intact glycan-based connectivity showed higher co-localization values compared to those where this connectivity has been compromised (Fig. 4.12F). Collectively, our data reveal that glycan-based interactions promote meso-scale

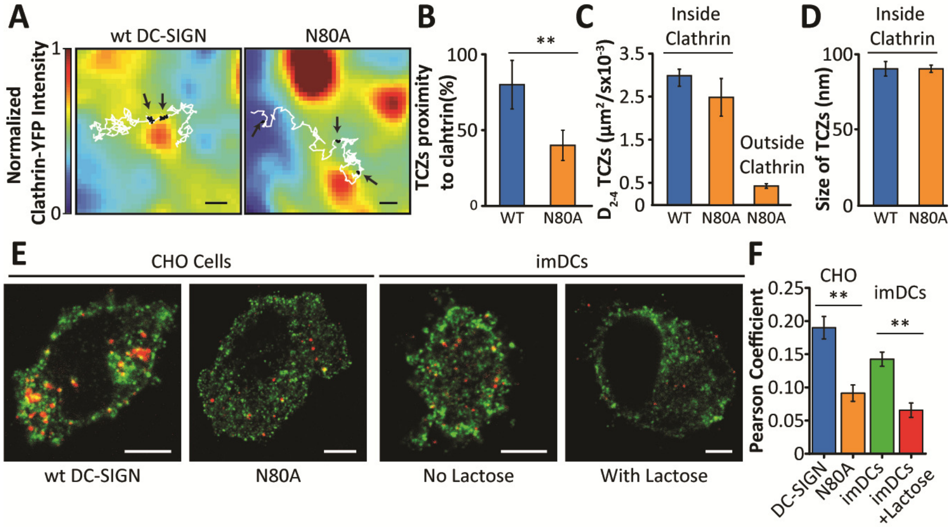

Figure 4.12 *N*-glycosylation enhances DC-SIGN clathrin interactions and virus-like particle internalization via CCPs. (**A**) Representative wt-DC-SIGN and N80A trajectories (white lines) overlaid on the normalized CLC-YFP image. Black points (highlighted with arrows) show the occurrence of TCZs (Video S3). Scale bars: 400 nm. (**B**) Percentage of TCZs near to clathrin-rich areas for wt-DC-SIGN and N80A. Since clathrin images are diffraction-limited we considered clathrin-rich regions as those having intensity > 0.7. Data from at least 8 cells from different days. ** $p < 0.01$ (**C**) D_{2-4} inside TCZs for wt-DC-SIGN and N80A, in relation to clathrin proximity. Due to the low number of wt-DC-SIGN-TCZ events outside clathrin we could not determine D_{2-4} values here. (**D**) Sizes of TCZ inside clathrin. Error bars in C & D correspond to the error on the fitting (Fig. 4.10). (**E**) Merged confocal microscopy images of internalized gp120-QD (red) and CCPs (green) on CHO cells expressing wt-DC-SIGN or N80A, and on untreated and lactose-treated imDCs. Images represent one focal plane in the middle of the cell body. Representative cells from multiple experiments are shown. Scale bars: 5 µm. (**F**) Pearson correlation coefficient between gp120-QD and clathrin. Values ± SEM are average of multiple images from several cells from different days of experiments .** $p<0.01$.

compartmentalization of DC-SIGN thereby fine-tuning the occurrence of dynamic interactions with clathrin and possibly enhancing CME of antigens bound to DC-SIGN.

We then sought to address the potential candidates of the glycan-network which could be regulating the spatiotemporal behavior of DC-SIGN on the cell membrane at the meso-scale. Since Galectin-9 and CD44 were enriched in the DC-SIGN phagosome (13), we studied by means of confocal microscopy wether Galectin-9, CD44 and DC-SIGN would also colocalize at the plasma membrane of immature dendritic cells (Fig. 4.13). Using copatching with secondary Abs, we obtained a significant colocalization of DC-SIGN with CD44 at the cell membrane (Fig. 4.13A). Galectin-9 also showed colocalization with CD44 (Fig. 4.13B). Remarkably, DC-SIGN also colocalizes with Galectin-9 at the cell membrane (Fig. 4.13C). The degree of colocalization between these molecules were quantified using the Pearson correlation coefficient revealing higher colocalization between CD44, Galectin-9 and DC-SIGN than the control case of the transferrin receptor (known to bind to Gaectin-3, reference) colocalizing with Galectin-9 (Fig. 4.13D). Thus, the copatching data suggests that there might be some pre-interaction between DC-SIGN, Galectin-9 and CD44 already at the cell membrane that can potentially be mediated by a glycan-based connectivity.

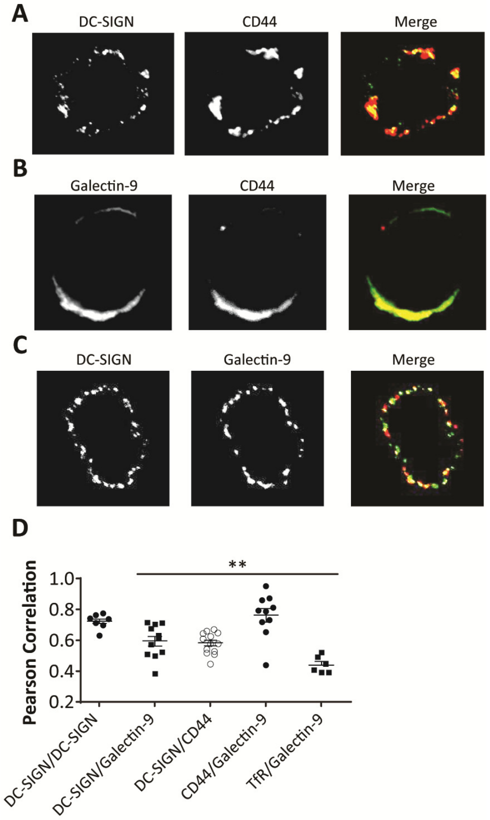

Figure 4.13 DC-SIGN colocalizes with galectin-9 and CD44 on the plasma membrane of imDCs. Panels A, B and C show representative confocal sections of imDCs subjected to copatching for the indicated combinations of antibodies against DC-SIGN, CD44 and Galectin-9. Figure D shows de degree of co-localization quantified by the Pearson correlation coefficient. Individual dots represent single cells from DCs of 2 different healthy donors. **p<0.01 as determined by an unpaired two tailed students t-test.

To gain insight on how this machinery might be laterally assembled, we generated dual-color cartography maps of CD44 and DC-SIGN on the cell membrane of imDCs (Fig. 4.14A). Zoom-in cartography regions reveal that CD44 explores regions enriched by DC-SIGN as well as regions that are spatially contiguous to DC-SIGN (Fig. 4.14B).

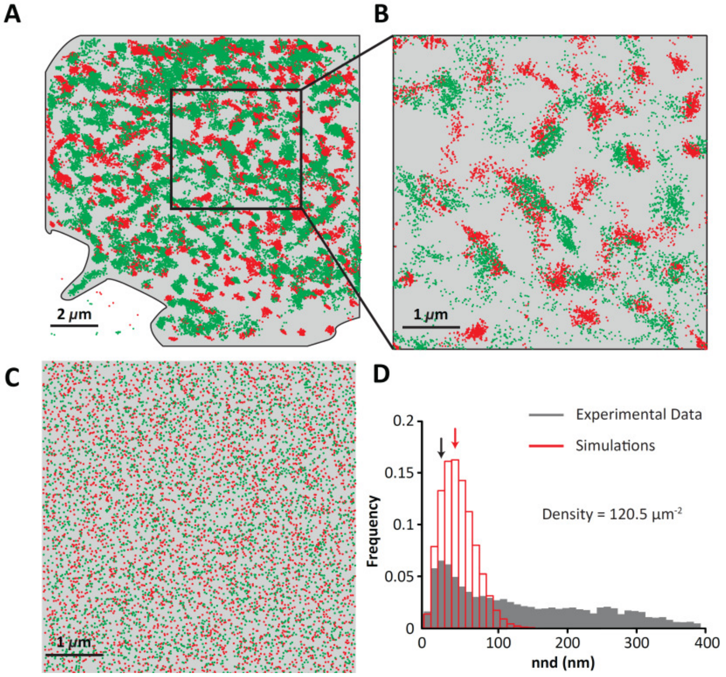

Figure 4.14 Spatiotemporal exploration of DC-SIGN and CD44 on the cell membrane of imDCs. (**A**) Dual color membrane cartography map of CD44 labeled with QD655 (red) and DC-SIGN labeled with QD585 (green) obtained on live day 6 imDCs. Cells were incubated on glass coverslips and CD44 and DC-SIGN were labeled with QD655-Ab (NKI-P2, NKI) and QD585-Ab (DCN46, Pharmingen) respectively. Dual-color imaging was performed with split channels imaged on the same chip of an EM-CCD Camera at a time resolution of 30 Hz and a total observation time of 13.3 s. 42000 localizations of CD44 (red) and DCSIGN (green) are displayed representing each one a localization event over the total observation time. (**B**) Zoom-in region displaying 4000 localizations of CD44 (red) and DCSIGN (green) on an area of 5.76 x 5.76 um collected over the total observation time. Note that CD44 explores regions enriched by DC-SIGN as well as regions that are spatially contiguous to DC-SIGN. (**C**) Simulated 2D plot of 4000 red particles and green particles randomly distributed 5.76 x 5.76 µm area. (**D**) Quantification of the nearest-neighbor distance (nnd) between red and green occurrences for the experimental and simulated data.

These results suggest that CD44 might work as a fence, delimiting the membrane regions that DC-SIGN is able to explore. Moreover, the lateral behavior of both molecules is restricted within regions of approximately 1 µm which is in excellent agreement with the meso-scale organization shown for DC-SIGN in Fig. 4.8. Monte-Carlo simulations of random organization of the two molecules (Fig. 4.14C) reveal that the maximum (black arrow) of the distribution of the nearest-neighbor distance (nnd) is shifted towards lower nnd values with respect to the simulated data (red arrow) (Fig. 4.14D), indicating true physical partitioning between CD44 and DCSIGN at the nanoscale. Interestingly, the experimental nnd distribution also shows a long tail, clearly deviating from random organization and strongly evidencing a spatiotemporal relationship between these two glycoproteins at characteristic spatial distances. Since copatching experiments show colocalization of Galectin-9 with CD44 and DC-SIGN at the level of the cell membrane, it is tempting to speculate at this stage that Galectin-9 might regulate the lateral organization between CD44 and DC-SIGN resulting in the confinement of DC-SIGN in micron-scale regions.

Discussion

In this work we directly visualize cell membrane micropatterning mediated by glycans using a combination of super-resolution imaging techniques and dual color single particle tracking. We find that this micropatterning corrals receptors into clathrin enriched regions, thereby increasing clathrin-receptor interactions, and potentially influencing clathrin-mediated endocytosis of receptor-bound ligands. We also establish that clathrin-receptor encounters do not occur in a random fashion and further substantiate the dynamic and transient behavior of clathrin interactions with their cargo before successful internalization.

Cell surface glycan-mediated interactions have been thought to promote the formation of high-order aggregates of several membrane proteins (1-3, 19). Contrasting with these expectations, one of the key observations of our work is that glycan-mediated interactions do not contribute to receptor nanoclustering, neither promote dynamic interactions *between* nanoclusters. However, the overall lateral mobility was considerably affected, with glycosylated DC-SIGN nanoclusters dynamically exploring restricted areas of the cell surface. These results demonstrate that glycan-based interactions regulate the micro-scale organization of the receptor and importantly, establish a novel extracellular mechanism of membrane organization based on the compartments of the membrane a molecule is able to (or unable to) explore. Moreover, our results indicate that these interactions are mediated (directly or indirectly) by cell surface galectins. Indeed, treatment of imDCs with lactose drastically affected the spatial exploration of the receptor and reduced galectin-9 surface levels (Fig. 4.4), an important glycan-binding protein found on imDCs phagosomes together with DC-SIGN and the transmembrane glycoprotein CD44 (13).

An interesting finding of our work is that glycan-based interactions seem fundamental in fine-tuning DC-SIGN interactions with clathrin, by confining the receptor in regions enriched with this endocytic protein. Remarkably, we observed that clathrin distribution is not homogenous but highly localized in permissive regions of the membrane, supporting earlier findings that indicated CCPs nucleation at predefined sites (25, 43). It has been further shown that these regions are specialized cortical actin patches that might efficiently organize CCP nucleations (43). How exactly glycan-based interactions sense these clathrin-rich regions is currently unknown. It is conceivable that there might be areas of the cell membrane enriched in actin where several key players colocalize in space and time, including CD44 (44) and clathrin (43). DC-SIGN could then be maintained in these regions through its interactions with CD44, most likely involving galectin-9, which would crosslink both proteins through their glycosylated motifs (Fig 4.14).

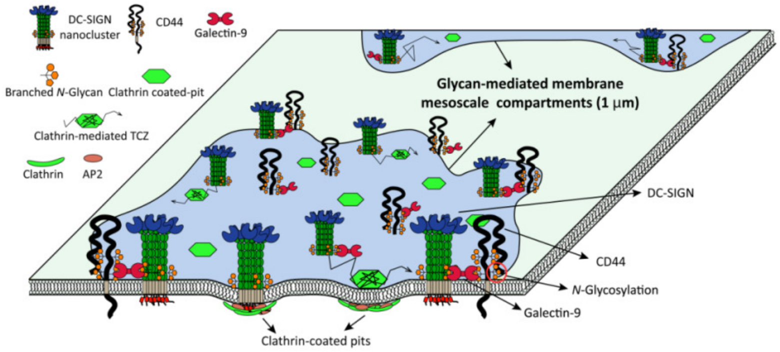

Figure 4.15 DC-SIGN glycan-mediated membrane mesoscale and nanoscale compartmentalization. DC-SIGN and CD44 interactions most likely involve their N-glycosylation motifs and cell surface galectin-9. This intricate molecular network results in DC-SIGN nanoclusters confinement to micrometer-size membrane regions (mesoscale confinement) enriched in clathrin, where the encounters of DC-SIGN nanoclusters with clathrin-coated pits (nanoscale transient confinement) are enhanced. Recent intriguing single molecule experiments have shown that CCPs do not permanently capture cargo molecules before internalization (26). Instead, cargos diffuse on the membrane until they randomly encounter CCPs and become transiently arrested in a “catch-and-release” fashion (26). Our results substantiate the dynamic and transient behavior of clathrin interactions with their cargo before successful internalization, and importantly extend these findings by showing that the spatial proximity of DC-SIGN to clathrin enhances the probability of successful cargo-clathrin interactions. Our data thus imply that CCP-cargo interactions do not proceed via random encountering but are greatly influenced by the micropatterning spatial regulation of the glycan network. Interestingly, receptor glycosylation does not affect the dynamical aspects of this interaction, suggesting that the rates of clathrin dependent endocytosis of DC-SIGN and its pathogenic ligands are not altered by glycosylation; merely the probability of encountering clathrin increases as compared to a purely random process.

Although this research is still ongoing in our lab, we have summarized our findings so far in an illustration (Fig. 4.15). CD44 would interact with DC-SIGN by means of one of its multiple glycosylation motifs. This interaction could be mediated by Galectin-9 which would temporally crosslink CD44 and DC-SIGN since Galectin-9 contains two homologous CRDs. This temporal crosslinking taking place along multiple CD44 over time results in DC-SIGN being confined to meso-scale regions on the cell membrane. Moreover, we also show that clathrin is enriched in those meso-scale regions building up a clathin-mediated endocytosis hotspot region. Thus, the glycan-based connectivity might possibly control clathrin-mediated endocytosis by controlling the spatiotemporal beavior of membrane receptors at multiple temporal and spatial scales.

In summary, the novel quantitative methods described in this thesis identify a novel mechanism of membrane organization and provide a visual and quantitative picture on how glycan-mediated interactions contribute with a new layer of complexity on the organization of the cell membrane. This meso-scale dynamic organization influences receptor interactions with clathrin, possibly impacting on CME but likely also influencing other cellular processes.

Materials & Methods

Single and dual-color SPT measurements. Experiments were performed using a home-made single molecule sensitive microscope, either under epi-fluorescence (single and dual color QDs measurements) or total internal reflection (TIRF) (dual color QD/clathrin measurements) excitation. Continuous excitation was provided by the 488-nm line of an Ar+ laser (0.3kW/cm2). Fluorescence was collected with a 1.4 NA oil immersion objective (Olympus) and guided into an intensified EM-CCD camera (Hamamatsu) after suitable filtering. Single QD movies were recorded at a frame rate of 30-60Hz. For dual-color measurements, emission light was split and selected with appropriate dichroic mirror and filters. Dual QD signals were collected by the same EM-CCD, whereas single QD and clathrin-YFP signal were recorded respectively by an EM-CCD and an intensified CCD camera. Movies frame rates were 30Hz for dual QD tracking, and 60Hz and 10Hz for QD and clathrin-YFP, respectively. Images of multi-fluorophore fluorescent beads (0.2 μm Tetraspeck, Invitrogen), having emission spectrum covering the two spectral windows were obtained to determine the spatial transformation leading to the overlay of the two spectral channels. To calculate the spatial transformation, at least 10 beads appearing on both channels were manually selected, their centroid positions calculated with subpixel accuracy and stored in two coordinate lists. The transformation matrix was inferred from the coordinate lists according to an affine transformation, correcting for displacement and small chromatic aberrations. Experiments were performed at 37ºC in 5% CO2 atmosphere. Trajectories were generated with Matlab routines based on an algorithm described in Serge et al. (45).

Stimulated Emission Depletion (STED) Nanoscopy. Confocal and STED images were obtained in a sequential manner using a 100x oil immersion objective (HCX PL APO 100x/1.4 Oil, Leica Microsystems, Germany) of a commercial CW-STED SP-7 microscope (Leica Microsystems, Germany) as described in Chapter 2.

Generation of time-dependent membrane exploration maps from SPT measurements. To quantify the differences between the exploration maps obtained for each experimental condition, we applied a box-counting algorithm. Coordinates maps were transformed into binary images with square pixels (box) at varying box sizes. Pixel values were set to one if at least one spatial coordinate was found within the pixel area and zero otherwise. The number of nonzero pixels over the total number of pixels ($n(box)$) was evaluated for each box size and fitted with a bi-exponential function:

$$n(box) = \alpha e^{\left(-\frac{box}{s_1}\right)} + (1-\alpha)e^{\left(-\frac{box}{s_2}\right)} \quad (1)$$

where α and $(1-\alpha) = \alpha_{\text{meso confinement}}$ are respectively the degree of the nanoscale and meso-scale compartments, *box* represents the pixel size and it is the size of the varying scan window and s_i are the characteristics length of nano- and meso-scale confinements. Results of the fitting for the different membrane exploration maps are shown in Table 1.

Membrane exploration maps of the receptors over clathrin fluorescence were gathered from single color SPT measurements of cells densely labeled with anti-DC-SIGN QD-conjugate, which have been previously transiently transfected with clathrin-YFP. For the duration of the SPT movies, the clathrin-YFP signal did not show any variation. Identification of single molecules in each movie frame was possible in these conditions, allowing the construction of single particle trajectories and their subsequent analysis. The distribution of the normalized clathrin-YFP intensity associated to each localization of wtDC-SIGN or N80A as generated by transforming the sub-pixel spatial coordinates of the receptor into a pixel with the same size as those of the clathrin-YFP images. To each pixel of the receptor localization, the corresponding clathrin-YFP signal was determined, and their distribution was obtained. To avoid false co-localization of the receptors with clathrin due to background, only localizations associated to clathrin-YFP intensities ≥ 0.2 were considered. The association of TCZs to clathrin-rich and -poor regions was done by comparing each TCZ localization with its respective clathrin-YFP signal. Since clathrin-YFP signal is diffraction-limited we used a normalized signal of clathrin ≥0.7 as the threshold to discriminate between both regions.

Identification of transient confinement zones (TCZs) and analysis. Transient confinement zones occurring within trajectories were detected by an algorithm described by Simson *et al.* (41). The algorithm identifies regions of the trajectory in which the receptor remains with duration considerably longer than a particle with a Brownian diffusion would. This is done by breaking the particle trajectories into shorter segments of successive points of variable length, and determining the likelihood that the receptor will remain in that segment according to its diffusion coefficient *D*. TCZs are considered when the average probability calculated for each point of the trajectory is higher than that of a random diffusing particle. For DC-SIGN and in our experimental conditions, the maximum segment S_m was 25 points, the probability level threshold L_c was 1.5 and the minimal time that DC-SIGN spends within a TCZ, t_c, was 133ms (8 frames).

We performed cumulative probability analysis to characterize the diffusion of DC-SIGN inside TCZs and to estimate the average size of the TCZs. Receptor square displacement (r^2) inside each detected TCZs was determined and its cumulative probability distribution for a time lag of 48ms (3 frames) was generated. This was fitted to a two-population model according to (46):

$$P(r^2,t) = 1 - \left[\alpha e^{-\frac{r^2}{r_1^2}} + (1-\alpha)e^{-\frac{r^2}{r_2^2}}\right] \tag{2}$$

where $P(r^2,t)$ is the probability that a particle starting at the origin will be found within a circle of radius *r*. α is the normalized fraction of slow receptor molecules, (1- α) the normalized fraction of fast receptor molecules, r_1 the radius of the confinement of the slow population and r_2, the radius of the confinement of the fast population. The average diffusion coefficient ($D_{2\text{-}4}$) of each population was determined by calculating their average MSD and fitting a straight line as explained in Chapter 2. From this fit, and according to our localization accuracy, the slow diffusing population was classified as immobile and was not further considered for the analysis. The average size of the TCZs associated to the fast/mobile population was determined according to (47):

$$r_i^2(t) = offset + \left(\frac{L_i^2}{3}\right)\left(1 - e^{\left(-\frac{\Delta t}{\tau_i}\right)}\right) \tag{3}$$

were $offset$, L and τ_i, are respectively the offset, the length of a square confinement region and its average duration. In addition, from the detected TCZ we directly measured the time that DC-SIGN spends in these regions and generated distributions for all individual TCZ detected. Fitting of the distribution using a single exponential decay renders the characteristic TCZ time, as shown in Figure 4.10.

Determination of interparticle distances and Monte Carlo simulations to assess the degree of dynamic nanocluster interactions. To investigate the possibility that individual DC-SIGN nanoclusters would dynamically interact with each other we performed two-color QD tracking at high label densities following a methodology similar to that described by Low-Nam et al and Bakker et al (48, 40). Two-dimensional fluorescence trajectories of spatially close QD (red: Ab-QD655 and green: Ab-QD585) were generated (Fig. 4.4) and the separation distance (interparticle distance) between QDs was determined from their dual-color pair trajectories. The initial Ab-QDs conjugates separation distance considered was 400nm and interparticle distances were calculated for each 40 subsequent frames (t = 1.33s). In conditions in which an individual nanocluster would interact with its neighbor, the separation distances between QDs should decrease and maintain below 160 nm (the size of the nanoclusters as measured by STED) and exhibit correlated motion (40). In contrast, large variations on the separation distance and/or absence of correlated motion indicate only random coincidence events. In our experiments we never observed correlated motion and the separation distances varied largely (Fig. 4.4). Furthermore, from the interparticle distance distribution we also measured the average times at which Ab-QDs conjugates remained at distances ≤ 160nm. We chose this interparticle distance threshold because it is the characteristic size of the DC-SIGN nanocluster obtained using STED nanoscopy (Fig. 4.3).

Monte Carlo simulations to identify spatial confinement of wt-DC-SIGN. Monte Carlo simulations of dual-color trajectories displaying purely Brownian 2D-diffusion (not hindered) and Brownian 2D-diffusion confined to a 1 μm^2 circular region with elastic borders were also performed to compare the experimental results shown in Fig. 4.5D with those obtained due to purely stochastic encounters between nanoclusters. The simulations took into account the initial experimental separation distance between each Ab-QDs conjugate (400nm) and the instantaneous diffusion coefficients experimentally determined for either wt-DC-SIGN or N80A mutant. A total of 200 trajectories per experimental pair of trajectories were simulated yielding a total amount of at least 5000 simulated trajectories per condition.

One or Dual-color cartography maps. Day 6 imDCs were pretreated with 100/200 nM lactose for 24h, wt-DCSIGN and N80A expressing CHO cells were labeled with a conjugate of QD655 and DCN46 monovalent antibody. Alternatively, Day 6 imDCs were incubated on glass coverslips and CD44 and DC-SIGN were labeled with QD655 monovalent Ab (NKI-P2, NKI) and QD585 monovalent Ab (DCN46, Pharmingen) respectively. Dual-color imaging was performed with split channels imaged on the same chip of an EM-CCD Camera at a time resolution of 30 Hz and a total observation time of 13.3 s. 42000 localizations of CD44 (red) and DCSIGN (green) are displayed representing each one a localization event over the total observation time.

The effect of lactose treatment on the surface expression of galectins. Day 5 imDCs were cultured for 2 days in the presence of 25mM Lactose, stained for Galectin-3 (RtIgG2a clone M3/38; Biolegend) or Galectin-9 (Goat polyclonal anti-human Galectin-9; R&D Systems) and analyzed by flow cytometry. Mean fluorescent intensities of specific signal corrected for the signal obtained on isotype control labeled cells are plotted (+/- SEM of cells of two healthy donors).

Secondary antibodies copatching experiments. Human imDCs were incubated on ice with primary antibodies against DC-SIGN (clone AZN-D1 or clone DCN46), Galectin-9 (Gt-human R&D systems), CD44 (G44.26 BD Biosciences) or Transferin receptor (clone B3/25) as indicated, followed by a copatching with a matching combination of species and isotype specific fluorescently labeled secondary antibodies at 15 °C. Subsequently cells were fixed, adhered to coverslips and analyzed with confocal microscopy.

References

1. Boscher C, Dennis JW, & Nabi IR (2011) Glycosylation, galectins and cellular signaling. *Curr. Opin. Cell Biol.* **23**,383-392.

2. Brewer CF, Miceli MC, & Baum LG (2002) Clusters, bundles, arrays and lattices: novel mechanisms for lectin-saccharide-mediated cellular interactions. *Curr. Opin. Struc. Biol.* **12**,616-623.

3. Dennis JW, Lau KS, Demetriou M, & Nabi IR (2009) Adaptive Regulation at the Cell Surface by N-Glycosylation. *Traffic* **10**,1569-1578.

4. Rabinovich GA, Toscano MA (2009) Turning 'sweet' on immunity: galectin–glycan interactions in immune tolerance and inflammation *Nat. Rev. Immunol.* **9**, 338-352.

5. Yang R, Rabinovich GA, Liu F (2008) Galectins: structure, function and therapeutic potential *Expert Rev. in Mol. Med.* **10**, 1-24.

6. Marth JD, Grewal PK (2008) Mammalian glycosylation in immunity *Nat. Rev. Immunol.* **8**, 874-887.

7. Nagae M, Nishi N, Nakamura-Tsuruta S, Hirabayashi J, Wakatsuki S, Kato R (2008) *J. Mol. Biol.* **375**, 119-135.

8. Chabot S, Kashio Y, Seki M, Shirato Y, Nakamura K, Nishi N, Nakamura T, Matsumoto R, Hirashima M (2002) *Glycobiology* **12**, 111-118.

9. Zhu C, Anderson A, Schubart A, Xiong H, Imitola J, Khoury SJ, Zheng XX, Strom TB, Kuchroo VK (2005) *Nat. Immunol.* **6**, 1245-1252.

10. Elahi S, Niki T, Hirashima M, Horton H (2012) *Blood* **119**, 4192-4204.

11. Katoh S, Ishii N, Nobumoto A, Takeshita K, Dai S, Shinonaga R, Niki T, Nishi N, Tominaga A, Yamauchi A, Hirashima M (2007) *Am. J. Respir. Crit. Care Med.* **176**, 27-35.

12. Wu C, Thalhamer T, Franca RF, Xiao S, Wang C, Hotta C, Zhu C, Hirashima M, Anderson AC, Kuchroo VK (2014) *Immunity* **41**, 270-282.

13. Buschow SI, et al. (2012) Unraveling the human dendritic cell phagosome proteome by organellar enrichment ranking. *J. Proteomics* **75**, 1547-1562.

14. Garner OB, Baum LG (2008) *Biochem. Soc. Trans.* **36**, 1472-1477.

15. Chen IJ, Chen HL, Demetriou M (2007) *J. Biol. Chem.* **282**, 35361-35372.

16. Lajoie P, et al. (2007) Plasma membrane domain organization regulates EGFR signaling in tumor cells. *J. Cell Biol.* **179**, 341-356.

17. Partridge EA, et al. (2004) Regulation of cytokine receptors by Golgi N-glycan processing and endocytosis. *Science* **306**, 120-124.

18. Dennis JW, Nabi IR, & Demetriou M (2009) Metabolism, Cell Surface Organization, and Disease. *Cell* **139**, 1229-1241.

19. Rabinovich GA, Toscano MA, Jackson SS, & Vasta GR (2007) Functions of cell surface galectin-glycoprotein lattices. *Curr. Opin. Struct. Biol.* **17**, 513-520.

20. van Kooyk Y & Rabinovich GA (2008) Protein-glycan interactions in the control of innate and adaptive immune responses. *Nat. Immunol.* **9**:593-601.

21. Belardi B, O'Donoghue GP, Smith AW, Groves JT, & Bertozzi CR (2012) Investigating cell surface galectin-mediated cross-linking on glycoengineered cells. *J. Am. Chem. Soc.* **134**, 9549-9552.

22. Lajoie P, Goetz JG, Dennis JW, & Nabi IR (2009) Lattices, rafts, and scaffolds: domain regulation of receptor signaling at the plasma membrane. *J. Cell Biol.* **185**,381-385.

23. McMahon HT & Boucrot E (2011) Molecular mechanism and physiological functions of clathrin-mediated endocytosis. *Nat. Rev. Mol. Cell Biol.* **12**,517-533.

24. Cocucci E, Aguet F, Boulant S, & Kirchhausen T (2012) The first five seconds in the life of a clathrin-coated pit. *Cell* **150**, 495-507.

25. Ehrlich M, et al. (2004) Endocytosis by random initiation and stabilization of clathrin-coated pits. *Cell* **118**, 591-605.

26. Weigel AV, Tamkun MM, & Krapf D (2013) Quantifying the dynamic interactions between a clathrin-coated pit and cargo molecules. *Proc. Natl. Acad. Sci. U S A* **110**, E4591-4600.

27. Cha SK, et al. (2008) Removal of sialic acid involving Klotho causes cell-surface retention of TRPV5 channel via binding to galectin-1. *Proc. Natl. Acad. Sci. U S A* **105**, 9805-9810.

28. Lau KS, et al. (2007) Complex N-glycan number and degree of branching cooperate to regulate cell proliferation and differentiation. *Cell* **129**, 123-134.

29. Ohtsubo K, et al. (2005) Dietary and genetic control of glucose transporter 2 glycosylation promotes insulin secretion in suppressing diabetes. *Cell* **123**, 1307-1321.

30. Cambi A, et al. (2004) Microdomains of the C-type lectin DC-SIGN are portals for virus entry into dendritic cells. *J. Cell Biol.* **164**, 145-155.

31. de Bakker BI, et al. (2007) Nanoscale organization of the pathogen receptor DC-SIGN mapped by single-molecule high-resolution fluorescence microscopy. *Chemphyschem* **8**, 1473-1480.

32. Itano MS, et al. (2012) Super-Resolution Imaging of C-Type Lectin and Influenza Hemagglutinin Nanodomains on Plasma Membranes Using Blink Microscopy. *Biophys. J.* **102**, 1534-1542.

33. Manzo C, et al. (2012) The neck region of the C-type lectin DC-SIGN regulates its surface spatiotemporal organization and virus-binding capacity on antigen-presenting cells. *J. Biol. Chem* **287**, 38946-38955.

34. Tacken PJ, et al. (2011) Targeting DC-SIGN via its neck region leads to prolonged antigen residence in early endosomes, delayed lysosomal degradation, and cross-presentation. *Blood* **118**, 4111-4119.

35. Cambi A, Beeren I, Joosten B, Fransen JA, & Figdorl CG (2009) The C-type lectin DC-SIGN internalizes soluble antigens and HIV-1 virions via a clathrin-dependent mechanism. *Eur. J. Immunol.* **39**, 1923-1928.

36. Cambi A, Lidke DS, Arndt-Jovin DJ, Figdor CG, & Jovin TM (2007) Ligand-conjugated quantum dots monitor antigen uptake and processing by dendritic cells. *Nano Lett.* **7**, 970-977.

37. Itano MS, et al. (2011) DC-SIGN and Influenza Hemagglutinin Dynamics in Plasma Membrane Microdomains Are Markedly Different. *Biophys. J.* **100**, 2662-2670.

38. Serrano-Gomez D, et al. (2008) Structural requirements for multimerization of the pathogen receptor dendritic cell-specific ICAM3-grabbing non-integrin (CD209) on the cell surface. *J. Biol. Chem.* **283**, 3889-3903.

39. Demetriou M, Granovsky M, Quaggin S, & Dennis JW (2001) Negative regulation of T-cell activation and autoimmunity by Mgat5 N-glycosylation. *Nature* **409**, 733-739.

40. Bakker GJ, et al. (2012) Lateral mobility of individual integrin nanoclusters orchestrates the onset for leukocyte adhesion. *Proc. Natl. Acad. Sci. U S A* **109**, 4869-4874.

41. Simson R, Sheets ED, & Jacobson K (1995) Detection of temporary lateral confinement of membrane proteins using single-particle tracking analysis. *Biophys. J.* **69**, 989-993.

42. Sheets ED, Lee GM, Simson R, & Jacobson K (1997) Transient confinement of a glycosylphosphatidylinositol-anchored protein in the plasma membrane. *Biochemistry* **36**, 12449-12458.

43. Nunez D, et al. (2011) Hotspots organize clathrin-mediated endocytosis by efficient recruitment and retention of nucleating resources. *Traffic* **12**, 1868-1878.

44. Ponta H, Sherman L, & Herrlich PA (2003) CD44: from adhesion molecules to signalling regulators. Nature reviews. *Mol. Cell. Biol.* **4**, 33-45.

45. Serge A, Bertaux N, Rigneault H, & Marguet D (2008) Dynamic multiple-target tracing to probe spatiotemporal cartography of cell membranes. *Nat. Methods* **5**, 687-694.

46. Schutz GJ, Schindler H, & Schmidt T (1997) Single-molecule microscopy on model membranes reveals anomalous diffusion. *Biophys. J.* **73**, 1073-1080.

47. Destainville N & Salome L (2006) Quantification and correction of systematic errors due to detector time-averaging in single-molecule tracking experiments. *Biophys. J.* **90**, L17-19.

48. Low-Nam ST, et al. (2011) ErbB1 dimerization is promoted by domain co-confinement and stabilized by ligand binding. *Nat. Struct. Mol. Biol.* **18**, 1244-U1288.

Chapter 5

Weak Ergodicity Breaking of Receptor Motion in Living Cells Stemming from Random Diffusivity

Molecular transport in living systems regulates numerous processes underlying biological function. Although many cellular components exhibit anomalous diffusion, only recently has the subdiffusive motion been associated with nonergodic behavior. These findings have stimulated new questions for their implications in statistical mechanics and cell biology. Is nonergodicity a common strategy shared by living systems? Which physical mechanisms generate it? What are its implications for biological function? Here, we use single-particle tracking to demonstrate that the motion of DC-SIGN reveals nonergodic subdiffusion on living-cell membranes. In contrast to previous studies, this behavior is incompatible with transient immobilization, and, therefore, it cannot be interpreted according to continuous-time random-walk theory. We show that the receptor undergoes changes of diffusivity, consistent with the current view of the cell membrane as a highly dynamic and diverse environment. Simulations based on a model of an ordinary random walk in complex media quantitatively reproduce all our observations, pointing toward diffusion heterogeneity as the cause of DC-SIGN behavior. By studying different receptor mutants, we further correlate receptor motion to its molecular structure, thus establishing a strong link between nonergodicity and biological function. These results underscore the role of disorder in cell membranes and its connection with function regulation. Because of its generality, our approach offers a framework to interpret anomalous transport in other complex media where dynamic heterogeneity might play a major role, such as those found, e.g., in soft condensed matter, geology, and ecology.

This work has been published as C. Manzo*, J.A. Torreno-Pina*, P. Massignan, G.J. Lapeyre Jr., M. Lewenstein, M.F. Garcia-Parajo, “Weak ergodicity breaking of receptor motion in living cells stemming from random diffusivity”, *Physical Review X* **5**, 011021 (2015).* Equally contributing authors.

Introduction

Cell function heavily relies on the occurrence of biochemical interactions between specific molecules. Encounters between interacting species within the cellular environment are mediated by active and/or diffusive molecular transport, with a motion characterized by directed displacements in the former case, and by random ones in the latter. The quantitative study of diffusion is thus essential for understanding molecular mechanisms underlying cellular function, including target search (1), kinetics of transport limited reactions (2, 3), trafficking and signaling (4). These processes take place in complex environments, crowded and compartmentalized by macromolecules and biopolymers. A prototypical example that we have addresses in this thesis is the plasma membrane. Here, the interplay of lipids and proteins with cytosolic (e.g., the actin cytoskeleton) and extracellular (e.g., glycans) components generates a highly dynamic and heterogeneous organization (5).

The diffusion of a single molecule j, whose position x_j is sampled at discrete time intervals Δt for a total time $N\Delta t$, is often characterized by the time-averaged mean-square displacement (T-MSD):

$$\text{T-MSD}\left(\mathrm{t}_{lag} = m\Delta t\right) = \frac{1}{N-m}\sum_{i=1}^{N-m}\left(x_j(t_i + m\Delta t) - x_j(t_i)\right)^2 \qquad (1)$$

which for a Brownian particle scales linearly in the time-lag t_{lag}. Application of fluorescence based techniques to living cells has evidenced striking deviations from Brownian behavior in the nucleus (6), cytoplasm (7–10) and plasma membrane (11, 12). Indeed, numerous cellular components show anomalous subdiffusion (13), characterized by a power law dependence of the MSD $\sim t^{\beta}$, with $\beta < 1$ (14–16). Owing to the implications of molecular transport for cellular function and the widespread evidence of subdiffusion in biology, major theoretical efforts have been devoted to understand its physical origin. Subdiffusion is generally understood to be the consequence of molecular crowding (17) and several models have been developed to capture its main features. In general, subdiffusion can be obtained by models of energetic and/or geometric disorder, such as: (i) the continuous-time random walk (CTRW), i.e., a walk with waiting times between steps drawn from a power law distribution (18); (ii) fractional Brownian motion, i.e., a process with correlated increments (19); (iii) obstructed diffusion, i.e., a walk on a percolation cluster or a fractal (15); (iv) diffusion in a spatially heterogeneous medium (26). Each of these models can be in turn associated with relevant biophysical mechanisms such as trapping (20), the viscoelastic properties of the environment (21) or the presence of barriers and obstacles to diffusion (22). Advances in single particle tracking (SPT) techniques have allowed the recording of long single-molecule trajectories and have revealed very complex diffusion patterns in living cell systems (5, 11). Recently, it has been shown that some cellular components show subdiffusion associated with weak ergodicity breaking (wEB) (9, 10, 12), with the most obvious signatures being the non-equivalence of the T-MSD and the ensemble-averaged MSD (E-MSD), defined as:

$$\text{E-MSD}\left(t_{lag} = m\Delta t\right) = \frac{1}{J}\sum_{j=1}^{J}\left(x_j(t_i + m\Delta t) - x_j(t_i)\right)^2 \qquad (2)$$

where J is the total number of observed single-particle trajectories, and t_i is a specific initial time. Moreover, ergodicity breaking has been further confirmed by the presence of aging (23, 24), i.e. the dependence of statistical quantities on the observation time. Based on these findings, several stochastic models presenting nonstationary (and thus nonergodic) subdiffusion have been proposed (25–28). Among these, CTRW has been used to model nonergodic subdiffusion in living cells (9, 10, 12) and has begun to provide theoretical insight into the physical origin of wEB in biological systems (25), associating the nonergodic behavior to the occurrence of particle immobilization with a heavy-tailed distribution of trapping times.

At the same time, these intriguing findings have generated new questions: Is nonergodic subdiffusion a strategy shared by other biological systems? Can biophysical mechanisms other than trapping lead to similar behaviors? What is its functional relevance? Elucidating these issues is crucial to unravel the role of nonergodic subdiffusion in cellular function. The main aim of this work is to explore other forms of transport in biological systems to provide answers to these questions.

In this Chapter we describe the use of SPT to study the diffusion of the pathogen-recognition receptor DC-SIGN (29) on living cell membranes. Our experiments and data analysis show that DC-SIGN dynamics display clear signatures of wEB and aging. However, in contrast to recent studies reporting nonergodic behavior of other membrane proteins (12), we find that DC-SIGN very rarely shows trapping events so that the observed wEB cannot be described by the CTRW model. Instead, our analysis shows that DC-SIGN displays a heterogeneous dynamics presenting frequent changes of diffusivity. Our numerical simulations, based on a novel theoretical model of Brownian diffusion in complex media (30), quantitatively reproduce DC-SIGN dynamics demonstrating that nonergodic subdiffusion is a consequence of temporal and/or spatial heterogeneity. Furthermore, structurally mutated variants of DC-SIGN, with impaired function, show very different dynamical features. These results allow us to link receptor transport to molecular structure and receptor function, such as the capability to capture and uptake pathogens.

Results

Weak ergodicity breaking and aging in DC-SIGN dynamics. We performed SPT experiments (5, 31) to follow the lateral diffusion of DC-SIGN (29, 32, 33, 34) on living cell membranes as previously described in Chapter 3 and 4. We also used in here stably DC-SIGN expressing CHO cells, in combination with the ΔRep-, N80A and the Δ35-DC-SIGN mutants. To characterize their dynamics, we labeled DC-SIGN receptors with quantum dots, and we recorded their mobility by tracking the quantum dot positions as explained in Chapter 2 (Fig. 5.1A-B).

The T-MSD of individual trajectories of wild-type (wt)-DC-SIGN displayed a linear behavior ($\beta \sim 1$), consistent with pure Brownian diffusion (Fig. 5.1C). The distribution of the exponents β obtained by nonlinear fitting of the T-MSDs of the individual trajectories (inset of Fig. 5.1C) showed an average $<\beta>= 0.98 \pm 0.06$. In addition, the fitting of the average T-MSD provided a value $\beta = 0.95 \pm 0.01$. Since the T-MSD values corresponding to different trajectories were broadly scattered, for each trajectory we calculated the diffusion coefficient D_s by a linear fit of the T-MSD at time lags < 10% of the trajectory duration (35). As expected, the resulting values of D_s were found to have a very broad distribution, spanning more than two orders of magnitude (Fig. 5.1D).

However, in marked contrast with the T-MSD, the E-MSD deviated significantly from linearity, showing subdiffusion with an exponent $\beta = 0.84 \pm 0.03$ (Fig. 5.1E). The difference between the scalings of T-MSD and E-MSD is a clear signature of wEB (36). To inquire whether wt-DC-SIGN dynamics also exhibits aging, we computed the time-ensemble-averaged MSD (TE-MSD) by truncating the data at different observation times T:

$$\text{TE-MSD}\left(t_{lag}, T\right) = \frac{1}{J}\frac{1}{\frac{T}{\Delta t}-m}\sum_{i=1}^{\frac{T}{\Delta t}-m}\sum_{j=1}^{J}\left(x_j(t_i+m\Delta t)-x_j(t_i)\right)^2 \qquad (3)$$

and extracting the corresponding diffusion coefficient D_{TE} by linear fitting (35). In systems with uncorrelated increments, it can be shown under rather general assumptions that $D_{\mathrm{TE}} \sim T^{\beta-1}$ (30, 37). The observed D_{TE} indeed scaled as a power law with an exponent of -0.17 ± 0.05 (Fig. 5.1F), yielding a value of β in good agreement with the exponent determined from E-MSD. These results thus demonstrate that wt-DC-SIGN dynamics exhibits aging.

Failure of the CTRW model. The motion of some biological components, including the Kv2.1 potassium channel in the plasma membrane (12), lipid granules in yeast cells (9) and insulin-containing vesicles in Pancreatic β-cells (10), has been reported to exhibit subdiffusion compatible with the coexistence of an ergodic and a nonergodic process. The nonergodic part of the process has been modeled within the framework of the CTRW (25, 36, 37).

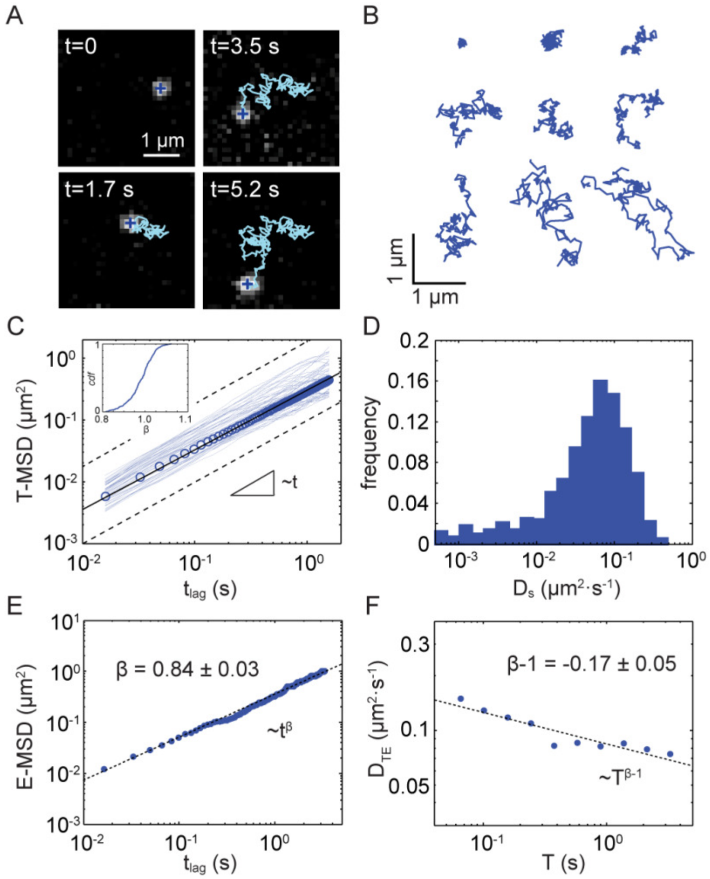

Figure 5.1 wt-DC-SIGN diffusion shows weak ergodicity breaking and aging. (**A**) Representative video frames of a quantum-dot-labeled wt-DC-SIGN molecule diffusing on the dorsal membrane of a CHO cell. The centroid position of the bright spot (+), corresponding to a single quantum-dot, is tracked and reconnected to build up the wt-DC-SIGN trajectory, shown by the cyan line. (**B**) Representative trajectories for the same recording time (3.2 s). (**C**) Log-log plot of the time-averaged MSD for individual trajectories (blue lines). The dashed lines scale linearly in time, showing that T-MSD is compatible with pure brownian motion (β = 1). The symbols (o) correspond to the average T-MSD. Nonlinear fit provided $\beta = 0.95 \pm 0.01$. (Inset) cdf of the exponent β obtained from nonlinear fitting of the T-MSD of all the trajectories. (**D**) Distribution of short-time diffusion coefficients as obtained from linear fitting of the time-averaged MSD for all the trajectories. (**E**) Log-log plot of the ensemble-averaged MSD. Power law fit of the data (dashed line) provides an exponent $\beta = 0.84$, showing subdiffusion. (**F**) Log-log plot of the time-ensemble-averaged diffusion coefficient as a function of the observation time T. The diffusion coefficients are obtained by linear fitting of the time-ensemble-averaged MSD. A power-law fit (dashed line) provides an exponent $\beta - 1 = -0.17$, revealing aging and in good agreement with the value of β found in (E).

CTRW is a random walk in which a particle performs jumps whose lengths have a finite mean, but between jumps the walker remains trapped for random dwell times, distributed with a power-law probability density ~ $t^{-(1+\beta)}$, which for $\beta \leq 1$ has an infinite mean. This model is annealed, in the sense that the duration of trapping events is independent of the past history of the system, even if the particle revisits the same trap after some time. The energy landscape of this process is characterized by potential wells with a broad depth distribution. Such energetic disorder yields nonergodicity, since no matter how long one measures, deep traps cause dwell times on the order of the measurement time. Within the biological context, these traps generally have been associated with chemical binding to stationary cellular components (e.g. actin cytoskeleton (12) or microtubuli (10)), with a distribution of dissociation times with varying lifetimes. T-MSDs of molecules performing CTRW show broadly scattered values, but are on average linear in the lag time t_{lag} (37, 38), similar to our observation in Fig. 5.1C. The subdiffusive behavior of the motion emerges in the E-MSD, scaling with the same exponent β describing the probability density of trapping dwell-times.

Since wt-DC-SIGN dynamics also showed nonergodic subdiffusion and aging, we sought to investigate whether DC-SIGN diffusion agrees with the predictions of the CTRW model. To this end, we searched for the occurrence of transient trapping events on individual trajectories. In SPT experiments, the limited localization accuracy for determining the particle position sets a lower limit for the diffusivity value that can experimentally be measured. In our experiment, this lower threshold lies at $D_{\mathrm{th}} = 6 \bullet 10^{-4}\ \mu\mathrm{m}^2\ \mathrm{s}^{-1}$. Therefore, a segmentation algorithm (39) was applied to the x- and y-displacements of our trajectories in order to detect events with diffusivity lower than D_{th}. Surprisingly, transient trapping was only detected over less than 5% of the total recording time (Fig. 5.2A-C). Moreover, the detected trapping times were rather short-lived, with average duration of 330 ± 30 ms (Fig. 5.2D). These values are remarkably similar to those reported in Chapter 4 when estimating the transient confinement regions experienced by wt-DC-SIGN. In order to understand the nature of these trapping events, we attempted to fit their distribution by means of both an exponential and a power law distribution function ~ $t^{-(1+\beta)}$, as expected for CTRW (12). The power law pdf provided a better fit to the data, yielding an exponent $\beta = 0.83 \pm 0.05$ (Fig. 5.2D), in agreement with the value obtained for the E-MSD. While a power-law distribution of trapping event durations would be compatible with the behavior expected for the CTRW, it is unlikely that these can have a major role in the ergodicity breaking we observe, given their very small probability of occurrence. We notice here that various other models predict a similar scaling of the trapping times; one such example will be discussed in detail later. To quantify to what extent the small percentage of trapping events actually influences the nonergodic behavior, we calculated the E-MSD excluding completely the trajectories showing events compatible with immobilization, even if these are transient ones. Interestingly, this analysis provided an exponent β = 0.84 ± 0.04 exactly coinciding with the value obtained for the full set of trajectories (Fig. 5.2D), thus confirming that trapping alone cannot account for the ergodicity breaking we observe in wt-DC-SIGN dynamics.

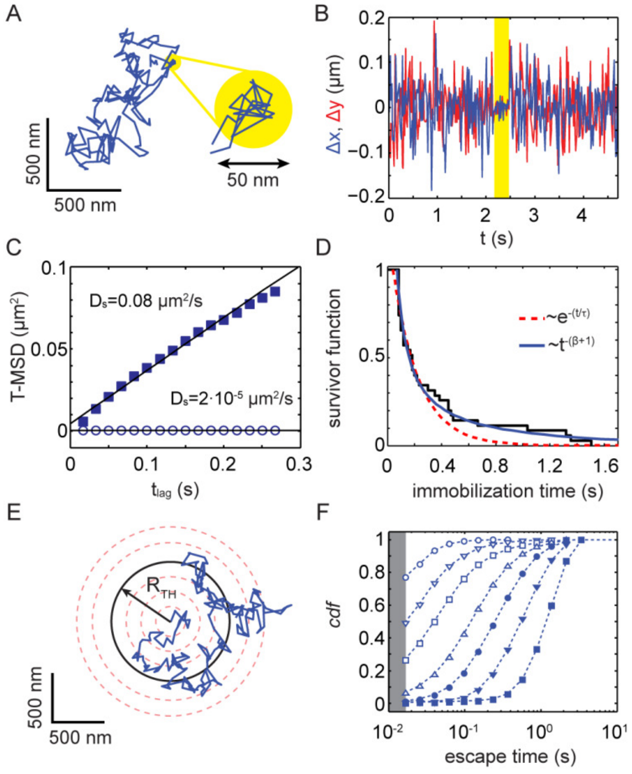

Figure 5.2 wt-DC-SIGN receptor dynamics is inconsistent with the CTRW model. (**A**) A trajectory of wt-DC-SIGN on living cell membranes showing a short-lived transient immobilization event, highlighted by the yellow circular area. (**B**) Plot of the x- (blue) and y-displacements (red) as a function of time. The occurrence of transient immobilization (yellow region) corresponds to a reduction in the trajectory displacement. (**C**) Time-averaged MSD for the entire trajectory (■) and for the immobilization region only (o). (**D**) Survivor function of the duration of immobilization events for wt-DC-SIGN trajectories (black line). Blue and red lines correspond to fits to exponential and power-law distribution functions. (**E**) Schematic representation of the calculation of the escape time probability from circular areas of different radius R_{TH} . (**F**) Cumulative probability distribution function (cdf) of trajectory escape time for different radii R_{TH} =20 (o), 50 (▽), 100 (□), 200 (△), 300 (•), 500 (▼) and to 1000 nm (■). Dashed lines are guides to the eye. The gray shaded region represents times shorter than the acquisition frame rate.

In addition, we constructed the distribution of escape times by identifying the duration of the events in which a trajectory remains within a given radius R_{TH} (Fig. 5.2E). For a

CTRW, the long-time dynamics is dominated by anomalous trapping events, and as a result this quantity is expected to be independent of R_{TH} (12). In strong contrast to the CTRW model, the escape-time distributions of DC-SIGN trajectories showed a marked dependence on R_{TH} (Fig. 5.2F). The rare occurrence of transient trapping events, the lack of long immobilization times, the dependence of escape-time distributions on R_{TH} and, most importantly, the fact that T-MSD and E-MSD show very different scaling even when the few trajectories showing immobilization are removed from the analysis, are all inconsistent with CTRW, indicating that the main features of wt-DC-SIGN dynamics may not be explained in terms of this model.

DC-SIGN displays changes of diffusivity. Recently, diffusion maps of the cell membrane have shown the presence of patches with strongly varying diffusivity (31, 42, 43). Based on this evidence, we have recently proposed a class of models describing ordinary Brownian motion with a diffusivity that varies randomly, but is constant on time intervals or spatial patches with random size (30). These models describe anomalous diffusion and wEB in complex and heterogeneous media, such as the cellular environment, without invoking transient trapping.

To address whether the observed nonergodic dynamics of wt-DC-SIGN can be described with this theoretical framework, we further analyzed individual trajectories by means of a change-point algorithm to detect variations of diffusivity in time (39). In brief, the algorithm consists in a likelihood-based approach to quantitatively recover time-dependent changes in diffusivity, based on the calculation of maximum likelihood estimators for the determination of diffusion coefficients and the application of a likelihood ratio test for the localization of the changes. Notably, DC-SIGN trajectories displayed a Brownian motion with relatively constant diffusivity over intervals of varying length, but that changed significantly between these intervals (Fig. 5.3A-C). Similar features were identified in a large fraction of trajectories, with 63% showing at least one diffusivity change (Fig. 5.3D), in qualitative agreement with the models of random diffusivity (30).

To obtain a comprehensive understanding of our data, we considered an annealed model in which randomly diffusing particles undergo sudden changes of diffusion coefficient (30). The distribution of diffusion coefficients D that a particle can experience is assumed to have a power-law behavior $\sim D^{\sigma-1}$ for small D (with $\sigma > 0$) and a fast decay for $D \rightarrow \infty$. Given D, the transit time τ (i.e., the time τ a particle moves with a given D) is taken to have a probability distribution with mean $\sim D^{-\gamma}$ (with $-\infty < \gamma < \infty$). Since the

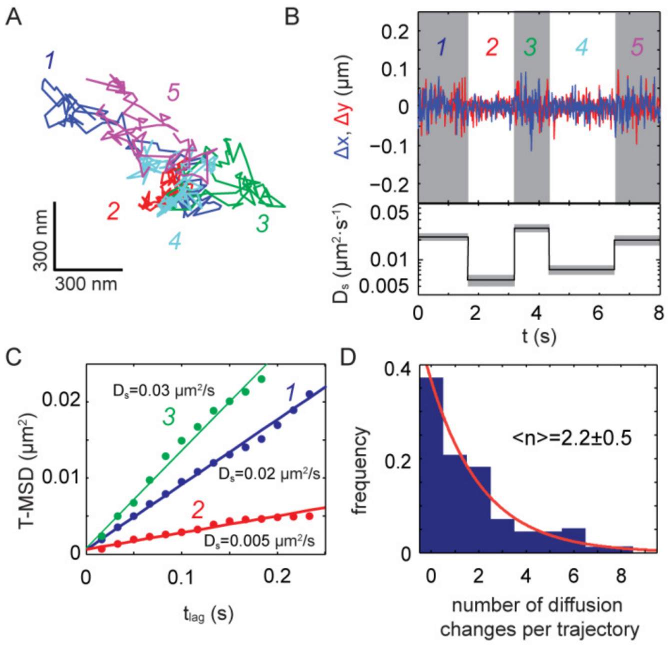

Figure 5.3 wt-DC-SIGN motion experiences changes in diffusivity. (**A**) Representative wt-DC-SIGN trajectory displaying changes of diffusivity. Change-point analysis evidenced 5 different regions represented with different colors. (**B**) Plot of the x- (blue) and y-displacement (red) for the trajectory in (**A**) as a function of time. The shaded areas indicate the regions of different diffusivity. The lower panel displays the corresponding short-time diffusion coefficient as obtained from a linear fit of the time-averaged MSD for the 5 different regions. Gray areas correspond to the 95% confidence level. (**C**) Plot of time-averaged MSD versus time lag for the first three regions of the trajectory in (A). (**D**) Histogram of the number of changes of diffusion per trajectory. Most of the trajectories (63%) display at least one dynamical change, with an average of 2.2 changes per trajectory.

motion during the transit time τ is Brownian, particles explore areas with radius $r \sim \sqrt{\tau}$ D, and the radius of the region explored with such diffusion coefficient has probability distribution with mean $\sim D^{(1-\gamma)/2}$. Depending on the values of the exponents σ and γ, this model predicts three regimes (30), namely: (0) for $\gamma < \sigma$, the long-time dynamics is compatible with ordinary Brownian motion and yields an E-MSD exponent $\beta = 1$; (I) for $\sigma < \gamma < \sigma + 1$, the average transit time τ diverges and particles undergo nonergodic subdiffusion with $\beta = \sigma/\gamma$; (II) for $\gamma > \sigma + 1$, both the average transit time τ and the average radius r of the explored area diverge and one obtains nonergodic subdiffusion with $\beta = 1 - 1/\gamma$. On the other hand, the T-MSD predicted by this model always remains linear in time, for every choice of σ and γ.

We performed *in-silico* experiments of 2D diffusion (Fig. 5.4A-B), assuming a distribution of diffusion coefficients D given by:

$$P_D(D) = \frac{D^{\sigma-1}e^{-D/b}}{b^{\sigma}\Gamma(\sigma)} \tag{4}$$

and a conditional distribution of transit times τ given by:

$$P_\tau(\tau|D) = \frac{D^{\gamma}}{k}e^{-\tau D^{\gamma}/k} \tag{5}$$

where b and k are dimensional constants and $\Gamma(x)$ is the Gamma function. The functional form of these two joint distributions is the minimal one complying with the requirements of our model, while at the same time it is the one ensuring the minimal number of free parameters, making these a natural choice for our theoretical analysis. However, we note here that the asymptotic behavior of the model is actually independent from the specific functional form of the joint distributions. We performed simulations for different values of σ, with $\gamma = \sigma/\beta$ as in regime (I), and $\beta = 0.84$, the exponent obtained from the experimental E-MSD. The simulations quantitatively reproduce not only subdiffusion, nonergodicity and aging, but also the heterogeneous distribution of diffusion coefficients and escape time distributions (Fig. 5.4C-H). The remarkable agreement between simulations and experimental data strongly supports heterogeneous diffusion as the origin for DC-SIGN nonergodicity.

It must be noticed that, in contrast to CTRW, our model does not assume particle immobilization, but a continuous distribution of diffusivity, with $P_D(D) \sim D^{\sigma-1}$ for small D. However, from the experimental point of view, it is not possible to distinguish immobilization events from very slow diffusion. In fact, the limited localization accuracy of SPT experiments translates into a lower limit for the diffusivity value D_{th} that can be detected. Therefore trajectories, or portion of trajectories, with diffusivity lower than D_{th} are identified by our algorithm as immobile, as shown in Fig. 5.2A-B. From the model described above, the distribution of the duration of these ”apparent” immobilization events can be calculated as:

$$P_{imm}(\tau) = \int_0^{D_{th}} P_D(D)P_\tau(\tau|D)dD \tag{6}$$

We neglect here the possibility that the trajectory of an *in-silico* particle contains two consecutive segments characterized by diffusivities D_i and D_{i+1} which are both smaller than D_{th}, as this probability is vanishingly small for the parameter regime of our setup.

Independently of D_{th} , the integral in Eq. (6) scales asymptotically as $\tau^{-1-\beta}$ with $\beta = \sigma/\gamma$ providing for the distribution of immobilization events the same behavior as predicted by the CTRW (12). Therefore, the distribution of immobilization times in Fig. 5.2D is fully compatible with the prediction of our model, further confirming the agreement with the experimental data.

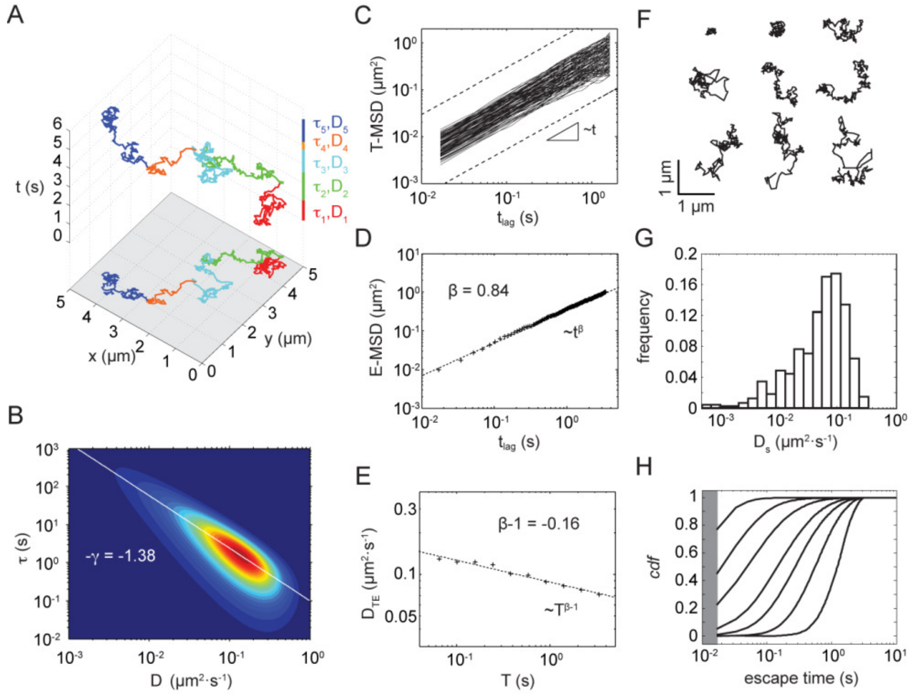

Figure 5.4 Annealed model of heterogeneous diffusion quantitatively reproduces wt-DC-SIGN motion. (**A**) A simulated trajectory composed by five time intervals with different transit time τ_i and diffusivity D_i . (**B**) Contour plot of the probability distribution of the simulated diffusion coefficient D and transit time τ for the parameters reproducing the dynamics of wt-DC-SIGN (σ = 1.16, γ = 1.38, b = 0.12 μm²/s, k = $0.10\mu m^{2\gamma}\, s^{\gamma+1}$). The white line represents the power law dependence between diffusivity and average transit time with exponent $-\gamma$. (**C**) Log-log plot of the time-averaged MSD for simulated trajectories (black lines). (**D**) Log-log plot of the ensemble-averaged MSD for the simulated trajectories. The dashed line represents a power law with the theoretical exponent $\beta = \sigma/\gamma = 0.84$. (**E**) Log-log plot of the time-ensemble averaged diffusion coefficient as a function of the observation time T. The dashed line represents a power law with the theoretical exponent $\beta - 1 = -0.16$. (**F**) Simulated trajectories for the same recording time (3.2 s). (**G**) Distribution of short-time diffusion coefficients as obtained from linear fitting of the time-averaged MSD for all the simulated trajectories. (**H**) cdf of trajectory escape time for different radii. Curves from left to right correspond to radii R_{TH} =20, 50, 100, 200, 300, 500 and1000 nm.

Dynamics of receptor mutants. To gain insight into the molecular mechanisms of DC-SIGN nonergodic diffusion, we performed the same analysis described so far for the Δ35, ΔRep and N80A mutants (Fig. 5.5A). As described in Chapters 3 and 4, each of the mutants is not able to interact with certain cellular components such as the actin cytoskeleton, clathrin coated pits (Δ35-DC-SIGN) or the glycan network (N80A mutant) (41,44,45,46). Moreover, the ΔRep mutant lacks part of the neck region, abrogating interactions between different DC-SIGN molecules and nanoclustering, as shown in Chapters 3 and 4 (47).

We found that each mutation has a very different effect on the dynamics of the receptor. The N80A mutant (Fig. 5.5C-F) showed nonergodic subdiffusion, with an exponent β similar to the one measured for wt-DC-SIGN. However, N80A showed a significantly larger extent of heterogeneity in the diffusion coefficients distribution, with a lower median diffusivity. The Δ35 mutant (Fig. 5.5G-L) also showed nonergodic subdiffusion. The anomalous exponent and the distribution of the diffusion coefficients were similar to that of wt-DC-SIGN, with only a slight reduction in median diffusivity. We accurately reproduced N80A and Δ35 dynamics by simulations performed in regime (I), i.e., nonergodic subdiffusion, using comparable values of γ for wt-DC-SIGN and Δ35, and a smaller value of γ for N80A (Fig. 5.5B). On the other hand, ΔRep dynamics yield ergodic Brownian diffusion (Figs. 5.5M-P) and a narrower distribution of diffusivity with the median value significantly higher than for WT DC-SIGN. Consistently, the behavior of ΔRep is fully captured by *in silico* experiments in regime (0), i.e., ordinary Brownian motion.

Nonergodicity and biological function. Together with Chapter 3 and 4, the data and analysis presented in this Chapter allow us to link the dynamical behavior of DC-SIGN to its functional role in pathogen capture and uptake. In terms of steady-state organization, wt-DC-SIGN, N80A and Δ35- preferentially form nanoclusters on the cell membrane, which are crucial for regulating pathogen binding (41, 47), whereas removal of the neck region (ΔRep) reduces nanoclustering and binding efficiency to small pathogens, such as viruses (47). Our results thus show that the diffusive behavior of the receptor is strongly linked to nanoclustering, but not merely due to size-dependent diffusivity and/or time-dependent cluster formation and breakdown. In fact, as shown in Chapter 4, dual-color SPT experiments performed at high labeling density did not reveal correlated motion between nearby DC-SIGN nanoclusters, excluding the occurrence of dynamic nanocluster coalescence (41). Moreover, although super-resolution imaging has revealed that wt-DC-SIGN, N80A and Δ35- form nanoclusters with similar distributions of size and stoichiometry (41, 47), our dynamical data evidence significant differences in their diffusion patterns (Figs. 5.1 and 5.5).

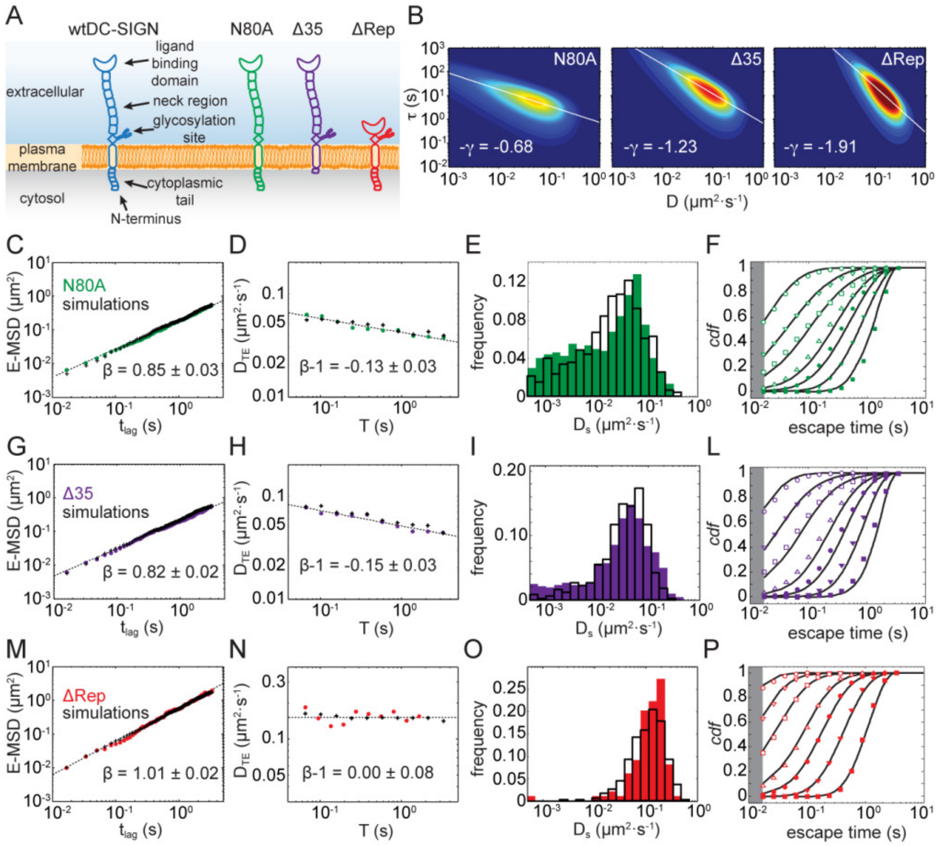

Figure 5.5 Effect of mutations on the dynamics of DC-SIGN. (**A**) Schematic representation of wt-DC-SIGN and its mutated forms. (**B**) Contour plot of the probability distribution of the simulated diffusion coefficient (D) and transit time (τ) for the parameters reproducing the dynamics of N80A ($\sigma = 0.58$, $\gamma = 0.68$, $b = 0.09\mu m^2/s$, $k = 0.74\mu m^{2\gamma}\, s^{\gamma+1}$), Δ35 ($\sigma = 1.04$, $\gamma = 1.23$, $b = 0.08\mu m^2/s$, $k = 0.07\mu m^{2\gamma} s^{\gamma+1}$) and ΔRep ($\sigma = 2.11$, $\gamma = 1.91$, $b = 0.07\mu m^2/s$, $k = 0.07\mu m^{2\gamma} s^{\gamma+1}$). The white line represents the power law dependence between diffusivity and average transit time with exponent $-\gamma$. (**C**) Log-log plot of the ensemble-averaged MSD for N80A trajectories (•) and simulated data (+). (**D**) Log-log plot of the time-ensemble averaged diffusion coefficient for N80A trajectories (•) and simulated data (+) as a function of the observation time T. (**E**) Distribution of short-time diffusion coefficients as obtained from linear fitting of the time-averaged MSD for the N80A (filled bars) and the simulated trajectories (empty bars). (**F**) cdf of the escape time for N80A (symbols) and simulated trajectories (lines) for different radii. The meaning of the symbols is the same as in Fig. 5.2F. (**G-L**) Dynamical behavior of the Δ35 mutant. (**M-P**) Dynamical behavior of the ΔRep mutant.

Our data are in fact consistent with the view of the plasma membrane as being a highly dynamic and heterogeneous medium, where wEB stems from the enhanced ability of DC-SIGN nanoclusters to interact with the membrane environment, including components from the outer and inner membrane leaflet. This interaction is inhibited (or strongly reduced) in the case of the ΔRep mutant since it does not form nanoclusters (47). As a result, the motion of ΔRep is Brownian and ergodic, and interestingly this dynamic behavior correlates with its impaired pathogen binding capability (33, 47).

In contrast, we observed that both wt-DC-SIGN and N80A, which show a similar degree of nanoclustering (41), exhibit wEB. But, the distribution of diffusivity of N80A is significantly broader than that of wt-DC-SIGN, and is shifted towards lower diffusivity values (Fig. 5.5C-F). This increased heterogeneity correlates with altered interactions of the N80A with extracellular components, resulting from the removal of the glycosylation site. Indeed, as shown in Chapter 4, the N80A mutant has a reduced capability to interact with extracellular sugar binding partners (41). Thus, it appears that the extracellular milieu next to the membrane contributes to the degree of dynamical heterogeneity sensed by the receptor. Remarkably, this correlation also extends to the functional level, as we also showed in Chapter 4 that interactions of DC-SIGN with extracellular sugar-binding proteins influence encounters of DC-SIGN with the main endocytic protein clathrin. In turn, this resulted in reduced clathrin-dependent endocytosis of the receptor and its pathogenic ligands (41).

Finally, the Δ35 mutant exhibits nanoclustering (47) and wEB similar to that of wt-DC-SIGN. From the biological point of view, however, this mutant is not able to interact with cytosolic components in close proximity to the inner membrane leaflet, including actin (46). Therefore, in contrast to the extracellular influence, observed for the N80A mutant, the results of Δ35 mutant indicate that interactions with the actin cytoskeleton, responsible for the CTRW-like behavior of other proteins (12), do not play a major role in DC-SIGN wEB. Nevertheless, it should be mentioned that the reduced endocytic capability of Δ35 (46) could not be uniquely attributed to its dynamic behavior on the cell membrane but rather to its impaired interaction with downstream partners involved in internalization (39).

Discussion

We have demonstrated that DC-SIGN displays subdiffusive dynamics, characterized by weak ergodicity breaking and aging. In contrast to other biological systems, receptor trajectories do not show significant evidence of transient immobilization with power-law distributed waiting times. Therefore, its nonergodic behavior cannot be explained in terms of the CTRW model. However, DC-SIGN dynamics is highly heterogeneous, with trajectories often displaying sudden changes of diffusivity. These features are accurately described by a novel model of ordinary diffusion in complex media, strongly suggesting inhomogeneous diffusivity as the cause of DC-SIGN nonergodic behavior. Comparative analysis of three mutated forms of DC-SIGN evidences the importance of specific regions of the receptor structure, known to mediate interactions with other molecules, in receptor dynamics. Since the mutations of these regions differently impair receptor function, the experiments allowed us to establish the relevance of nonergodicity for the regulation of functional mechanisms, such as capacity for pathogen recognition and internalization.

The evidence that temporal and/or spatial disorder induces subdiffusion and wEB agrees remarkably well with the current view of the plasma membrane as an extremely complex environment. Here, precise tuning of the spatiotemporal organization of membrane components, in addition to biochemical interactions with molecules in the inner and outer membrane leaflet, orchestrate the triggering of cell signaling pathways. A detailed understanding of how these specific interactions occur and affect dynamics is still lacking. Future experiments, involving simultaneous tracking of several proteins by means of multicolor SPT (42) might provide a deeper comprehension of these mechanisms at the molecular level.

The model used to interpret our data provides a flexible and realistic framework to describe anomalous motion in cell membranes. Although in the present work we have focused our simulations on time-dependent changes of diffusivity, similar conclusions can be obtained assuming a spatial dependence, with constant diffusivity on membrane patches of random size (30). The current data do not allow discrimination between the two scenarios. The application of techniques that combine dynamic and spatial mapping at high labeling conditions (43, 48) would be necessary to verify the occurrence of spatial maps of diffusivity. In addition, numerical simulations of spatial-dependent random diffusivity require the arrangement of a 2-dimensional geometry consistent with the probability density of diffusivity, which is a non-trivial task.

While the work presented here focuses on the cell plasma membrane, we point out that these results have much broader implications. In fact, our model and analysis are very general and can be applied to any diffusive system that shows wEB, in order to investigate the role that heterogeneous diffusivity plays in observed anomalies. Fundamental questions about the nature of anomalous and nonergodic diffusion in disordered media arise in many fields, such as life sciences (25), soft condensed matter (49, 50), ultracold gases (51, 52), geology (53) and ecology (54).

Materials & Methods

Single particle tracking experiments. We performed video microscopy using a custom single-molecule sensitive epi-fluorescence microscope. SPT was performed on the dorsal membrane of CHO cells at 60 Hz as explained in Chapter 2.

Data analysis. Time-, ensemble- and time-ensemble-averaged mean-squared displacements were calculated as described in (12). Exponents of the E-MSD and $D_{t,ens}$ were obtained by linear fitting of the log-log transformed data. Errors were calculated as the 99% confidence interval of the fitting parameters. Short-time diffusion coefficients were extracted from the linear fit of the first 10% of the points of T-MSD curves [35].

Dynamical changes in the motion of DC-SIGN receptors were identified by application of the change-point algorithm described in Ref. (39). In brief, the trajectories were recursively segmented and a maximum-likelihood-ratio test was applied to the trajectory displacements (Δx, Δy) in order to identify sudden changes of diffusivity. The critical values for Type I error rates were set to a confidence level of 99%, corresponding to 1% probability of having a false-positive identification of a change-point. For each dynamical region identified by the algorithm, the short-time diffusion coefficient was calculated from a linear fit of the first 10% of the points of the corresponding MSD curves (35). Regions showing a short-time diffusion coefficient lower than D_{th} were considered compatible with transient immobilization.

Simulations. Simulated trajectories (500 per parameter set) were obtained by generating random diffusion coefficients D according to the probability distribution given in Eq. (4). For each diffusion coefficient, the corresponding transit time τ was calculated as a random number drawn from the distribution given in Eq. (5). Particle coordinates $r = \{x, y\}$ were generated as:

$$r_{t+\Delta t'} = r_t + \sqrt{2D\Delta t'}\xi \tag{7}$$

where $\xi = \{\xi_x, \xi_y\}$ are pairs of random numbers from a Gaussian distribution with zero mean and unitary standard deviation. The time increment was calculated as $\Delta t' = \Delta t/n$, where Δt is the camera acquisition rate and n is a integer depending on D and τ, chosen in order to have at least 10 points for each interval. For comparison with SPT data, trajectories were sub-sampled at the camera acquisition rate. Simulated trajectory were generated with duration $T_{sim} >> T_{exp}$, where T_{exp} is the duration of the experimental trajectory. The starting point was randomly drawn from a uniform distribution defined within 0 and $T_{sim} - T_{exp}$. Trajectories were then cut to have the same duration T_{exp} as the experimental ones. Gaussian noise corresponding to the experimental localization accuracy (σ_{acc} = 20 nm) was subsequently added to the trajectories.

References

1. Condamin, S, B´nichou, O, Tejedor, V, Voituriez R, and Klafter, J (2007) First-passage times in complex scale-invariant media. *Nature* **450**, 77.

2. Lomholt, M A, Zaid, I M, and Metzler, R (2007) Subdiffusion and Weak Ergodicity Breaking in the Presence of a Reactive Boundary. *Phys. Rev. Lett.* **98**, 200603.

3. Condamin, S, Tejedor, V, Voituriez, R, B´nichou, O and Klafter, J (2008) Probing microscopic origins of confined subdiffusion by first-passage observables., *Proc. Natl. Acad. Sci. U. S. A.* **105**, 5675.

4. Choquet, D and Triller, A (2003) The role of receptor diffusion in the organization of the postsynaptic membrane, *Nat. Rev. Neurosci.* **4**, 251.

5. Kusumi, A, Tsunoyama, TA, Hirosawa, KM, Kasai, RS and Fujiwara, TK (2014) Tracking single molecules at work in living cells., *Nat. Chem. Biol.* **10**, 524.

6. Bronstein, I, Israel, Y, Kepten, E, Mai, S, Shav-Tal, Y, Barkai, E and Garini, Y (2009) Transient Anomalous Diffusion of Telomeres in the Nucleus of Mammalian Cells, *Phys. Rev. Lett.* **103**,018102.

7. Weiss, M, Elsner, M, Kartberg, F and Nilsson, T (2004) Anomalous subdiffusion is a measure for cytoplasmic crowding in living cells, *Biophys. J.* **87**, 3518.

8. Golding, I and Cox, EC (2006) Physical Nature of Bacterial Cytoplasm, *Phys. Rev. Lett.* **96**, 098102.

9. Jeon, J-H, Tejedor, V, Burov, S, Barkai, E, Selhuber-Unkel, C, Berg-Sø rensen, K, Odder-shede, L and Metzler, R (2011) In Vivo Anomalous Diffusion and Weak Ergodicity Breaking of Lipid Granules, *Phys. Rev. Lett.* **106**, 048103.

10. Tabei, SMA, Burov, S, Kim, HY, Kuznetsov, A, Huynh, T, Jureller, J, Philipson, LH, Dinner, AR and Scherer, NF (2013) Intracellular transport of insulin granules is a subordinated random walk., *Proc. Natl. Acad. Sci. U. S. A.* **110**, 4911.

11. Saxton, MJ and Jacobson, K (1997) Single-particle tracking: applications to membrane dynamics., *Annu. Rev. Biophys. Biomol. Struct.* **26**, 373.

12. Weigel, AV, Simon, B, Tamkun, MM and Krapf, D (2011) Ergodic and nonergodic processes coexist in the plasma membrane as observed by single-molecule tracking., *Proc. Natl. Acad. Sci. U. S. A.* **108**, 6438.

13. Höfling, F and Franosch, T (2013) Anomalous transport in the crowded world of biological cells, *Rep. Prog. Phys.* **76**, 046602.

14. Bouchaud, J-P and Georges, A (1990) Anomalous diffusion in disordered media: statistical mechanisms, models and physical applications, *Phys. Rep.* **195**, 127.

15. Havlin, S and Ben-Avraham, D (2002) Diffusion in disordered media, *Adv. Phys.* **51**, 187.

16. Klafter, J and Sokolov, IM (2011) First Steps in Random Walks, *Oxford University Press, Oxford.*

17. Saxton, MJ (1994) Anomalous diffusion due to obstacles: a Monte Carlo study, *Biophys. J.* **66**, 394.

18. Klafter, J, Blumen, A and Shlesinger, M F (1987) Stochastic pathway to anomalous diffusion, *Phys. Rev. A* **35**, 3081.

19. Mandelbrot, BB and Van Ness, JW (1968) Fractional Brownian motions, fractional noises and applications, *SIAM Rev.* **10**, 422.

20. Saxton, MJ (1996) Anomalous diffusion due to binding: a Monte Carlo study, *Biophys. J.* **70**, 1250.

21. Ernst, D, Hellmann, M, Köhler, J and Weiss, M Fractional Brownian motion in crowded fluids, *Soft Matter* **8**, 4886.

22. Weigel, AV, Ragi, S, Reid, ML, Chong, EKP, Tamkun, MM and Krapf, D(2012) Obstructed diffusion propagator analysis for single-particle tracking, *Phys. Rev. E* **85**, 041924.

23. Young, AP (1997) Spin glasses and random fields (*World Scientific*).

24. Barkai, E (2003) Aging in Subdiffusion Generated by a Deterministic Dynamical System, *Phys. Rev. Lett.* **90**, 104101.

25. Barkai, E, Garini, Y and Metzler, R Strange kinetics of single molecules in living cells, *Phys. Today* **65**, 29.

26. Cherstvy, AG, Chechkin, AV and Metzler, R (2013) Anomalous diffusion and ergodicity breaking in heterogeneous diffusion processes, *New J. Phys.* **15**, 083039.

27. Metzler, R, Jeon, J-H, Cherstvy, AG and Barkai, E (2014) Anomalous diffusion models and their properties: non-stationarity, non-ergodicity, and ageing at the centenary of single particle tracking, *Phys. Chem. Chem. Phys.* **16**, 24128.

28. Cherstvy, AG , Chechkin, AV and Metzler, R (2014) Particle invasion, survival, and nonergodicity in 2D diffusion processes with space-dependent diffusivity, *Soft Matter* **10**, 1591.

29. Geijtenbeek, TB, Kwon, DS, Torensma, R, van Vliet, SJ, van Duijnhoven, GC, Middel, J, Cornelissen, IL, Nottet, HS, KewalRamani, VN, Littman, DR, Figdor, CG and van Kooyk, Y. (2000) DC-SIGN, a dendritic cell-specific HIV-1-binding protein that enhances trans-infection of T cells, *Cell* **100**, 587.

30. Massignan, P, Manzo, C, Torreno-Pina, JA, Garcia-Parajo, MF, Lewenstein, M and Lapeyre, GJ (2014) Nonergodic Subdiffusion from Brownian Motion in an Inhomogeneous Medium, *Phys. Rev. Lett.* **112**, 150603.

31. Sergé, A, Bertaux, N, Rigneault, H and Marguet, D (2008) Dynamic multiple-target tracing to probe spatiotemporal cartography of cell membranes, *Nat. Methods* **5**, 687.

32. van Kooyk, Y and Geijtenbeek, TBH (2003) DC-SIGN: escape mechanism for pathogens, *Nat. Rev. Immunol.* **3**, 697.

33. Cambi, A, Lidke, DS, Arndt-Jovin, DJ, Figdor, CG and Jovin, TM (2007) Ligand-Conjugated Quantum Dots Monitor Antigen Uptake and Processing by Dendritic Cells, *Nano Lett.* **7**, 970.

34. Cambi, A, Beeren, I, Joosten, B,Fransen, JA and Figdor, CG The C-type lectin DC-SIGN internalizes soluble antigens and HIV-1 virions via a clathrin-dependent mechanism, *Eur. J. Immunol.* **39**, 1923.

35. Michalet, X (2010) Mean square displacement analysis of single-particle trajectories with localization error: Brownian motion in an isotropic medium, *Phys. Rev. E* **82**, 041914.

36. Bel, G and Barkai, E (2005) Weak Ergodicity Breaking in the Continuous-Time Random Walk, *Phys. Rev. Lett.* **94**, 240602.

37. Lubelski, A, Sokolov, IM and Klafter, J Nonergodicity Mimics Inhomogeneity in Single Particle Tracking, *Phys. Rev. Lett.* **100**, 250602.

38. He, Y, Burov, S, Metzler, R and Barkai, E Random Time-Scale Invariant Diffusion and Transport Coefficients, *Phys. Rev. Lett.* **101**, 058101.

39. Montiel, D, Cang, H and Yang, H (2006) Quantitative characterization of changes in dynamical behavior for single-particle tracking studies., *J. Phys. Chem. B* **110**, 19763.

40. Simson, R, Sheets, ED and Jacobson, K (1995) Detection of temporary lateral confinement of membrane proteins using single-particle tracking analysis, *Biophys. J.* **69**, 989.

41. Torreno-Pina, JA, Castro, BM, Manzo, C, Buschow, SI, Cambi, A and Garcia-Parajo, MF (2014) Enhanced receptor-clathrin interactions induced by N-glycan-mediated membrane micropatterning, *Proc. Natl. Acad. Sci. U. S. A.* **111**, 11037.

42. Cutler, PJ, Malik, MD, Liu, S, Byars, JM, Lidke, DS and Lidke, KA (2013) Multi-color quantum dot tracking using a high-speed hyperspectral line-scanning microscope, *PLOS One* **8**, e64320.

43. Masson, J-B, Dionne, P, Salvatico, C, Renner, M, Specht, CG, Triller, A and Dahan, M (2014) Mapping the energy and diffusion landscapes of membrane proteins at the cell surface using high-density single-molecule imaging and Bayesian Inference: application to the multiscale dynamics of glycine receptors in the neuronal membrane, *Biophys. J.* **106**, 74.

44. Feinberg, H, Mitchell, DA, Drickamer, K and Weis, WI (2001) Structural Basis for Selective Recognition of Oligosaccharides by DC-SIGN and DC-SIGNR, *Science* **294**, 2163.

45. Mitchell, DA, Fadden, AJ and Drickamer, K (2001) A novel mechanism of carbohydrate recognition by the C-type lectins DC-SIGN and DC-SIGNR Subunit organization and binding to multivalent ligands, *J. Biol. Chem.* **276**, 28939.

46. Smith, A L, Ganesh, L, Leung, K, Jongstra-Bilen, J, Jongstra, J and Nabel,GJ (2007) Leukocyte specific protein 1 interacts with DC-SIGN and mediates transport of HIV to the proteasome in dendritic cells., *J. Exp. Med.* **204**, 421.

47. Manzo, C, Torreno-Pina, JA, Joosten, B, Reinieren-Beeren, I, Gualda, EJ, Loza-Alvarez, P, Figdor, CG, Garcia-Parajo, MF and Cambi, A (2012) The neck region of the C-type lectin DC-SIGN regulates its surface spatiotemporal organization and virus-binding capacity on antigen-presenting cells., *J. Biol. Chem.* **287**, 38946.

48. Manley, S, Gillette, JM, Patterson, GH, Shroff, H, Hess, HF, Betzig, E and Lippincott-Schwartz, J (2008) High-density mapping of single-molecule trajectories with photoactivated localization microscopy, *Nat. Methods* **5**, 155.

49. Vall´e, RAL, Tomczak, N, Kuipers, L, Vancso, GJ and van Hulst, NF (2003) Single Molecule Lifetime Fluctuations Reveal Segmental Dynamics in Polymers, *Phys. Rev. Lett.* **91**, 038301.

50. Volpe, G, Volpe, G and Gigan, S (2014) Brownian Motion in a Speckle Light Field: Tunable Anomalous Diffusion and Selective Optical Manipulation, *Sci. Rep.* **4**, 3936.

51. Lucioni, E, Deissler, B, Tanzi, L, Roati, G, Zaccanti, M, Modugno, M Larcher, M, Dalfovo, F, Inguscio, M and Modugno, G (2011) Observation of Subdiffusion in a Disordered Interacting System, *Phys. Rev. Lett.* **106**, 230403.

52. Krinner, S, Stadler, D, Meineke, J, Brantut, J-P and Esslinger, T (2013) Direct Observation of Fragmentation in a Disordered, Strongly Interacting Fermi Gas, arXiv:1311.5174.

53. Berkowitz, B, Cortis, A, Dentz, M and Scher, H (2006) Modeling non-Fickian transport in geological formations as a continuous time random walk, *Rev. Geophys.* **44**, n/a.

54. Bascompte, J and Solé, R (1998) Modeling spatiotemporal dynamics in ecology, Environmental intelligence unit (*Springer*).

Chapter 6

The actin cytoskeleton modulates the activation of iNKT cells by segregating CD1d nanoclusters on the cell membrane

In the previous Chapters of this thesis, we have focused in addressing the role of the spatiotemporal behavior of DC-SIGN in controlling its function on the cell membrane of antigen presenting cells. In this Chapter, we focus on the spatiotemporal behavior of the antigen presenting protein CD1d. The aim of choosing an antigen protein, complementary to a receptor such as DC-SIGN, is to demonstrate that the spatiotemporal behavior of a protein on the cell membrane of a leukocyte can control the outcome of an immune reaction as a general principle in human immunology. By using super-resolution nanoscopy and dual-color single particle tracking, we demonstrate that CD1d molecules form nanoclusters at the surface of antigen presenting cells (APCs), whose size, density and lateral mobility is constrained by interactions between CD1d cytosolic tail and the actin cytoskeleton. Formation of larger nanoclusters upon disruption of actin cytoskeleton interactions enhances invariant Natural Killer T (iNKT) cell activation. Importantly, and consistently with iNKT cell activation during inflammatory conditions, exposure of APCs to the TLR7/8 agonist R848 increases nanocluster density and iNKT cell activation. Overall, these results define a novel mechanism that modulates iNKT cell autoreactivity based on the tight control by the APC cytoskeleton of the sizes and densities of endogenous antigen loaded CD1d nanoclusters.

This work is currently under review in *Immunity*: J.A. Torreno-Pina, C. Manzo, M. Salio, M. Aichinger, V. Cerundolo, M.F. Garcia-Parajo, “The Actin Cytoskeleton down-regulates the activation of NKT cells by segregating CD1d nanoclusters on antigen presenting cells”.

Introduction

It is well established that different populations of T lymphocytes can recognize not only peptides in the context of MHC class I and class II molecules, but also foreign and self-lipids in association with CD1 proteins (1), antigen-presenting molecules which share structural similarities with MHC-class I molecules (Fig. 6.1). Of the five CD1 isoforms, CD1d restricts the activity of a family of cells known as invariant Natural Killer T (iNKT) cells, because of their semi-invariant T Cell Receptor (TCR) usage (2). To date, the exogenous glycolipid α-GalactosylCeramide (α-GalCer) represents the strongest CD1d-restricted agonist for iNKT cells (3). Unlike conventional peptide specific T cells, iNKT cells react against CD1d$^+$ antigen presenting cells (APCs) in the absence of exogenous antigens, a feature defined as autoreactivity (4). iNKT cell autoreactivity underpins the constitutive memory phenotype of iNKT cells and their ability to be activated during a variety of immune responses, from infections to cancer and autoimmunity (1). Some of the endogenous antigens known to elicit iNKT cell autoreactivity belong to glycosphingolipid families, with a mix of α and β anomeric configurations (5-8). How iNKT cell autoreactivity is fine-tuned to prevent autoimmunity is subject of much investigation. Previous results have shown that exposure of APCs to TLR agonists enhances iNKT cell autoreactivity (9,10), consistent with the proposed mechanism by which ligand availability is regulated by lysosomal glycosidases (5,7).

The recent application of advanced optical techniques (11-19) in combination with substrate patterning and functionalization (20-22) is providing detailed information on how the lateral organization of a variety of molecules located on both sides of the immunological synapse contributes to controlling T cell activation (23-25). Specifically, single molecule dynamic approaches and super-resolution optical nanoscopy experiments have provided indisputable proof that many receptors on the cell membrane organize in small nanoclusters prior to ligand activation as described in Chapter 1 (27). Membrane nanodomains enriched in cholesterol and sphingolipids (28), protein-protein

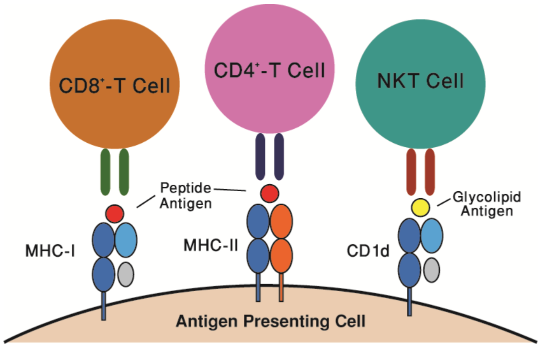

Figure 6.1 Unlike classical peptide presenting MHC complexes, CD1d presents glycolipid antigens to iNKT cells (adapted from Van Kaer (26)). Moreover, CD1d can prime iNKT cells by presenting self-lipids under inflammatory conditions via Toll-like receptor stimulation.

interactions (29) and interactions between transmembrane proteins and the cytoskeleton (29-32) have been all implicated in regulating receptor dynamics and nanoclustering. An emerging concept attributes the actin cytoskeleton the ability of imposing barriers or fences on the cell membrane restricting the lateral mobility of transmembrane proteins (30,33). This transient restriction would in turn increase the local concentration of transmembrane proteins leading to protein nanoclusters. For instance, it has been shown that the actin cytoskeleton promotes the dimerization rate of EGF receptors by monomer co-confinement and facilitates ligand binding and signaling activation (29,31). Confinement of CD36 has also been observed as a result of its diffusion along linear channels dependent on the integrity of the actin cytoskeleton (34). This constrained diffusion promotes CD36 clustering, influencing CD36-mediated signaling and internalization. A similar mechanism has been proposed for the maintenance of MHCI clusters on the cell membrane by the actin cytoskeleton, with loss of MHCI clustering resulting in a decreased CD8-T Cell activation (35-37). Recent confocal microscopy studies have revealed that the association between agonist loaded-CD1d molecules and lipid rafts might contribute to the regulation of iNKT cell activation (38). This elegant study for the first time linked the spatial organization of CD1d molecules using standard fluorescence microscopy on the cell membrane of APCs with the activation profile of iNKT cells. However, it remains unclear whether the results of these experiments obtained using mouse cells can be extended to human cells and whether further insights can be obtained by using higher resolution microscopy. Indeed, it is not yet known whether CD1d molecules exist as monomers or as nanoclusters and whether the actin cytoskeleton might regulate CD1d lateral organization and iNKT cell activation.

In this Chapter, we describe the combination of dual-color single molecule dynamic approaches with super-resolution optical nanoscopy to characterize for the first time the spatiotemporal behavior of CD1d on living human myeloid cells. We find that α-GalCer loaded human CD1d (hCD1d) molecules are organized in nanoclusters on the cell membrane of APCs. We report that the actin cytoskeleton prevents enhanced hCD1d nanoclustering by hindering physical encountering between hCD1d diffusing nanoclusters, thus reducing basal iNKT cell activation. Furthermore, we observed an increase in nanocluster density upon activation of APCs with inflammatory stimuli, such as Toll like receptor (TLR) stimulation, mirroring the increased iNKT cell stimulation. Notably, even during inflammation the actin cytoskeleton retains an important role to limit hCD1d cluster size and iNKT cell activation. Overall, our results suggest that regulation of CD1d nanoclustering through the actin cytoskeleton represents a novel mechanism to fine tune peripheral iNKT cell autoreactivity.

Results

The actin cytoskeleton regulates the mobility of α-GalCer loaded human CD1d molecules. To study the lateral behavior of CD1d on the cell membrane of APCs, we first performed high-speed single particle tracking (SPT) on the human myelomonocytic cell line THP-1, transduced with lentiviral vectors encoding human CD1d (hCD1d) molecules and pulsed with the iNKT cell agonist α-GalCer. α-GalCer loaded hCD1d molecules were labeled at low density using a conjugate consisting of an iNKT- T cell receptor (iNKT-TCR) (39,40) and a quantum dot (QD655) (Fig. 6.2A). To ensure a single iNKT-TCR per QD, the iNKT-TCR-QD conjugate was prepared in a 10x excess of free biotin to occlude QD excess binding sites. As further control to rule out any potential cross-linking effects induced by the QD multivalency, we also used the α-GalCer-hCD1d specific Fab fragment (Fab9b) covalently attached to the small dye Atto647N (39,40). As a third control for the iNKT-TCR probe, α-GalCer loaded hCD1d molecules were also labeled using the monovalent anti-CD1d antibody (CD1d42) conjugated to a QD under similar excess of free biotin. THP-1 cells were imaged on the ventral side using total internal reflection fluorescence microscopy (TIRFM). Individual features were detected and tracked to generate mobility trajectories (Fig. 6.2B). Individual trajectories were analyzed using custom-made algorithms to derive their instantaneous diffusion coefficient at short diffusion times (time lags 2 to 4) D_{2-4} (Fig. 6.2C-F). The median D_{2-4} from multiple trajectories of α-GalCer loaded hCD1d molecules labeled with the iNKT-TCR-QD conjugate on different cells was 0.029 $\mu m^2/s$ (Fig. 6.2C). Similar diffusion profiles and median diffusion coefficients were also obtained with Fab9b-Atto647N (Fig. 6.2C) or when labeling α-GalCer loaded hCD1d using the monovalent CD1d42-QD Ab (Fig. 6.3). Altogether, these controls demonstrate that the lateral mobility of α-GalCer loaded hCD1d molecules is not affected by the iNKT-TCR-QD conjugate used throughout this study.

To address the potential role of the actin cytoskeleton in regulating the lateral mobility of CD1d on the cell membrane of APCs, we then treated THP-1 cells with the actin cytoskeleton-perturbing drug CytochalasinD (CytoD) (32). CytoD treatment at a concentration of 10 μM for 60 min resulted in a nearly three-fold reduction in the instantaneous mobility of α-GalCer loaded hCD1d with a median D_{2-4} of 0.011 $\mu m^2/s$ (Fig. 6.2D). Cell viability was not compromised under these conditions, as shown by propidium iodide staining (Fig. 6.4). Similar results were obtained when we followed the lateral mobility of α-GalCer loaded hCD1d molecules upon CytoD treatment using the monovalent CD1d42-QD Ab (Fig. 6.3).

It has previously been shown that treatment of cells with a range of cytoskeleton perturbing drugs increases the instantaneous mobility of receptors, such as the FcεRI receptor (30) and the B-Cell receptor (32), which has been accounted for by the breaking of actin barriers, which otherwise restrict the diffusion of receptors on the plasma membrane. To enquire whether the unexpectedly observed reduced mobility of hCD1d molecules is CD1d specific or whether it results from an overall change of the membrane environment due to the CytoD treatment, we compared it with the mobility of CD71 molecules on THP-1 cells. In marked contrast to the behavior of hCD1d molecules and consistent with the literature (41), treatment of THP1 cells with 10 µM of CytoD led to a significant increase of CD71 diffusion (Fig. 6.5), indicating that the

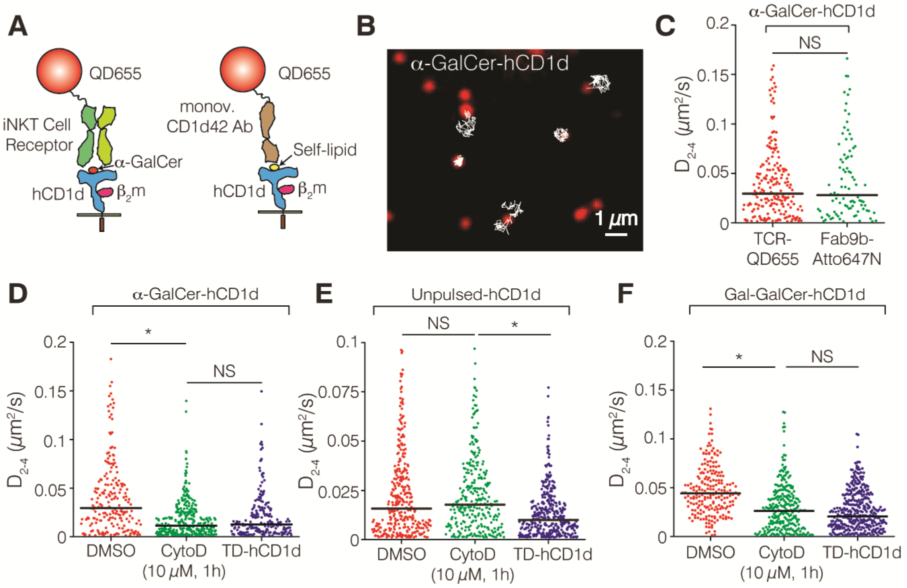

Figure 6.2 The actin cytoskeleton affects the mobility of hCD1d molecules on the surface of APCs. (**A**) Schematic illustration of the labeling procedure. (Left) α-GalCer loaded hCD1d (blue) were labeled using a conjugate of an iNKT-TCR (light and dark green) and a QD (red). (Right) Unpulsed hCD1d molecules were labeled using a monovalent anti-CD1d42 Ab conjugated to a QD. Not to scale. (**B**) Selected TIRFM image of the ventral side of a α-GalCer pulsed THP-1 cell displaying individual iNKT-TCR-QD-labeled hCD1d molecules (red) on the cell membrane. Representative 2D trajectories (white) are overlaid on the raw image (frame rate=100 Hz). (**C**) Distributions of the $D_{2\text{-}4}$ values of α-GalCer loaded hCD1d labeled with the iNKT-TCR-QD conjugate or with Fab9b-Atto647N. (**D**,**E**) Distributions of the $D_{2\text{-}4}$ values for α-GalCer-pulsed (**D**) or unpulsed (**E**) THP-1 cells treated with 10 µM CytoD or expressing TD-hCD1d mutant molecules. (**F**) Distribution of the $D_{2\text{-}4}$ values of Gal-GalCer loaded hCD1d, after treatment with 10 µM CytoD or expressing TD-hCD1d mutant molecules. Data are representative from typically 200 trajectories per condition (90 trajectories in the case of hCD1d labeled with Fab9b-Atto647N) from at least 25 cells over 8 different experiments. *$P<0.0001$, NS: not significant ($P>0.05$) (Student's t-test).

observed reduced mobility of hCD1d is specific. Finally, to rule out any other potential secondary effects induced by CytoD, we measured the mobility of a cytoplasmic tail deleted hCD1d (TD-hCD1d) mutant, which lacks the final 10 amino acid residues including the AP-2 and AP-3 internalization motif and the lysine residue which is a target for ubiquitination (42). Consistent with the results obtained with CytoD treated THP-1 cells, the mobility of the α-GalCer loaded TD-hCD1d mutant was slower than that of α-GalCer loaded wild type (WT) hCD1d (Fig. 6.2D).

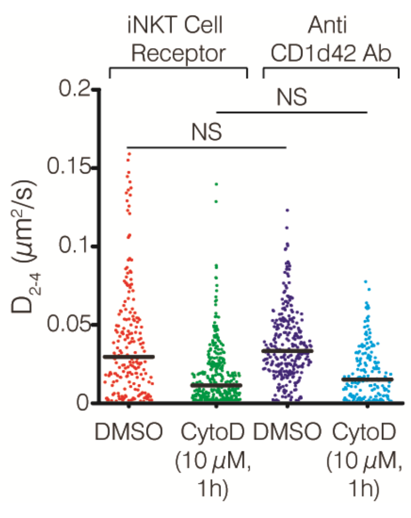

Figure 6.3 The iNKT-TCR-QD conjugate does not influence the mobility of α-GalCer loaded hCD1d on THP-1 cells. To rule out the possibility that the iNKT-TCR-QD conjugate influenced the lateral mobility of α-GalCer loaded hCD1d molecules, we performed an extra control experiment in addition to the Fab-Atto647N labeling experiments shown in Fig. 6.2C. Specifically, we labeled α-GalCer loaded hCD1d molecules with a monovalent anti-CD1d42 Ab conjugated to a QD655 and found no difference in terms of hCD1d lateral mobility as compared to iNKT-TCR-QD labeling. Moreover, equal reduction of lateral mobility was observed after treating the cells with CytoD, using the two different probes, demonstrating that the iNKT-TCR does not have any influence in the mobility of hCD1d. At least 189 trajectories on 14 cells over 2 different experiments per condition. NS: not significant ($P>0.05$) (Student's t-test).

Upon biosynthesis and egress from the ER, CD1d molecules reach the cell surface and continuously recycle through the endolysosomal compartment, where they sample different pools of self and foreign lipid antigens (43). While presentation of complex exogenous antigens requires CD1d molecules to traffic deep into the lysosomes (44), autoreactivity of human iNKT cells has been shown to have different requirements for CD1d lysosomal trafficking, possibly as a result of the different APCs used in the experiments (40,45). To test whether these different trafficking pathways have an influ-

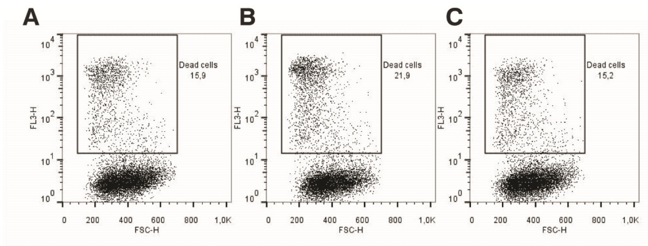

Figure 6.4 Cell viability was not compromised under CytoD treatemtent. Propidium iodide staining of (**A**) control, (**B**) DMSO and (**C**) CytoD treated THP1 cells.

ence on the lateral mobility of human CD1d, we imaged unpulsed THP-1 cells and tracked hCD1d molecules labeled with anti-CD1d42-QD (Fig. 6.2). The lateral mobility of unpulsed WT-hCD1d molecules was almost half of α-GalCer loaded molecules (Fig. 6.2E). In strong contrast to α-GalCer loaded molecules, however, the lateral mobility of unpulsed WT-hCD1d molecules was not affected by CytoD treatment (median D_{2-4} of 0.017 $\mu m^2/s$ compared to the control case of 0.015 $\mu m^2/s$). Moreover, the mobility of the unpulsed TD-CD1d mutant modestly reduced 1.5-fold as compared to the WT counterpart (0.009 $\mu m^2/s$) (Fig. 6.2E). These results therefore suggest that the mobility of hCD1d molecules differs depending on whether we sample molecules that have just reached the cell surface from the ER (i.e., unpulsed and thus presenting self-lipids) or whether they have been recycling through the early and late endosomes. To further strengthen these observations, we analyzed the lateral mobility of WT-hCD1d and TD-hCD1d molecules loaded with Gal(α1->2)GalCer (hereafter referred to as Gal-GalCer) which requires cleavage of the terminal galactose by α-galactosidase A in the lysosome for recognition by the iNKT-TCR (44). Recognition of this pool of hCD1d molecules by the iNKT-TCR-QD thus identifies a cohort of hCD1d molecules that has exclusively trafficked through the endolysosomes and recycled back to the cell surface. These experiments indicated that the lateral mobility of Gal-GalCer loaded hCD1d molecules was significantly reduced upon CytoD treatment or deletion of the cytosolic tail (Fig. 6.2F), in analogy to the results obtained for α-GalCer loaded hCD1d. Altogether, these results demonstrate that in the absence of interactions between CD1d

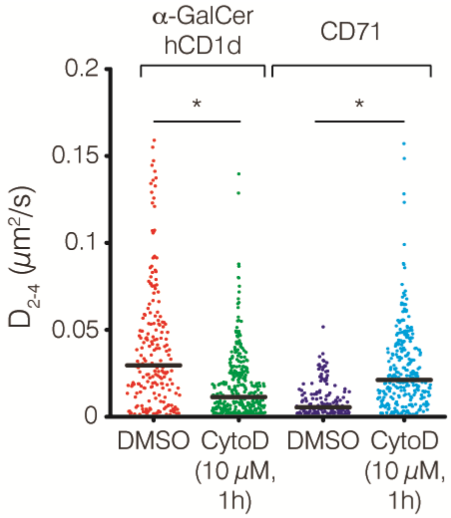

Figure 6.5 Reduction of hCD1d lateral mobility upon CytoD treatment is CD1d specific. To rule out the possibility that the strong CytoD treatment (10 μM, 60 min) to THP-1 cells could induce an overall change on the cell membrane affecting the mobility of all receptors, including hCD1d, we performed SPT of the transferrin receptor (CD71) whose mobility has been reported to increase upon perturbation of the actin cytoskeleton (41). CD71 was labeled using a monoclonal Ab against CD71 labeled with QD655. Changes in the lateral mobility of hCD1d upon CytoD treatment are hCD1d specific since the lateral mobility of CD71 on the cell membrane of THP-1 cells is increased using the same CytoD treatment, as opposed to the reduced mobility measured on α-GalCer loaded hCD1d labeled with iNKT-TCR-QD. Data on CD71 are representative from at least 194 trajectories, 9 cells and 2 different experiments. *$P<0.0001$ (Student's t-test).

molecules and the actin cytoskeleton, the lateral mobility of hCD1d recycled through the endosomes is drastically reduced.

The actin cytoskeleton regulates the nanoclustering of α-GalCer loaded hCD1d molecules. Previous reports indicate that the actin cytoskeleton regulates the lateral organization and nanoclustering of receptors on the cell membrane (34,46). Given the marked effect of the actin cytoskeleton on the lateral mobility of hCD1d molecules that traffic through endosomes, we thought to visualize the nanoscale organization of unpulsed and α-GalCer loaded hCD1d on the surface of THP-1 cells using stimulated emission depletion (STED) nanoscopy (47,48). We focused on WT-hCD1d and the TD-hCD1d mutant since SPT experiments showed a significant difference in their lateral mobility. STED images of anti-CD1d42 labeled hCD1d were performed on the dorsal side of fixed THP-1 cells. Images were analyzed using a custom-made algorithm based on Bayesian inference of the fluorescence intensity distribution as described in Chapter 2, improving data quantification and increasing the effective resolution beyond that of STED raw images (49). Interestingly, α-GalCer loaded WT-hCD1d molecules formed small nanoclusters on the surface of THP-1 cells with a median cluster size of 78 nm, containing 3.8 median number of hCD1d molecules/cluster (Fig. 6.6A-C) resulting in a nanocluster density of ~75 hCD1d/μm^2 (Fig. 6.6D). Unpulsed WT-hCD1d molecules also formed nanoclusters on the cell surface of THP-1 with comparable nanocluster density to α-GalCer loaded hCD1d (Fig. 6.6D). To rule out the possibility that nanoclustering results from the enhanced expression of hCD1d on transduced THP-1 cells, we imaged hCD1d on blood-derived primary human CD14$^+$ monocytes. Analysis of STED images confirmed the presence of hCD1d nanoclusters, albeit being smaller in size (49 nm as median cluster size) compared to THP-1 cells (Fig. 6.7). These data demonstrate that hCD1d forms nanoclusters on the plasma membrane of APCs.

Remarkably, α-GalCer loaded TD-hCD1d molecules, lacking the cytoplasmic tail, showed significantly larger and denser nanoclusters with a molecular density nearly three-fold higher (197 ± 17 hCD1d/μm^2) than α-GalCer loaded WT-hCD1d (Fig. 6.6E-G). In contrast, although self-lipid loaded TD-hCD1d molecules displayed slightly larger nanoclusters compared to self-lipid loaded WT-hCD1d molecules, no significant difference in molecular density was observed (Fig. 6.6H-J). Since truncation of the cytoplasmic tail leads to larger nanoclusters, the STED data indicate that α-GalCer loaded hCD1d nanocluster size and density are tightly regulated by the actin cytoskeleton. Importantly and consistent with our SPT results, the increased nanoclustering of α-GalCer loaded TD-hCD1d directly correlates with its reduced mobility on the membrane (Fig. 2D). Moreover, the lack of changes in nanocluster density on unpulsed TD-hCD1d compared to WT-hCD1d indicates once more that the effect of the actin cytoskeleton on hCD1d organization is predominantly on the pool of molecules that has trafficked through the lysosome. Consistent with these observations,

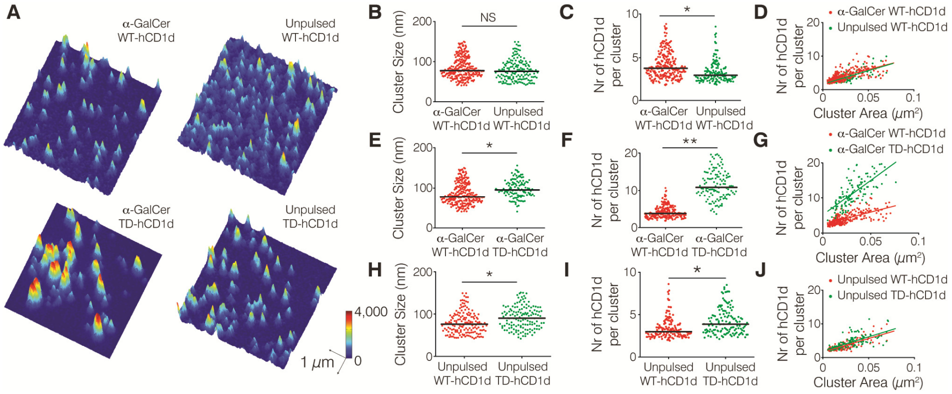

Figure 6.6 The actin cytoskeleton regulates the nanoclustering of α-GalCer loaded hCD1d on the plasma membrane of APCs. (**A**) STED images of α-GalCer pulsed (left) and unpulsed (right) THP-1 cells transfected with WT-hCD1d (upper) or TD-hCD1d (lower) mutant. Cells were stretched onto PLL-coated coverslips and labeled with anti-CD1d42 Ab. (**B**,**E**,**H**) Cluster size distribution, (**C**,**F**,**I**) distribution of the number of hCD1d molecules per cluster and (**D**,**G**,**J**) scatterplots of number of hCD1d molecules per cluster vs. cluster area corresponding to the quantification of the STED images. STED nanoscopy data are representative from at least 45 different images per condition, of 3x3 μm in size from at least 2 different experiments. *P<0.0001 and **P<1•10-7 (Student's t-test).

Gal-GalCer loaded TD-hCD1d also formed larger nanoclusters with increased density compared to Gal-GalCer loaded WT-hCD1d molecules (Fig. 6.8).

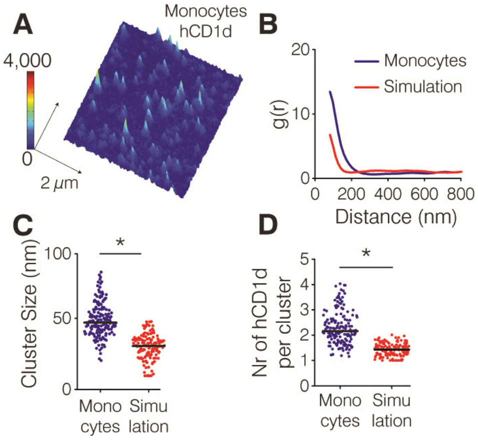

Figure 6.7 CD1d forms nanoclusters on the cell membrane of human monocytes. (**A**) Representative STED image of hCD1d on the cell membrane of monocytes. (**B**) Comparison between the correlation functions of the experimental data (blue) and corresponding Monte-Carlo simulations (red) of CD1d molecules randomly organized on the cell membrane using the same particle density as the experimental data. (**C**) Comparison between the experimental CD1d cluster size (blue) and simulations of random organization (red). (**D**) Comparison between the number of molecules per cluster obtained on the experimental data (blue) and the simulations (red). Experimental and simulated data are representative from at least 52 different STED images of 3x3 μm in size belonging to at least 2 different experiments. *P<0.0001 (Student's t-test).

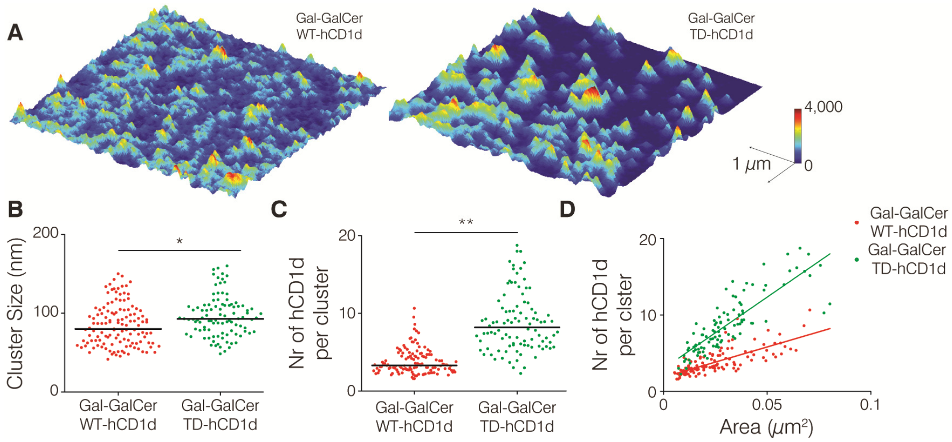

Figure 6.8 The actin cytoskeleton regulates the nanoclustering degree of Gal-GalCer loaded hCD1d molecules on the cell membrane. (**A**) STED images of Gal-GalCer-pulsed THP-1 cells transfected with WT-hCD1d (left) or TD-hCD1d mutant (right). Cells were stretched onto PLL-coated coverslips and labeled with anti-CD1d42 Ab. (**B**) The cluster size of Gal-GalCer loaded TD-hCD1d nanoclusters is increased compared to Gal-GalCer loaded WT-hCD1d nanoclusters. (**C**) Strong increase in the number of hCD1d molecules per cluster when deleting the cytoplasmic tail of hCD1d. (**D**) Increased density of TD-hCD1d nanoclusters compared to WT-hCD1d nanoclusters. Analysis data correspond to at least 43 different STED images of 3x3 µm in size belonging to at least 2 different experiments. *$P<0.001$, **$P<0.0001$ (Student's t-test).

Perturbation of the actin cytoskeleton increases dynamic interactions between α-GalCer loaded hCD1d nanoclusters. We hypothesized that the increased nanoclustering observed on α-GalCer loaded TD-hCD1d might result from dynamic encounters between individual nanoclusters that could favorably merge with each other in the absence of cytoskeleton interactions. To test this possibility in living cells we applied dual color SPT. We labeled α-GalCer loaded hCD1d using two different QDs (Fig. 6.9A) at equimolar concentrations to increase the probability of detecting nano cluster interaction events (Fig. 6.9B), while allowing for single pair trajectory recording. Two-dimensional trajectories of spatially close QDs (red and green) were generated (Fig. 6.9C) and their separation distance was plotted vs. time (Fig. 6.9D). In the case of truly interacting nanoclusters, their separation distances should remain small (close to the nanocluster size) for periods longer than random encounter events. As expected, CytoD treatment of α-GalCer loaded WT-hCD1d and α-GalCer loaded TD-hCD1d showed significantly shorter separation distances over time compared to the untreated pulsed WT-hCD1d control (Fig. 6.9B,D,E) (median interparticle distance of 106 nm for CytoD treated cells, 130 nm for TD-hCD1d and 284 nm for the control case). These results were further validated by Monte-Carlo simulations of random encounters while accounting for the respective diffusion coefficients in the three different cases. The shorter distances experimentally obtained as compared to the simulations (Fig. 6.9E) confirm real interactions between hCD1d nanoclusters upon perturbation of actin cytoskeleton interactions, following either CytoD treatment or removal of the hCD1d cytoplasmic tail. These sustained interactions (lasting at least 1s in our experiments) would effectively increase hCD1d nanoclustering in the absence of actin cytoskeleton interactions, consistent with the super-resolution data.

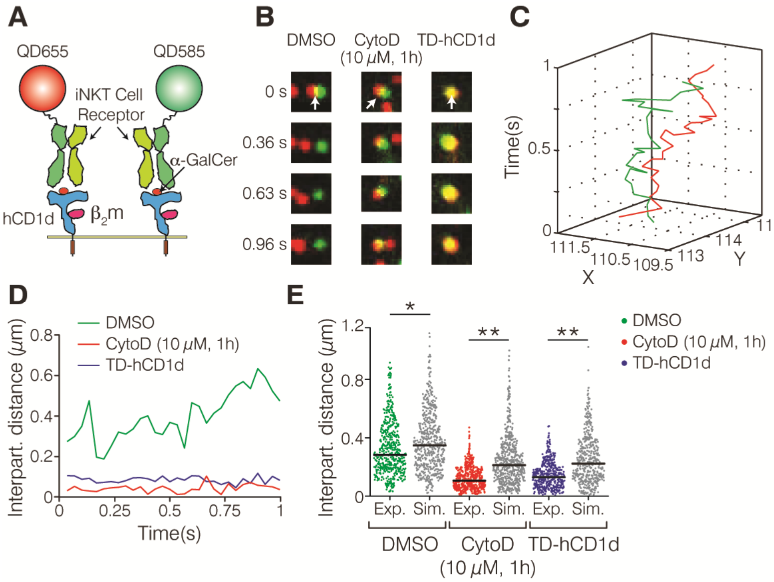

Figure 6.9 The actin cytoskeleton regulates dynamic interactions between α-GalCer loaded hCD1d nanoclusters. (**A**) Schematic illustration of two α-GalCer loaded hCD1d molecules (blue) labeled with two different iNKT-TCR-QD-conjugates (green and red) at equimolar concentrations. Not to scale. (**B**) Magnified dual-color TIRFM images (1.9 μm in size) displaying two diffusing hCD1d nanoclusters over time, for the control case (left column), CytoD treated samples (middle column) and the TD-hCD1d mutant (right column). White arrows indicate the starting time of the interaction. (**C**) Representative dual-color trajectories of two different hCD1d nanoclusters reconnected over a total observation time of 1s (frame rate: 30 Hz). (**D**) Separation distances of two α-GalCer loaded hCD1d nanoclusters over time for untreated WT–hCD1d (green), CytoD treated WT-hCD1d (red) and the TD-hCD1d mutant (blue). (**E**) Distributions of the interparticle distances from experimental data (color dots) together with Monte Carlo simulations of random encounters (gray dots). Data are representative of at least 20 different trajectories on 9 different cells per condition over 6 different experiments. *P<0.0001 and **P<1•10-5 (Student's t-test).

The actin cytoskeleton spatiotemporally arrests diffusing α-GalCer loaded hCD1d nanoclusters on the cell membrane. The data presented so far indicate that the actin cytoskeleton somehow hinders dynamic interactions between hCD1d nanoclusters preventing their further coalescence into larger clusters. To directly visualize how actin might accomplish such a role we performed dual-color TIRFM imaging of hCD1d and actin. We used hCD1d transduced THP-1 cells expressing lifeact-GFP (50), a fluorescent marker of F-actin. We labeled individual α-GalCer loaded hCD1d nanoclusters with the iNKT-TCR-QD conjugate and followed their lateral mobility with respect to actin, as previously reported for other cell membrane receptors (30,32) (Fig. 6.10A). Individual trajectories of diffusing WT-hCD1d nanoclusters were reconnected and superimposed on the actin image (Fig. 6.10B,C). Interestingly, WT-hCD1d nanoclusters exhibited a highly restricted mobility in actin-rich regions (Fig. 6.10B). In contrast, WT-hCD1d mobility increased in actin-poor regions (Fig. 6.10C). These

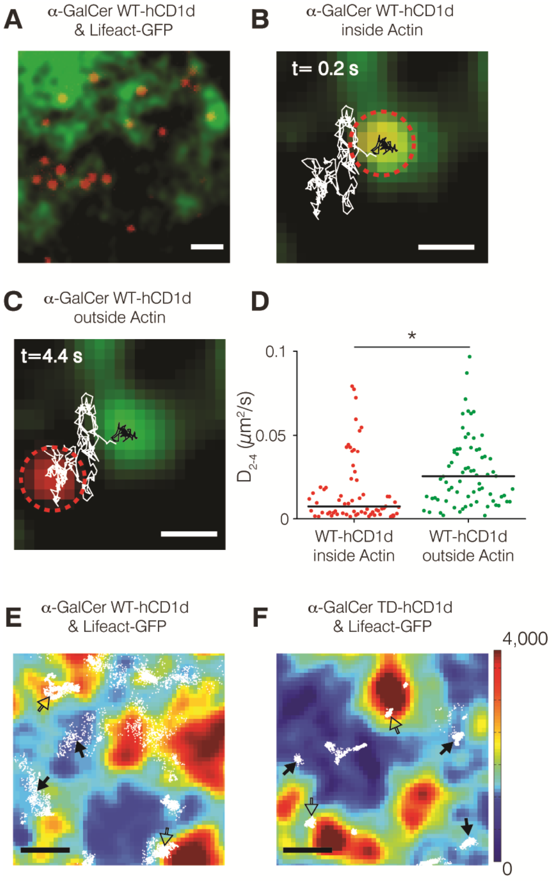

Figure 6.10 The actin cytoskeleton actively arrests diffusing α-GalCer loaded hCD1d nanoclusters on the cell membrane. (**A**) Snapshot of a dual-color TIRFM video displaying lifeact-GFP labeled actin (green) and α-GalCer loaded hCD1d nanoclusters (red). Scale bar: 2 μm. (**B**,**C**) Representative magnified TIRFM images at two different time sequences with an example of a 2D trajectory of α-GalCer loaded hCD1d diffusing inside (black line) and outside (white line) actin-rich regions, with the diffusing particle outlined with a red-dashed circle. In panel (**B**) hCD1d is inside actin, while (**C**) shows the time sequence when hCD1d is outside actin. Scale bar: 500 nm. (**D**) Distributions of the D_{2-4} values for α-GalCer loaded hCD1d nanoclusters inside and outside high-actin regions. (**E**,**F**) Cumulated cartography maps containing 8000 localizations from α-GalCer loaded WT-hCD1d (**E**) and TD-hCD1d (**F**) overlaid onto a lifeact-GFP TIRFM image. The white dots correspond to the different spatial positions explored by hCD1d during the observation time (20s). The pseudo-colored image corresponds to the actin intensity, going from blue (actin-low) to red (actin-rich). The black filled arrows point to hCD1d diffusion on actin-poor regions, whereas empty-black arrows point to hCD1d diffusing close to actin-rich regions. Scale bar: 1 μm. SPT data from at least 87 trajectories on 30 different cells over 5 different experiments. *$P<0.0001$ (Student's t-test).

observations were substantiated by calculating the instantaneous mobility of individual trajectories inside and outside actin-rich regions. Indeed, WT-hCD1d nanoclusters displayed a remarkably slow diffusion inside actin-rich regions (median $D_{2-4} = 0.0074$ $\mu m^2/s$) compared to outside ($D_{2-4} = 0.025$ $\mu m^2/s$), revealing that the actin cytoskeleton arrests mobile α-GalCer loaded hCD1d nanoclusters once they enter into actin-rich regions (Fig. 6.10D).

To obtain a more robust quantification of the data we generated cartography maps of α-GalCer loaded WT-hCD1d and α-GalCer loaded TD-hCD1d superimposed on actin fluorescence images. These maps provide the spatial positions of hCD1d nanoclusters as they dynamically explore the cell membrane in relation to actin, with a localization accuracy of 20nm (51) (Fig. 6.10E,F). Cartography maps of α-GalCer loaded WT-hCD1d showed two different features: a) more dispersed localization positions outside actin regions resulting from its dynamic exploration of the cell membrane and; b) highly concentrated localization positions in actin-rich areas consistent with the arrest of the receptor in these regions (Fig. 6.10E). In contrast, no noticeable difference in terms of localization distribution with respect to actin was observed for α-GalCer loaded TD-hCD1d (Fig. 6.10F), already suggesting that the dynamic exploration of α-GalCer loaded TD-hCD1d is actin-independent.

To quantify these observations in a more robust way we developed an algorithm that computes the spatial localizations of CD1d as a function of the actin signal. Specifically, we generated two concentric circles with different radii R_1 and R_2 (R_1=225 nm and R_2=1035 nm) and having each time a given localization of the cartography map as the center for both circles (Fig. 6.11A,B). The total number of localizations enclosed in each circle was then quantified; with N_1 being the total number of localizations enclosed by circle R_1 and N_2 = (# of localizations in $R_2 - N_1$). Moreover, the mean raw fluorescence intensity value of actin (A_1 and A_2 from R_1 and R_2, respectively) enclosed by each radius was also extracted from the superimposition of the circles on top of the actin image. This procedure was repeated by positioning the center of the two concentric circles at each hCD1d localization value. Then, the behavior of WT-CD1d and TD-CD1d molecules with respect to the actin cytoskeleton was extracted by plotting the relative fraction of hCD1d localizations (N_1/N_2) against $(A_1-A_2)/A_1=\Delta$Actin. Only cells with a similar expression of lifeact-GFP were selected for this analysis. WT-hCD1d displayed a clear linear relationship between the number of localizations positions and the amount of actin, with a positive slope of 0.34 ± 0.03, indicating that higher number of WT-hCD1d localization positions directly correlates with higher values of actin intensity (Fig. 6.11C). This increased number of spatial positions in actin-rich areas means that the receptor explores multiple times the same region, remaining spatiotemporally confined by actin. Together with the restricted mobility of WT-hCD1d observed on the actin-rich regions (Fig. 6.10D), these results prove that the actin cytoskeleton actively arrests WT-hCD1d nanoclusters on the cell membrane, preventing their further aggregation. In marked contrast, the number of localizations positions for TD-hCD1d shows only a weak dependence on actin (slope of 0.07 ± 0.08) (Fig. 6.11C) demonstrating no preferred interactions between TD-hCD1d and the actin cytoskeleton.

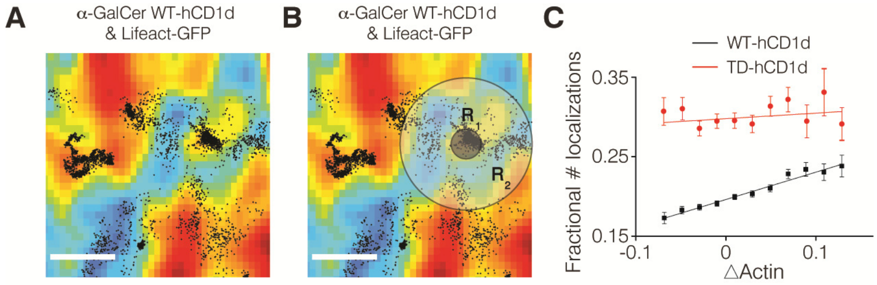

Figure 6.11 Quantification of cartography maps. At each given hCD1d localization position two concentric circles of radii R_1 and R_2 and drawn and the number of localization positions and actin intensity signal in each circle is measured to derive the fractional occurrence of localization positions as a function of actin intensity changes between the two circles. (**A**) Representative magnified cartography map of the spatial localization positions explored by hCD1d with respect to actin. (**B**) Illustration of the methodology used for data quantification. Notice that in this example, a large number of concentrated localizations are obtained on an actin-rich region delimited by the circle with radius R_1, whereas more dispersed localizations are obtained within the circle of radius R_2. Scale bars are 1 µm. (**C**) Fractional occurrence of hCD1d localization positions vs. changes in actin intensity, ΔActin for α-GalCer loaded WT-hCD1d (black) and α-GalCer loaded TD-hCD1d (red). Data were fitted with a straight line and the slope was obtained. Cartography maps data contain at least 8000 localizations. Analysis has been performed on 6 different cells and 3 different experiments per condition.

Perturbation of the actin cytoskeleton of APCs results in enhanced iNKT cell activation. Given that perturbing actin cytoskeleton interactions resulted in enhanced α-GalCer loaded hCD1d nanoclustering on APCs, we sought to address the consequences consequences of such altered spatiotemporal organization on iNKT cell activation (Fig. 6.12). APCs were pulsed with different α-GalCer concentrations and treated with CytoD (10uM for 1h). APCs were then fixed and incubated with iNKT cells. IFN-γ production upon iNKT cell activation was measured by ELISA. Notably, CytoD-treated hCD1d-tranduced THP-1 cells (Fig. 6.12A) and CytoD-treated immature dendritic cells (Fig. 6.12B) elicited increased iNKT cell activation compared to untreated controls. The increase in IFN-γ production was not due to increased hCD1d expression upon CytoD treatment (Fig. 6.12C). Interestingly, enhanced iNKT cell activation was more pronounced at low antigen dose (2.7 fold increase at 5 ng/ml compared to 1.2 fold increase at 150 ng/ml α-GalCer concentration) in agreement with other reports where nanoclustering of antigen presenting proteins have been shown to enhance more effectively T cell activation at low agonist densities (52,53).

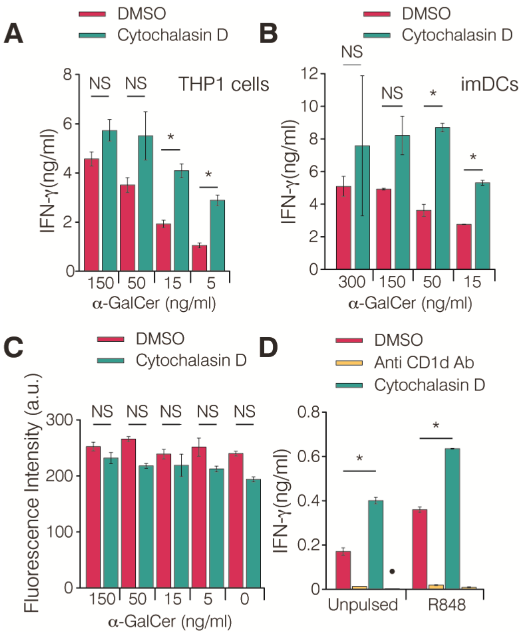

Figure 6.12 Perturbation of the actin cytoskeleton on α-GalCer pulsed APCs enhances iNKT cell activation. (**A**,**B**) IFN-γ production upon iNKT cell activation by (**A**) hCD1d transduced THP1 cells or (**B**) immature dendritic cells (imDCs), pulsed with the given α-GalCer concentrations overnight before treatment with CytoD. (**C**) Expression levels of hCD1d as measured by FACS after treating THP1 cells with CytoD (10 μM, 60 min). (**D**) IFN-γ production upon iNKT cell activation by hCD1d THP1 cells stimulated with 10 μg/ml of TLR 7/8 ligand R848 for 30h before CytoD treatment. (•) Intensity value below the detection limit. Data are representative of 3 different experiments. *P<0.05, NS: not significant (P>0.05) (Student's t-test).

The actin cytoskeleton regulates hCD1d nanoclustering under inflammatory conditions. It has been described that innate stimuli, such as Toll-like receptor (TLR) stimulation, can trigger iNKT cell activation in a CD1d-dependent manner (9,10,40). To test whether perturbation of the actin cytoskeleton of APCs exposed to inflammatory conditions also resulted in enhanced iNKT cell activation, we treated hCD1d transduced THP-1 cells with the TLR7/8 ligand R848. After CytoD treatment and fixation, APCs were incubated with iNKT cells. Increased IFN-γ production by R848-matured CytoD treated WT-hCD1d THP1 cells was observed, in line with the results with lipid pulsed cells (Fig. 6.12D). Moreover, increased IFN-γ production was hCD1d-dependent since blocking with an anti-CD1d Ab resulted in total abrogation of iNKT cell activation. Altogether these results strongly indicate that the actin cytoskeleton of APCs controls the activation of iNKT cells under innate and adaptive stimuli.

Since perturbation of the actin cytoskeleton of APCs resulted in enhanced iNKT cell activation upon R848 treatment of THP1 cells, we next addressed whether the actin cytoskeleton regulates hCD1d nanoclustering under inflammatory conditions. We stimulated both WT-hCD1d and TD-hCD1d transduced cells with the TLR7/8 ligand R848, performed STED nanoscopy (Fig. 6.13A) and analyzed hCD1d cluster size and composition. Interestingly, R848 stimulated WT-hCD1d formed smaller nanoclusters (47 nm as median cluster size) (Fig. 6.13B) than the unstimulated controls (77 nm as median cluster size). However, those nanoclusters displayed a significantly higher number of hCD1d molecules (3.9 compared to 2.9 median number of unstimulated hCD1d molecules) (Fig. 6.13C) resulting in a strong increase of nanocluster density (180 ± 20 compared to 80 ± 5 hCD1d/μm^2) of WT-hCD1d molecules under inflammatory conditions (Fig. 6.13D). Moreover, R848 stimulated TD-hCD1d nanoclusters had a larger size (90 nm compared to 47 nm) (Fig. 6.13E) and contained a

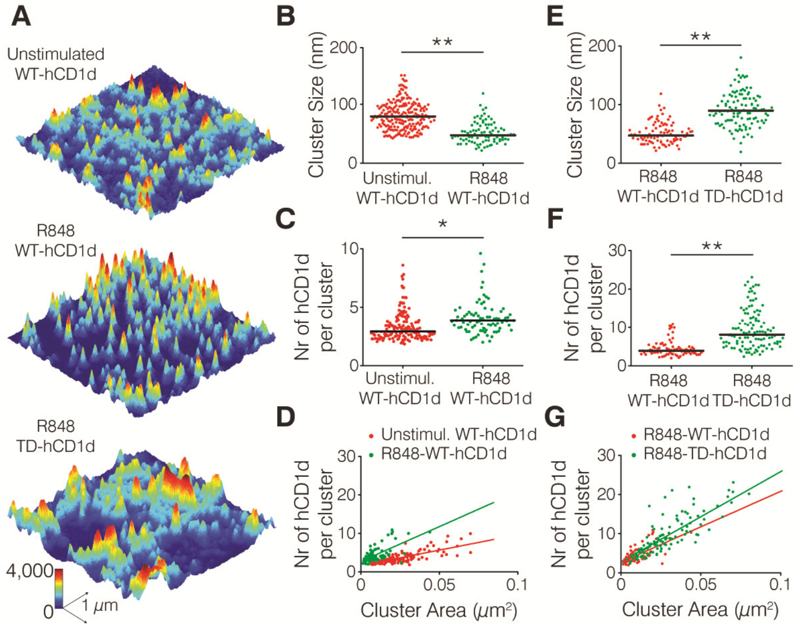

Figure 6.13 The actin cytoskeleton regulates hDC1d nanoclustering under inflammatory conditions. (**A**) STED images of hCD1d nanoclusters on the cell membrane of R848 stimulated THP-1 cells stretched on PLL-coated glass coverslips. (**B**,**E**) Distributions of cluster size; (**C**,**F**) distribution of the number of hCD1d molecules per cluster; and (**D**,**G**) scatterplots of the number of hCD1d molecules per cluster vs. cluster area corresponding to the quantification of the STED images. STED nanoscopy analysis data from at least 30 different images of 3x3 µm in size, from at least 2 different experiments. *P<0.0001 and **P<1•10-7 (Student's t-test).

higher number of molecules (8.1 compared to 3.9 hCD1d molecules) (Fig. 6.13F) than the WT counterpart resulting in an increased nanocluster density of TD-hCD1d (231 ± 15 compared to 180 ± 20 CD1d/μm^2) (Fig. 6.13G), in analogy with the results obtained with α-GalCer-TD-hCD1d (Fig. 6.6E-G). These results evidence an important role of the actin cytoskeleton in controlling the extent of CD1d nanoclustering on the cell membrane of APCs during inflammatory conditions. Moreover, since hCD1d undergoes lysosomal trafficking under inflammatory conditions in analogy to α-GalCer pulsing (40), these data provide further support for the role of the actin cytoskeleton in modulating hCD1d nanoclustering after endosome recycling.

Discussion

We have for the first time characterized the spatiotemporal behavior of hCD1d on the cell membrane of APCs at the nanoscale level. We found that hCD1d molecules organize in small nanoclusters on the cell membrane. Moreover, we observed that the actin cytoskeleton plays a major role in regulating the degree of hCD1d nanoclustering by actively arresting the diffusion of α-GalCer loaded hCD1d nanoclusters, maintaining them away from each other. Indeed, treatment of THP-1 cells with CytoD or deletion of the hCD1d cytoplasmic tail led to larger nanoclusters and a concomitant reduction of hCD1d mobility. Furthermore, increased hCD1d nanoclustering directly correlated with enhanced iNKT cell activation. Notably, under inflammatory conditions hCD1d formed denser nanoclusters whose organization also depended on the actin cytoskeleton, in remarkable analogy to α-GalCer presentation. Altogether our results reveal a novel mechanism by which APCs regulate iNKT cell activation by fine-tuning the spatial organization of hCD1d on the cell membrane.

CD1d is structurally related to the classical MHC-I complex (54). Using super-resolution near-field microscopy, clusters of MHC-I from 70-600 nm in size were observed on the plasma membrane of fibroblasts (55). More recently, it was shown that this nanoclustering strongly depends on the actin cytoskeleton, which acts as a barrier to spatially concentrate MHC-I molecules (36). Consistent with this, deletion of the cytoplasmic tail increased the lateral mobility of MHC-I (56). Clustering of MHC-II complexes on the plasma membrane of APCs has also been reported (57-60). Using SPT approaches, it was shown that MHC-II displays hop-diffusion on the cell membrane in a manner that is dependent on the integrity of the actin cytoskeleton (61). Disruption of the actin cytoskeleton interactions by either perturbing the actin network or by truncation of the MHC-II cytoplasmic tail increased the lateral mobility of MHC-II (61,62). In these experiments, the lateral organization of MHC molecules also had an impact on the extent of T cell activation, with larger clusters enhancing peptide-specific T cell effector functions, particularly at low antigen density (52,63). The role of actin on the spatiotemporal organization of MHC-I and MHC-II on the cell membrane of APCs however is markedly different to the results reported here for hCD1d molecules. Whereas the actin cytoskeleton is essential to actively maintain the clustering of MHC-I and MHC-II, in the case of hCD1d, perturbation of actin cytoskeleton interactions leads to enhanced aggregation of hCD1d. Consistent with this, and also in contrast to MHC-I and MHC-II, disruption of the actin cytoskeleton or deletion of the hCD1d cytoplasmic tail results in reduced mobility of hCD1d nanoclusters. Altogether our results indicate that hCD1d-mediated antigen presentation is differently regulated at the cell surface of APCs as compared with MHC-restricted peptide presentation. We speculate that the contrasting role played by the actin cytoskeleton in regulating MHC and hCD1d nanoclustering reflects an important functional difference between conventional peptide-specific T cells and innate-like lipid specific T cells. Indeed, while peptide-specific T cells undergo extensive negative selection in the thymus (64), to purge the autoreactive peptide repertoire, peripheral iNKT cells retain the ability to react to self-lipids presented by CD1d molecules. This "autoreactivity by design" (4) underpins iNKT cells essential immunoregulatory role.

Much research is being undertaken to understand how iNKT cell autoreactivity in the periphery is fine-tuned to prevent overt autoimmunity. Initial results suggested that β-anomeric self-lipids were the main target of the iNKT cell autoreactive response (5), and that a combination of increased lipid biosynthesis, increased CD1d expression and co-stimulatory cytokines was driving iNKT cell reactivity following APC activation (5,9,10). Costimulation by inflammatory cytokines is essential to achieve iNKT cell activation in these infectious settings, as extensive structural analysis revealed that the iNKT TCR interact with β-anomeric self-lipids CD1d complexes with low affinity (65). Recently, evidence has emerged for recognition of α-anomeric self-lipids bound to CD1d (6,7). As the affinity of the iNKT TCR for α-anomeric lipids CD1d complexes is much higher (65), an even tighter regulation of their availability is required, for example through the concerted action of biosynthetic and catabolic pathways, which in turn are modulated during inflammation (7). Our results are consistent with and extend the above observations, underscoring the importance of hCD1d clustering at the cell surface of APCs as a further mechanism to fine tune iNKT cell autoreactivity in peripheral tissues. Indeed, while at steady state the actin network plays an important role in limiting basal iNKT cell autoreactivity, the observed increase in hCD1d nanocluster density upon TLR stimulation suggests that the actin cytoskeleton might also regulate iNKT cell activation under inflammatory conditions, increasing the overall avidity of self-lipid loaded CD1d nanoclusters. This hypothesis is consistent with the previously reported increased staining of TLR-matured APCs with a soluble iNKT TCR detecting self-lipid CD1d complexes (10).

Endogenous lipid loaded CD1d molecules traffic from the ER to the cell surface via the Golgi system, where they acquire a variety of self-lipids (6,66). From the plasma membrane, CD1d molecules constitutively traffic through the endolysosomal compartment. A tyrosine based internalization motif in the cytoplasmic tail initiates clathrin dependent endocytosis, while association with the adaptor AP-2 and the Arf-like GTPase Arl8b control lysosomal trafficking (5,67). It has been previously reported that the association of exogenous lipid loaded CD1d with membrane lipid rafts on the plasma membrane of murine cells was dependent on the internal trafficking of CD1d molecules (38). Furthemore, it has also been shown that upon inflammatory stimuli, loading of self-lipids also requires trafficking of CD1d molecules through the lysosomal compartment (54). Our data extend these observations and suggest that regulation of hCD1d nanoclustering by the actin cytoskeleton selectively occurs on the pool of hCD1d molecules that has trafficked through endolysosomal compartments. Indeed, we observed actin-dependent regulation of hCD1d nanoclustering only on molecules presenting exogenous lipids such as α-GalCer and GalGalCer, or self-lipids under inflammatory conditions. Conversely, no actin-dependent changes in hCD1d organization were observed with endogenous lipid loaded hCD1d. It will be of interest to investigate how the spatiotemporal behavior of hCD1d might also be affected by the absence of lysosomal lipid transfer proteins such as saposins, which have been shown to facilitate exogenous as well as self-lipid antigen presentation (40,68).

The general consensus on the emerging role of the actin cytoskeleton in regulating cell membrane organization is that it restricts the lateral diffusion of transmembrane proteins by creating temporal physical barriers close to the cell membrane (30). These barriers locally confine membrane receptors increasing their local concentration and promoting clustering (34). In the case of hCD1d, we also observed similar arrest on its mobility in actin-rich regions. However, although hCD1d nanoclustering might be locally enhanced on certain hotspots of the cell membrane by actin, long-range hCD1d clustering is prevented by lowering the encountering probability of distant diffusing hCD1d nanoclusters. These results might bring new insights on how the actin cytoskeleton fine-regulates the lateral behavior of membrane proteins at multiple temporal and spatial scales. Recent results have shown the importance of ERM proteins in linking the transmembrane region of surface receptors, such as the BCR, to the actin cytoskeleton (32). Further experiments are warranted to assess whether this family of proteins is also controlling the interaction between the CD1d cytosolic tail and the cortical actin cytoskeleton. Consistent with this possibility, it has recently been shown that Rho kinase controls antigen presentation by CD1d molecules by prohibiting actin fiber de-polymerization68.

Summarizing, our results highlight a novel mechanism that APCs employ to regulate lipid antigen presentation via CD1d molecules, in order to modulate iNKT cell autoreactivity, a property which distinguishes this cell subset from conventional CD4+and CD8+ T cells. The observation that a similar actin-dependent mechanism regulates presentation of exogenous lipids and self-lipids upon inflammatory stimuli further adds to the singularity of the CD1d-iNKT cell system in bridging innate and adaptive immune responses. Importantly, this study underscores the importance of emerging concepts such as protein nanoclustering in deepening our understanding of how leukocytes can fine-regulate at the molecular level the outcome of an immune reaction. We predict this type of studies will provide essential information for the future optimization of novel immune-based therapeutic strategies.

Materials & Methods

Antibodies and Reagents. Monoclonal mouse anti-human CD1d (CD1d42) and monoclonal mouse anti-human CD71 (write clone number) antibodies were purchased from BD Pharmingen. Poly-L-lysine (PLL), Cytochalasin D (CytoD), DMSO, Atto647N-NHS ester and di-thiothreithol (DTT) were purchased from Sigma Aldrich. Human fibronectin (FN) was purchased from Roche. Streptavidin coated QD655 and QD585, goat-anti-mouse Alexa Fluor 488 antibody and D-biotin were purchased from Invitrogen. Maleimide-PEG2-Biotin and Slide-A-Lyzer MINI Dialysis Units were purchased from Thermo Scientific.

Cell Medium and specific reagents. The complete medium (CM) used throughout this study was RPMI 1640 (Gibco) for THP-1 and IMDM (Gibco) for iNKT cells. CM was supplemented with 2 mM L-glutamine, 1% non-essential amino acids, 1% sodium pyruvate, 1% pen/strep, 5 x10-5 2ME (all from Gibco) and serum: 10% FCS (Sigma) for THP-1; 5% Human AB Serum (Sigma) for iNKT cells. Recombinant human IL-2 was produced in our laboratory as described69.

Lipids: α-GalCer, C20:2, Gal(α1->2)GalCer and C20:2 were synthesized by a strategy described previously70, 71 and their structures were confirmed by mass spectrometry. The dried lipids were dissolved at 10 mg/ml in a solution of chloroform:methanol:water (10:10:3; v/v/v), followed by dilution in 150mM NaCl, 0.5% Tween 20 (vehicle solution) at 100-200 μg/ml stock solution (depending on solubility). The solution was heated at 80oC for 5 minutes followed by sonication for 5 minutes in an ultrasonic water bath. 14C-Threitol Ceramide was synthesized as described.

Soluble iNKT-TCR heterodimers were generated as described (10).

Generation of iNKT cells and Dendritic Cells. Blood was purchased from the UK National Blood Service. Human iNKT cells were isolated by cell sorting with CD1d-α-GalCer tetramers and/or Vα24 and Vβ11 antibodies (Immunotech, Marseille, France) directly from PBMC or after expansion with autologous DCs pulsed with α-GalCer as described (40). iNKT cells were grown in CM (containing 5% human AB serum instead of FCS) supplemented with 1000 U/ml IL-2 and periodically re-stimulated. Dendritic Cells (DCs) were differentiated from MACS-purified CD14 monocytes from healthy blood donors as described10.

Generation of THP-1 cells over-expressing human CD1d constructs. Full length human CD1d was cloned in the pHR-SIN lentiviral vector. Lentivirus particles were made as described (40) and used to infect THP-1 cells (ATCC). Tail deleted (TD) human CD1d, lacking the last 10 AA, was cloned in the pHR-SIN lentiviral vector using a strategy previously described (40). THP1-CD1d cells were transduced with a lentivirus encoding lifeact GFP as previously described10. GFP positive cells were enriched by cell sorting. We acknowledge the gift of the lentiviral life-act GFP plasmid from Prof M. Sixt.

iNKT cell stimulation assays. DCs and THP-1-CD1d cells were plated at 50000/well in U bottom 96 well plates and pulsed overnight at the indicated concentration of lipids. In some experiments, cells were matured for 36 hours with the TLR7/8 ligand R848 (Invivogen, 5-10 μg/ml). Cells were extensively washed, treated for 1 hour at 37ºC with CytoD used at 10μM in HBSS (Gibco) and immediately fixed in glutaraldehyde 72. Fixed APCs were used to stimulate iNKT cells (20000-30000/well in duplicate or triplicate). iNKT cell activation was assessed by IFN-γ ELISA (BD Pharmingen) on supernatants harvested after 36 hours. When indicated, blocking anti CD1d antibody (clone 42.1, BD Pharmingen) was added at 20 μg/ml 30 min before adding iNKT cells. Viability of APCs and hCD1d expression after CytoD treatment was assessed by Flow cytometry upon staining with anti CD1d PE (BD Pharmingen) and propidium iodide (BD Pharmingen). Data were acquired on a Cyan DAKO flow cytometer and analyzed with Flowjo.

Labeling conjugates for SPT experiments in living cells. Monovalent anti-human CD1d or CD71 Abs were prepared from CD1d42 and CD71 Ab by reduction with dithiothreitol (DTT) following manufacturer's instructions. Reduced Abs were then biotinylated with Maleimide-PEG2-Biotin and non-reacted DTT. Unbound biotin was removed by overnight dialysis at 4ºC using Slide-A-Lyzer MINI Dialysis Units. To monitor each reaction step, a 4-12% Bis-Tris gel under denaturing and non-denaturing conditions was performed.

Biotinylated iNKT cell receptor/monovalent Abs were mixed with streptavidine coated QD655 or QD585 in equimolar concentrations and stirred for at least 2h at 4ºC. 10x excess of free biotin in the case of the iNKT cell receptor or 50x in the case of the monovalent Ab was added to the solution to ensure a single iNKT cell receptor or monovalent Ab per quantum dot.
Atto647N-NHS Ester labeling of the Fab9b (39,74) was performed following manufacturer's instructions.

Single Particle Tracking. hCD1d transduced THP-1 cells were pulsed overnight with 50 ng/ml of α-GalCer or 400 ng/ml of Gal-GalCer. After 30 min of incubation on FN-coated coverslips at 37ºC and 5% CO2, cells were labeled with 2nM of the iNKT-TCR-QD655 conjugate for 5 min at room temperature. Cells were then washed with cell medium three times to remove unbound iNKT-TCR-QD655 conjugates. When labeling the cells with antibody-derived probes, 2% human serum incubation was performed for 5 min at room temperature before adding monovalent antibodies or Fab fragments. Monovalent CD1d42-QD655 labeling was done at 0.2 nM concentration. Fab9b-Atto647N labeling was done at 10nM concentration. On CytoD treated samples, treatment (10 μM CytoD for 1 hour) was performed before labeling, on cells seeded on FN-coated coverslips for unpulsed hCD1d-THP-1 cells or after overnight pulsing with α-GalCer or Gal-GalCer. CytoD was maintained in the medium while imaging. CytoD controls were performed with DMSO diluted in the imaging medium with the same dilution used for CytoD experiments. Single Particle Tracking experiments were performed on a custom built EPI single molecule sensitive fluorescence microscope with a Hamamtsu EM-CCD Camera at 60 Hz and analyzed using the mean-square displacement as described in Chapter 2.

Dual color hCD1d trajectory analysis. Two-color QD tracking of labeled hCD1d (WT and TD) nanoclusters was performed at 2 nM concentrations to increase the probability of finding nanocluster interaction events. Two-dimensional fluorescence trajectories of spatially close QD (red: Ab-QD655 and green: Ab-QD585) were generated and the separation distance (interparticle distance) between QDs was determined from their dual-color pair trajectories by measuring the effective distance between the centroid positions of the diffusing QDs. The initial QDs separation distance considered was 350 nm and interparticle distances were calculated at every frame for a total observation time of 1s yielding 30 data points per QD pair. Interparticle distances of all pairs at every frame were collected into a histogram. Monte-Carlo simulations were performed to discriminate between random encounters of diffusing hCD1d nanoclusters or true enhanced interaction between hCD1d nanoclusters. 100 pairs of randomly diffusing nanoclusters were simulated yielding 3000 simulated interparticle distances per simulated pair. The instantaneous diffusion coefficient for each experimental condition was used for simulating the dual-color trajectories.

Dual color trajectory analysis of iNKT-TCR-QD labeled hCD1d on Lifeact-GFP labeled actin. A single Lifeact-GFP fluorescence image was bandpass-filtered in the frequency domain using standard ImageJ image processing. Only QDs that visited both low-actin and high-actin regions during the time course of an experiment (20s) were manually tracked. The trajectories were then divided into 10 points segments and the instantaneous diffusion coefficients of every segment were calculated as earlier described. The segments of the trajectories were visually classified to belong to either low-actin or high-actin regions after thresholding (>75%) the normalized Lifeact-GFP fluorescence images.

Generation of time-dependent membrane exploration maps from SPT measurements. Time-dependent membrane exploration maps of iNKT cell receptor-Qdot655 labeled CD1d were obtained using single particle tracking as described in Chapter 2 and as reported in Ref. 51. Briefly, the position of each single quantum dot with sub-pixel accuracy was determined in every frame using a custom Matlab algorithm based on Serge et al (76). The frame rate of the camera was 60 Hz and the total observation time was 1200 frames. The total number of localizations of all quantum dots in all the frames was collapsed into one single image and overlaid into one single Lifeact-GFP fluorescence image. Cells with an actin cytoskeleton that did not change over the time course of an experiment were carefully selected for this analysis.

Sample preparation for STED Nanoscopy. To avoid any potential artifacts due to CytoD treatment on membrane morphology that could affect the STED imaging, we exclusively focused on WT-hCD1d or TD-hCD1d transduced THP1 cells. WT-hCD1d or TD-hCD1d transduced THP1 cells were pulsed overnight with 100 ng/ml α-GalCer or 400 ng/ml Gal-GalCer. Alternatively, WT-hCD1d or TD-hCD1d transduced THP1 cells were stimulated with 10 μg/ml R-848 for 30h. Cells were then stretched on PLL-coated coverslips for 30 min at 37ºC and with 5% CO2. After cell fixation with 2% paraformaldehyde (77), Fc-receptors were blocked with 2% human serum. CDd1 molecules on the cell membrane were labeled with 5 μg/ml anti-CD1d42 Ab. Fluorescent secondary antibody labeling was performed with a 5 μg/ml goat anti-mouse Alexa Fluor 488-labeled antibody. Isotype controls were performed in order to test the specificity of the labeling procedure.

Stimulated Emission Depletion (STED) Nanoscopy. Confocal and STED images were obtained in a sequential manner using a 100x oil immersion objective (HCX PL APO 100x/1.4 Oil, Leica Microsystems, Germany) of a commercial CW-STED SP-7 microscope (Leica Microsystems, Germany) as described in Chapter 2.

Analysis of the STED images. STED images were analyzed using the custom-made algorithm based on Bayesian inference as described in Chapter 2. Briefly, the algorithm essentially relies on the detection of fluorescence features and their fitting as a sum of different point spread functions (PSFs) whose width and intensity distribution are estimated from images of sparse markers. For each image, the localization positions of all the retrieved PSFs were used to reconstruct an image that contains the molecular localizations belonging to each fluorescent feature of the raw STED image. Cluster size and number of hCD1d molecules per cluster were then calculated from the reconstructed images as described in Chapter 2.

References

1. Salio M, Silk JD, Yvonne Jones E, Cerundolo V (2014) Biology of CD1-and MR1-Restricted T Cells. *Annu. Rev. Immunol.* **32**: 323-366.
2. Brennan PJ, Brigl M, Brenner MB (2013) Invariant natural killer T cells: an innate activation scheme linked to diverse effector functions. *Nat. Rev. Immunol.* **13**, 101-117.
3. Kawano T, et al. (1997) CD1d-restricted and TCR-mediated activation of Vα14 NKT cells by glycosylceramides. *Science* **278**, 1626-1629.
4. Bendelac A, Bonneville M, Kearney JF (2001) Autoreactivity by design: innate B and T lymphocytes. *Nat. Rev. Immunol.* **1**, 177-186.
5. Brennan PJ, et al. (2011) Invariant natural killer T cells recognize lipid self antigen induced by microbial danger signals. *Nat. Immunol.* **12**, 1202-1211.
6. Brennan PJ, et al. (2014) Activation of iNKT cells by a distinct constituent of the endogenous glucosylceramide fraction. *P. Natl. Acad. Sci. USA* **111**, 13433-13438.
7. Kain L, et al. (2014) The Identification of the Endogenous Ligands of Natural Killer T Cells Reveals the Presence of Mammalian α-Linked Glycosylceramides. Immunity **41**, 543-554.
8. Zhou D, et al. (2004) Lysosomal glycosphingolipid recognition by NKT cells. *Science* **306**, 1786-1789.
9. Paget C, et al. (2007) Activation of invariant NKT cells by toll-like receptor 9-stimulated dendritic cells requires type I interferon and charged glycosphingolipids. *Immunity* **27**, 597-609.
10. Salio M, et al. (2007) Modulation of human natural killer T cell ligands on TLR-mediated antigen-presenting cell activation. *P. Natl. Acad. Sci. USA* **104**, 20490-20495.

11. Choudhuri K, et al. (2014) Polarized release of T-cell-receptor-enriched microvesicles at the immunological synapse. *Nature* **507**, 118-123.

12. Douglass AD, Vale RD (2005) Single-molecule microscopy reveals plasma membrane microdomains created by protein-protein networks that exclude or trap signaling molecules in T cells. *Cell* **121**, 937-950.

13. Dustin ML, Depoil D (2011) New insights into the T cell synapse from single molecule techniques. *Nat. Rev. Immunol.* **11**(10): 672-684.

14. Huppa JB, et al. (2010) TCR–peptide–MHC interactions in situ show accelerated kinetics and increased affinity. *Nature* **463**, 963-967.

15. Lillemeier BF, et al. (2010) TCR and Lat are expressed on separate protein islands on T cell membranes and concatenate during activation. *Nat. Immunol.* **11**, 90-96.

16. O'Donoghue GP, Pielak RM, Smoligovets AA, Lin JJ, Groves JT (2013) Direct single molecule measurement of TCR triggering by agonist pMHC in living primary T cells. Elife **2**.

17. Vardhana S, Choudhuri K, Varma R, Dustin ML (2010) Essential role of ubiquitin and TSG101 protein in formation and function of the central supramolecular activation cluster. *Immunity* **32**, 531-540.

18. Varma R, Campi G, Yokosuka T, Saito T, Dustin ML (2006) T cell receptor-proximal signals are sustained in peripheral microclusters and terminated in the central supramolecular activation cluster. *Immunity* **25**, 117-127.

19. Williamson DJ, et al. (2011) Pre-existing clusters of the adaptor Lat do not participate in early T cell signaling events. *Nat. Immunol.* **12**, 655-662.

20. Groves JT, Dustin ML (2003) Supported planar bilayers in studies on immune cell adhesion and communication. *J. Immunol. Methods* **278**, 19-32.

21. Manz BN, Jackson BL, Petit RS, Dustin ML, Groves J (2011) T-cell triggering thresholds are modulated by the number of antigen within individual T-cell receptor clusters. *P. Natl. Acad. Sci. USA* **108**, 9089-9094.

22. Mossman KD, Campi G, Groves JT, Dustin ML (2005) Altered TCR signaling from geometrically repatterned immunological synapses. *Science* **310**, 1191-1193.

23. Dustin ML, et al. (1998) A novel adaptor protein orchestrates receptor patterning and cytoskeletal polarity in T-cell contacts. *Cell* **94**, 667-677.

24. Grakoui A, et al. (1999) The immunological synapse: a molecular machine controlling T cell activation. *Science* **285**, 221-227.

25. Monks CR, Freiberg BA, Kupfer H, Sciaky N, Kupfer A (1998) Three-dimensional segregation of supramolecular activation clusters in T cells. *Nature* **395**, 82-86.

26. Van Ker L (2005) alpha-Galactosylceramide therapy for autoimmune diseases: prospects and obstacles. *Nat. Rev. Immunol.* **5**, 31-42.

27. Garcia-Parajo MF, Cambi A, Torreno-Pina JA, Thompson N, Jacobson K (2014) Nanoclustering as a dominant feature of plasma membrane organization. *J. Cell Sci.* **127**, 4995-5005.

28. Lingwood D, Simons K (2010) Lipid rafts as a membrane-organizing principle. *Science* **327**, 46-50.

29. Chung I, et al (2010) Spatial control of EGF receptor activation by reversible dimerization on living cells. *Nature* **464**, 783-787.

30. Andrews NL, et al. (2008) Actin restricts Fcϵ RI diffusion and facilitates antigen-induced receptor immobilization. *Nat. Cell Biol.* **10**, 955-963.

31. Low-Nam ST, et al. (2011) ErbB1 dimerization is promoted by domain co-confinement and stabilized by ligand binding. *Nat. Struc. Mol. Biol.* **18**, 1244-1249.

32. Treanor B, et al. (2010) The membrane skeleton controls diffusion dynamics and signaling through the B cell receptor. *Immunity* **32**, 187-199.

33. Morone N, et al. (2006) Three-dimensional reconstruction of the membrane skeleton at the plasma membrane interface by electron tomography. *J. Cell Biol.* **174**, 851-862.

34. Jaqaman K, et al. (2011) Cytoskeletal control of CD36 diffusion promotes its receptor and signaling function. *Cell* **146**, 593-606.

35. Fooksman DR, Grönvall GK, Tang Q, Edidin M (2006) Clustering class I MHC modulates sensitivity of T cell recognition. *J. Immunol.* **176**, 6673-6680.

36. Lavi Y, Gov N, Edidin M, Gheber LA (2012) Lifetime of major histocompatibility complex class-I membrane clusters is controlled by the actin cytoskeleton. *Biophys. J.* **102**, 1543-1550.

37. Segura J-M, et al. (2008) Increased mobility of major histocompatibility complex I-peptide complexes decreases the sensitivity of antigen recognition. *J. Biol. Chem.* **283**, 24254-24263.

38. Im JS, et al. (2009) Kinetics and cellular site of glycolipid loading control the outcome of natural killer T cell activation. *Immunity* **30**, 888-898.

39. McCarthy C, et al. (2007) The length of lipids bound to human CD1d molecules modulates the affinity of NKT cell TCR and the threshold of NKT cell activation. *J. Exp. Med.* **204**, 1131-1144.

40. Salio M, et al. (2013) Saposins modulate human invariant Natural Killer T cells self-reactivity and facilitate lipid exchange with CD1d molecules during antigen presentation. *P. Natl. Acad. Sci. USA* **110**, E4753-E4761.

41. Di Rienzo C, Gratton E, Beltram F, Cardarelli F (2013) Fast spatiotemporal correlation spectroscopy to determine protein lateral diffusion laws in live cell membranes. *P. Natl. Acad. Sci. USA* **110**, 12307-12312.

42. Sugita M, et al. (2002) Failure of trafficking and antigen presentation by CD1 in AP-3-deficient cells. *Immunity* **16**, 697-706.

43. Moody DB, Porcelli SA (2003) Intracellular pathways of CD1 antigen presentation. *Nat. Rev. Immunol.* **3**, 11-22.

44. Prigozy TI, et al. (2001) Glycolipid antigen processing for presentation by CD1d molecules. *Science* **291**, 664-667.

45. Chen X, et al. (2007) Distinct endosomal trafficking requirements for presentation of autoantigens and exogenous lipids by human CD1d molecules. *J. Immunol.* **178**, 6181-6190.

46. Jaumouillé V, et al. (2014) Actin Cytoskeleton Reorganization by Syk Regulates Fcγ Receptor Responsiveness by Increasing Its Lateral Mobility and Clustering. Dev. *Cell* **29**, 534-546.

47. Hell SW (2007) Far-field optical nanoscopy. *Science* **316**, 1153-1158.

48. Manzo C, et al. (2012) The neck region of the C-type lectin DC-SIGN regulates its surface spatiotemporal organization and virus-binding capacity on antigen-presenting cells. *J. Biol. Chem.* **287**, 38946-38955.

49. Manzo C, et al. (2014) PSF decomposition of nanoscopy images via Bayesian analysis unravels distinct molecular organization of the cell membrane. *Sci. Rep.* **4**.

50. Riedl J, et al. (2008) Lifeact: a versatile marker to visualize F-actin. *Nat. Methods* **5**, 605-607.

51. Torreno-Pina JA, et al. (2014) Enhanced receptor–clathrin interactions induced by N-glycan–mediated membrane micropatterning. *P. Natl. Acad. Sci. USA* **111**, 11037-11042.

52. Anderson HA, Hiltbold EM, Roche PA (2000) Concentration of MHC class II molecules in lipid rafts facilitates antigen presentation. *Nat. Immunol.* **1**, 156-162.

53. Hiltbold EM, Poloso NJ, Roche PA (2003) MHC class II-peptide complexes and APC lipid rafts accumulate at the immunological synapse. *J. Immunol.* **170**, 1329-1338.

54. Moody DB, Zajonc DM, Wilson IA (2005) Anatomy of CD1–lipid antigen complexes. *Nat. Rev. Immunol.* **5**, 387-399.

55. Hwang J, Gheber LA, Margolis L, Edidin M (1998) Domains in cell plasma membranes investigated by near-field scanning optical microscopy. *Biophys. J.* **74**, 2184-2190.

56. Capps GG, Pine S, Edidin M, Zúniga MC (2004) Short class I major histocompatibility complex cytoplasmic tails differing in charge detect arbiters of lateral diffusion in the plasma membrane. *Biophys. J.* **86**, 2896-2909.

57. Bosch B, Heipertz EL, Drake JR, Roche PA (2013) Major histocompatibility complex (MHC) class II-peptide complexes arrive at the plasma membrane in cholesterol-rich microclusters. *J. Biol. Chem.* **288**, 13236-13242.

58. Fooksman DR (2014) Organizing MHC class II presentation. *Front. Immunol.* **5**.

59. Jenei A, et al. (1997) HLA class I and II antigens are partially co-clustered in the plasma membrane of human lymphoblastoid cells. *P. Natl. Acad. Sci. USA* **94**, 7269-7274.

60. Turley SJ, et al. (2000) Transport of peptide-MHC class II complexes in developing dendritic cells. *Science* **288**, 522-527.

61. Umemura YM, et al. (2008) Both MHC class II and its GPI-anchored form undergo hop diffusion as observed by single-molecule tracking. *Biophys. J.* **95**, 435-450.

62. Wade WF, Freed JH, Edidin M (1989) Translational diffusion of class II major histocompatibility complex molecules is constrained by their cytoplasmic domains. *J. Cell Biol.* **109**, 3325-3331.

63. Gombos I, Detre C, Vámosi G, Matkó J (2004) Rafting MHC-II domains in the APC (presynaptic) plasma membrane and the thresholds for T-cell activation and immunological synapse formation. *Immunol. Lett.* **92**, 117-124.

64. Klein L, Kyewski B, Allen PM, Hogquist KA (2014) Positive and negative selection of the T cell repertoire: what thymocytes see (and don't see). *Nat. Rev. Immunol.* **14**, 377-391.

65. Rossjohn J, Pellicci DG, Patel O, Gapin L, Godfrey DI (2012) Recognition of CD1d-restricted antigens by natural killer T cells. *Nat. Rev. Immunol.* **12**, 845-857.

66. Fox LM, et al. (2009) Recognition of lyso-phospholipids by human natural killer T lymphocytes. *PLoS Biol.* **7**(10): e1000228.

67. Barral DC, Brenner MB (2007) CD1 antigen presentation: how it works. *Nat. Rev. Immunol.* **7**, 929-941.

68. Kang S-J, Cresswell P (2004) Saposins facilitate CD1d-restricted presentation of an exogenous lipid antigen to T cells. *Nat. Immunol.* **5**, 175-181.

69. Gallo RM, et al. (2012) Regulation of the actin cytoskeleton by rho kinase controls antigen presentation by CD1d. *J. Immunol.* **189**, 1689-1698.

70. Traunecker A, Oliveri F, Karjalainen K (1991) Myeloma based expression system for production of large mammalian proteins. *Trends Biotechnol.* **9**, 109-113.

71. Jervis PJ, et al. (2010) Synthesis and biological activity of α-glucosyl C24: 0 and C20: 2 ceramides. *Bioorg. Med. Chem. Lett.* **20**, 3475-3478.

72. Veerapen N, et al. (2009) Synthesis and biological activity of α-galactosyl ceramide KRN7000 and galactosyl (α1→ 2) galactosyl ceramide. *Bioorg. Med. Chem. Lett.* **19**, 4288-4291.

73. Lanzavecchia A (1985) Antigen-specific interaction between T and B cells. *Nature* **314**, 537-539.

74. Denkberg G, et al. (2008) Phage display-derived recombinant antibodies with TCR-like specificity against α-galactosylceramide and its analogues in complex with human CD1d molecules. *Eur. J. Immunol.* **38**, 829-840.

75. Kusumi A, Sako Y, Yamamoto M (1993) Confined Lateral Diffusion of Membrane-Receptors as Studied by Single-Particle Tracking (Nanovid Microscopy) - Effects of Calcium-Induced Differentiation in Cultured Epithelial-Cells. *Biophys. J.* **65**, 2021-2040.

76. Sergé A, Bertaux N, Rigneault H, Marguet D (2008) Dynamic multiple-target tracing to probe spatiotemporal cartography of cell membranes. *Nat. Methods* **5**, 687-694.

77. van Zanten TS, et al. (2010) Direct mapping of nanoscale compositional connectivity on intact cell membranes. *P. Natl. Acad. Sci. USA* **107**, 15437-15442.

Chapter 7

Conclusions and future perspectives

In this Chapter, we draw some general conclusion of this thesis about the spatiotemporal behavior of DC-SIGN and CD1d. Moreover, we discuss the different imaging techniques used throughout this thesis in order to address the lateral behavior of these two membrane proteins at multiple spatial and temporal scales. We also discuss potential developments in, e.g., multi-color single particle tracking, cartography maps or STED nanoscopy experiments as future instrumental perspectives of this thesis. Then, we draw the general findings of DC-SIGN in terms of its nanoclustering and its mesoscale organization. Moreover, we also propose how to visualize and characterize the glycan-based connectivity in the case of DC-SIGN with potential interaction partners such as CD44 and Galectin-9. We then discuss the results obtained when studying the spatiotemporal behavior of CD1d on the surface of antigen presenting cells. Finally, we also propose how to address the role of lysosomal trafficking in the regulation of the control of the actin cytoskeleton on the behavior of CD1d.

A new microscopy era to investigate nanoscale receptor organization and function.

In the last decade, the modulation of the biological function of membrane immune receptors by their lateral behavior is emerging as a new concept in immunology (1-3). This has been possible due to the development of super-resolution microscopy in combination with single molecule imaging approaches featuring high temporal resolution (4-7). The combination of these techniques has been a major breakthrough in the study of immune cells. In this context, it is becoming more widely accepted that nanoclustering of membrane receptors represents a crucial mechanism to regulate, e.g, the downstream signaling of an activated leukocyte (2).

Cartography maps, as developed in this thesis research, represent a suitable imaging technique when combining high temporal resolution with microscale spatial information without the need of reconnecting trajectories. This is particularly beneficial when using QDs as labeling probes since their on-off blinking impose a limitation when trying to collect long trajectories in a standard SPT experiment (8, 5). Due to the need of reconnecting individual trajectories (9, 10), SPT is a very low throughput technique. In this context, cartography maps can provide data at a much higher yield than SPT. Moreover, extending cartography maps to multi-color imaging allows the simultaneous visualization of the global nanoscale but also microscale organization of multi-protein complexes, including signaling complexes at the cell membrane (11, 3, 12, 13), clathrin-mediated endocytosis machinery (14) or cell-cell adhesion processes such as the immunological synapse (15).

The main challenge of standard SPT experiments is still to find a minimally invasive probe featuring photostability in time (for obtaining long trajectories) together with high photon emission, which could allow nanometer localization precision even at microsecond integration times. The use of quantum dots (QDs) has been a major breakthrough in SPT experiments (8, 5). However, their characteristic blinking impose limitations when trying to acquire long (>1000 points) trajectories at a fast frame rate. Non-blinking QDs have been recently used to performed SPT allowing enhanced acquisition compared to blinking QDs (16-18). Moreover, the narrow emission band of QDs makes them a powerful probe when performing multi-color imaging experiments (1). It has to be noted that QDs dual-color experiments carried out throughout this thesis to address the interaction between different nanoclusters were performed at video rate (30 Hz). It would be very interesting to perform similar type of experiments but at a much higher frame rate (>1000 Hz) to address the stability of nanoclusters in time. Moreover, by extending this approach to three or four colors, multi homo- or hetero-cluster interactions could be addressed very efficiently.

In the context of this thesis, several imaging techniques were developed and/or applied in order to directly visualize transmembrane proteins in leukocytes with high temporal and spatial resolution, such as STED nanoscopy and multi-color SPT. The consistent combination of STED nanoscopy with mobility data is one of the hallmarks of this thesis. For instance, we used the DC-SIGN nanocluster size obtained with STED nanoscopy to infer the interaction threshold for mobile interacting DC-SIGN nanoclusters imaged using dual-color SPT (Chapter 4, Fig. 4.6). Moreover, in Chapter 6, we confirmed the enhanced CD1d nanoclustering obtained with STED nanoscopy by measuring reduced dual-color CD1d interparticle distances over a given period of time (Fig. 6.9). Indeed, the combination of both STED nanoscopy and multi-color SPT provides complementary information. Hence, an imaging technique both featuring super-resolution capability and high temporal resolution would be the ideal instrumentation to characterize dynamic events on the cell membrane. TOCCSL (19) offers the possibility of combining mobility data with the quantification of the number of particles of the diffusing diffraction limited spot. Nevertheless, in case that the diameter of the diffusing nanocluster is below the diffraction limit, TOCCSL could reveal the number of particles within the nanocluster but not its true size. In my opinion, one suitable solution for *single monomer/nanocluster tracking* would be STED nanoscopy with very high temporal resolution (20). By focusing on one individual nanocluster on the cell membrane and by following it in time, single nanocluster tracking could be possible. The advantage of focusing on one individual nanocluster is that the size of the scan area in every frame can be reduced as much as 2-4 times the diameter of the diffusing nanocluster which contributes to a higher temporal resolution. Moreover, single nanocluster tracking using STED would allow the quantification of the nanocluster in terms of size and number of proteins. This would allow addressing whether the number of molecules or the size of the nanocluster changes in time. The main limitation of this approach is the commonly high protein density on the cell membrane, which would first limit the identification of individual nanoclusters (this is the in fact main limitation in any SPT approach, so that sub-labeling conditions must be applied to reconnect individual trajectories) and second, the reconnection of trajectories even using small STED scan areas. Nevertheless, the reconnection of trajectories at high density labeling conditions could be enhanced by using a multiple-target tracing algorithm (21). Moreover, by extending the setup to a multicolor approach, multicolor STED single nanocluster tracking could be feasible. However, as for any STED applications, the dye represents the main limitation. If the dye photobleaches after a few frames, long-term single nanocluster tracking stops being feasible. Nevertheless, STED with <25 nm lateral resolution was demonstrated using nitrogen-vacancy centers which could be bio-functionalized for protein labeling (22). In this particular case, the challenge remains as to the fabrication of vacancy centers of nanometer size. With their current developments, I would discard any PALM/STORM technique for single nanocluster tracking due to their stochastic readout in time (4).

Characterizing the Glyconnectome

In Chapter 3, we demonstrated that the neck region of DC-SIGN determines its spatiotemporal behavior on the cell membrane. For instance, the mutant missing the neck region (-ΔRep mutant) showed reduced nanoclustering compared to wt-DC-SIGN. Moreover, and consistent with this reduced nanoclustering, ΔRep-DC-SIGN also exhibited enhanced lateral diffusion on the cell membrane. Interestingly, ΔRep-DC-SIGN was shown to bind to either soluble or to micron-sized antigens but not to virus-sized particles. Monte-Carlo simulations showed that the integrity of the DC-SIGN nanoclusters is essential to the virus-binding capacity of the receptor. Altogether, these results suggest that the nanoclustering of a membrane receptor can widen the spectrum of potential ligands the receptor is able to bind to. Furthermore, in Chapter 4, we showed that the glycosylation motif of DC-SIGN does not influence the nanoclustering degree or the potential interaction of preformed nanoclusters. However, we showed that the glycosylation motif is critical for the stable confinement of DC-SIGN in ≈ 1 μm regions of the cell membrane. By using cartography maps, a novel imaging approach developed in this thesis, we directly visualized these preferential regions of the cell membrane explored by DC-SIGN. Furthermore, we showed a favored enrichment of clathrin-coated pits within those glycosylation dependent regions and a related enhanced clathrin-dependent endocytosis of HIV-like particles. These data defines a novel *biophysical* membrane organizing principle, together with the actin cytoskeleton and lipid rafts (23, 24), based on an extracellular glycan-based connectivity at the microscale on the cell membrane. From now on, I will refer to this glycan-based connectivity as *glyconnectome* (from the words glyco- and connectome).

Although we were able to visualize for the first time the impact of the glyconnectome on the lateral behavior of a membrane receptor at the microscale with high temporal resolution, it remains still as an open question how galectins (25), believed to crosslink glycoproteins, might regulate dynamically this connectivity. There have been major steps in the visualization of galectins at the nanoscale using super-resolution microscopy (26). For instance, dSTORM revealed that Galectin-3 organizes in nanoclusters with a cluster radius of around 80 nm on the cell membrane. Moreover, it was also shown than CD44 organizes in nanoclusters on the cell membrane whose integrity is dependent on the glycosylation state of CD44 (26). The lateral organization of Galectin-3 was also addressed using PALM on the cell membrane of HeLa cells using the photoconvertible protein EosFP (27). It was shown that Galecin-3 also forms nanoclusters with a size ranging from 30 to 300 nm which is consistent with the work of Lakshminarayan et al. (26). Although these studies achieved the direct visualization of Galectin-3 on the cell membrane, they lack any information about the dynamic behavior of the protein. Since we show that the glyconnectome operate at the microscale (Chapter 4, Fig. 4.8), cartography maps of Galectin-3 would be ideal to characterize this *N*-glycosylation dependent network. Moreover, it is still to be established whether the different galectins (proto-type, tandem repeat-type or chimera-type) might regulate the glyconnectome in a different manner. Such different behavior could explain the differences observed in our work described in Chapter 4 and those reported by Lakshminarayan et al. (26). Indeed, whereas we postulate that CD44 and Galectin-9 enhance clathrin dependent endocytosis, Lakshminarayan et al. found that CD44 and Galectin-3 promote clathrin independent endocytosis (26). Nevertheless, it has also been proposed that CD44 can undergo internalization via clathrin (28). Probably the glyconnectome might regulate CD44 endocytosis depending on the different external stimuli in a very sensitive manner.

Another important consideration on the DC-SIGN work presented in this thesis is that all the biophysical measurements on its lateral organization were performed in the basal sate, i.e., before ligand engagement by DC-SIGN. It would be very interesting to determine the spatiotemporal behavior of DC-SIGN before and after ligand binding in real time. The ideal experiment would be to perform SPT while adding, e.g., HIV virus-like particles into the imaging medium. Moreover, the virus like particles could be tagged with a fluorescent protein or a QD so that DC-SIGN and the virus like particles could be tracked simultaneously (29, 30). Nevertheless, there is an important limitation when performing SPT under these conditions. The probability of finding and tracking a DC-SIGN molecule bound to a virus-like particle would be extremely low considering the very high density of DC-SIGN molecules on the cell membrane and the very low concentration of dye needed for SPT. Cartography maps, on the other hand, offer an ideal solution, considering that individual trajectories do not need to be reconnected. By adding a high concentration of virus-like particles and anti-DC-SIGN dye-labeled antibodies, dual color cartography maps of DC-SIGN molecules bound to virus-like particles could be performed. Moreover, by modulating the observation times, the different global reorganization of DC-SIGN molecules on the cell membrane could be mapped during viral infection. This would provide unprecedented information on how the large-scale organization of membrane receptors changes their lateral organization from a single-molecule perspective (cartography maps originate from single molecule localizations) during an infection event. Moreover, by extending this approach to, e.g., to four-color cartography maps experiments, the global organization of the DC-SIGN glyconnectome: the cargo protein CD44, the membrane receptor DC-SIGN, the crosslinking protein Galectin-9 and the virus-like particle, could be simultaneously characterized.

Furthermore, it has been reported that the DC-SIGN signalosome is strongly dependent on the type of sugar bound by DC-SIGN (31). Mannose-containing pathogens activate the Raf1-signaling pathway while fucose-containing pathogens dissociate the DC-SIGN signalosome suppressing a pro-inflammatory response by DCs (31). In this context, it is important would be interesting to address whether the different signaling pathways of the DC-SIGN signalosome could be already modulated at the level of the cell membrane by, e.g., a different lateral organization of the DC-SIGN glyconnectome. Hence, mapping and correlating the DC-SIGN glyconnectome in the presence of different ligands with downstream signaling pathways could be relevant to understand the potential link between the glyconnectome and the different signaling pathways of DC-SIGN. As I am convinced that the glyconnectome is a general membrane organizing principle, the concepts extracted from the experiments with DC-SIGN could be, under my very personal opinion, applied to many other cell membrane glycoproteins.

Another important finding of this thesis is that the interaction of DC-SIGN with clathrin is transient rather than stable. This is consistent with the findings of the "catch-and-release" model between cargo and clathrin reported by Weigel et al. (14). However, in their case, the binding of the cargo protein by clathrin led to a transient immobilization. Moreover, the distribution of the binding times between the cargo and clathrin exhibited a slow component that followed a power-law behavior (14). In our case, the interaction of clathrin with DC-SIGN led to confinement of DC-SIGN and not to its immobilization, while the distribution of the dwell times of DC-SIGN within clathrin-coated pits followed a single exponential behavior (Chapter 4, Fig. 4.10). Nevertheless, it should be mentioned that all of our experiments were performed in the absence of DC-SIGN ligand. It will be exciting to address whether in the presence of a ligand the interaction between DC-SIGN and clathrin would become stronger and power-law immobilization events would be observed, as shown for the interaction between K^+ channels and clathrin-coated pits (14).

In the context of experiments of DC-SIGN with ligands, one could address whether the behavior of DC-SIGN will still show weak ergodicity breaking (Chapter 5) in the presence of a ligand as it does in the resting state. Moreover, since upon engagement of the ligand, the nearby area of the cell membrane would be rearranged through the recruitment of the signaling or the clathrin mediated endocytosis machinery, it will be important to develop theoretical models that could take into account the fact that the diffusing particle modifies the environment where it is diffusing through.

Nanoscale lateral organization of CD1d and its implication on iNKT cell activation

For a long time, it was known that the spatiotemporal behavior of MHC-I and MHC-II complexes impact on the activation of CD8- and CD4-T cells respectively (32-34), but virtually nothing was known regarding the lateral organization of CD1d on antigen presenting cells (APCs) and its consequences on invariant natural killer T (iNKT) cell activation. We showed in Chapter 6 that CD1d forms nanoclusters on the surface of APCs. We also showed that the size and density of these nanoclusters are tightly controlled by the actin cytoskeleton and that alteration of CD1d nanoclustering had an impact on the degree of activation of iNKT cells. These results introduce a new concept of controlling iNKT cell activation by means of lateral organization of CD1d molecules. Moreover, we also showed that the actin cytoskeleton regulates the lateral behavior of CD1d in a complete different manner than it does for MHC-I and MHC-II complexes (35, 36). Hence, the APC regulates the activation of iNKT cells in a complete different manner as it does for classical T cells. This might be explained by the constitutive autoreactivity displayed by iNKT cells, a property not shared by classical T cells (37).

In Chapter 6 we also suggested that the tight control of CD1d nanoclustering by the actin cytoskeleton predominantly occurs on the pool of CD1d molecules that has trafficked through the lysosome, either when pulsing the cells with exogenous lipids or when stimulating them with toll-like receptor (TLR) ligands. This implies that there is a general mechanism of CD1d nanocluster editing in lysosomal compartments. Hence, complementary to the rather biochemical concept of CD1d lipid editing in the lysosome (38), I would like to also suggest a “CD1d nanocluster editing” capability of the lysosome. The lysosome would make CD1d nanoclusters prone to aggregation while the actin cytoskeleton on the cell membrane would prevent it by segregating away diffusing CD1d nanoclusters as much as possible. Nevertheless, it remains to be clarified the mechanism by which CD1d molecules are prone to aggregation after lysosomal recycling. Moreover, it should be addressed how is the interaction between CD1d molecules and the actin cytoskeleton differently regulated after lysosomal trafficking of CD1d molecules. A possible explanation for the latter case is that members of the Ezrin-Radixin-Moesin (39, 40), proteins known to mediate the interaction between transmembrane proteins and the actin cytoskeleton, might be activated on CD1d molecules having undergone lysosomal trafficking. In this scenario, the anchoring of CD1d molecules to the actin cytoskeleton would only occur after CD1d lysosomal trafficking. To test this hypothesis, members of the ERM family could be silenced and the nanoclustering of CD1d addressed. Alternatively, cell lines with ERM mutants lacking the actin binding domain could be used (40). Complementary to these experiments, it would be useful to address the phosphorylation degree of ERM proteins after pulsing the cells with exogenous lipids or to stimulate them with TLR ligands (40). Since phosphorylation of ERM proteins is an essential step for their activation, it would be reasonable to think that parallel to CD1d lysosomal recycling, ERM proteins would get phosphorylated and activated in order to actively bind CD1d to the actin cytoskeleton.

It has to be noted that all the biophysical experiments performed on CD1d throughout this thesis were performed in presynaptic conditions, i.e., before the engagement of CD1d molecules by the iNKT cell receptor. Future experiments addressing the lateral organization of CD1d nanoclusters upon binding of an iNKT cell could be performed in order to visualize changes in the spatiotemporal behavior of both the iNKT cell receptor, on the side of the T cell, and CD1d molecules on the APC before and during the formation of the immunological synapse (41). In this context, there is already available a large palette of different tools that have been developed and used to study the interaction between MHC-I and MHC-II complexes and classical CD4+- and CD8+-T cells (42, 43). This methodology could help to further confirm whether the CD1d-iNKT cell system behaves in a complete different manner as classical MHC-I/MHC-II and CD8- and CD4-T cells.

Summary

In this thesis we have addressed the lateral organization of two transmembrane proteins (DC-SIGN and CD1d) on the surface of APCs. We have showed how the spatiotemporal behavior of these two proteins can control their biological function. The nanoclustering of DC-SIGN is crucial for the binding of virus-like particles. Moreover, the glyconnectome patterns the lateral behavior of DC-SIGN at the microscale and favors the encountering rate between DC-SIGN and clathrin on the cell membrane. DC-SIGN shows subdiffusion and weak ergodicity breaking which is dependent on the nanoclustering degree of the receptor. Finally, we showed that the actin cytoskeleton controls the density and size of iNKT cell stimulating CD1d nanoclusters on the cell membrane of APCs.

The full visualization of the glyconnectome is certainly one of the main, if not the most important experiment to be performed as a future perspective of this thesis. The multicolor visualization of DC-SIGN and its potential *N*-glycosylation dependent interaction partners CD44 and Galectin-9 represent a very powerful tool palette as a starting point of the characterization of a glyconnectome on the extracellular part of the cell membrane. The second main future perspective of this thesis is to confirm whether the CD1d-iNKT cell system displays a very different lateral behavior as the classical MHC-I/II CD4+-CD8+-T cell system. A different spatiotemporal behavior of the CD1d-iNKT system would contribute in a complementary manner to the rather traditional biochemical approaches, to confirm that this system shows unique properties completely different compared to classical T cells.

The overall overview of this thesis deals with the importance of the spatiotemporal behavior of proteins in general. Traditional biochemical approaches have tried to understand the interaction between, e.g., different proteins or receptor and ligand as a one dimensional problem where only the binding between the different *single* components was taking into account. However, the cell membrane can be understood as a system where chemical reactants such as proteins or sugars are trapped in a two dimensional space. Hence, any alteration in the two dimensional organization of any of the reactants will have an impact on their potential (*cis* and *trans*) interaction on the cell membrane.

I am convinced that the spatiotemporal behavior of proteins is going to play a crucial role in the future development of clinical treatments such as cancer immunotherapy. In analogy to the use of macromolecular crystallography in modern medicine to improve drug design (44), the characterization of the lateral organization of proteins in space and time at the relevant scales will have a big impact in the rational development of, e.g., human immunology based therapies against cancer.

References

1. Andrews NL, Lidke KA, Pfeiffer JR, Burns AR, Wilson BS, Oliver JM*, et al.* (2008) Actin restricts Fcϵ RI diffusion and facilitates antigen-induced receptor immobilization. *Nat. Cell Biol.* **10**, 955-963.
2. Garcia-Parajo MF, Cambi A, Torreno-Pina JA, Thompson N, Jacobson K (2014) Nanoclustering as a dominant feature of plasma membrane organization. *J. Cell Sci.* **127**, 4995-5005.
3. Mattila PK, Feest C, Depoil D, Treanor B, Montaner B, Otipoby KL*, et al.* (2013) The actin and tetraspanin networks organize receptor nanoclusters to regulate B cell receptor-mediated signaling. *Immunity* **38**, 461-474.
4. Hell SW (2007), Far-field optical nanoscopy. *Science* **316**, 1153-1158.
5. Pinaud F, Clarke S, Sittner A, Dahan M (2010) Probing cellular events, one quantum dot at a time. *Nat. Methods* **7**, 275-285.

6. Reits EA, Neefjes JJ (2001) From fixed to FRAP: measuring protein mobility and activity in living cells. *Nat. Cell Biol.* **3**, E145-E147.

7. van Zanten TS, Cambi A, Koopman M, Joosten B, Figdor CG, Garcia-Parajo MF (2009) Hotspots of GPI-anchored proteins and integrin nanoclusters function as nucleation sites for cell adhesion. *Proc. Natl. Acad. Sci.* **106**, 18557-18562.

8. Dahan M, Levi S, Luccardini C, Rostaing P, Riveau B, Triller A (2003) Diffusion dynamics of glycine receptors revealed by single-quantum dot tracking. *Science* **302**, 442-445.

9. Kusumi A, Sako Y, Yamamoto M (1993) Confined lateral diffusion of membrane receptors as studied by single particle tracking (nanovid microscopy). Effects of calcium-induced differentiation in cultured epithelial cells. *Biophys. J.* **65**, 2021-2040.

10. Saxton MJ, Jacobson K (1997) Single-particle tracking: applications to membrane dynamics. *Annu. Rev. Biophys. Biomol. Struct.* **26**, 373-399.

11. Lillemeier BF, Mörtelmaier MA, Forstner MB, Huppa JB, Groves JT, Davis MM (2010) TCR and Lat are expressed on separate protein islands on T cell membranes and concatenate during activation. *Nat. Immunol.* **11**, 90-96.

12. Treanor B, Depoil D, Gonzalez-Granja A, Barral P, Weber M, Dushek O*, et al.* (2010) The membrane skeleton controls diffusion dynamics and signaling through the B cell receptor. *Immunity* **32**, 187-199.

13. Williamson DJ, Owen DM, Rossy J, Magenau A, Wehrmann M, Gooding JJ*, et al.* (2011) Pre-existing clusters of the adaptor Lat do not participate in early T cell signaling events. *Nat. Immunol.* **12**, 655-662.

14. Weigel AV, Tamkun MM, Krapf D (2013) Quantifying the dynamic interactions between a clathrin-coated pit and cargo molecules. *Proc. Natl. Acad. Sci.* **110**, E4591-E4600.

15. Grakoui A, Bromley SK, Sumen C, Davis MM, Shaw AS, Allen PM*, et al.* (1999) The immunological synapse: a molecular machine controlling T cell activation. *Science* **285**, 221-227.

16. DeVore MS, Stich DG, Keller AM, Ghosh Y, Goodwin PM, Phipps ME*, et al.* Three dimensional time-gated tracking of non-blinking quantum dots in live cells. SPIE BiOS; 2015: International Society for Optics and Photonics; 2015. p. 933812-933812-933815.

17. Marchuk K, Guo Y, Sun W, Vela J, Fang N (2012) High-precision tracking with non-blinking quantum dots resolves nanoscale vertical displacement. *J. Am. Chem. Soc.* **134**, 6108-6111.

18. Wang X, Ren X, Kahen K, Hahn MA, Rajeswaran M, Maccagnano-Zacher S*, et al.* (2009) Non-blinking semiconductor nanocrystals. *Nature* **459**, 686-689.

19. Brameshuber M, Schütz GJ (2012) 9 Detection and Quantification of Biomolecular Association in Living Cells using Single-Molecule Microscopy. *Methods Enzymol.* **505**, 159.

20. Nägerl UV, Willig KI, Hein B, Hell SW, Bonhoeffer T (2008) Live-cell imaging of dendritic spines by STED microscopy. *Proc. Natl. Acad. Sci.* **105**, 18982-18987.

21. Sergé A, Bertaux N, Rigneault H, Marguet D (2008) Dynamic multiple-target tracing to probe spatiotemporal cartography of cell membranes. *Nat. Methods* **5**, 687-694.

22. Rittweger E, Han KY, Irvine SE, Eggeling C, Hell SW (2009) STED microscopy reveals crystal colour centres with nanometric resolution. *Nat. Photonics* **3**, 144-147.

23. Kusumi A, Nakada C, Ritchie K, Murase K, Suzuki K, Murakoshi H*, et al.* (2005) Paradigm shift of the plasma membrane concept from the two-dimensional continuum fluid to the partitioned fluid: high-speed single-molecule tracking of membrane molecules. *Annu. Rev. Biophys. Biomol. Struct.* **34**, 351-378.

24. Mayor S, Rao M (2004) Rafts: scale-dependent, active lipid organization at the cell surface. *Traffic* **5**, 231-240.

25. Rabinovich GA, Toscano MA, Jackson SS, Vasta GR (2007) Functions of cell surface galectin-glycoprotein lattices. *Curr. Opin. Struct. Biol.* **17**, 513-520.

26. Lakshminarayan R, Wunder C, Becken U, Howes MT, Benzing C, Arumugam S*, et al.* (2014) Galectin-3 drives glycosphingolipid-dependent biogenesis of clathrin-independent carriers. *Nat. Cell Biol.*

27. Ehsani S, Santos JC, Rodrigues CD, Henriques R, Audry L, Zimmer C*, et al.* (2012) Hierarchies of host factor dynamics at the entry site of Shigella flexneri during host cell invasion. *Infect. Immun.* **80**, 2548-2557.

28. Perrot G, Langlois B, Devy J, Jeanne A, Verzeaux L, Almagro S*, et al.* (2012) LRP-1–CD44, a new cell surface complex regulating tumor cell adhesion. *Mol. Cell. Biol.* **32**, 3293-3307.

29. Cambi A, Lidke DS, Arndt-Jovin DJ, Figdor CG, Jovin TM (2007) Ligand-conjugated quantum dots monitor antigen uptake and processing by dendritic cells. *Nano Lett.* **7**, 970-977.

30. Izquierdo-Useros N, Esteban O, Rodriguez-Plata MT, Erkizia I, Prado JG, Blanco J*, et al.* (2011) Dynamic Imaging of Cell-Free and Cell-Associated Viral Capture in Mature Dendritic Cells. *Traffic* **12**, 1702-1713.

31. Gringhuis SI, den Dunnen J, Litjens M, van der Vlist M, Geijtenbeek TB (2009) Carbohydrate-specific signaling through the DC-SIGN signalosome tailors immunity to Mycobacterium tuberculosis, HIV-1 and Helicobacter pylori. *Nat. Immunol.* **10**, 1081-1088.

32. Anderson HA, Hiltbold EM, Roche PA (2000) Concentration of MHC class II molecules in lipid rafts facilitates antigen presentation. *Nat. Immunol.* **1**, 156-162.

33. Fooksman DR, Grönvall GK, Tang Q, Edidin M (2006) Clustering class I MHC modulates sensitivity of T cell recognition. *J. Immunol.* **176**, 6673-6680.

34. Gombos I, Detre C, Vámosi G, Matkó J (2004) Rafting MHC-II domains in the APC (presynaptic) plasma membrane and the thresholds for T-cell activation and immunological synapse formation. *Immunol. Lett.* **92**, 117-124.

35. Lavi Y, Gov N, Edidin M, Gheber LA (2012) Lifetime of major histocompatibility complex class-I membrane clusters is controlled by the actin cytoskeleton. *Biophys. J.* **102**, 1543-1550.

36. Umemura YM, Vrljic M, Nishimura SY, Fujiwara TK, Suzuki KG, Kusumi A (2008) Both MHC class II and its GPI-anchored form undergo hop diffusion as observed by single-molecule tracking. *Biophys. J.* **95**, 435-450.

37. Bendelac A, Bonneville M, Kearney JF (2001) Autoreactivity by design: innate B and T lymphocytes. *Nat. Rev. Immunol.* **1**, 177-186.

38. Moody DB, Porcelli SA (2003) Intracellular pathways of CD1 antigen presentation. *Nat. Rev. Immunol.* **3**, 11-22.

39. Ivetic A, Ridley AJ (2004) Ezrin/radixin/moesin proteins and Rho GTPase signalling in leucocytes. *Immunology* **112**, 165-176.

40. Treanor B, Depoil D, Bruckbauer A, Batista FD (2011) Dynamic cortical actin remodeling by ERM proteins controls BCR microcluster organization and integrity. *J. Exp. Med.* **208**, 1055-1068.

41. McCarthy C, Shepherd D, Fleire S, Stronge VS, Koch M, Illarionov PA*, et al.* (2007) The length of lipids bound to human CD1d molecules modulates the affinity of NKT cell TCR and the threshold of NKT cell activation. *J. Exp. Med.* **204**, 1131-1144.

42. Manz BN, Jackson BL, Petit RS, Dustin ML, Groves J (2011) T-cell triggering thresholds are modulated by the number of antigen within individual T-cell receptor clusters. *Proc. Natl. Acad. Sci.* **108**, 9089-9094.

43. Mossman KD, Campi G, Groves JT, Dustin ML (2005) Altered TCR signaling from geometrically repatterned immunological synapses. *Science* **310**, 1191-1193.

44. Deschamps JR The role of crystallography in drug design. *Drug Addiction*. Springer, 2008, pp 343-355.

Acknowledgements

This thesis has been quite a long journey, which helped my development from both the professional and the personal side. Such personal development has been possible due to some key people that have been surrounding me throughout the whole thesis.

My supervisor Maria Garcia-Parajo has been certainly the most important person during these years. She understood from the very first moment the ideal condition that I need to work under: absolute freedom. Little interference on my work, few but key advices at the right moments, letting me decide which direction to go at any time… All of them have been key elements that have driven this thesis to a final, successful end. From the personal side, I think she also quickly understood the way I am and how to deal with me on a personal basis. This is probably the *true* key point that has permitted us to work together for such a long time.

Another key person throughout these years has been… *Manzo!* I always think of him as not only my physics teacher but also as a reference person that I can ask anything in general about life. The amount of information that I have absorbed from him during this thesis is nearly infinite. For that, I am going to be always thankful to him. Our interaction, based on my chemist-biochemist background and his physics expertise has been fundamental for the development of this thesis. I am convinced that we have done a great job together and, hopefully, we will somehow continue doing it in the future!

The next crucial person in my thesis has been *Merchita*. Not only we shared really great time in the lab, but we also laughed a lot together. Thanks for helping me so much with all the cell culturing and other biolab related activities! And I hope that you keep on organizing all those activities that you like so much.

Bruno has also been a fundamental person in this thesis. I think he really joined at the right time, when the DC-SIGN project was getting shaped up, and his final contributions helped a lot to define the final paper. From the personal side, it has been (and it is) a big pleasure to share with him so many moments both inside and outside ICFO.

Sonja came like a hurricane into my life. She spent only 3 months at ICFO but her imprinting in my thesis has been tremendous. Her passion and endless motivation are really impressive and certainly helped me a lot in understanding the DC-SIGN data and the glyconnectome. I am sure she will deliver crucial data in glycobiology in the future!

I would also like to thank Alessandra for her constant input throughout these years on the DC-SIGN project. It is really interesting to see how things have developed from the very initial interactions between us. I think we came to a happy ending, don’t you think?

If doing my thesis in a physicists’ environment was not already a challenge for me, the interaction with the theoreticians of Prof. Maciej Lewenstein’s group at ICFO has been one of the weirdest but most stimulating and rewarding experiences of my thesis. It has been a tremendously mind-opening experience for a chemist like me sitting in a room and see how theoreticians perform their work. I am certainly very impressed by the experience and I am looking forward to continue doing work like that in the future. Pietro, John and Maciej, thank you so much!

Parallel to the DC-SIGN project, I have been developing another monumental research project: CD1d. It has been a very big pleasure interacting with Enzo all these years. He has been one of the main, if not the main, driving force of this project. His patience has been fundamental in many moments of the project where we had lots of difficulties, especially at the beginning.

Mariolina is another key person in this project. It is impressive to see how efficiently she can work and how good ideas she can have. The work of Michael has also been fundamental, particularly at the beginning, to shape up and tune the overall outcome of the project. I am sure this project will end up nicely!

I am very thankful to the STED super-resolution facility at ICFO. I would like to thank Emilio for performing all the initial measurements and Jordi for his constant technical input throughout these years.

From the personal side, this thesis has been possible due to the personal interactions with many different people. I had great times with Ruth, Gemma, Olga, Jeff, Martin, Mathieu, Alberto, Biagio, Claude, Kyra, Iza, Erik and of course… Van Zanten! (Oldies forever!).

Special thanks to the futbolin gang for so many great games at ICFO: Lukasz, Miquel, Profe, Carmelo, Ivan, Pablo, Xavi, Ramaldinho, Robert, Valeria, Gaetan, Masia, Renaud, Ester, Ion, Jiri and many more!

And my most special thanks go obviously for my closest circle: Isabel and Lidia. They have been a fundamental support in my personal life and they have played a

fundamental role throughout these years. Finally, many special thanks to my parents for their continuous support throughout my entire life.

List of Publications

1. **Torreno-Pina JA**, Manzo C, Garcia-Parajo MF "Receptor nanodomains on cell membranes: sub diffusion behavior and ergodicity breaking", in preparation as an invited review for *J. Phys. D.*

2. **Torreno-Pina JA**, Manzo C, Salio M, Aichinger M, Cerundolo V, Garcia-Parajo MF "The Actin Cytoskeleton down-regulates the activation of NKT cells by segregating CD1d nanoclusters on antigen presenting cells", under review in *Immunity*.

3. Manzo C*, **Torreno-Pina JA***, Massignan P, Lapeyre Jr. GJ, Lewenstein M, Garcia-Parajo MF (2015), "Weak ergodicity breaking of receptor motion in living cells stemming from random diffusivity", *Physical Review X* **5**, 011021.

4. Garcia-Parajo MF, Cambi A, **Torreno-Pina JA**, Thompson N, Jacobson K (2014) "Nanoclustering as a dominant feature of plasma membrane organization", *Journal of Cell Science* **127**, 4995.

- Human Frontier Science Program Awardees' Article -

5. **Torreno-Pina JA***, Castro BM*, Manzo C, Buschow SI, Cambi A, Garcia-Parajo MF (2014) "Enhanced receptor-clathrin interactions induced by N-glycan-mediated membrane micropatterning", *Proc. Natl. Acad. Sci.U S A* **111**, 11037.

- **Highlighted in F1000Prime** -
- **Human Frontier Science Program Awardees' Article** -

6. Massignan P, Manzo C, **Torreno-Pina JA**, García-Parajo MF, Lewenstein M, Lapeyre Jr. GJ (2014) "Nonergodic subdiffusion from Brownian motion in an inhomogeneous medium", *Physical Review Letters* **112**, 150603.

7. Manzo C, van Zanten TS, Saha S, **Torreno-Pina JA**, Mayor S, Garcia-Parajo MF (2014) "PSF decomposition of nanoscopy images via Bayesian analysis unravels distinct molecular organization of the cell membrane", *Scientific Reports* **4**, 4354.

8. Castro BM, **Torreno-Pina JA**, van Zanten TS, Gracia-Parajo MF (2013) “Biochemical and imaging methods to study receptor membrane organization and association with lipid rafts”, *Methods in Cell Biology* **117**, 105.

9. Manzo C*, **Torreno-Pina JA***, Joosten B, Reinieren-Beeren I, Gualda EJ, Loza-Alvarez P, Figdor CG, Garcia-Parajo MF, Cambi A(2012) “The neck region of the C-type lectin DC-SIGN regulates its surface spatiotemporal organization and virus-binding capacity on antigen-presenting cells”, *Journal of Biological Chemistry* **287**, 38946.

- Highlighted in F1000Prime -

10. Bakker GJ, Eich C, **Torreno-Pina JA**, Diez-Ahedo R, Perez-Samper G, van Zanten TS, Figdor CG, Cambi A, Garcia-Parajo MF (2012) “Lateral mobility of individual integrin nanoclusters orchestrates the onset for leukocyte adhesion”, *Proc. Natl. Acad. Sci. U S A* **109**, 4869.

*equally contributing authors